

FAULTS AND FRACTURES IN THE SURAT BASIN

Relationships with Permeability

Final Report
Celoxis System ID: 149310
Report release date: 22 September 2017



Research Team

J. Copley, S. Mukherjee, A. Babaahmadi, F. Zhou, K. Barbosa, S. Hurter, S. Tyson
School of Earth and Environmental Sciences

Acknowledgements

The authors would like to thank the CCSG and member companies (Shell/QGC, Santos, Arrow, Origin) for funding the project.

The Queensland Geological Survey and Department of Natural Resources and Mines, Integrated Geoscience as well as the participating companies provided data and discussion about the content of this report. The project was conceived and initiated by J. Esterle and R. Sliwa of Integrated Geoscience.

Special thanks to Owen Dixon (GSQ) and Andrew Aouad (Origin) for their contributions.

ISBN: 798-1-74272-310-5

Disclosure

This research was undertaken during Term 1 of the UQ Centre for Coal Seam Gas. Term 1 funding was provided by The University of Queensland 22% (\$5 million) and the industry members 78% (17.5 million) over 5 years. An additional \$3.0 million was provided by industry members for research infrastructure costs. The industry members are Shell (QGC), Santos, Arrow Energy and APLNG. The Centre conducts research across Water, Geoscience, Petroleum Engineering and Social Performance themes.

For more information about the Centre's activities and governance see <https://ccsg.centre.uq.edu.au/>

Disclaimer

The information, opinions and views expressed in this report do not necessarily represent those of The University of Queensland, the Centre for Coal Seam Gas or its constituent members or associated companies. Researchers within or working with the Centre for Coal Seam Gas are bound by the same policies and procedures as other researchers within The University of Queensland, which are designed to ensure the integrity of research. You can view these policies at:

<http://ppl.app.uq.edu.au/content/4.-research-and-research-training>

The Australian Code for the Responsible Conduct of Research outlines expectations and responsibilities of researchers to further ensure independent and rigorous investigations.

This report has not yet been independently peer reviewed.

Document Control Sheet

Version #	Reviewed by	Revision Date	Brief description of changes
Earlier versions			Not recorded (early drafts)
V24	AJG	27/02/2017	Updates on working file " <i>CCSG_Report - Faults and Fractures V223 - 8bFeb2017_SM edit JE working AssocProj</i> ". Minor edits made and comments addressed, incorporated as notes in the text or removed in preparation for circulation to CCSG members.
V25 - 27	All authors	various	Revision of all sections following technical working group review
V28	M Sommer and H Schultz	13 July – 10 August 2017	Final edits and formatting
V29	H Schultz	22 September 2017	Watermark removed

Executive Summary

Late Cenozoic deformation affecting the Surat sedimentary succession has resulted in the creation of faults and fractures which can enhance permeability related to coal seam gas (CSG) recovery from the Walloon Coal Measures. These faults and fractures can also create pathways for vertical migration of fluids into and between aquifers. This CCSG project was intended to develop an improved understanding of the nature of the Cenozoic Surat deformation, particularly as it relates to permeability for CSG production. The development of concepts relating to the predictability of fracture distribution and resulting permeability relationship was a core objective for the project.

Faults affecting the Walloon Coal Measures (WCM) are in general small displacement (less than 50m), the majority of which are related to a distinctive style of deformation. Folding of the Jurassic and younger section is often observed to coincide with earlier larger scale Bowen deformation with structural reactivation resulting in broad gentle folds with amplitudes that are a small fraction of the underlying uplift. The deformation observed to primarily affect the WCM is that which forms an often narrow, down-dropped graben block that is tightly folded. These have been termed “keystone” blocks and have been interpreted to reflect a combined compressive and shear or transpressive deformation. In some cases, these features can have a lateral extent of 5-10km but individual faults are discontinuous as displacement is transferred. The majority of faulting or folding observed in the WCM is associated with the keystone structures. An important working hypothesis is that the fracture systems developed by the keystone deformation can be an important contributor to permeability distribution in areas such as Undulla Nose, Kogan Anticline and other areas.

Potentially, these structures can also contribute to CSG flow compartmentalization of parts of the Surat section. In this regard, the relationship between the structural orientation relative to present day stress needs to be further explored.

In addition to the effects of Cenozoic deformation on permeability are the impacts on groundwater. Again the importance of the keystone structures is observed. The primary bounding faults of these features are found to often offset the base Condamine alluvium where data quality is sufficient to image this shallow boundary.

The abundance of the smaller scale structures (compared to the larger regional faults such as the Moonie-Goondiwindi) is expected to have significant influence on pressure distribution in fractured formations and therefore on fluid flow. This work should be integrated to create improved models for fluid flow in the basin.

This CCSG project has assembled and integrated an improved seismic database with well data providing a more comprehensive view of both Bowen and Surat deformation. The regional tectonic compression is interpreted to be transferred as shear into the Surat Basin by underlying zones of weakness oriented at an angle to the dominant NE-SW forces. Reactivation

of Bowen faults is less pervasive than previously proposed in the 2016 Milestone report of this project.

The utilization of all of the available data (wells, 2D/3D seismic) in this final stage of the project presents more detailed mapping than earlier work. The integration of nearly 600 wells to support the seismic interpretation has improved the understanding of deposition and stratigraphic architecture of the Surat Basin.

The integration of over 5000 2D seismic surveys, 10 3D surveys and 580 wells has greatly improved the framework upon which deeper and new understanding of this basin's structure and evolutions will be gained in future work.

While not the original aim of the study, it has highlighted important inconsistencies between historical formation top identification and well to well correlations and seismic data. The inconsistencies appear to be due, at least in part, to the lack of routine reference to the seismic data. The importance of these inconsistencies is likely to be in the dynamic modelling, especially but not limited to the groundwater domain. It is strongly recommended to reassess Walloon and post-Walloon sequence and formation identifications and correlations to make a chronostratigraphic, internally consistent, new set, between core, wireline and seismic data and thus it can serve as a more robust framework for dynamic modelling. By bringing the wells and seismic data together to develop an integrated stratigraphy, new insights will be gained into the depositional architecture of the basins.

This was an unanticipated but valuable result of the final stage of the project leading to CCSG approval for Phase 1 of an integrated chronostratigraphic correlation project, which has since commenced. It also shows the need to not over-define or over-constrain research projects and allow some "room" for discovery of the important but unexpected.

Table of Contents

1	Introduction.....	1
1.1	Research Hypotheses.....	1
1.2	Project Objectives	2
1.3	Project Workflow	2
1.4	Project Deliverables	4
1.5	Structure of this Report	5
2	Regional Geologic Setting.....	6
2.1	Current Understanding of the Tectonic Setting of the Surat Basin	6
2.1.1	The Bowen Basin as precursor to the Surat Basin.....	7
2.1.2	The Surat Basin	7
2.2	Insights from this Project	9
3	Potential Field Interpretation.....	11
3.1	Potential Field Data and Analysis.....	11
3.2	Potential Field Results.....	14
3.2.1	Discussion of potential field interpretations.....	17
3.2.2	Potential Field data: Conclusions and Future work.....	19
4	Integrated Well-Seismic Interpretation	20
4.1	Seismic Data.....	20
4.1.1	2D seismic surveys.....	20
4.1.2	3D seismic surveys	21
4.2	Seismic Data Compilation	22
4.2.1	Data loading and quality control	22
4.2.2	Seismic-to-well ties and horizons	22
4.2.3	Fault interpretation	25
4.2.4	Depth conversion.....	27
4.3	Integrated Well and Seismic Interpretations: Major Structures	29
4.3.1	Goondiwindi Fault System.....	32
4.3.2	Moonie Fault System	36
4.3.3	Transition Zone from Moonie to Leichhardt Fault System	41
4.3.4	Leichhardt-Burunga	43

4.3.5	Hutton-Wallumbilla Fault System	45
4.3.6	Merrivale Block.....	50
4.3.7	The Keystone Structures.....	54
4.3.8	Potential Impact of Faults on Fluid Flow	72
5	Image Log Analysis	79
5.1	Well Data.....	79
5.1.1	Basic logging suites	79
5.1.2	Image logs.....	81
5.2	Image Log Analysis.....	83
5.2.1	In-situ Stress Indicators and Azimuths	85
5.2.2	Faults and Fractures Identification	85
5.3	Image Log Interpretation	87
5.3.1	In-situ stress and fracture variation with structure	87
5.3.2	Seismic sections showing in situ stress and fracture variation	91
5.3.3	Permeability relationship with in-situ stress and fracture orientation.....	94
5.3.4	Image log analysis summary.....	96
5.3.5	Future Work.....	97
6	Mine site photogrammetry and characterisation of joint systems in the SE Surat and western Clarence Moreton Basins	97
6.1	Summary	97
6.2	Introduction	98
6.3	Geological Setting	99
6.4	Methods.....	100
6.5	Results.....	101
6.5.1	Observations.....	102
6.5.2	Joint spacing vs bed thickness	106
6.6	Discussion and Conclusions	111
6.6.1	Origin of Joints.....	111
6.6.2	Joints Associated with Faults.....	111
6.6.3	Joints Associated with Folds	112
6.6.4	Timing of Jointing	112
6.6.5	Bed Thickness vs. Joint Spacing	113
6.7	Acknowledgements.....	113

7	Discrete fracture network model - an approach.....	113
7.1	Introduction	113
7.2	Methods and Results for the field scale DFN.....	115
7.3	Build DFN near well Dalwogan 2.....	120
7.4	A new workflow to build cleats distribution at small scale	125
7.5	Conclusions and future works	132
8	Coal Strength and Fracture Toughness Testing for Synthetic Rock Mass Models.....	133
8.1	Summary	133
8.2	Introduction	133
8.3	Materials and methods	136
8.3.1	JK Drop Weight Test (JK DWT)	137
8.3.2	Short Impact Load Cell (SILC).....	139
8.3.3	Shore Scleroscope Rebound Hardness (SSRH)	144
8.4	Results and Discussion	146
8.4.1	JK DWT	146
8.4.2	SILC.....	147
8.4.3	Tensile strength and UCS on particles	154
8.4.4	SSRH.....	154
8.5	Conclusions	158
9	Conclusions, Outlook and Recommendations	160
10	Acknowledgement.....	166
11	References (by report section)	166
11.1	Regional geologic setting	166
11.2	Potential field Interpretation	167
11.3	Integrated well-seismic interpretation	169
11.4	Image Log Analysis.....	169
11.5	Mine site photogrammetry and joints.....	171
11.6	Discrete Fracture Network Modelling	172
11.7	Coal strength and fracture toughness	174
12	Appendices	177
12.1	Appendix 1	177
12.1.1	JK DWT: The mass distribution as a function of particle size for different samples	177

12.2	Appendix 2	178
12.2.1	SILC particles.....	178
12.3	Appendix 3	180
12.3.1	SSRH.....	180

List of Figures

Figure 2.1 Map views of the (left) Bowen and (right) Surat Basins (© Commonwealth of Australia (Geoscience Australia) 2015).	6
Figure 2.2 Regional Seismic cross section illustrating the major surfaces of the Surat Basin and the more structurally deformed underlying Bowen Basin (image from Martin et al., 2013).	9
Figure 3.1 (a) Outline of airborne magnetic surveys with various resolutions that underpin the mosaic images interpreted in this study; (b) Distribution of gravity measurements across the Surat Basin. Average spacing is between 4 and >10 km.	11
Figure 3.2. (a) Shaded, gridded aeromagnetic data reduced-to-pole (RTP). This grid provides the base data for (b) Downward continuation up to 400 m; (c) Upward continuation up to 600 m; (d) Tilt angle derivative; (e) High Pass filter (cut-off:100km) ; (f) Total Horizontal Derivative of High Pass filtered RTP, overlaying High Pass filtered RTP image. The white line in all figures shows the Surat Basin border.....	13
Figure 3.3 (a) Shaded gridded Bouguer gravity data (Bouguer density: 2.67 g/cc). This grid provides the base data for (b) Downward continuation; (c) Upward continuation up to 1000 m; (d) Tilt angle derivative; (e) High Pass filter (cut-off:100km); (f) Total Horizontal Derivative of High Pass filtered Bouguer, overlaying High Pass filtered Bouguer image. The white line in all figures shows the Surat Basin border.....	13
Figure 3.4 (a) Shaded gridded Bouguer gravity data (Bouguer density: 2.4 g/cc). This grid provides the base data for (b) Downward continuation; (c) Upward continuation up to 1000 m; (d) Tilt angle derivative; (e) High Pass filter (cut-off: 100km); (f) Total Horizontal Derivative of High Pass filtered Bouguer, overlaying High Pass filtered Bouguer image. The white line in all figures shows the Surat Basin border.....	14
Figure 3.5 (a) Tilt angle derivative map of the reduced to pole (RTP) total magnetic intensity with interpreted lineaments. Dashed lines are the lineaments interpreted from the gravity data (Figure 9). (b) A sinistral NW-striking fault separates and drags magnetic anomalies related to Palaeozoic basement rocks. (c) Another NW-striking fault separates Cenozoic basalts sinistrally (Babaahmadi and Rosenbaum, 2016).	15
Figure 3.6 The interpretation of total horizontal derivative image of the high pass image (cut-off: 100km) of gridded Bouguer gravity data, overlying the Bouguer image in the western part of the Surat Basin, indicating major faults in this area. HWF, Hutton-Wallumbilla Fault; MF, Merivale Fault.....	16
Figure 3.7 A map of the basement faults mapped from seismic lines and lineaments interpreted from magnetic and gravity data in the Bowen and Surat Basins (Babaahmadi et al., 2016b). The base image is the Phanerozoic SEEBASE map showing the depth to the Basement.	17
Figure 3.8 Regional lineaments in the Bowen and Surat Basins interpreted from aeromagnetic and gravity data. The lineaments are colour coded based on their location in different orogenic systems.	18
Figure 4.1 (left) Map showing seismic lines included in the project as of 2015 and (right) present-day data base of seismic lines integrated into this project.	21

Figure 4.2 Location of 3D seismic surveys (note North pointing to the right). Grid of 2D lines & Base Surat interpretation.	22
Figure 4.3 Discrete base Surat fault picks (red dot) and keystone structures (magenta) – (CI – 20ms).	26
Figure 4.4 Location map for 90 wells with checkshot data (compiled - blue, all QDEX - green).	28
Figure 4.5 Time versus Depth graph from checkshot surveys. Representative collection.	29
Figure 4.6 A comparison between top Permian structure (left) and base Surat unconformity (right) with equal contour intervals (20ms) shows the maximum Surat depth to be well south of the deeper Taroom trough of the Bowen succession. Major Bowen structures have only minor reactivation during the Cenozoic.	31
Figure 4.7 Eastern margin Surat Basin - deformation components. Underlying Bowen fault trends (dashed) (CI-20ms).	32
Figure 4.8 Goondiwindi: Southernmost profile showing tightly folded Permian in Bowen section with monoclinial dip in overlying Surat. Map to the left shows location of seismic line relative to the base Surat time structure map (CI – 20ms).	33
Figure 4.9 Southern Goondiwindi profile: High angle reverse faults with tightly folded Permian. Map to the left is time structure for the base Surat unconformity (CI – 20ms) with line locations for Figures 23/24. Note monoclinial dip over frontal Bowen structure, with Cenozoic uplift reactivating one fault in the system. The GFS appears related to a small subsidiary structure about 15km to the west.	34
Figure 4.10 A subsidiary, related fault complex west of the GFS also creates gentle folding in the Surat succession.	35
Figure 4.11 Goondiwindi at transition to Moonie, scan profile location in Figure 4.9.	36
Figure 4.12 Moonie Fault System - profile location map. Note change in trend for folds in Surat (CI – 20ms).	37
Figure 4.13 Moonie Fault System - Profile 2, strike along structure crest. Illustrates cross faults offsetting Permian strata below Moonie field and the abrupt fold coinciding with offset of the base Surat fold trend.	38
Figure 4.14 Profile 1 through the Moonie structure from 3D survey. Line location Figure 4.12.	39
Figure 4.15 Profile 3 - through the Moonie structure to NE of 3D, location on Figure 4.12. Fault system becomes more complex with multiple high angle faults representing Bowen deformation, with gentle slightly asymmetric folding in the Surat.	40
Figure 4.16 Moonie Fault System - Profile 4. Note reduced magnitude of Bowen Uplift from previous.	41
Figure 4.17 NE Moonie Fault, profiles located on Figure 4.12. Profiles show progressive development of tightly folded Permian section below gently folded Surat succession. The development of keystone structures in the Surat appears preferentially located at the margin of Bowen deformation.	42
Figure 4.18 Eastern Margin Surat Basin: comparison of structure at top Permian, base Surat and Intra-Springbok. Contour intervals equal (20ms), same color bar and scale.	42
Figure 4.19 Composite view of Burunga anticline and example profiles. Left panel is “3D”	

structure on top Permian coal, with a horizon grid for the base Surat unconformity above. Right panel shows profile location and seismic data grid.43

Figure 4.20 Burunga Anticline Profile 1.....44

Figure 4.21 Burunga Anticline Profile 2.....44

Figure 4.22 Burunga Anticline Profile 3.....45

Figure 4.23 Hutton-Wallumbilla, late inversion, south end. Yellow line on the left index map is section location.46

Figure 4.24 Hutton-Wallumbilla, late inversion, south end, initial faulting. Yellow line on the left index map is section location.46

Figure 4.25 Hutton-Wallumbilla in Coxon Creek area.....47

Figure 4.26 Hutton-Wallumbilla,. Yellow line on the left index map is section location. Progressive development and additional deformation to the west.47

Figure 4.27 The northern Hutton-Wallumbilla and interaction with the Merivale, Simmie and other major fault systems. On the east side of HWFS, an area of Cenozoic keystone faulting is overprinted on Bowen deformation. This is an area of high productivity CSG production from the Permian coals.48

Figure 4.28 Hutton-Wallumbilla, Yellow line on the left index map is section location. Major deformation shown by the complex faulting and to the left the remnant fault.49

Figure 4.29 Hutton-Wallumbilla, Yellow line on the left index map is section location. Development of the graben with increasing offset on the western fault.49

Figure 4.30 Hutton-Wallumbilla, Yellow line on the left index map is section location. Northern end of this structure with minimal deformation in the Surat.50

Figure 4.31 Merivale to Hutton-Wallumbilla area with locations for Profiles 1-3.....51

Figure 4.32 Merivale Fault: Profile 1.52

Figure 4.33 Merivale Fault: Profile 2.52

Figure 4.34 Merivale Fault: Profile 3.53

Figure 4.35 The Merivale Block, relative amplitude at Top Permian (left) and Base Surat (right) levels.54

Figure 4.36 Keystone structure examples, faults shown in red. Common characteristics are multiple faults diverging upwards with generally net negative displacement between bounding faults, often with internal anticlinal folding.55

Figure 4.37 Illustration of the development of a keystone fault structure (Ben-Avraham & Zoback, 1992) The schematic diagrams provide a conceptual basis for keystone formation. Shear can develop either positive or negative flower structures depending on the geometry of the transfer zone which may be controlled by underlying zones of weakness.56

Figure 4.38 Development of Riedel shear and conjugate faulting. The figure shows a time slice (498ms, approximating the local base Walloon) through the coherency volume created with a 15 sample correlation window. Discontinuities show as red in the display colour bar.....57

Figure 4.39 Base Surat on the eastern margin (c.i. 20 ms). Identified keystone features in pink. (C.I.-20ms).....58

Figure 4.40 3D surveys with coherency slices through the Walloons in each survey (C.I.-20ms).59

Figure 4.41 Undulla Nose Area - base Surat unconformity (C.I.-20ms).60

Figure 4.42 Undulla Nose 2D profile showing uplift at margin of Surat Basin. Near flat lying Permian subcrops below the base Surat unconformity. The WCM is nearly undeformed with the exception of keystone faulting on the west side of the uplift.60

Figure 4.43 Undulla 3D coherency slice (left) at Base Surat showing the root of the keystone highlighted in yellow and (right) the profile marked red on the map.61

Figure 4.44 Undulla 3D coherency slice (left) at base of Walloon (yellow on profile). The faults are dark lines in the coherency display.61

Figure 4.45: Undulla 3D coherency slice (left) at base of Walloon (yellow on profile) and shows transition in deformation from the northern keystone to the southern keystone.62

Figure 4.46 Keystone structure development in the Lauren 3D survey.....63

Figure 4.47 3D view of J45 horizon (upper WCM) with keystone fault trend.63

Figure 4.48 DC3D to Scotia area base Surat structure (c.i.-20ms).64

Figure 4.49 Dalwogan-Condabri (DC-3D) coherency slice below Base Surat. Shear offset within the Permian section. Conjugate faults observed as part of the shear zone.65

Figure 4.50 Profile DC-3D profile along the yellow line in Figure 34 and slice location indicated in yellow. The faults on both the slice and the profile are shown by the fat arrows.65

Figure 4.51 A coherency time slice in WCM showing complex keystone fault deformation. ...66

Figure 4.52 Profile from the Dalwogan-Condabri 3D volume. Dipping reflectors below the base Surat unconformity are the subcropping Permian coals. Note the offset continues to the very shallow section, with displacement above the WCM. The base Alluvium reflector appears to preferentially erode deeper above the keystone.67

Figure 4.53 Keystone faulting on the eastern Surat margin observed to be controlled by underlying NE-SW structural weakness.68

Figure 4.54 Top Permian structure and location of Fairview 3D.69

Figure 4.55 Keystone example A on 2D Permian SW Surat.70

Figure 4.56 Keystone example B on 2D Permian SW Surat.....70

Figure 4.57 Fairview 3D coherency slice.71

Figure 4.58 Profile through SE of larger scale structure.....72

Figure 4.59 Profile through SE of larger scale structure.....72

Figure 4.60 Location of Condamine gas seeps from Summary Technical Report.....74

Figure 4.61 Seismic profile close to gas seeps in Condamine River (projected). Inset shows profile location (red) and 2 gas seeps with the line of projection to the seismic profile.75

Figure 4.62 W to E profile displaying impact of the keystone structure on ‘topography’ of the base Condamine. Structure of unconformity to left (C.I.-5ms, yellow-shallow, purple-deep). Note conformance of keystone faults with abrupt erosional features. These features have a trend parallel to the deformation.76

Figure 4.63 Contour of c.i. 5ms of the Base Condamine (left) and coherency superimposed (right). This demonstrates the relationship between faulting and the erosional topography. .77

Figure 4.64 Coherency slice, Google Earth image and seismic profile show location of a spring coinciding with the location of keystone faulting.78

Figure 5.1 Map showing wells used in this study. Wells with sonic logs, red for well ties (~580).80

Figure 5.2 Map showing Base Surat time surface and image logs included in this study (also

reported in Milestone 3a Mukherjee et al., 2016).....	82
Figure 5.3 Methodology flow chart: Image logs.....	84
Figure 5.4 Image log interpretation classification scheme.	84
Figure 5.5 Examples of in-situ stress indicators observed in borehole image logs (Mukherjee et al. 2017, unpublished).	85
Figure 5.6 Examples of micro-faults and fractures observed in borehole image logs. Micro-faults, conductive and resistive fractures are indicated by red, green and light blue colour, respectively.....	86
Figure 5.7 Fracture abundance measures (source: Dershowitz & Herda, 1992; Mauldon & Dershowitz, 2000).....	86
Figure 5.8 Map showing major structures observed in the Surat sedimentary succession (Babaahmadi et al. 2016, Copley et al. 2017) along with location of analysed wells and structural domains within the study area. The map overlies the Base Surat time structure map.	88
Figure 5.9 Orientation of present day maximum horizontal stress (S_{Hmax}), interburden and coal fractures in the Leichhardt – Burunga Fault system (LBFS) area, Undulla Nose and near Kogan anticline and south east Moonie – Goondiwindi Fault System (MGFS). The number of each for each area / domain is indicated below the rose diagram. Stress orientations are measured in True North. Rose diagrams are in linear radial scaling.....	89
Figure 5.10 Map showing fracture density distribution (P10) within Walloon Coal Measures from the interpreted wells.	90
Figure 5.11 Seismic section showing in-situ stress and fracture variation in the Leichhardt – Burunga Fault System.....	91
Figure 5.12 Seismic section showing change of stress orientation observed through the WSG within Hopeland 17 well in the Undulla Nose area. The stress orientation variability attributed to the structural complexity present within and near vicinity to the well.	92
Figure 5.13 Seismic section showing the variation of in situ stress and fracture orientation in Maire Rae 2 well within the WSG in the SE part of Moonie – Goondiwindi Fault System.	93
Figure 5.14 Seismic section showing in-situ stress and fracture variation in the SE of Moonie - Goondiwindi Fault System.....	93
Figure 5.15 Permeability (calculated from well test) relationship with effective vertical stress (σ_v) and in-situ stress orientation.....	94
Figure 5.16 Permeability relationship with effective vertical stress (σ_v) and angle between in-situ stress and coal fractures.....	95
Figure 5.17 Seismic section showing keystone structures on and near the Hopeland 2 well. ..	96
Figure 6.1 A simplified tectonic framework showing the Permian and Mesozoic sedimentary basins in the eastern Australia. CMB = Clarence-Moreton Basin.	99
Figure 6.2 A map showing the faults and folds and the location of mine sites in the SE Surat Basin. The base map is the Phanerozoic SEEBASE map showing the burial depth to the Basement (FrogTech, 2006) which underlies the gridded image of the top of the Durabilla Formation. Faults and folds interpreted by Babaahmadi et al., 2015.	100
Figure 6.3 An example of a spatially registered photogrammetric model of a highwall is used for analysis of joints. Inset higher resolution photo was taken along the strip outlined in yellow. The joints were marked as green planes in the insert figure to show the joint spacing along one	

orientation (Rudd, 2016). Note that this highwall is not necessarily representative of all highwalls and seams.....101

Figure 6.4 NW- and NE-striking faults and lineaments parallel to eastern and western limbs of the Texas Orocline, respectively (Babaahmadi and Rosenbaum, 2015).....102

Figure 6.5 (a) A map shows the location of the New Acland Mine and the faults are interpreted as sinistral strike-slip. The background image is the first vertical derivative of aeromagnetic data showing the magnetic lineaments and the shallow Cenozoic volcanic rocks. (b) The southern lineament which is interpreted as a fault displacing Cenozoic basalts and a basaltic lava flow (Babaahmadi and Rosenbaum, 2015). (c) Faults provided by company geologists, illustrating the general orientation of and distance between the normal faults as mapped..103

Figure 6.6 Example of a small scale thrust fault with a throw of about 1.5m forming kink band. The strike orientation of the high angle reverse fault is ESE.104

Figure 6.7. Examples of faulting in the coal measures. (a) Strike-slip normal faults. The overlap between two faults produced a restraining step-over zone, producing small reverse faults and folds in the upper part. The photo view is toward ESE. (b) A schematic map - view cartoon of a restraining step-over zone between two strike-slip normal faults, thought to be a mechanism for fault formation.....104

Figure 6.8 The highwall for photogrammetric survey (March 2016). The photo was taken approximately 30m away from the highwall face. The basal seam that is exposed in the foreground is the D8 Seam; black and white sheets of an A3 card (42 x 30 cm) were put at the base of the highwall. The inset figure shows the inclined joints in sandstone.105

Figure 6.9 Example of a stereo-image pair was used to measure the thickness of joint and lithological bedding, and joint azimuths. Bedding boundaries are indicated by red lines. Large vertical joints were also observed in sandstone (marked by the V) as were inclined joints. These joints penetrate multiple horizons and were excluded from the test of joint spacing against bed thickness.105

Figure 6.10 Vertical joint azimuths from the coal-clastic units (photogrammetry; azimuthal range; black, "C"), vertical joints (compass line of sight; single line; pink, "V"), inclined joints (compass line of sight; single line; red, "I"), floor shale (compass on pavement, single line, black, "F").....106

Figure 6.11 The relationship between the bed thickness and joint spacing measured from 4 photogrammetric stereo pairs.107

Figure 6.12 Comparison of coal joints and clastic joints measured from 4 photogrammetric stereo pairs.107

Figure 6.13 A north-striking gentle anticline in the Wilkie Creek Mine deformed the Walloon Coal Measures and Springbok Sandstone. This anticline is disrupted by two small thrusts. .108

Figure 6.14 Comparison of coal joint, surface fault and fold azimuths at the Wilkie Creek Mine. Inset shows surface faults (blue lines) and faults in basement- (hatched). The mine did not disclose the style and throw of these faults.....108

Figure 6.15 A scatter plot showing the joint spacing against bed thickness for two joint sets through the analysis of high resolution 2D small scale photos from the Kogan Creek, Wilkie Creek, and Commodore Mines.....109

Figure 6.16 Azimuths of joints in coal and thrust faults from the Kogan Creek Mine. The azimuth

of the Wambo Fault is also shown for comparison.....	109
Figure 6.17 A map shows the observed thrust faults in the Kogan Creek Mine. Faults 1 and 2 have approximately strike azimuths of 147 and 135, respectively.....	110
Figure 6.18 (a) One of the thrust faults associated with a hanging-wall anticline in the Kogan creek mine. (b) The development of conjugate joints in the crest of the anticline.....	110
Figure 6.19 Azimuths of joints in coal and shale, faults (and dykes that have intruded faults), and folds/rolls, Commodore Mine.	111
Figure 6.20 A schematic model (map view) showing the development of joints in the overlap zone of the two ENE-, N- and NW-striking normal faults.....	112
Figure 6.21 3D representation of various joints that form in folded strata (based on Twiss and Moores, 2007). Brown = cross joints (equivalent to face cleat), green = longitudinal joints, pink – diagonal joints.....	112
Figure 7.1 Wireline log example and well markers at a borehole near a photo showing the coal beds from a highwall. GR is Gamma ray; CALI is caliper; and SD-DEN is shallow depth density. B, C, D, and E are coal seam name and numbers are ply or coal bed number.	116
Figure 7.2. Density distribution of fracture diameters, illustration on a log-log diagram. (a) from Darcel et al. (2006); (b) length distribution of 69 faults from the mine.	116
Figure 7.3 Comparison of fracture distribution with different scale and dimension parameters.	117
Figure 7.4 Joint spacing increases with the increase of bed thickness in different lithological units (Babaahmadi et al., 2016, report).	118
Figure 7.5 Processing figures at each phase of generating the DFN near the borehole.....	119
Figure 7.6 Rose diagram of the average orientations of two dominant joint sets in coal (black) and sandstone (pink) of the study area (Babaahmadi et al., 2016, report).....	119
Figure 7.7 Joints distribution was generated for coal beds from A4 to D8. Results illustrate that thinner coal beds have narrower joint spacing and higher joint density than thicker coal beds and interburden partings.....	120
Figure 7.8 DFN at wellbores from the interpreted fractures by image logs.	121
Figure 7.9 Wireline logs, lithology, depositional facies, image log interpreted fractures and their properties and formation markers (data were from Mukherjee et al., 2016, report). In rose diagrams, purple points are coal seam fractures. DST=drill stem test.	122
Figure 7.10 Fracture density (P32; fracture area per volume) distribution near well Dalwogan 2.	123
Figure 7.11 DFN modelling results near well Dalwogan 2.....	124
Figure 7.12 (a) DST analysis in Fekete; (b) DFN model; (c) simulated pressure profile at the end of well test; and (d) pressure comparisons of measured, simulated by using a homogeneous and DFN models.....	125
Figure 7.13 Diagram showing the fractures at different scale.....	126
Figure 7.14 Location of wells for this study in the Surat Basin.	127
Figure 7.15 Workflow for cleats modelling by MPS used in this study.....	127
Figure 7.16 Histogram of coal cleat spacing from borehole A, B, and C which were shown in Figure 7.12. Data were sourced from the well completion reports for these three wells. Statistics of cleat spacing showing three peaks, e.g. 10mm (average from 3mm to12 mm),	

20mm and 30mm.	128
Figure 7.17 One realisation of cleats distribution. Plan view from top.	128
Figure 7.18 Cleats distribution in Petrel with horizontal grid size of 1 mm. Model size is 1m by 1m by 0.1 m.	129
Figure 7.19 Interpreted coal cleats for four thin coal seams. Thicknesses of CS1 to CS4 are 5, 6, 5 and 6 cm, respectively (data were from Mukherjee et al., 2016, report).....	129
Figure 7.20 Strikes for conductive fracture and fault which was assumed as the azimuth of face cleats.....	130
Figure 7.21 (a) Geological model shows the zones for each coal bed; (b) coal beds identified from image log.....	130
Figure 7.22 Image log interpreted coal cleats were converted to probability which is used in MPS modelling for cleats.....	131
Figure 7.23 One realisation of coal cleats distribution near wellbore (a), and a ring showing cleat distribution at borehole wall.	131
Figure 7.24 Cleats distribution compared with CT extracted cleats. Note that the position of this CT image is not exact.	132
Figure 8.1 Photographs of a coal seam within the Walloon Coal Measures showing a) the interbedded nature of the plies and b) the interbedded and banded nature of the coals plies.	135
Figure 8.2 Variation in coal strength relative to rank as estimated by carbon content. From Palmer et al., 2005 cited in Deisman, 2016.	135
Figure 8.3 Characterisation of sub bituminous coal using destructive and non-destructive tests.	136
Figure 8.4 The machine, standard sizes and energies used in the JK DWT test.....	138
Figure 8.5 The machine and sizes used in the SILC test.	140
Figure 8.6 Examples of graphics for force and energy absorbed as a function of time from cylinders.....	141
Figure 8.7 Examples of graphics for force and energy absorbed as a function of time from single particles.	141
Figure 8.8 Example of selecting distinct fracture point, in this case from a difficult curve.	142
Figure 8.9 The equipment and sizes used in the SSRH test.....	145
Figure 8.10 SSRH conversion table - IMAI SIKENKI Co. equipment (Tokyo – Nov. 1970, No 700756) - extrapolated for shore >80.	145
Figure 8.11 Comparison of t10 % produced at different size distribution.....	146
Figure 8.12 Breakage characteristics of the mine sub bituminous coal compared with Goonyella Lower seam dull banded bituminous coals.	147
Figure 8.13 Example of cylinders drilled for sample #1 at C8 ply banded (a) sample before and (b) after drilling.	148
Figure 8.14 Specific fracture energy distributions for sub bituminous coal C8 ply banded of 125 mini-core cylinders ($\approx 12\text{mm}$ in diameter and ratio >0.8) of subbituminous coal.	148
Figure 8.15 Specific fracture energy distributions of cylinders drilled perpendicular to band. Lines represent the fit to the log-normal distribution.	149
Figure 8.16. Specific fracture energy distributions of cylinders drilled parallel to bands. Lines	

represent the fit to the log-normal distribution.	150
Figure 8.17 Specific fracture energy distributions of cylinders drilled perpendicular and parallel to bands. Lines represent the fit to the log-normal distribution.	150
Figure 8.18 Histograms for DTS values estimated from BTS for (a) C8 ply with banded coal and (b) C6 ply with dull coal.	151
Figure 8.19 Histograms for UCS values estimated for (a) C8 ply banded and (b) C6 ply dull (Altindag and Gurney, 2010).	151
Figure 8.20 Histograms for m_i values estimated for (a) C8 ply banded and (b) C6 ply dull (Altindag and Gurney, 2010).	152
Figure 8.21 Particle fracture energy distributions for C6 ply - dull of the mine sub bituminous coal comparing different size distribution.	152
Figure 8.22 Particle fracture energy distributions for mudstone of the mine comparing different size distribution.	153
Figure 8.23 Particle fracture energy distributions for C6 ply - dull of the mine sub bituminous coal comparing different size distribution.	153
Figure 8.24 Particle fracture energy distributions for D8 ply – banded low ash of the mine sub bituminous coal comparing different size distribution.	154
Figure 8.25 SSRH test of dull category from the C8 ply banded mine sub bituminous coal....	155
Figure 8.26 Bright band versus dull category from C8 ply banded, the mine sub bituminous coal.	156
Figure 8.27 SSRH test at bright and dull samples from Guluguba-2 sub bituminous coal.....	157
Figure 9.1 Comparison between OGIA well picks and those defined by well-seismic integration. Figure is from the Surat Framework Milestone Report, Oct-2015, bin size is increased from the original display to 10m. Annotation is added for statistical clarity. The broad range of difference (~100m) for the Top Springbok illustrates demonstrates the inconsistency. [See footnote for historical context]	162
Figure 9.2 Representative profile showing inconsistent Springbok correlation in regional correlations (OGIA, 2015) with seismic profile. This is the Muggleton area near Reedy Creek.	163
Figure 9.3 Lauren area profile with OGIA lithologic correlation inconsistency relative to interpreted seismic horizon.....	163
Figure 9.4 OGIA correlations from Burunga area profile.	164
Figure 9.5 Representative profile showing integrated sequence stratigraphic correlations, Lauren area. Profile flattened on the J50.2 (above top WCM). Synthetic traces are shown to match seismic data. Note 6 correlated sequences within WCM.	165

List of Tables

Table 1: Project Workflow (Stages and Tasks)	4
Table 2: Parameters from image log interpreted data for DFN modelling.	123
Table 3: Locations, rock material and conducted laboratory tests.....	137

Table 4: Summary SILC results for particles and cylinders154
 Table 5: Average SSRH results shore and tensile strength (approximate) of dull coal C8 ply banded156
 Table 6: Summary SSRH results158

List of Digital Deliverables

File Name	Content
	A1 scale map of structural framework
	GIS layers for faults and folds
	GIS layers for data sources
	Petrel project for seismic interpretation (w/logs & well ties)
	GSQ open file 2D survey folders for Surat
	GSQ open file 3D survey folders for Surat
	Excel spreadsheet – Checkshot surveys

1 Introduction

Understanding and predicting permeability is a major factor affecting CSG reservoir performance and is a fundamental technical challenge for bringing LNG to market in Queensland. A similar challenge will exist as the industry moves towards accessing future lower permeability resources. Fault and fracture systems in coal measures can compartmentalize a reservoir vertically and horizontally or alternatively enhance flow and recovery. The ability to predict faults and fractures which enhance permeability is less than perfect. This project was intended to develop a robust structural framework for the Surat Basin fully utilizing all available geophysical and well data.

Primary focus was to develop a more detailed understanding of those faults and associated fracture systems that intersect the Jurassic Walloon subgroup and younger sequence from integrated analysis of seismic, well and potential field data, coupled with more detailed analysis of open cut coal exposures and subsurface image logs. Hypotheses for basement control and Cenozoic reactivation of structures are evaluated.

In parallel, two PhD theses in progress are associated with this project and the Surat Geological Framework Project. One examines the relationship between structure, stress and field scale fractures using image log analysis (Mukherjee) and the other is to develop a “synthetic rock mass model” of the Jurassic coals (in comparison with Permian) to assist in the prediction of reservoir response to gas production (Barbosa). The results from those studies to date are included in this report.

1.1 Research Hypotheses

This project was proposed with the following *research hypotheses*:

- A consistent structural model for the Surat Basin can be developed
- Faults and fractures intersecting the Walloon Subgroup can be related to regional tectonic events and the influence of underlying zones of weakness during the Mesozoic and Cainozoic deformation events
- The relative orientation of fractures and local stress influences permeability
- Changes in stress orientation during reservoir depletion can affect decline rates
- Fracture character (length, spacing, aperture, persistence) is related to the rheology of the material, and this relationship can be used to condition fracture network models
- An understanding of the fault and fracture network in the Surat Basin can inform reservoir models, in particular permeability variation

1.2 Project Objectives

The initial *project objectives* and task were to:

- Compile a consistent database of 2D seismic profiles throughout the Surat Basin
- Integrate well for horizon interpretation
- Compile regional to local potential field (gravity and magnetics)
- Document variations of fault style and fracture character between structural domains within the basin (from seismic survey and potential field data)
- Examine re-activation of faults and fracture systems during various tectonic events, with particular focus on the Cenozoic period and present day stress
- Examine the role of “basement” in fault and fracture network development
- Establish links between fault style, fractures and lithology (coal and interburden) using image logs and 3D photogrammetry
- Develop discrete fracture network model(s) for the Walloon Subgroup coal measures and selected overburden
- Develop a synthetic rock mass model for Surat coals (in comparison to Bowen coals) that will assist in reservoir assessment and modelling

The data and knowledge compiled in this report has relevance for coal seam gas production, but also the interconnectivity with and behaviour of aquifers within the Surat Basin.

1.3 Project Workflow

Project development (workflow) was structured into two stages (with a possible extension to Stage 3) with tasks assembled in

Table 1. Stage 1 consisted of the compilation and development of a consistent structural framework. Stage 2 comprised an integrated fault and fracture analysis that supports development of a discrete fracture network model (DFN) and rock mass/reservoir modelling. Stage 3 would be a project extension with further work to establish links between fault and fracture character, permeability, and geotechnical behaviour in the wells and to document relative distribution of fault and fault fracture networks within the Walloon Subgroup and between adjacent aquifers, including future geodynamic modelling of Surat Basin deformation. This report is for Stages 1 and 2.

Table 1 Project Workflow (Stages and Tasks).

Stage 1 Tasks	
1	Compile a consistent database of open file 2D seismic sections across the Surat Basin, with focus on gas fairway domains (eastern, northern, and north western)
2	Compile regional and local potential field data sets (gravity, magnetics)
3	Conduct 3D photogrammetry at available mine sites for detailed fault/fracture characterisation and development of discrete fracture network models
4	Compile image logs (and company interpretations where available) as input to synthetic rock mass model for prediction of coal behaviour under varying stress conditions (PhD projects-Mukherjee and Barbosa)
5	Document variations of fault style and preliminary fracture character between structural domains within the basin based on seismic survey and photogrammetry
6	Preliminary report
Stage 2 Tasks	
1	Detailed analysis of borehole image data and integration with mine-scale photogrammetry to establish links between fault/fracture statistics and lithology (coal and overburden) (PhD project-Mukherjee)
2	Develop of coal indices (based on rank, type and grade) that contribute to synthetic rock mass model as input to Surat Basin reservoir modelling (PhD project-Barbosa)
3	Examine re-activation of major structures during various tectonic events, with particular focus on the Cenozoic period and present day stress (links in with ACARP project on Bowen Basin)
4	Examine the role of “basement” in fault and fracture network development through integrated analysis (inversion) of potential field and seismic data, coupled with available well control)
5	Project report and development of Stage 3 activities focused on reservoir behaviour, but also geodynamic modelling to test hypotheses for the development of structures

1.4 Project Deliverables

The project deliverables would be:

1. Structural interpretation maps and digital data (GIS format) at the level of the Jurassic unconformity and from within the Surat Basin sequence:
 - a. Fault picks from the seismic interpretation
 - b. Characterization of “keystone” features
 - c. Fault picks from potential field data, assessed against subsurface information
 - d. Horizon interpretation is required to support fault interpretation
2. Final Petrel project (2D/3D seismic, attributes, well ties, horizons)
3. Fault and fracture maps from available outcrop and mine sites, documented by photogrammetry
4. A discrete fracture network model for coal measures
5. A synthetic rock mass model for coal
6. Reports discussing the:
 - a. Method of structural interpretation

- b. Fault characterization including the style, throw, orientation and reactivation history of fault types during Meso- and Cainozoic events
 - c. Structural domains that can be used to compartmentalize the deformational style across the region
 - d. Impact of basement controls on the distribution of faults in the Surat Basin
7. Application of coal synthetic rock mass models (PhD thesis-Barbosa)

1.5 Structure of this Report

This document is the final report of the Faults and Fractures Project and summarises the work of Stages 1 and 2. Following this introduction (Chapter 1), Chapter 2 describes the data assembled for this project (potential field, seismic, wells) and Chapter 3 discusses the methodologies used to manipulate and interpret each data type. Results are discussed in Chapter 4. In Chapter 5, several associated projects are described: photogrammetry of mine sites, synthetic rock mass and derived GIS products. The project is pulled together for an integrated discussion on the Surat Structural Framework and additional insights gained in this project in Chapter 6. Finally, Chapter 7 discusses briefly the potential impact of faults and fractures on flow in the Walloon Subgroup and relevant aquifers. The report is closed with a summary of insights developed and an outlook on recommended future work.

2 Regional Geologic Setting

2.1 Current Understanding of the Tectonic Setting of the Surat Basin

Eastern Australia has undergone a series of major tectonic events. Often these are followed by extensive erosional periods, perhaps due to the continental uplift resulting from the plate interactions. In the nomenclature adopted for the region, the depositional successions between major unconformities are given a separate basin name.

The Surat Basin is a large Early Jurassic to Early Cretaceous intra-cratonic basin (~ 300,000 km²) in eastern Australia. It overlies the Permo-Triassic Bowen Basin (~ 240,000 km²) in southern Queensland. Gas is being extracted from extensive coal seams deposited in both basins (Figure 2.1).

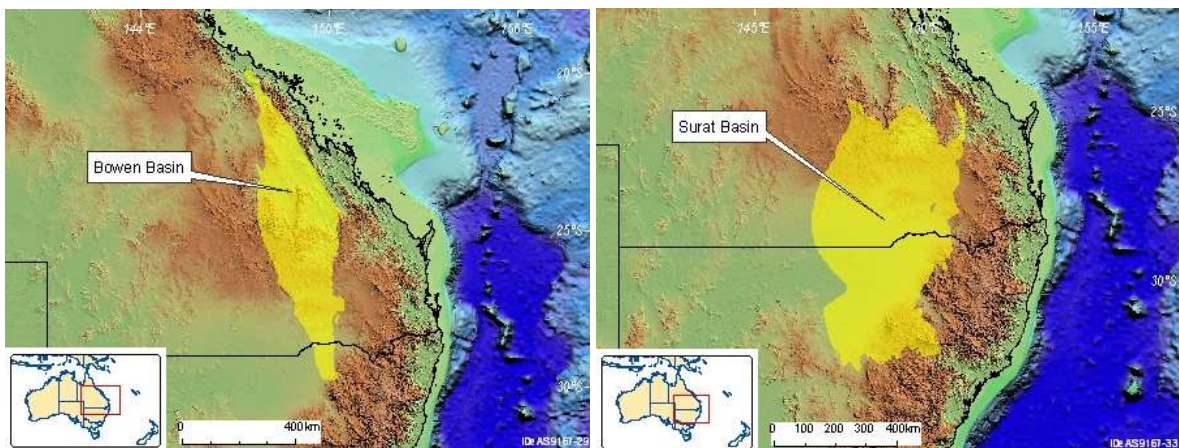


Figure 2.1 Map views of the (left) Bowen and (right) Surat Basins (© Commonwealth of Australia (Geoscience Australia) 2015).

As the Surat Basin may be influenced by structural features of the Bowen Basin, the geological elements of interest for and the evolution of the two basins based on the work of Korsch and Totterdell (2009) are described with other references as cited. The stratigraphy of Korsch and Totterdell (2009) is used with much of the previous work based largely on the schemes of Exon (1976) and Elliott and Brown (1988). These units are based on lithologic criteria as summarized in Green¹ et al. (1997) and Hoffmann² et al. (2009).

Some of the work mentioned above is the result of The Sedimentary Basins of Eastern Australia project by Geoscience Australia (SBEA, 1994), a multidisciplinary study of several eastern Australian basins (Bowen, Surat, Gunnedah) under a collaboration of federal and state government organizations. It consisted of an integrated basin analysis (tectonic, structural, sequence stratigraphic and sedimentary analysis and thermal histories). Regional seismic interpretation was undertaken guided by sequence stratigraphic principles, though

¹ LITHOSTRATIGRAPHIC UNITS IN THE BOWEN AND SURAT BASINS, QUEENSLAND P.M. Green, D.C. Carmichael, T.J. Brain, C.G. Murray, J.L. McKellar, J.W. Beeston & A.R.G. Gray.

² HOFFMANN K. L., TOTTERDELL J. M., DIXON O., SIMPSON G. A., BRAKEL A. T., WELLS A. T. & MCKELLAR J. L. 2009. Sequence stratigraphy of Jurassic strata in the lower Surat Basin succession, Queensland. *Australian Journal of Earth Sciences* 56, 461 - 476.

limited well-seismic ties are presented. Furthermore, SRK Consulting was funded by the Queensland Department of Natural Resources and several gas and mining companies for the Bowen and Surat Basin Structural Framework Study in the period 2005-2007 (Woodfull, 2008).

2.1.1 The Bowen Basin as precursor to the Surat Basin

The north-south elongate diamond shaped Bowen Basin extends from the New South Wales border in the south about 1200km to the north over a width of 200km. Its history spans the Early Permian to Middle Triassic with deposits from fluvial, lacustrine and deltaic settings with minor marine influx. It developed upon a basement of Early Paleozoic metamorphic and sedimentary rocks and initiated with rifting that resulted in a series of isolated fault-bounded rapidly subsiding basins filled with volcanic rock and sediments. These grabens and half-grabens trended NS to NW; NE and NW trending normal faults and transfer faults, respectively, subsequently influenced deposition and deformation of the late Permian coal measures (Esterle and Sliwa, 2002). Rifting ceased by Middle Permian and a thermal relaxation phase ensued causing widespread subsidence and marine dominated sedimentation up to the Late Permian. Foreland loading during the latest Permian caused progressive filling of the basin in alluvial environment. In the Middle Triassic, the thrust front of the New England Orogen in the east moved to the west, effectively terminating sedimentation and concluding the history of this basin.

The Bowen Basin is structurally very complex, with extensional fault systems, volcanic activity and thrust faults as well as repeated reactivation of structures. Large scale compressional structures resulting in dominantly vertical movement with an interpreted shear component are observed in this report throughout the deeper Bowen basin within the study area. The major zones of deformation are often observed to have a series of high angle reverse faults and tightly folded Permian across a zone of 3-5km in width. Net uplift across this zone substantial to the north (Burunga) and somewhat less to the south (Goondiwindi) could be as much as 2-4 km. Total shortening is variable (estimate ~5-10 km). Major structures developed along the eastern margin have limited net shortening considering the regional extent of the deformation zones.

Where seismic data is of sufficient quality to image the pre-Permian graben structural boundaries, it appears that this earlier deformation controls in part the orientation of Bowen structures. These were also documented in the northern Bowen Basin by Sliwa (Esterle and Sliwa, 2002). Each tectonic event is influenced by the previous zones of weakness.

2.1.2 The Surat Basin

After deformation ceased, extensive erosion in the Late Triassic created a peneplain upon which the Surat Basin accumulated. Its geometry is broadly north-south elongate typical of an intracratonic sag basin, suggesting subsidence was driven by thermal relaxation of the lithosphere. However, another mechanism may fit better tectonic subsidence curves obtained from back-stripping: subduction induced convection in the upper mantle (Korsch

and Totterdell, 2009; Waschbusch et al., 2009). Subsidence rates were much lower than those in the Bowen Basin and stopped about 95Ma followed by basin inversion, uplift due to rebound of the lithosphere and denudation. Several erosional outliers and down-faulted areas of Surat Basin sediments occur to the east and north-east, suggesting that the original Surat Basin extended much further east, at least as far as the present coast of Queensland.

The major part of the Surat Basin is preserved as the single large Mimosa Syncline which plunges gently southward in southern Queensland. Dips are mainly low and centripetal. A thickness of up to 2500m of sediments is preserved. Accommodation rates varied widely during the accumulation of the dominantly clastic succession, increasing rapidly during deposition of the WCM. For example, the thickness of the WCM and the base Surat to top Hutton are roughly equivalent. Dates assigned to the boundaries of the intervals show some 35 Myr for the basal units but ~5 Myr for the WCM (Reilly, 2016, Wainman, et al., 2015), suggesting a differential accommodation rate factor of about 7:1.

The Surat Basin fill is more extensive than that of the underlying Bowen Basin. Component formations therefore have a more widespread distribution. Sediments were deposited in predominantly fluvio-lacustrine environments in the latest Triassic–Early Jurassic. Marine influences are reported from core observations in Evergreen-Hutton intervals preceding the WCM. The Cretaceous sequence in the Surat Basin shows a dominantly marine character culminating in a widespread marine mudrock interval (Bungil). Tectonic events to the east and north of the Bowen/Surat Basin area led to the intermittent continuation of flexure influenced by pre-existing zones of weakness. In Late Cretaceous times, sediment accumulation ceased and the area was uplifted, giving rise to widespread erosion (Raza et al., 2009). A suite of mainly acidic intrusive bodies were also emplaced during this time. Faults displacing the Surat age fill are generally mapped as small with localized throws of 5-20m (Exon, 1976).

The preserved structures recording the Palaeocene opening of the Coral Sea is surprisingly minor in the Bowen-Surat area. A later Tertiary (Oligocene-Miocene) period of compressive structuring has been recognized (Brown et al., 1983; Finlayson et al., 1988) and is visible in exploration seismic records (Elliott and Brown, 1988). This modest upheaval involved gentle folding and reactivation along prior structural trends. Present day structural configurations were achieved during these Tertiary events; late Tertiary and Quaternary times have been characterized mainly by crustal stability and erosion. Major faults and fold axes associated with the Surat Basin sequence may be divided into three trends; (1) north-south trending structures (which are mainly reactivated Bowen Basin structures), (2) north-north-west to north-west trending structures, and (3) north-east trending structures. Generally, there are few faults and throws are small (30-40m). Nearly all faults mapped by the author are high-angle structures, interpreted to have little significant thrust faulting recognized in this study. Small scale thrusts are observed in the mine highwalls (see Section 5). The major faults, such as the Goondiwindi-Moonie structure, show evidence of a polyphase history of movement

(Fielding et al., 1990). The basin has, in general, suffered only minor levels of deformation and is much less deformed than the underlying Bowen Basin sequence (Figure 2.2). However, the earlier structural weaknesses are observed to guide formation of the structural features such as Kogan Nose, Undulla Nose and Wandoan Anticline (Sliwa and Esterle, 2008) in the Surat Basin.

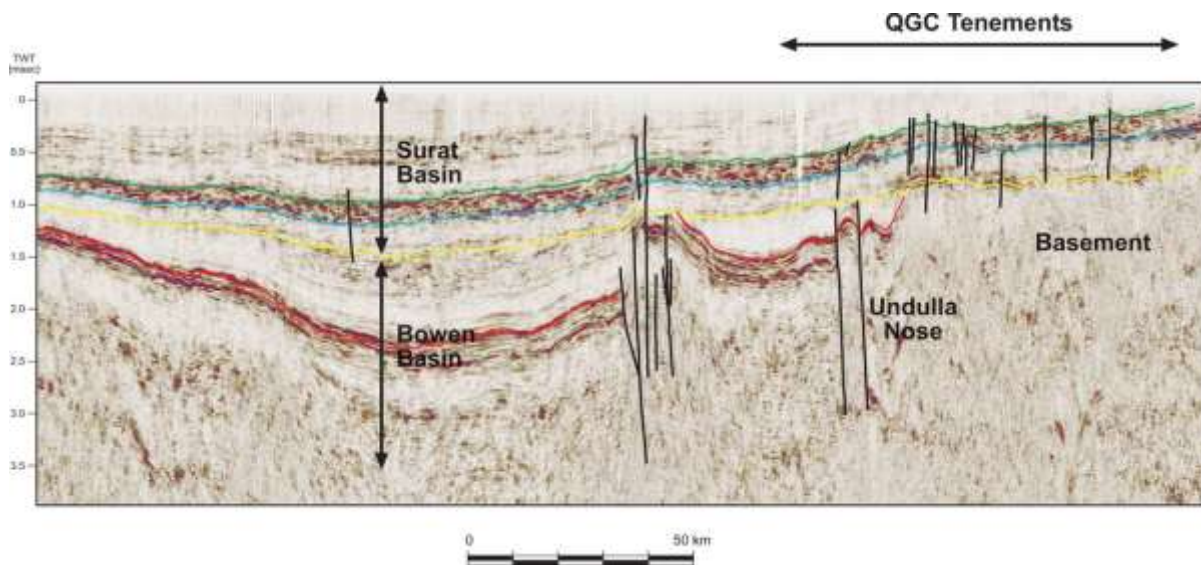


Figure 2.2 Regional Seismic cross section illustrating the major surfaces of the Surat Basin and the more structurally deformed underlying Bowen Basin (image from Martin et al., 2013).

2.2 Insights from this Project

In many ways, this project represents the early stages of a re-interpretation of Surat Basin evolution. Many aspects have been revealed and will require further work to evaluate fully.

This project represents a significant advancement in defining the structural framework of the Surat Basin. With contributions from the companies and the DNRM, it has assembled one of the largest (especially seismic) databases to be integrated with well data and other geophysical surveys to date and will form an important basis for more detailed studies. Most published works have focused on larger scale regional features (faults) with limited data. This study was able to examine smaller scale structures and therefore increase the resolution of information on selected areas. The use of the 3D volumes has improved the understanding of the complex, subtle deformation important to fracture development affecting the WCM and impacting permeability.

The more subtle deformation is an important component in the study of permeability dependency within the WCM. Related to this is the distortion of the regional stress field in proximity to both styles of deformation which serves to preferentially open or close fractures, thereby affecting permeability. This is discussed by Mukherjee (Section 5) where the concept of stress rotation by local deformation and the relative angle between fractures and stress is presented.

The late Tertiary tectonic features related to the Surat Basin are expressed in 3 basic styles of deformation, which may also be overprinted on Bowen structures (e.g. Dennison Trough):

- folds and faults overlying the major Bowen structures
- smaller scale, subtle faulting
- “keystone” style structures

3 Potential Field Interpretation

3.1 Potential Field Data and Analysis

The location of magnetic and gravity surveys is shown in Figure 3.1. This data was compiled as part of the initial stage of the project. It was utilized to provide a general interpretation of major regional structures and was delivered as Milestone Reports 1 and 2 (Babaahmadi et al., 2016a and b).

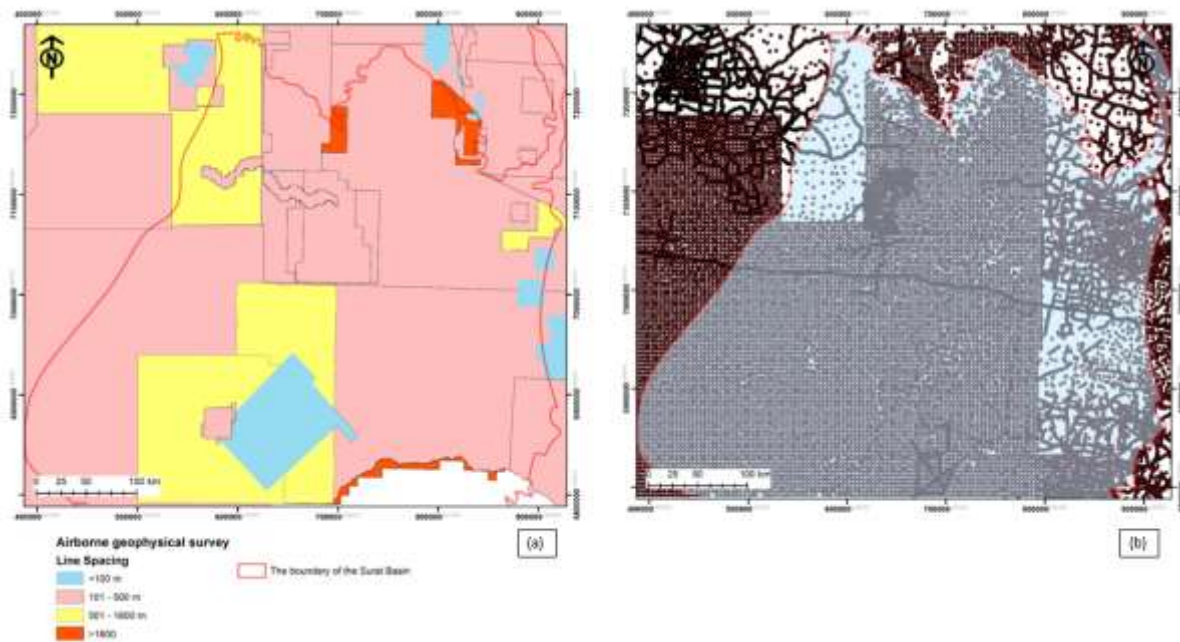


Figure 3.1 (a) Outline of airborne magnetic surveys with various resolutions that underpin the mosaic images interpreted in this study; (b) Distribution of gravity measurements across the Surat Basin. Average spacing is between 4 and >10 km.

Potential field data were used to map lineaments, which in some cases are related to basement faulting or other important zones of weakness. Due to the limited number of well-preserved outcrops in the study area, potential field data provide tools for the recognition of deep-seated geological structures. In this study, we used Bouguer gravity images with a grid spacing of 800m (point spacing between 4 and >10km) (Figure 3.2, Figure 3.3, Figure 3.4), and aeromagnetic images with a grid spacing of 80m (line spacing of 200 m, 400 m, and 1600 m, and an average flight height of 80m).

The data were provided by Geoscience Australia (through the “Geophysical Archive Data Delivery System” website) and the Geological Survey of Queensland. In this study, we focused on the aeromagnetic data which have higher resolution than the gravity data. However, in some regions where the magnetic response is almost flat (such as the western part of the Surat Basin), the Bouguer gravity data were prioritized. The Bouguer anomaly data provided by Geoscience Australia had been calculated based on a background density of 2.67 gm/cc. We recalculated the anomaly data from the free air anomaly data using a background density of 2.4 gm/cm³ (the baseline in the Surat Basin well logs) to take into account the lower

regional background gravity over the Surat and Bowen Basins.

Before applying various image enhancing processes, the magnetic anomalies were directly located above their sources, by reducing gridded aeromagnetic data to the pole, producing reduced-to-pole (RTP) gridded data (Swain, 2000; Cooper and Cowan, 2005) (Figure 3.2). In order to enhance both shallow and deep features, we operated a number of filters, such as tilt angle derivative, first vertical derivative, high pass filters, total horizontal derivative, and downward and upward continuations, in the Fourier domain on aeromagnetic and Bouguer gravity data (Figure 3.3). For better recognition of magnetic bodies and faults in Palaeozoic basement, we utilized a tilt angle derivative map of gridded Bouguer gravity data. Tilt angle derivative is a filter that enhances edges of magnetic sources from both shallow and deep sources and is calculated as the arc tangent of the ratio of the first vertical derivative to the absolute value of the total horizontal derivatives (Miller and Singh, 1994).

The first vertical derivative was used to sharpen short wavelength sources and especially fault lineaments (Nabighian et al., 2005). These filters allow us to interpret faults acting in shallow sources. To further accentuate shallower structures, we employed a high pass filter with a cut-off of 100km on the potential field data and then applied a total horizontal derivative to the resultant high pass filtered images. The total horizontal derivative is the square root of the sum of squares of the X and Y derivatives, and it is one of the most common filters to map near-vertical boundaries such as faults and geological contacts (Nabighian et al., 2005). Downward and upward continuation methods are the processes whereby the potential field is measured on a plane closer and farther from all sources, respectively (Blakely, 1995). Downward continuation is beneficial to highlight shallower sources and reduce the effect of deeper sources, whereas upward continuation accentuates deeper sources and reduces the effect of shallower sources (Blakely, 1995).

The potential field data allows us to recognize major faults based on: (1) offset and dragging of magnetic anomalies along linear trends, (2) pronounced structural lineaments, and (3) lensoid and en-echelon structures (method as discussed by Babaahmadi and Rosenbaum 2014, 2016).

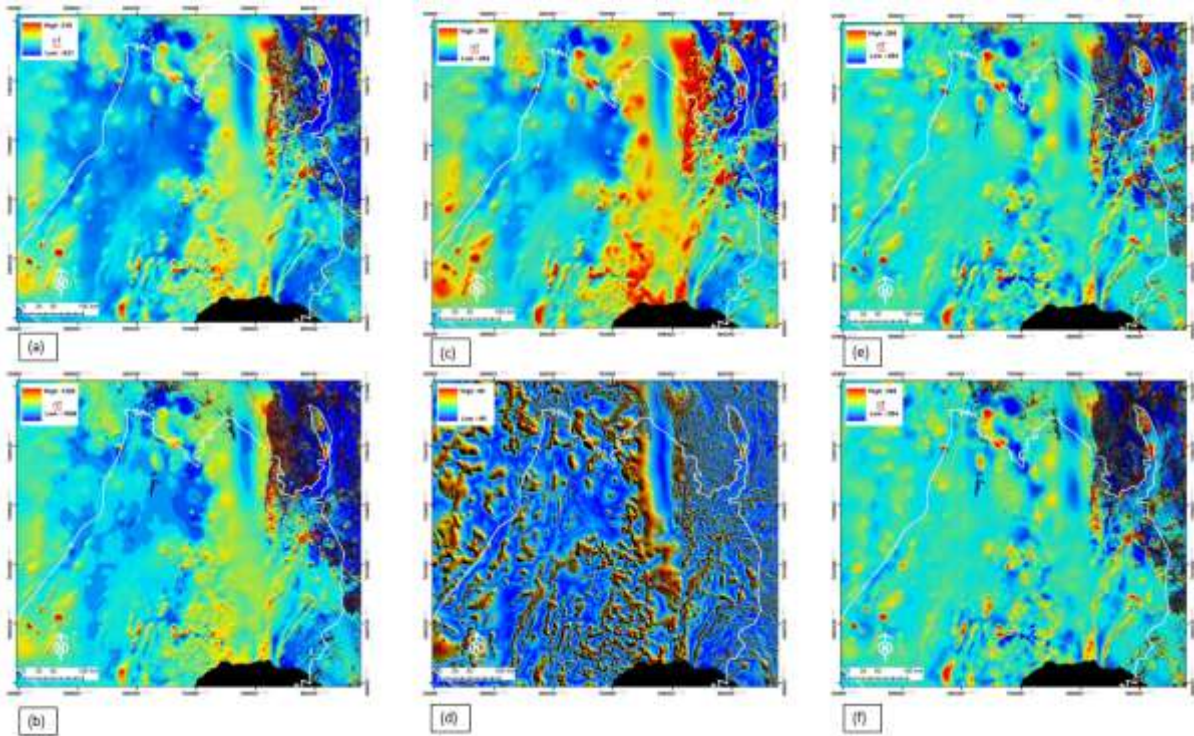


Figure 3.2. (a) Shaded, gridded aeromagnetic data reduced-to-pole (RTP). This grid provides the base data for (b) Downward continuation up to 400 m; (c) Upward continuation up to 600 m; (d) Tilt angle derivative; (e) High Pass filter (cut-off: 100 km); (f) Total Horizontal Derivative of High Pass filtered RTP, overlaying High Pass filtered RTP image. The white line in all figures shows the Surat Basin border.

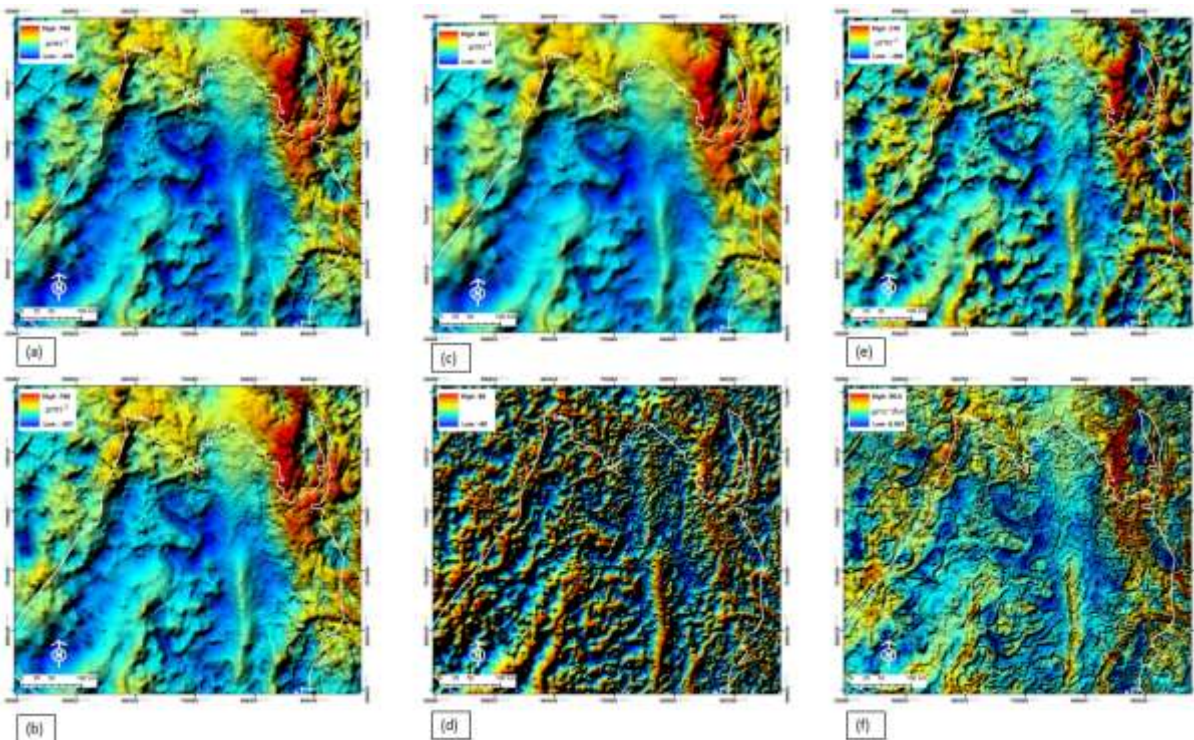


Figure 3.3 (a) Shaded gridded Bouguer gravity data (Bouguer density: 2.67 g/cc). This grid provides the base data for (b) Downward continuation; (c) Upward continuation up to 1000 m; (d) Tilt angle derivative; (e) High Pass filter (cut-off: 100 km); (f) Total Horizontal Derivative of High Pass filtered Bouguer, overlaying High Pass filtered Bouguer image. The white line in all figures shows the Surat Basin border.

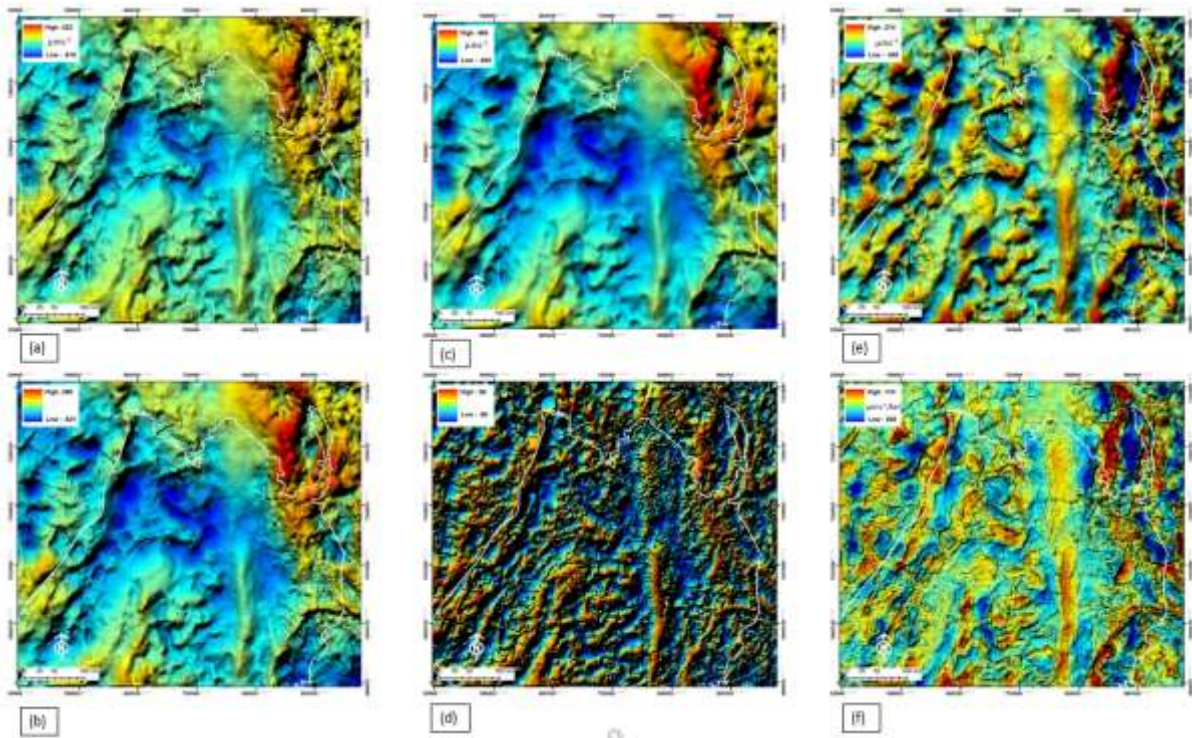


Figure 3.4 (a) Shaded gridded Bouguer gravity data (Bouguer density: 2.4 g/cc). This grid provides the base data for (b) Downward continuation; (c) Upward continuation up to 1000 m; (d) Tilt angle derivative; (e) High Pass filter (cut-off: 100km); (f) Total Horizontal Derivative of High Pass filtered Bouguer, overlaying High Pass filtered Bouguer image. The white line in all figures shows the Surat Basin border.

3.2 Potential Field Results

Interpretation of the gridded aeromagnetic data indicates that the basement rocks below the sedimentary rocks of the eastern part of the Bowen and Surat Basins were affected by N-, NE- and NNW-striking lineaments (Figure 3.5). N- and NE-striking lineaments are the most dominant.

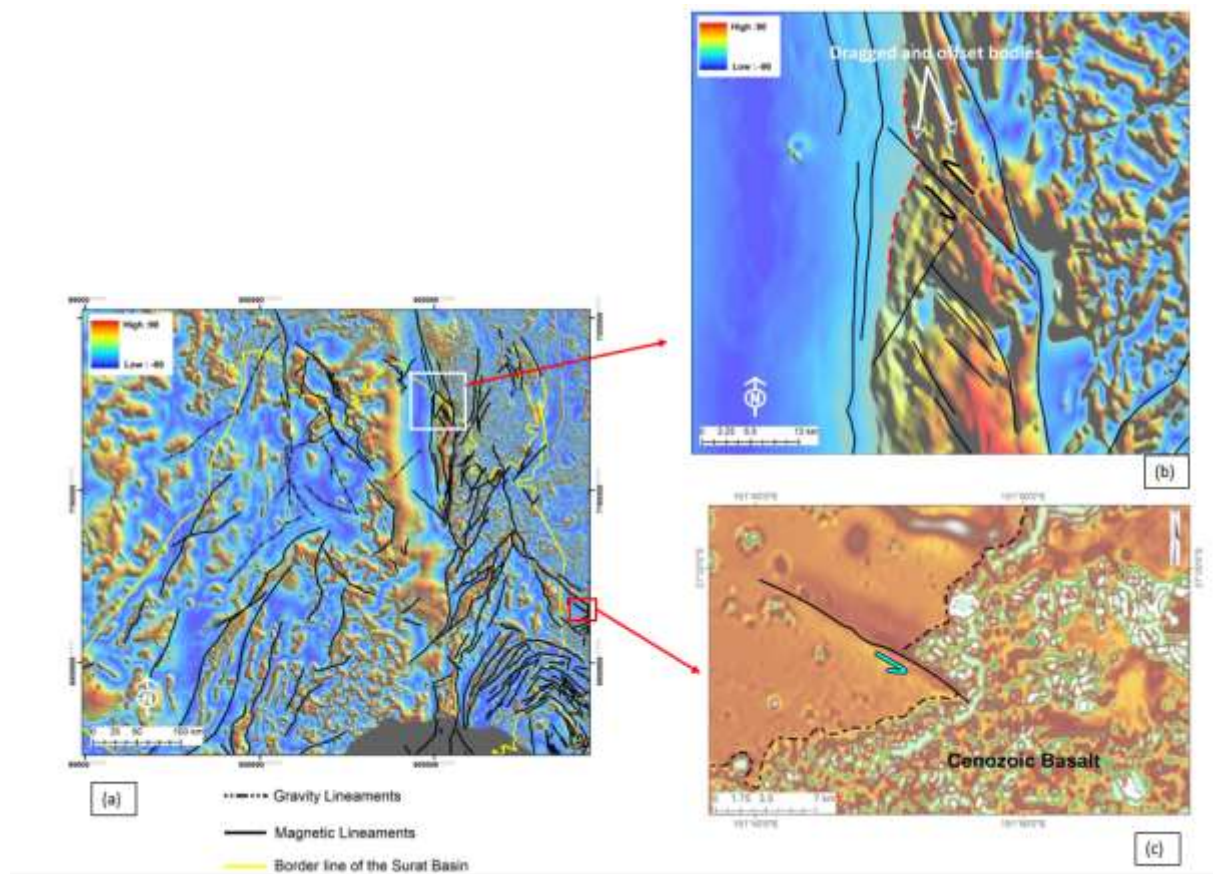


Figure 3.5 (a) Tilt angle derivative map of the reduced to pole (RTP) total magnetic intensity with interpreted lineaments. Dashed lines are the lineaments interpreted from the gravity data (Figure 9). (b) A sinistral NW-striking fault separates and drags magnetic anomalies related to Palaeozoic basement rocks. (c) Another NW-striking fault separates Cenozoic basalts sinistrally (Babaahmadi and Rosenbaum, 2016).

Lineaments are better defined in the eastern part, as gridded aeromagnetic data have better quality because of closer line spacing in contrast to data from the central and western parts of the basin. Although there are a few clear offset markers along some lineaments (Figure 3.5b, c), we interpret many of the lineaments as probable faults in the eastern part, as they are observed as sharp and narrow negative magnetic discontinuities, which cut magnetic anomalies related to Palaeozoic rock units.

The magnetic response in the western part is low. Therefore, we interpreted the total horizontal derivative of high pass filtered Bouguer gravity data of this area. It shows NNW-, N-, NNE, and ENE-striking lineaments (Figure 3.6).

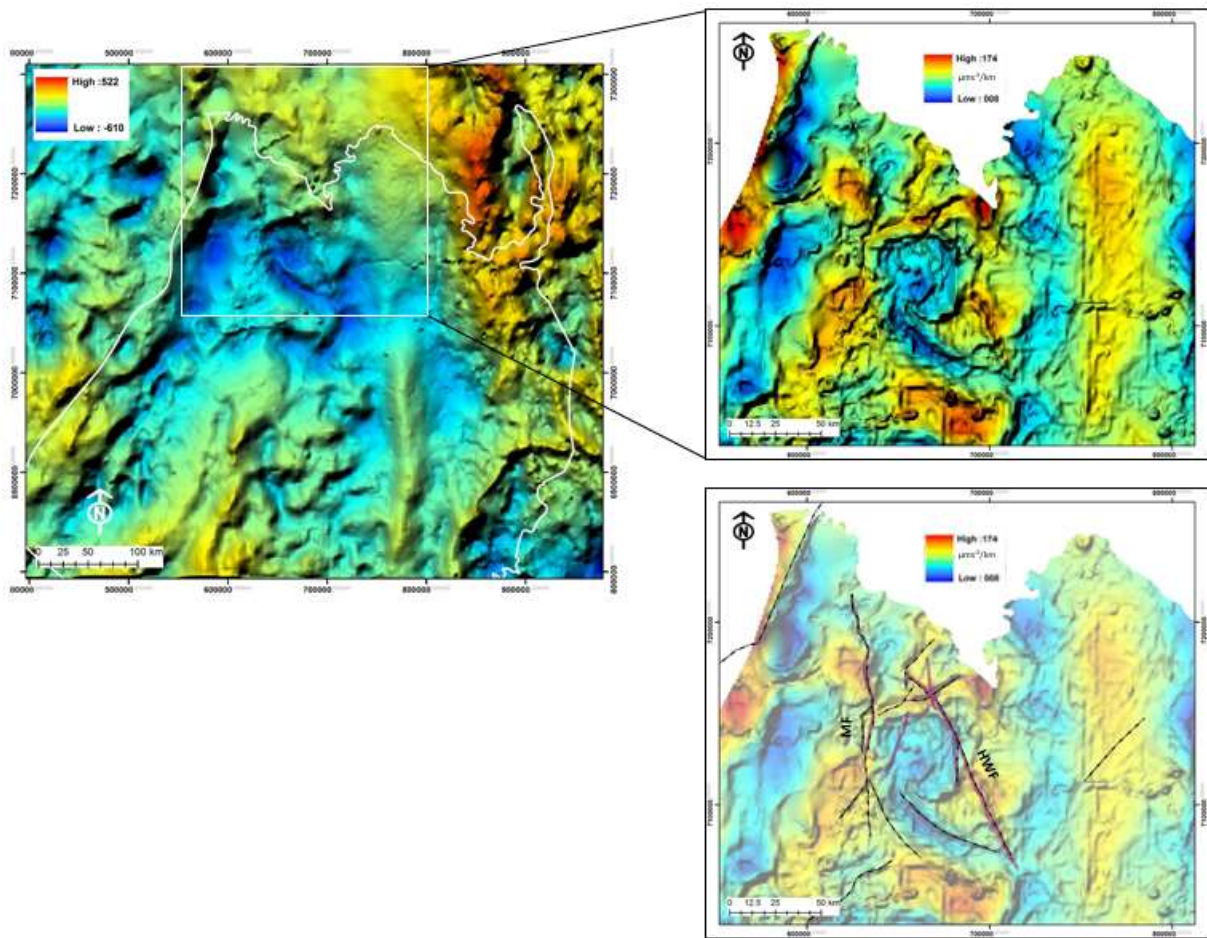


Figure 3.6 The interpretation of total horizontal derivative image of the high pass image (cut-off: 100km) of gridded Bouguer gravity data, overlying the Bouguer image in the western part of the Surat Basin, indicating major faults in this area. HWF, Hutton-Wallumbilla Fault; MF, Merivale Fault.

Some of lineaments are interpreted as the basement traces of mapped faults on the seismic lines (Figure 3.7). N-striking faults include the Glebe, Taroom, Cockatoo, Burunga, Leichardt, and Goondiwindi Faults, whereas NE-striking faults are the Moonie and Wambo Faults in eastern part of the Surat Basin (Figure 3.7).

In the western part of the Surat Basin, the Hutton-Wallumbilla and Merivale Faults are major N- and NNW-striking faults and have sharp expressions in the Bouguer gravity data.

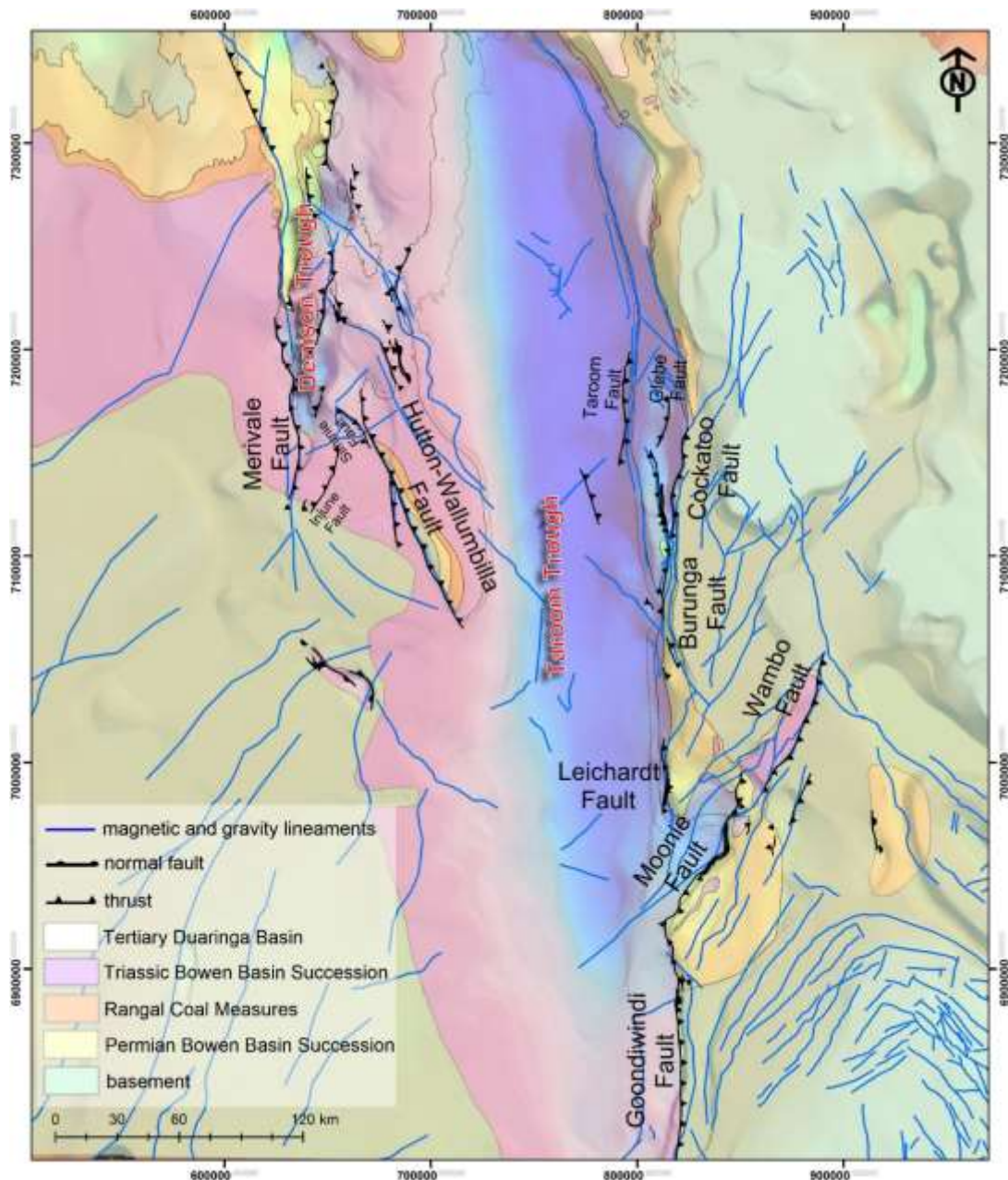


Figure 3.7 A map of the basement faults mapped from seismic lines and lineaments interpreted from magnetic and gravity data in the Bowen and Surat Basins (Babaahmadi et al., 2016b). The base image is the Phanerozoic SEEBASE map showing the depth to the Basement.

3.2.1 Discussion of potential field interpretations

We produced a map showing how lineaments with different orientations may have originated in different Palaeozoic orogenic systems such as the Thomson, Lachlan, and New England Orogens. We used the approximate distribution of these Orogens interpreted by Glen (2005), to classify the lineaments. Basement Thomson Orogen lineaments mostly strike NE and less NNW and N, whereas NNE-striking lineaments are dominant in the Lachlan Orogen. Lineaments in the New England Orogen have various orientations of NW, NNW, NE, NNE, and N (Figure 3.8).

There is a concentration of NW- and NE-striking lineaments in the south-eastern part of the map, which are located in the highly deformed area of the Texas Orocline. Some of these lineaments are interpreted to have been developed during the Early-Middle Permian oroclinal bending of the Texas Orocline (Brooke-Barnett and Rosenbaum, 2015; Babaahmadi and Rosenbaum, 2016). The results of a recent study indicate that faults, usually with a strike-slip separation, are parallel to the structural fabrics of the Texas Orocline, which is consistent with the idea that oroclinal bending was at least partly facilitated by a flexural slip mechanism (Babaahmadi and Rosenbaum, 2016). The Early Permian oroclinal bending also resulted in the rotation of some major faults, such as the Goondiwindi-Moonie Faults, which was possibly associated with the deposition in the Bowen Basin (Brooke-Barnet and Rosenbaum, 2015).

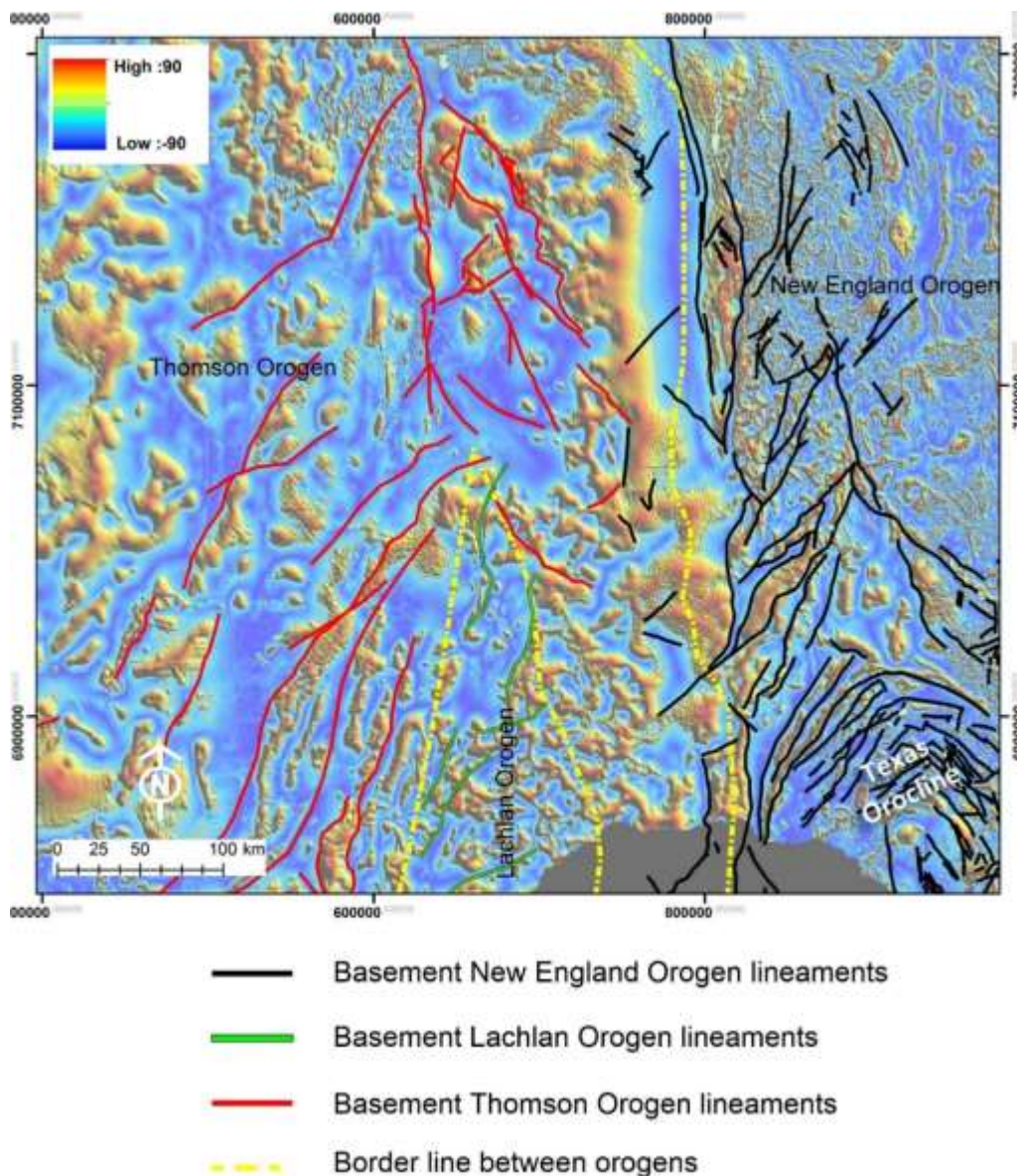


Figure 3.8 Regional lineaments in the Bowen and Surat Basins interpreted from aeromagnetic and gravity data. The lineaments are colour coded based on their location in different orogenic systems.

The interpretation of the tilt angle derivative of upward continued RTP image (which is suitable for deep structures) indicates that most of the faults are deep-seated into the Palaeozoic basement rock units. This idea is supported by interpretation of seismic lines, which show the major faults penetrate into the Palaeozoic basement (Sliwa 2013; Babaahmadi et al., 2015).

3.2.2 Potential Field data: Conclusions and Future work

- (1) Our observations confirm previous interpretations that major faults in the Surat and Bowen Basins are deep-seated into the Palaeozoic basement.
- (2) Basement fault lineaments with various trends in different parts of the Surat Basin are suggested to have originated within the different orogenic systems, such as the New England, Lachlan, and Thomson Orogens, during the Palaeozoic.
- (3) NW- and NE-striking lineaments in the south-eastern part of the basins are interpreted to have developed in the highly deformed area of the Texas Orocline.

The interpretation of potential field data in this report successfully identified basement structures that may impact on the fault and fracture distribution in the overlying Surat basin. Lineaments result from lateral change in magnetic susceptibility; these are often due to structural offset at basement as sedimentary clastics have minimal susceptibility. Linear patterns can also be caused by metamorphic basement anomalies or other paleo-structures and are not necessarily an indication of underlying offset relevant to either the Bowen or Surat basins. A careful review of the available seismic data is required to determine whether the interpreted anomaly is due to faulting of some type or some other cause. Direction of offset is not revealed without additional modeling.

In addition, there are many other minor but important faults which are not picked up in the lineament interpretation. These are often minimal offset, but importantly Cenozoic based on observed upward propagation of deformation into Cretaceous or younger section.

The next section of the report focusses on the interpretation of 2D seismic data to further characterise the basement faults and their relationship to younger deformation in the Surat Basin.

4 Integrated Well-Seismic Interpretation

4.1 Seismic Data

4.1.1 2D seismic surveys

This CCSG project has developed and greatly expanded the seismic database throughout the Surat and Bowen basins, providing a valuable asset from which further studies can be made. The Petrel database of 2D seismic has been expanded from the ~1200 lines referred to in the previous milestone report (12/2015) to over 5100 in the current database (Figure 4.1 and Figure 4.2). In turn, this provides a dramatic increase in granularity of interpretation and a comprehensive view of all deformation in the Surat. Numerous subsequent studies will be made possible from this work.

Most of the data has been provisionally tied (shifted to common T_0) and balanced (amplitude adjusted to proper dynamic range). Just prior to the completion of this phase of the project, the GSQ completed the compilation of all available seismic data in Queensland which included an adjustment to a common datum, corrected navigation and development of a consistent SEG-Y header. The CCSG was provided with a full copy of this data archive in December 2016. About 900 2D lines were added from this archive to improve coverage of the southern Goondiwindi and western/southern portions of the Surat Basin. This data has not yet been fully integrated (shifted/balanced) into the interpretation project but does inform observations.

The project database now extends from the Northern Dennison Trough to southern Surat Basin³. The more extensive coverage has provided much more detail on the major structures and a view of the subtle inversion observed in the southern Surat Basin. This results in very shallow extensional faulting not previously recognized, which will be important to groundwater flow studies and the resulting dynamic models. This will also serve as an important foundation for the 2017 CCSG project to establish an integrated well-seismic chronostratigraphic framework for the basin with the potential to be extended to other basins in Queensland including the pre-Jurassic section. A substantial collection of *checkshot surveys* has been compiled, with over 100 wells distributed throughout the Surat and Bowen basins. As most of these important velocity surveys have yet to be compiled, the CCSG has developed “data scraping” software tools which have revealed hundreds of additional checkshots not yet compiled from the GSQ database. Developing a full archive of this data will allow the development of a basin wide velocity model.

³ Additional contributions to the database from Santos, Arrow, Origin, Shell/QGC are all greatly appreciated. GSQ’s effort to standardize SEG-Y headers, correct navigation, along with the compilation/transcription of available field data are all major contributions to future studies.

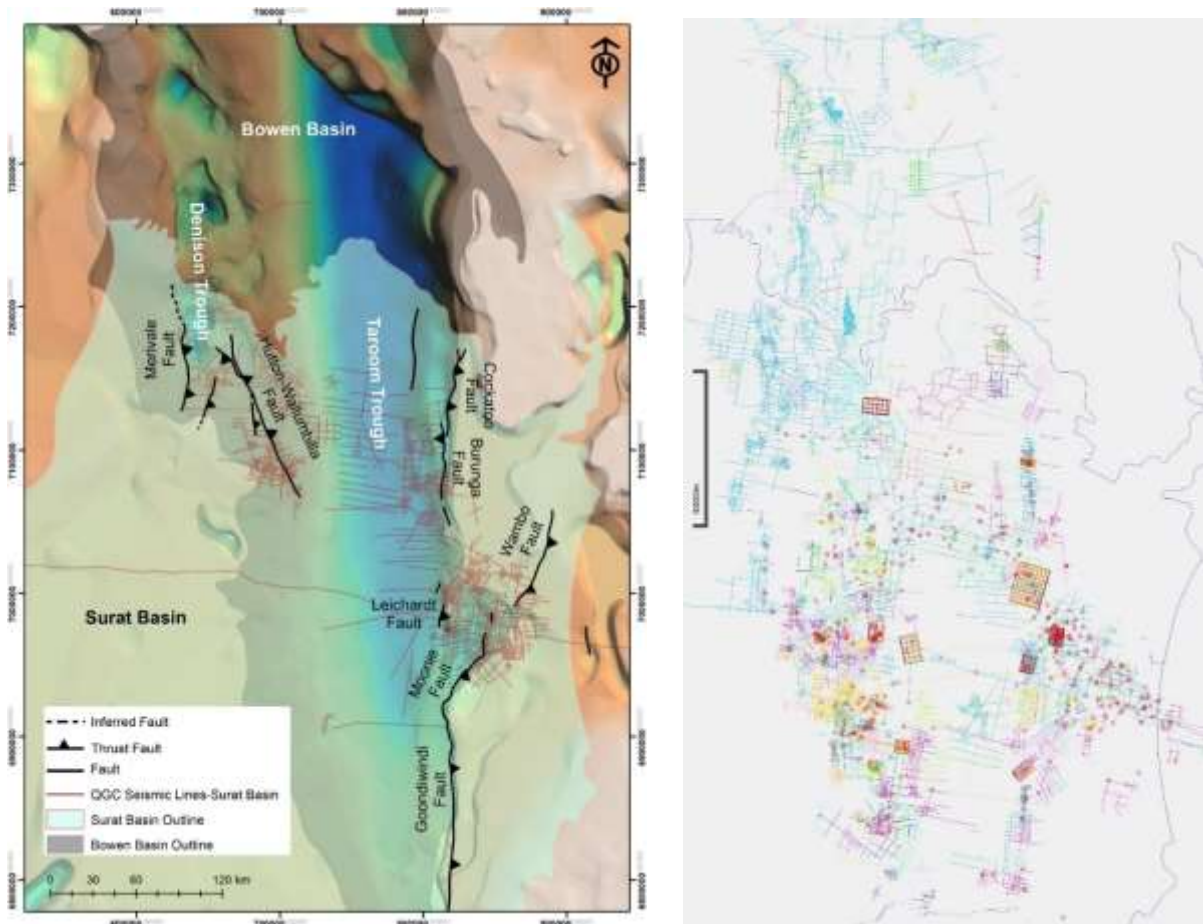


Figure 4.1 (left) Map showing seismic lines included in the project as of 2015 and (right) present-day data base of seismic lines integrated into this project.

4.1.2 3D seismic surveys

Data for 3D surveys were loaded for 10 open file areas: Dalwogan-Condabri, Lauren (aka – Werona), Undulla, Moonie, Scotia, Waggamba, Overston, Myall Creek, Fairview and New Royal. There are additional 3D surveys which have not yet been loaded to the project due to file format issues. Each of these 3D areas have been interpreted at several levels and relevant attribute volumes created (coherency, sweetness, etc.). Flattened volumes (amplitude and attributes) were created to examine basic stratigraphic morphology in the WCM to compare depositional systems. These are incorporated into the interpretation.

The 3D seismic volumes in some cases offer the opportunity to better characterize the important deformation affecting CSG permeability in the Walloon section and the flow models for shallower aquifers. Of the available data, the open file Undulla 3D provides insight into the style of deformation termed “keystone” faulting as described earlier. Also instructive is the Surat deformation observed in the Dalwogan-Condabri 3D from Origin. A more limited example is found in the Lauren 3D from Shell/QGC. The Fairview 3D provides an important example of Cenozoic keystone development overprinted on the Permian section on the Western Shelf. The Undulla survey is located along the western margin of the Undulla Nose as shown on the relevant structure maps.

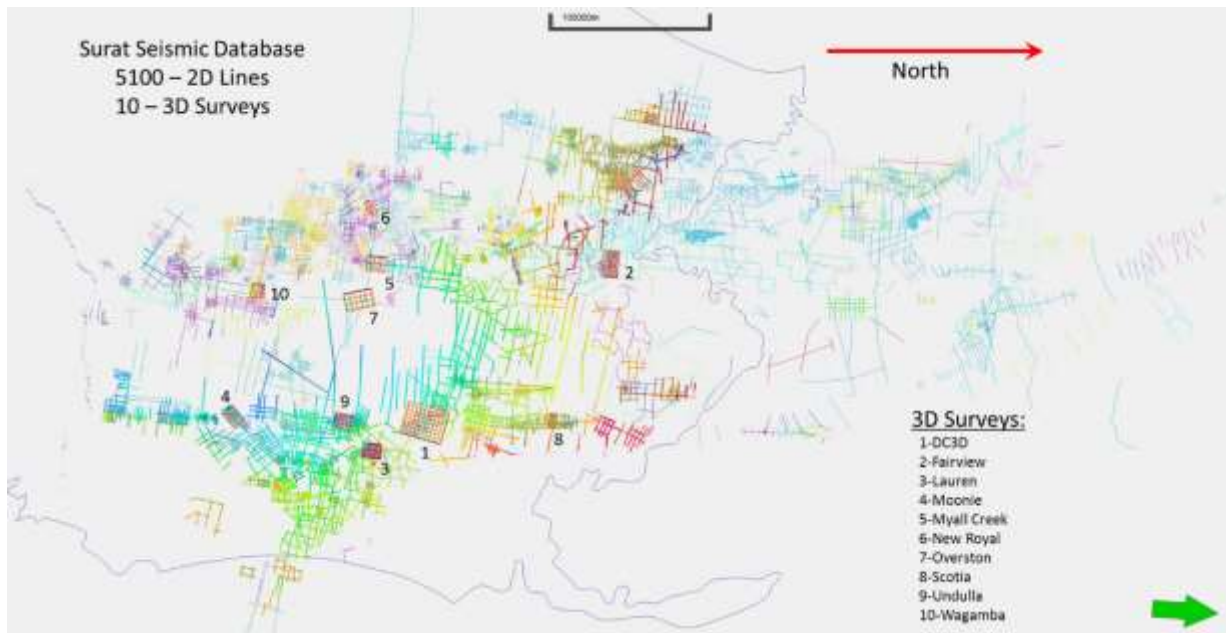


Figure 4.2 Location of 3D seismic surveys (note North pointing to the right). Grid of 2D lines & Base Surat interpretation.

4.2 Seismic Data Compilation

4.2.1 Data loading and quality control

Data has been loaded into the interpretation project primarily from GSQ SEG-Y files along with contributions from Shell/QGC, Origin and Arrow. Shifting of surveys to a common T_0 is a major challenge with such a large collection of data from multiple sources. The Origin data set (*_mig_tied_time) was determined to have the most consistent line to line ties on nearly 300 lines. The Arrow data was found to be generally inconsistent within itself and did not match the Origin data nominally shifted to a 244m (ASL) datum. Where duplicate lines existed they were retained with the following hierarchy: 1-Origin, 2-GSQ and 3-Arrow. Data have been time shifted to a preliminary state, but additional adjustments are still required for many lines. All surveys were also adjusted for display amplitude to capture the dynamic range available from the data.

The resulting CCSG seismic database in its current state consists of over 90% of available open file GSQ data for the greater Surat and Bowen basins in Queensland. The horizon mapping provides detail which has not previously been available. Data quality is remarkably good given the 50 year history of acquisition. Most of the data from the 1980's on are of good quality; even the scanned images are surprisingly good. Much of the data ties "wobble for wobble" indicating a consistent processing phase. The database would benefit from phase adjustment to a minor portion of the surveys (<20%). Most of the data is of sufficiently high quality to support regional intra-well stratigraphic interpretation.

4.2.2 Seismic-to-well ties and horizons

Horizons are correlated by integrating the well logs with the seismic data to determine the regional chronostratigraphic depositional boundaries as is common industry practice. This is

accomplished by developing well ties using synthetic traces based on sonic and density logs with the time-depth relation created by integrating the sonic log. The well is further adjusted in time to provide a best fit to the seismic data at that location. This was done for 580 wells throughout the Surat basin (Figure 4.1 and Figure 4.2). Horizons representing stratigraphic boundaries are then correlated on the seismic data where spatially consistent reflectors are observed. Seismic reflection data is inherently stratigraphic and where extensive coherent “events” exist, these are generally representative of depositional boundaries between successive sequences. Integrating the well correlation with the seismic data provides an important benchmark for the stratigraphic interpretation.

The OGIA formation tops are based on lithologic identification and correlations between wells following wireline signatures proposed by Green et al. (1997), without reference to the more limited seismic data available at that time. The resulting well-seismic correlations were found to be inconsistent with the seismic data available to this project, which includes data from before 1997 as well as more recent data, including 3D. The OGIA correlations also differ from the company correlations based on the same data. OGIA correlations were produced by a single operator, rather than multiple operators, while the operators report a process of internal ‘picking rules’ and quality assurance as well as cross-company comparison (per discussion with CCSG member companies). Adjustments in the OGIA tops were also made purposefully for some horizons, e.g. the top Springbok to Westbourne transition, to assign a lithostratigraphy for regional hydrology modelling. The implicit assumption seems to have been that such a correlation would represent adequately groundwater flow continuity and pressure connectivity, at least initially.

Extensive use of seismic data is reported in neither OGIA nor company formation-top identification or subsequent inter-well correlations. This ‘faults and fractures’ project as well as the availability of additional seismic survey data in the public domain between 2014 and 2017 has resulted in the need for a follow-on CCSG project to develop an integrated well-seismic, chrono-stratigraphic correlation framework for the basin. This exercise will update earlier attempts at sequence stratigraphic interpretation of seismic reflectors from Wells et al., 1993, Dixon, 1993 as part of the Sedimentary Basins of Eastern Australia (SBEA) project and later reviewed and updated by Hoffman et al., 2009 and Dixon et al., 2011. These concepts will be more fully presented in the Phase 1 report for the CCSG Correlation Project in progress.

The initial sequence stratigraphic correlations used in this project are tightly integrated with the seismic data through synthetic matching. The nomenclature system adopted and partially introduced in this report is based on work done for a consortium of companies working the Northwest Shelf (Australia). It utilizes a decimal number system for each major sequence with a prefix indicating age (e.g. J = Jurassic), incrementing from the base upwards at each successive depositional boundary. In this way, as work continues, additional boundaries can be easily fitted into the column. As sequence stratigraphy develops a hierarchy of cyclicity

present in every depositional system and these interpretations evolve over time, this concept is part of the nomenclature to easily allow modification.

The preliminary correlations of the follow-on CCSG project were adopted for horizon correlations in this project as they provide a more consistent fit to the seismic data. The horizons and their approximate lithologic correlation equivalent are noted below. Note that the SBEA project proposed a series of sequence boundaries which will be compared with interpretations from the new CCSG project in this area.

Correlated Horizons

Bowen Succession

Within the Bowen succession only the Top Rangal (“Top Permian”) was correlated on a regional basis, from the north Dennison to southernmost Surat. This was included to provide a view of the underlying Bowen structures and a comparison of deformation. As the Permian coals are extensively represented across the Surat, this is effectively a seismic character based correlation. The contact between the Rangal and overlying clastics does change character substantially so the horizon attempts to maintain a consistent seismic correlation.

An “Intra-Triassic” horizon was correlated, which defines a change in character between the lower and upper portions of the Triassic clastic section across the northern portion of the Surat to provide a view of Bowen basin subsidence geometry. No effort was made to identify this explicitly on logs as it was outside the scope of the project.

Surat Succession

Base Surat (J10.0)

The basal unconformity of the Surat depositional succession (J10.0 - Buncon) is most easily identified in those areas where the Triassic and older sediment subcrop at a sufficient angle to be distinctive. These correlations are then carried into the basin where the boundary surface is less obvious. Well correlations to support the seismic interpretation are important in the deeper portions of the basin where Bowen and Surat sediments are near parallel. To the east of Leichhardt-Moonie, the unconformity shows increased rugosity due in part to subcrop dependent erosional topography, tight folding and faulting. In some portions of the eastern margin, particularly where Permian coals subcrop, erosional topography is apparent.

J20.0 (~EverLow & ~S20 – Wells, 1993)

The OGIA “EverLow” lithologic correlation represents a distinctive regional sequence boundary contemporaneous with a major, Gondwana-wide, global extinction event (Ziolkowski, et al. 2014). This is the top of the Westgrove ironstone, a tightly cemented sand, characterized by distinct sonic and high density spikes and is one of the few regional lithologic correlations. On the seismic data, this event marks a transition in seismic character from

Precipice/Lower Evergreen to Upper Evergreen, which is often striking in contrast. This is the major chrono-stratigraphic sequence boundary of the lower Surat succession and is a stratigraphic boundary recognized and mapped in Wells, 1993.

J40.0 (nominal base Walloon Coal Measure)

The J40 (~ Durabilla) is mapped as the nominal base of Walloon Coal Measure sequence boundary. This event has been mapped in part around the basin and is a relatively consistent event.

J50.2 (~SPBAS-OGIA, in places *[see note]*)

The J50.2 is represented on logs often as a maximum gamma which correlates with a distinct reflection event just above the J50.0 (nominal top WCM). This is often at the top of a fining upward sequence above the top WCM, and as such it represents the continental equivalent of a maximum flooding surface or a time of minimal energy in the system. As a more consistent point of correlation with the seismic data, this was mapped primarily across the eastern margin of the basin in place of the top WCM.

NB: There also seems to be an unconformable surface at the base, based on age date and isotopic differences on the "basal Springbok. The nature of this interface and the aerial extent of the juxtaposition across it is likely to be important for groundwater draw-down predictive modeling and requires further work.

4.2.3 Fault interpretation

Fault identification is based on observations of lateral discontinuity across a set of reflections. Interpretation is further guided by the more detailed observations of common fault morphology available from the 3D volumes. In all 3D volumes, coherency attributes were generated ("Variance" in Petrel). This is a great aid in understanding complex fault systems. These attribute volumes are then "sliced" at a constant time value and the colour bar adjusted to provide optimal visual fidelity. Abrupt, lateral discontinuities (low coherency) such as a fault appear as darker, linear features in the displays. Reference to the profiles is made to review the source of the observed discontinuity. The coherency attribute will show the best view of a fault where reflections are better developed. In zones of generally poor reflectivity (e.g. Hutton, upper Evergreen), the faults will be poorly defined by coherency and difficult to identify in profile.

Given the decay of higher frequency with increasing depth, a small lateral discontinuity (i.e. fault) identified at the top Walloon Coal Measures (WCM) or above can be difficult to follow to depth. Across the WCM, the lateral variation in facies can make it difficult to follow small faults. Below the WCM, the Hutton has little relative reflectivity and at the J20 (Westgrove/OGIA-EverLow), the lower frequency content may show a small fault to look like a subtle change in slope. In addition, as much of the small-scale faulting is interpreted in this study to be related to keystone structures, zones of deformation are laterally discontinuous

and show abrupt changes in fault morphology (assemblage of related faults within a structure). Keystone features are described and illustrated in a following section.

All seismic data was scrutinized for faults that could be identified at the Base Surat horizon (~Base Precipice). These discrete fault picks are shown in Figure 4.3 (red dots). As discussed in subsequent sections, these faults are: a) small displacement and b) have very limited lateral extent. For this reason, fault planes are very difficult to generate. Where it was possible to correlate faults between profiles this was done and they are part of the interpretation contained in the Petrel project.

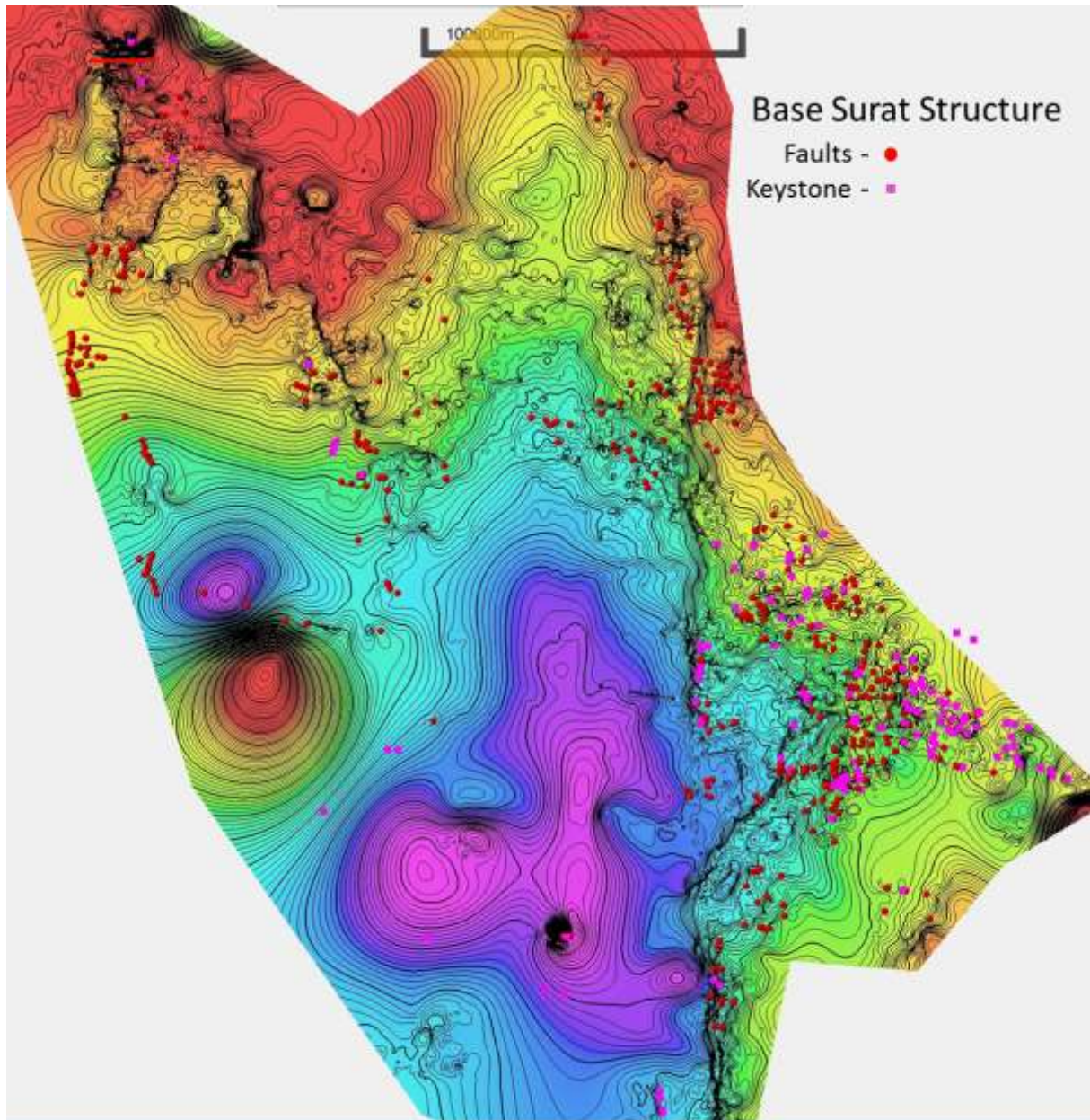


Figure 4.3 Discrete base Surat fault picks (red dot) and keystone structures (magenta) – (CI – 20ms).

4.2.4 Depth conversion

This project has compiled the large number of checkshot surveys provided by GSQ and Origin into a spreadsheet which includes image captures of the original data and a tabulation of data for each well (well locations in Figure 4.4). An additional 700 wells have been sorted out of the GSQ database as having velocity surveys listed in the well completion report. These could be compiled and used for the development of a comprehensive layered velocity model for the basin in a subsequent CCSG project. A representative composite time vs. depth plot is shown in Figure 4.5. It is readily apparent from the figure that the average velocity is a well behaved function with minor spatial variation. This model in combination with the depositional architecture developed by the Integrated Chrono-Stratigraphic Correlation Project would allow structural and depositional reconstructions to be created.

In Figure 4.4, locations for 90 wells with checkshot data are shown for the Surat Basin. This data was added late in the project (early December), so it has not been used as of yet for time-depth relations. A representative collection of checkshots from 13 of these wells are shown in the following time vs. depth plot (Figure 4.5). As can be observed, the data is tightly clustered and there is minor spatial variation in average velocity with depth.



Figure 4.4 Location map for 90 wells with checkshot data (compiled - blue, all QDEX - green).

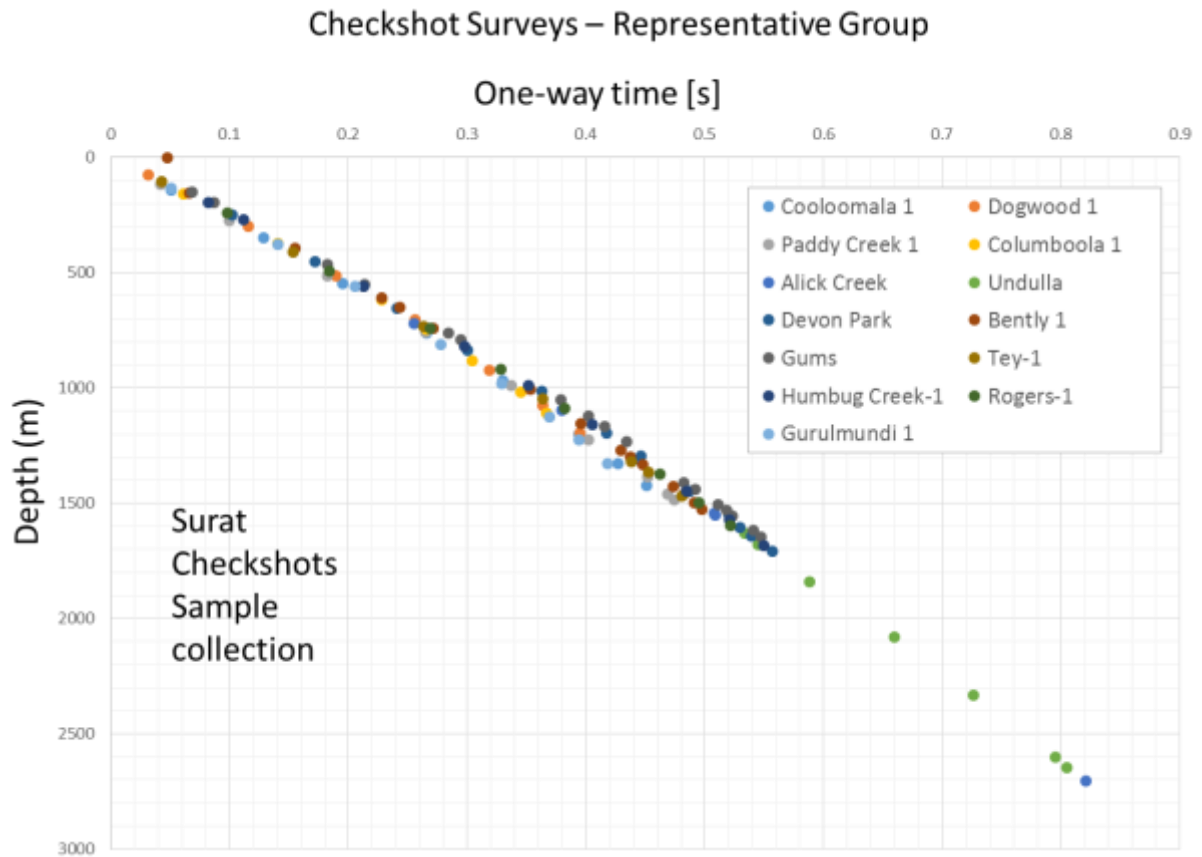


Figure 4.5 Time versus Depth graph from checkshot surveys. Representative collection.

4.3 Integrated Well and Seismic Interpretations: Major Structures

In general, the large Bowen structures underlying the Surat succession are the result of dominantly vertical uplift under regional compression, bounded by zones of major deformation which generally have a complex fault morphology. Deformation resulted from regional crustal contraction during the Hunter-Bowen Orogeny that initiated in the early Permian, influencing Bowen Basin subsidence and sedimentation patterns. Deformation extended into the Triassic before terminating with the New England Orogen (Korsch and Totterdell, 2009; Holcombe in Jell, 2013).

The net uplift in many cases is on the order of ~1km or more with a zone of complex deformation involving multiple high angle reverse faults with a morphology that indicates a minor, but significant component of shear along with very tight folding of the Permian coal section. The deformed zone bounding the uplift can be as much as 3-5km in width and serves to accommodate the lateral shortening. Multiple, major faults are observed to bound tight folds often composed of lower Permian strata.

Net shortening due to the compressional component of the deformation is difficult to estimate. Based on the observations of tightly folded Permian units and rotation of major fault blocks, net shortening across these zones could be equal to or perhaps double the width of the zone. This would imply an estimate on the order of ~5-10km with net uplift ~1-2km. The morphology of the deformed zone is consistent with an interpreted component of strike-slip movement, which was suggested in Korsch and Totterdell (2009) but not mapped with the detail presented in this project.

The overlying Surat succession is deformed in the Tertiary and is characterized by mostly gentle folding above the complex Bowen fault zones (similar to observations by Ryan et al., 2012) and the development of numerous keystone structures, particularly on the eastern margin. The amplitude of Surat folding is a minor fraction of that in underlying structure and reactivation is variable along the trend. For example, the Burunga anticline is one of the larger Bowen structures tightly folded with over 1km of net uplift, however, the Surat section only develops a subtle fold (Figure 4.6). In comparison, the Hutton-Wallumbilla has – in places – Surat uplift nearly equal to that in Bowen but was only reactivated along the southern portion of the Bowen deformation. The keystone structures where they occur and the locally intense fracture development are thought to have a strong influence on permeability and fluid flow. Depending on relative stress orientation, fractures can enhance or impede flow (see Mukherjee Section – Image Log Analysis).

Figure 4.6 shows structure at both the top Permian coal and base Surat unconformity, at the same scale and contour interval, to contrast the relative deformation between them. The top Permian structure is overprinted with the regional uplift and tilting of the Surat during Cenozoic tectonics. It can be observed that the deepest portion of the Bowen is located well to the north while the deepest part of the Surat is to the south. This is in part a result of uplift and block rotation during the late Triassic tectonic deformation. The depositional center of the Surat Basin is west of Undulla-Moonie Fault Systems, while the Taroom Trough of the Bowen is well north of Burunga. This illustrates the differences in subsidence during each of the depositional successions.

Very few of the faults that formed the Bowen structures are reactivated along similar fault planes into the Surat succession. However, the Bowen fault systems are often locations for gentle folding developed in the Surat succession. In some cases (e.g. Hutton-Wallumbilla), the Bowen deformation appears to be reactivated, whereas along the Leichhardt - Burunga basin subsidence (relaxation) may be an important mechanism.

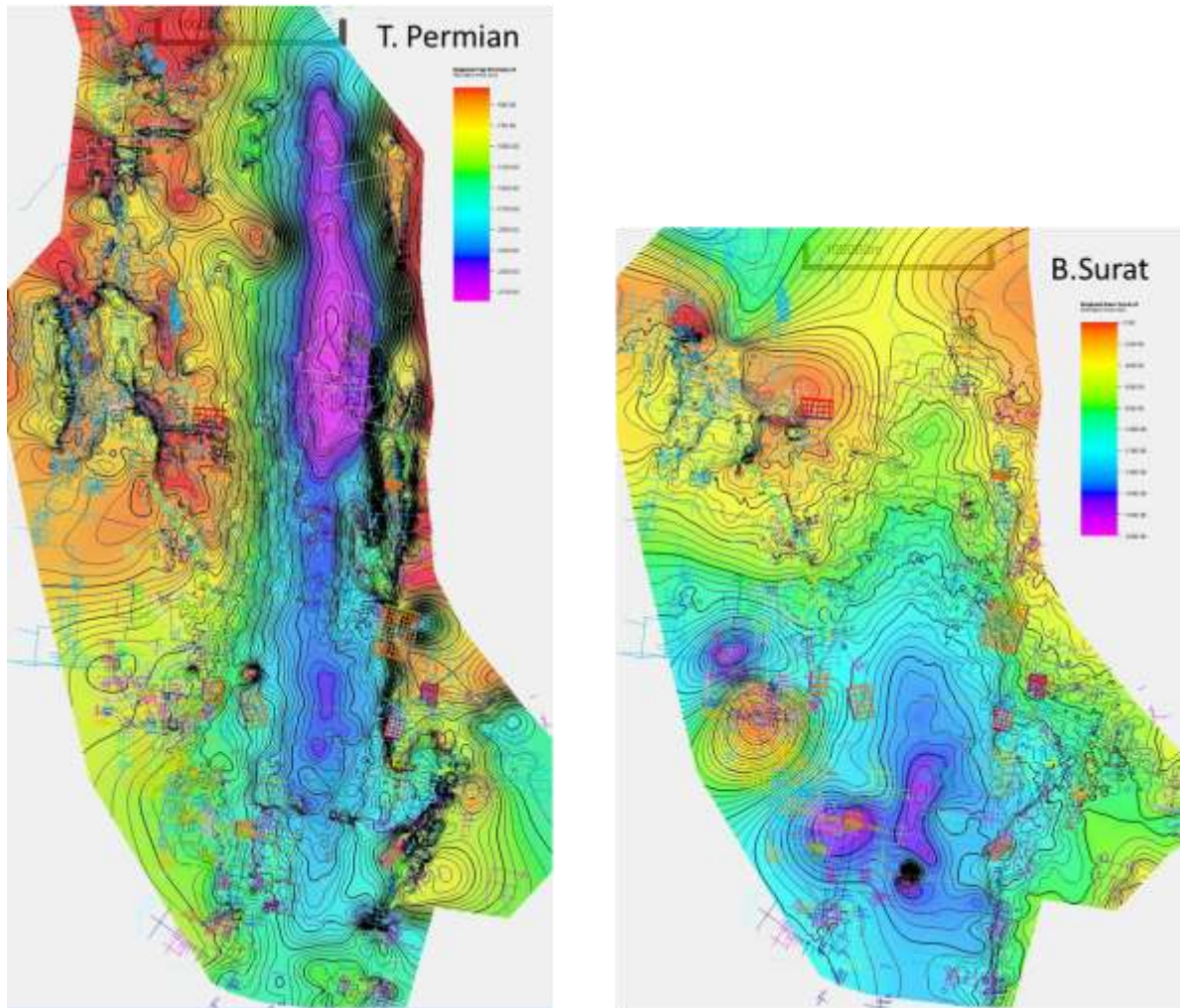


Figure 4.6 A comparison between top Permian structure (left) and base Surat unconformity (right) with equal contour intervals (20ms) shows the maximum Surat depth to be well south of the deeper Taroom trough of the Bowen succession. Major Bowen structures have only minor reactivation during the Cenozoic.

The major structural trends of the eastern Surat/Bowen can be divided into four key sections as shown in Figure 4.7 from south to north: Goondiwindi, Moonie, Transition zone and Leichhardt to Burunga. This series of fault zones forms the eastern boundary of the formal Bowen Basin. Major deformation occurred during the late Triassic forming the “Bowen structures” which underpin the later (Cenozoic) Surat structures of particular interest to this project.

In general, the amplitude of deformation for the Surat structures is a small fraction of that observed for the Bowen. Also, most of the deformation that is coincident with the major Bowen structures is observed to be ductile folding of the Surat succession related to structural reactivation, with only very limited portions showing structural offset at the base Surat. Although the amplitude of deformation may be considered small in relative terms, its expression is likely to have a major impact on natural and production induced flow in affected formations. As discussed in a following section, the faulting which is observed within the Surat, primarily the WCM, is associated with the “keystone” structures.

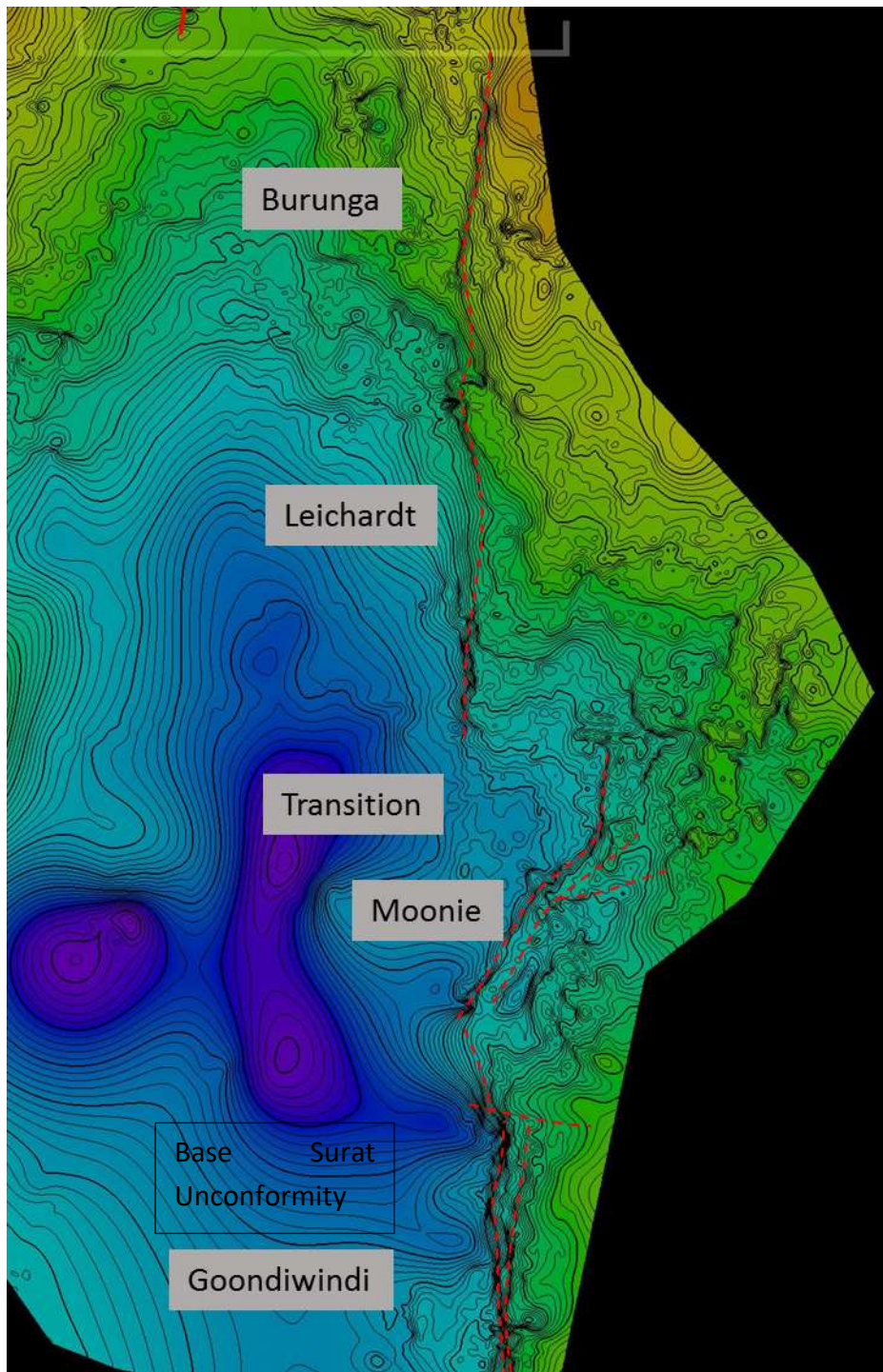


Figure 4.7 Eastern margin Surat Basin - deformation components. Underlying Bowen fault trends (dashed) (CI-20ms).

Each of the segments of this eastern margin system is discussed in more detail below proceeding from south to north:

4.3.1 Goondiwindi Fault System

The Goondiwindi fault system (GFS) begins south of the south-eastern Surat Basin margin and extends over 75km north where the N-S zone of deformation intersects with the Moonie fault system which trends NE-SW. This is one of several major Bowen structural features in the basin.

The southern portion is characterized by vertical uplift and with major compression, the fault morphology varies along strike, moving north, with common elements including a major high angle reverse fault at the basin boundary and 2-3 additional high angle faults accommodating the compression (Figure 4.8). The Permian section is found to be rotated and tightly folded within a ~4km zone of primary deformation.

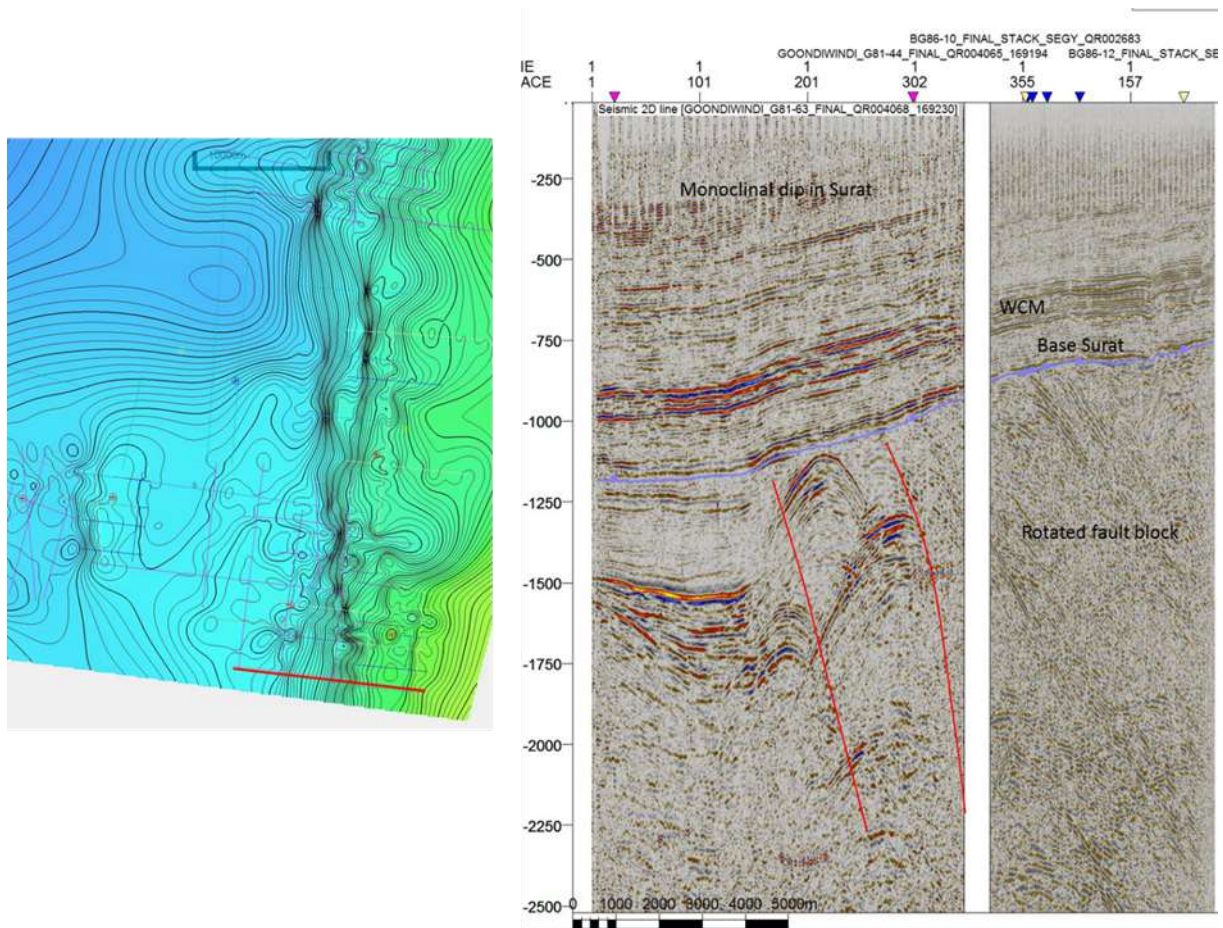


Figure 4.8 Goondiwindi: Southernmost profile showing tightly folded Permian in Bowen section with monoclinally dipping Surat. Map to the left shows location of seismic line relative to the base Surat time structure map (CI – 20ms).

In Figure 4.9, which is a few km north of the previous example, the Permian folds tighten and the uplifted block has developed additional complex faulting. The Surat structure is gently monoclinally dipping with minor reactivation of the major Bowen fault.

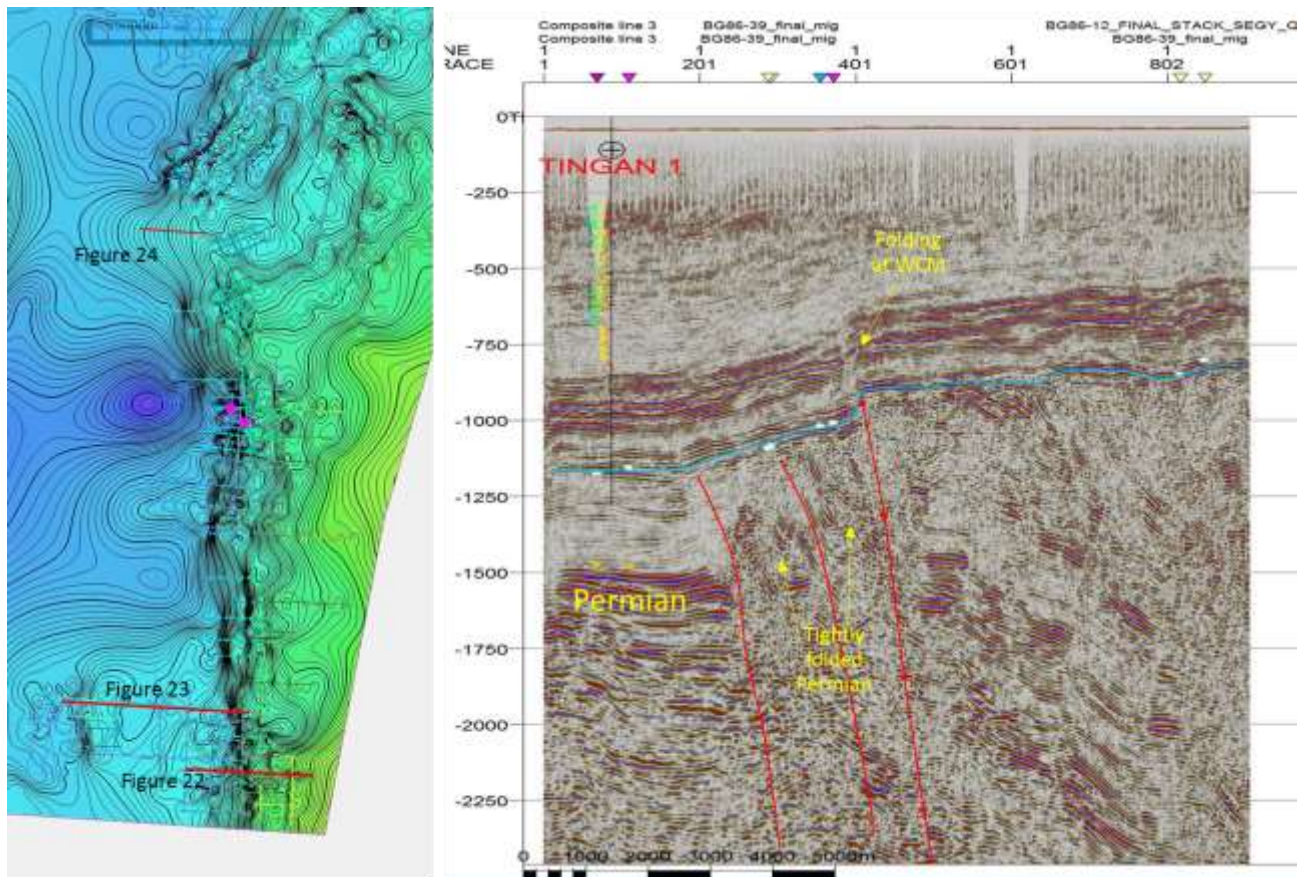


Figure 4.9 Southern Goondiwindi profile: High angle reverse faults with tightly folded Permian. Map to the left is time structure for the base Surat unconformity (CI – 20ms) with line locations for Figures 23/24. Note monoclonal dip over frontal Bowen structure, with Cenozoic uplift reactivating one fault in the system. The GFS appears related to a small subsidiary structure about 15km to the west.

As the GFS is mapped northwards, the fault system remains high angle with a similar morphology as shown in the figures. From the base Surat structure map (Figure 4.9), a divergence of the frontal reverse fault and the eastern reverse fault is observed. The fault trend appears to terminate where the shortening is taken up by a westward thrust fault of Bowen age.

Minor high angle, reverse faults are observed in the Permian section, creating a broad, low amplitude fold in the Surat succession (Figure 25). This structure originates from an earlier Devonian structure across which the Permian section thins.

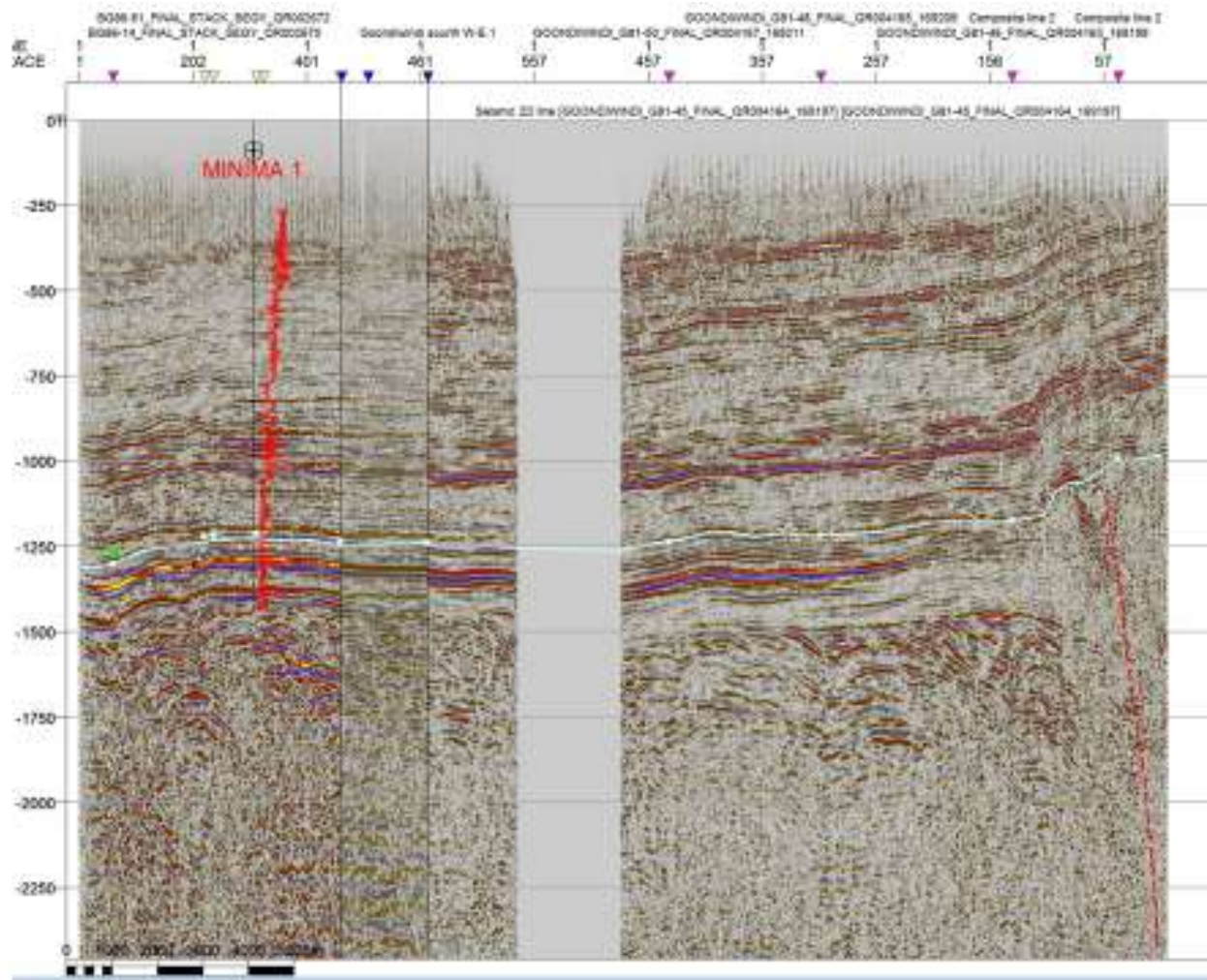


Figure 4.10 A subsidiary, related fault complex west of the GFS also creates gentle folding in the Surat succession.

The transition from the N-S oriented GFS to the NE-SW Moonie fault system is poorly covered by available seismic in the project. A scanned line is presented (Figure 4.11) to illustrate important changes in deformation morphology as the orientation has a major change in direction. The profile shows a lower angle Bowen fault which overrides the basin by over ~4.5km with uplifted dipping section (lower Permian) to the east. This fault character is quite different from that observed to the south and is limited to this ~15km portion. The uplifted section lacks the tight folding and complex faulting observed to the south. It is this E-W shortening which accommodates the proposed strike slip movement across the Bowen deformation along the Moonie Fault System. The overlying Surat has minor deformation, perhaps resulting from gentle relaxation of the deeper basin during the Cenozoic deformation.

At the northern end of the GFS, there is a transition from the N-S trend of deformation to the E-W trend of the Moonie fault system. Here (Figure 4.11), the GFS shows a lower angle fault which overrides the adjacent basin by some 4.5km. The over-riding block of Permian sediments is rotated to dip east.

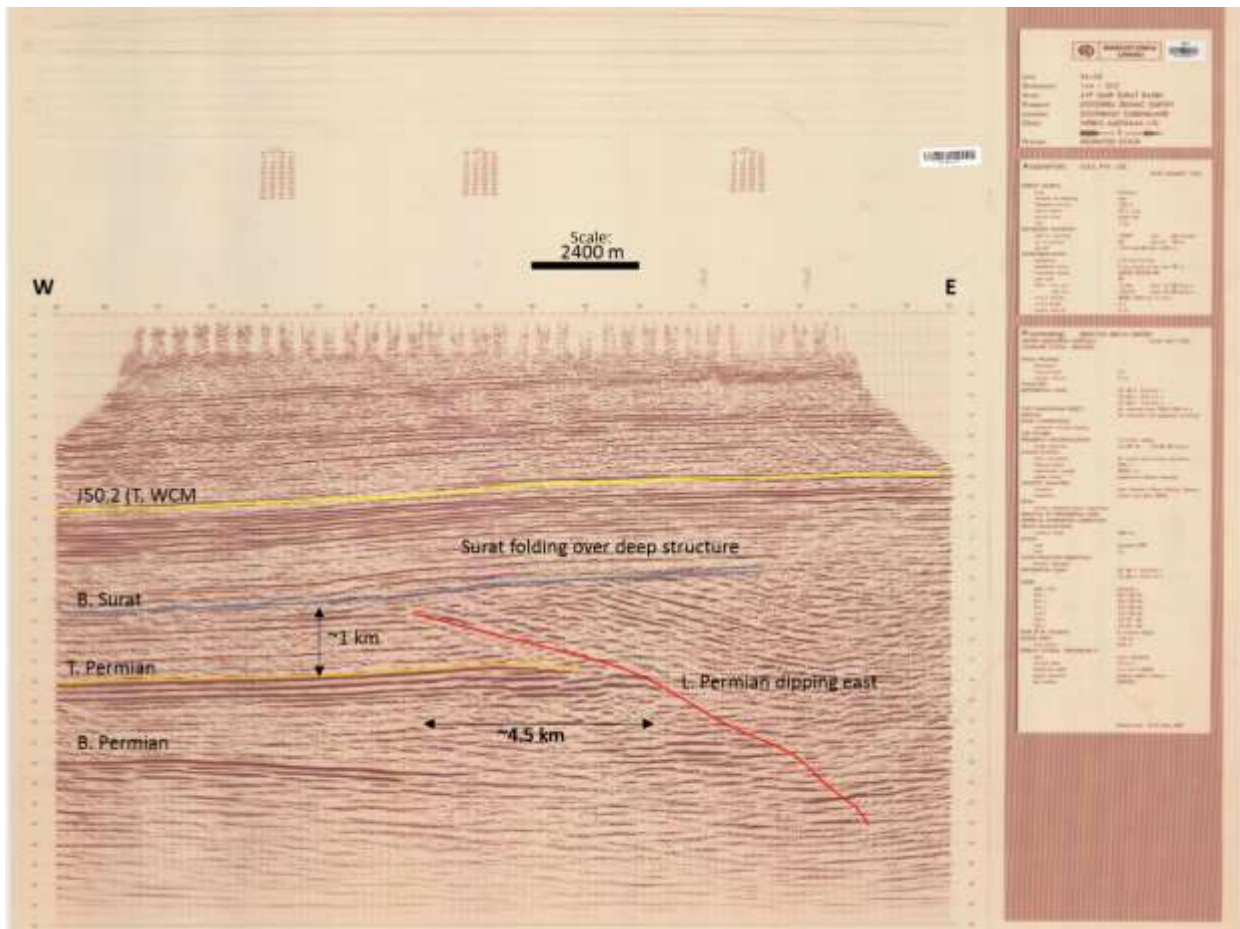


Figure 4.11 Goondiwindi at transition to Moonie, scan profile location in Figure 4.9.

4.3.2 Moonie Fault System

The Moonie Fault System (MFS) is mapped in some detail using the 3D survey and the well distributed 2D data. Multiple faults and complex morphology is revealed with a tightly folded Permian with major conjugate deformation in the Bowen Basin. The later Tertiary deformation in the Surat causes modest to gentle folding with no significant faulting across the Moonie area. The coherency volume created from the 3D volume reveals very limited faulting above the J20 (Westgrove) as shown in the representative coherency time slice through the upper WCM. No doubt this was an important factor in the preservation of sufficient seal capacity above the Precipice to trap hydrocarbons.

A series of 2D profiles at representative locations along the Moonie Fault System are depicted in Figure 4.12. The area was also mapped in a previous study (Wartenburg, 2005), where low-angle thrusting was hypothesized. The data supporting these interpretations is all “final stack” rather than the migrated versions used in this project. These unmigrated data present a distorted view of the structures as diffractions are not collapsed and steeply dipping reflectors are improperly located. This study finds the complex higher angle faults to be a preferred interpretation. The previous work does not address the interaction between the Goondiwindi and Moonie fault systems, nor the change in structural morphology in the transition NE towards the Leichhardt fault system.

Figure 4.14 is a NW-SE profile through Moonie field, the primary bounding fault for the Bowen structure is a high angle reverse fault with the hanging wall block steeply rotated. The fault has small additional movement in the Cenozoic and does displace the base Surat unconformity by a small amount within the Moonie3D survey, though the overlying section is conformably folded. The asymmetric folding in the Surat succession above the Bowen structure has a NE-SW trend with a notable offset just NE of the 3D outline.

The fold within the Surat succession has a prominent offset in strike just NE of the 3D survey. A 2D strike line along the axis of the fold is shown in Figure 4.13. The SW portion of the line dips steeply in the Permian, underlying the Surat, while to the NE the Bowen section is more flat lying.

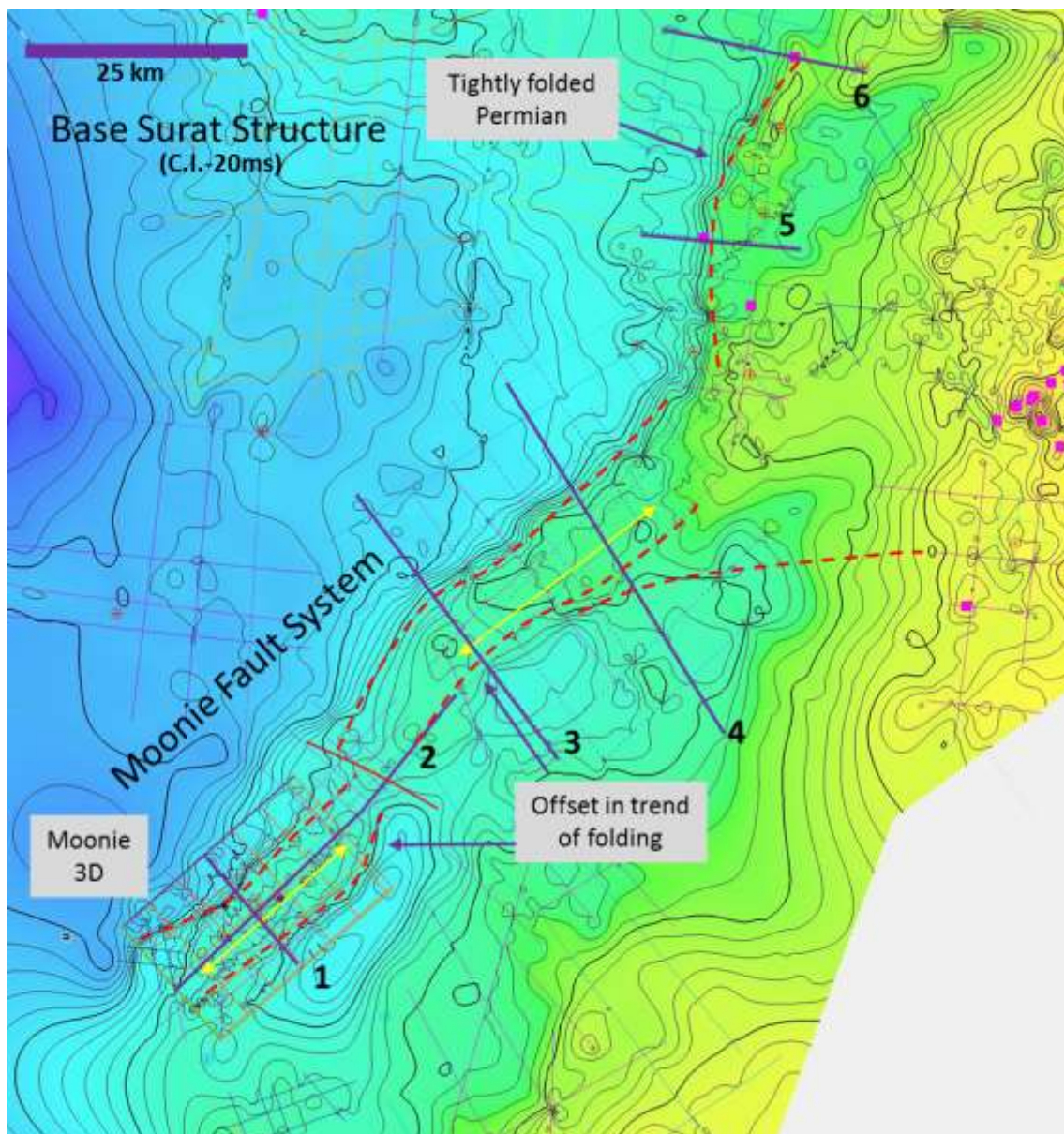


Figure 4.12 Moonie Fault System - profile location map. Note change in trend for folds in Surat (CI – 20ms).

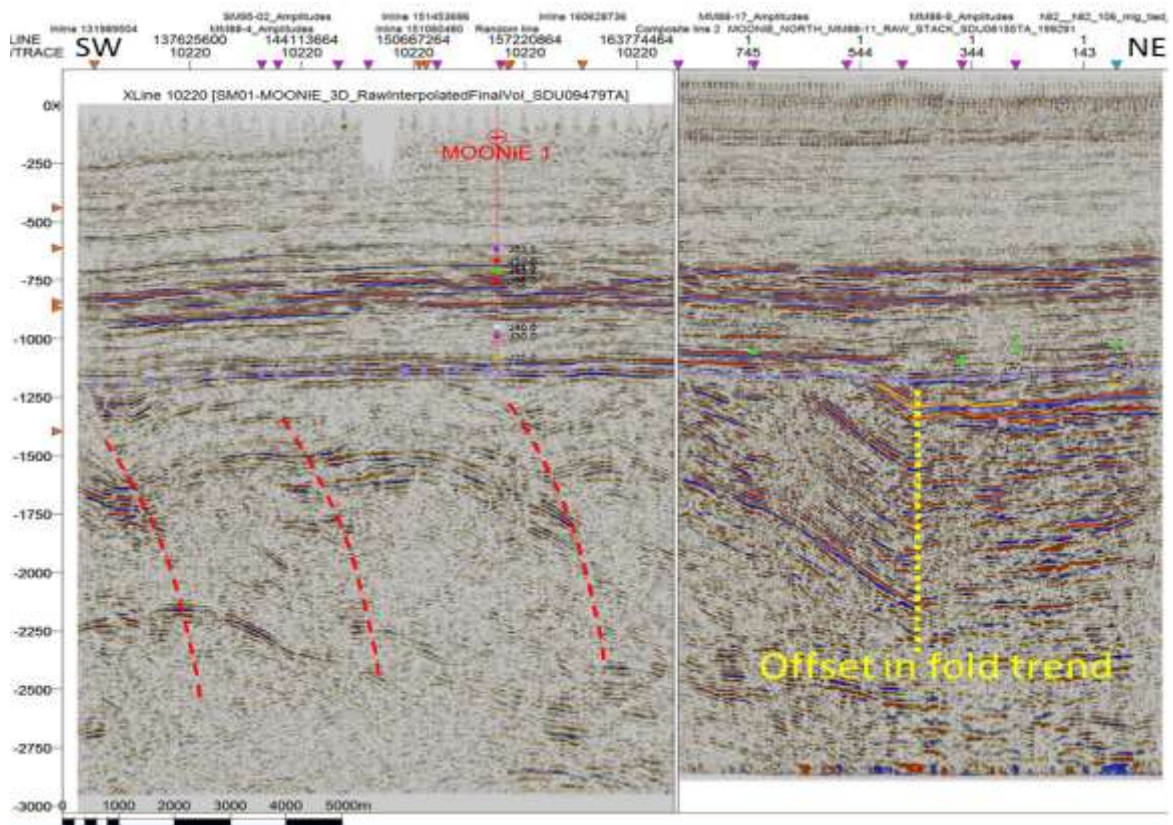


Figure 4.13 Moonie Fault System - Profile 2, strike along structure crest. Illustrates cross faults offsetting Permian strata below Moonie field and the abrupt fold coinciding with offset of the base Surat fold trend.

Interpretation note on Figure 4.13. The fault interpretation on these lines (in isolation) is problematic at least in part due to poorly migrated data (possible 'bow-ties' in the Permian). This means that alternative structural interpretations could arise. In part, this is mitigated by using all lines and biasing style to the better quality lines thus ensuring structural consistency. Note that in general, improved imaging will cause imaged faults to become steeper. However, the overall interpretation and some key seismic lines would benefit from selective reprocessing.

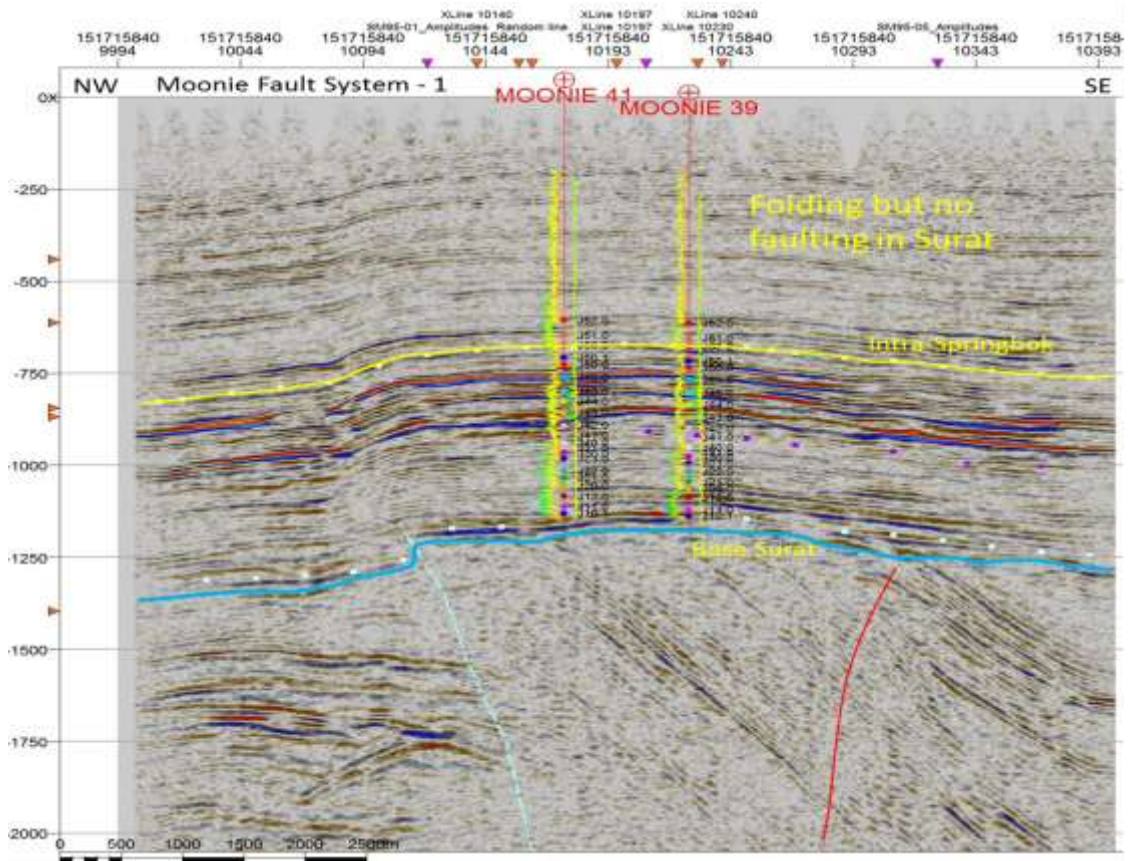


Figure 4.14 Profile 1 through the Moonie structure from 3D survey. Line location Figure 4.12.

The following example (Figure 4.15) depicts the MFS farther to the NE where additional complexity is apparent. Here, added internal faulting allows the block to cause steep rotation of Permian sediments.

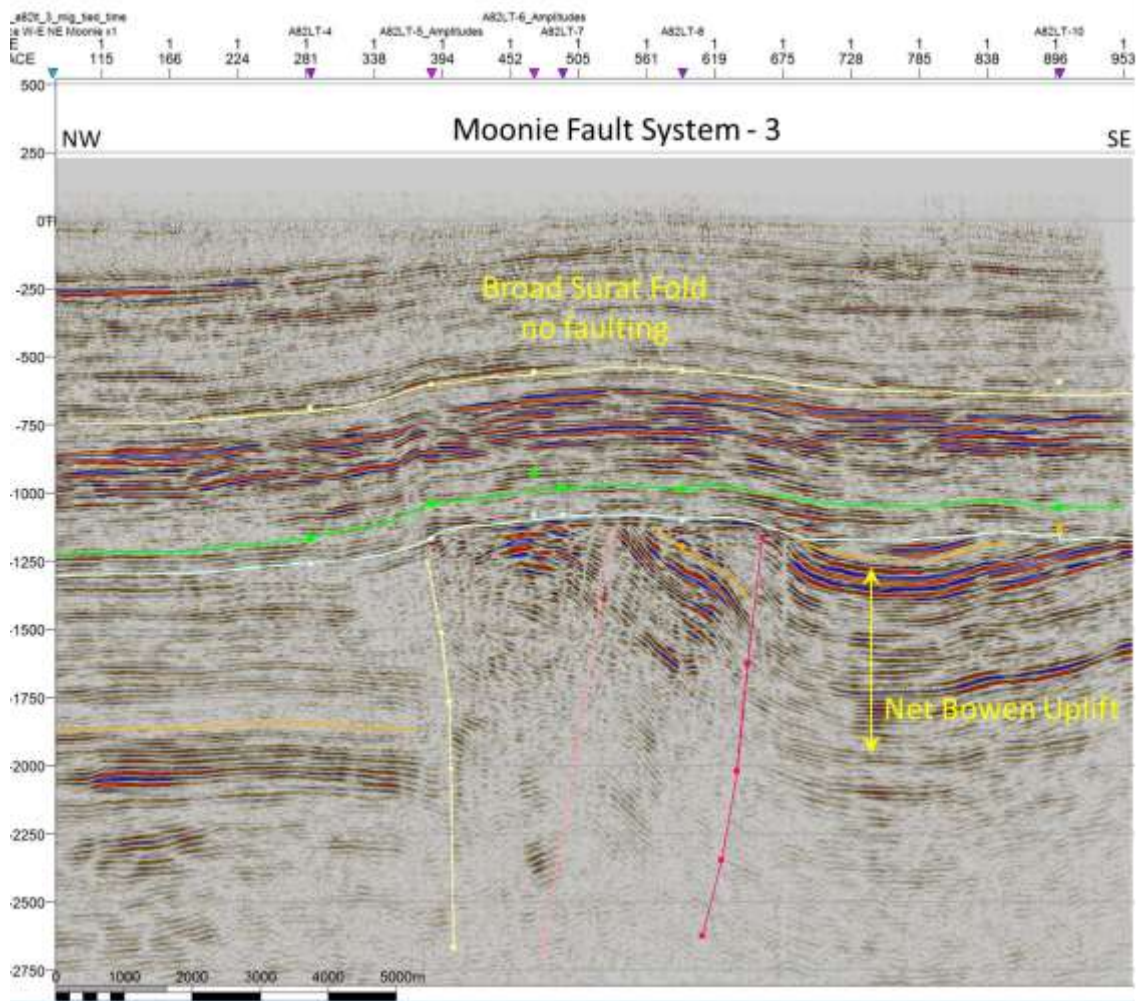


Figure 4.15 Profile 3 - through the Moonie structure to NE of 3D, location on Figure 4.12. Fault system becomes more complex with multiple high angle faults representing Bowen deformation, with gentle slightly asymmetric folding in the Surat.

The morphology of the complex Bowen faulting along the Moonie system appears to be partly related to shear. The sense of motion would be right-lateral and would account for the higher degree of compression observed in the N-S oriented fault systems (e.g. Goondiwindi, Transition, Burunga). As deformation is transferred from the MFS to the Leichhardt-Burunga, a “transition zone” is developed as folding observed at base Surat strikes more northerly.

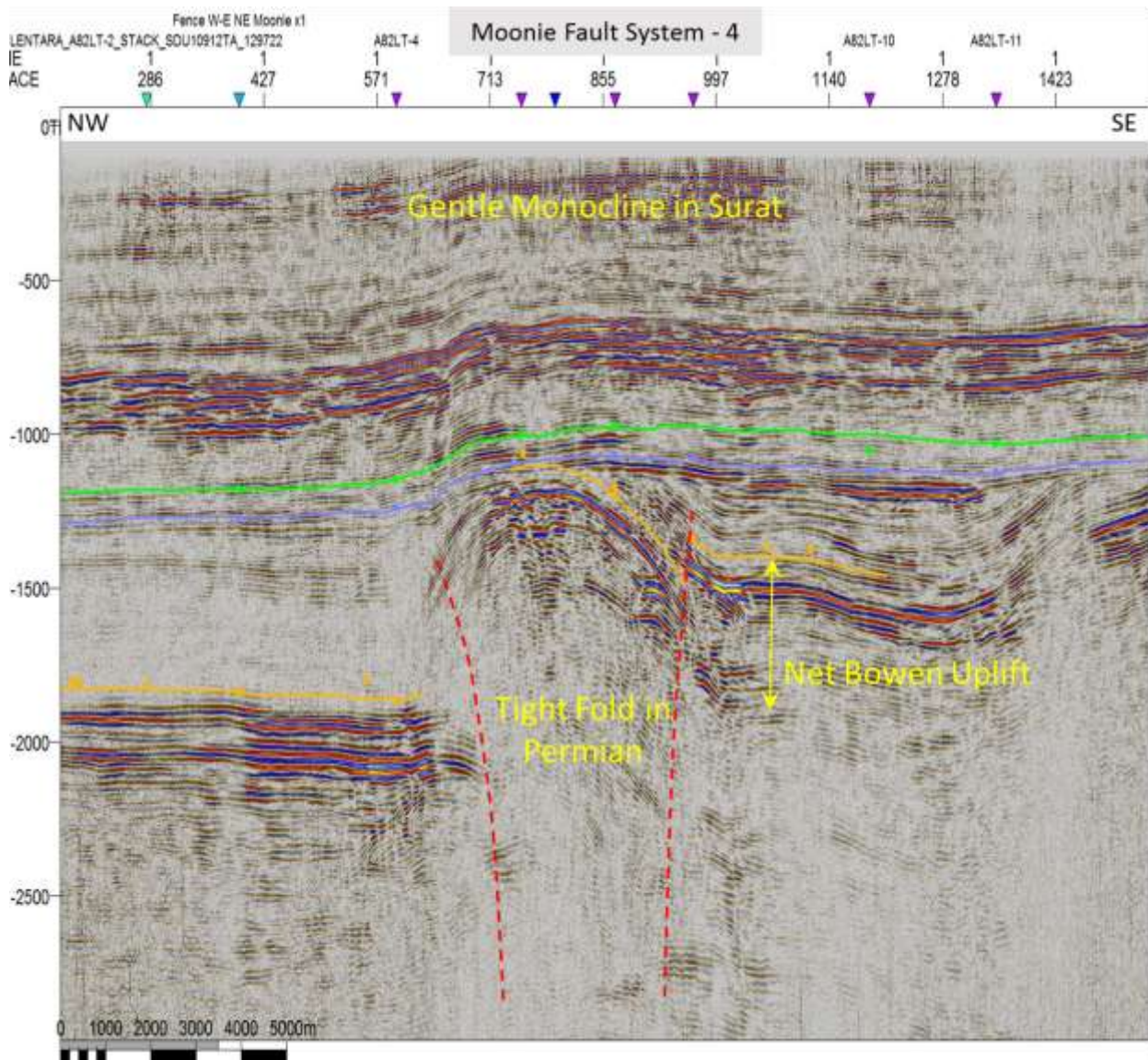


Figure 4.16 Moonie Fault System - Profile 4. Note reduced magnitude of Bowen Uplift from previous.

4.3.3 Transition Zone from Moonie to Leichhardt Fault System

This is an area of apparent displacement transfer where the larger amplitude, more vertical uplift of the major Bowen deformation, is dominated by compression results in tightly folded Permian. Deformation is similar to that along the Moonie trend and the Surat succession is again gently folded. This is also the transition into an area where the keystone faulting is the dominant deformation within the WCM. Keystone faults seem to be developed above the trends of weakness established in the Devonian extensional systems, though imaging is poor on the seismic grid. There seems to be some conformance of folding in the Surat succession and underlying Devonian fault systems.

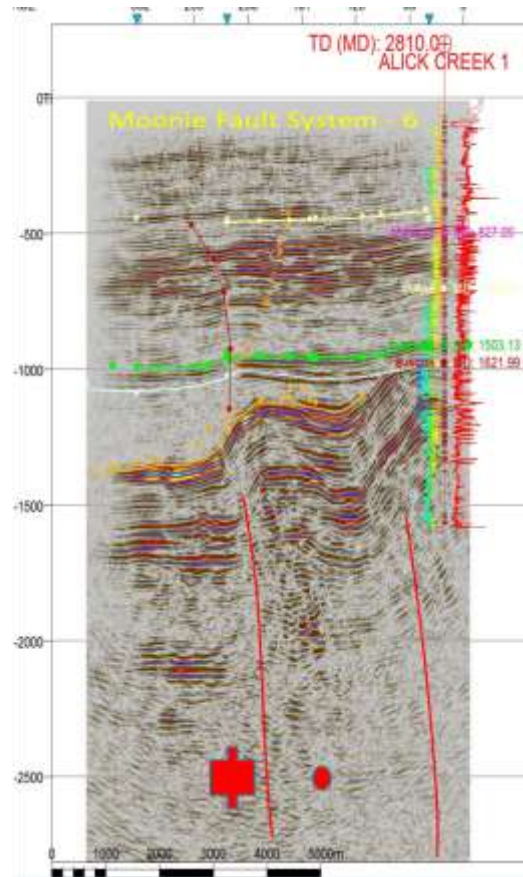
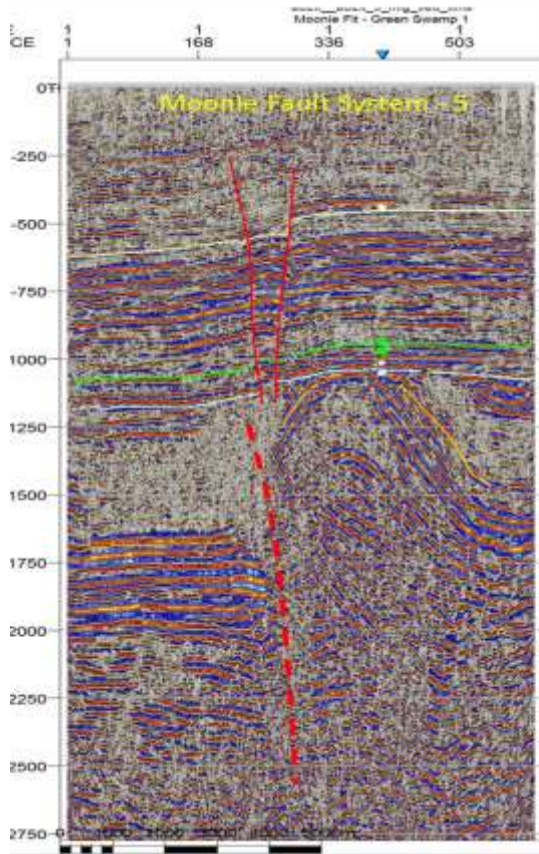


Figure 4.17 NE Moonie Fault, profiles located on Figure 4.12. Profiles show progressive development of tightly folded Permian section below gently folded Surat succession. The development of keystone structures in the Surat appears preferentially located at the margin of Bowen deformation.

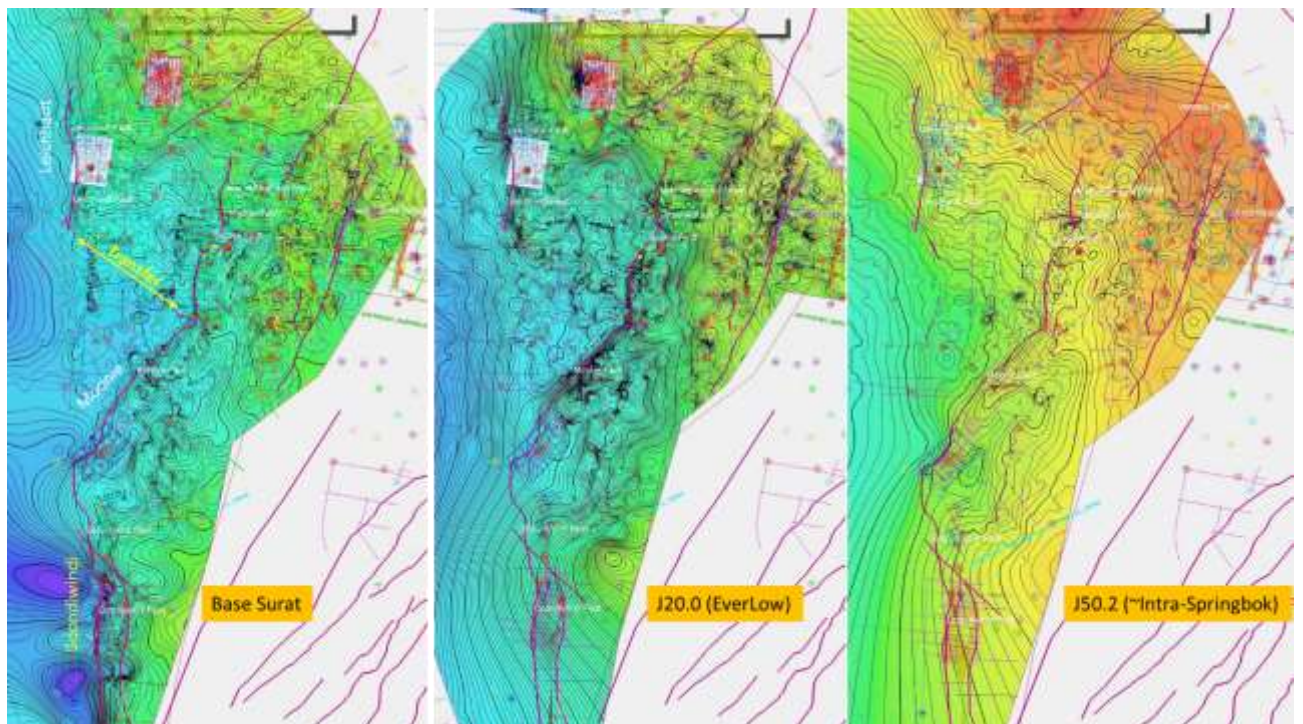


Figure 4.18 Eastern Margin Surat Basin: comparison of structure at top Permian, base Surat and Intra-Springbok. Contour intervals equal (20ms), same color bar and scale.

4.3.4 Leichhardt-Burunga

The Leichhardt-Burunga Fault System (LBFS) is a major deformation feature of both the Bowen and Surat Basins (Figure 4.7). The eastern boundary of the Bowen is defined by the subcrop of the Permian section at the base Surat unconformity.

The Burunga anticline is a major feature on the eastern margin of the Bowen basin. A large compressional anticline oriented N-S extends for 50 km. Folded Permian coals are highly fractured and have excellent reservoir characteristics. However, only subtle folding is observed in the Surat succession indicating little reactivation. In Figure 4.19, structure on the top Permian is shown (left) in a 3D view, with a grid of the interpreted lines for base Surat horizon overlain on it. As the same vertical exaggeration applies to both horizons, the relative amplitude is striking. This can also be seen further in the previous regional comparison display (Figure 4.6).

In the first example profile (Figure 4.20) from the south end of the anticline, the structure is very low amplitude adjacent to the much larger uplift along the Cockatoo Fault Zone. Moving north 15km to Profile 2 (Figure 4.21), the structure is much better developed and shallower relative to the base Surat unconformity (blue). In the final example (Figure 4.22), top Permian has been eroded at the unconformity. At this point, the underlying Devonian block reactivated to form the uplift is apparent.

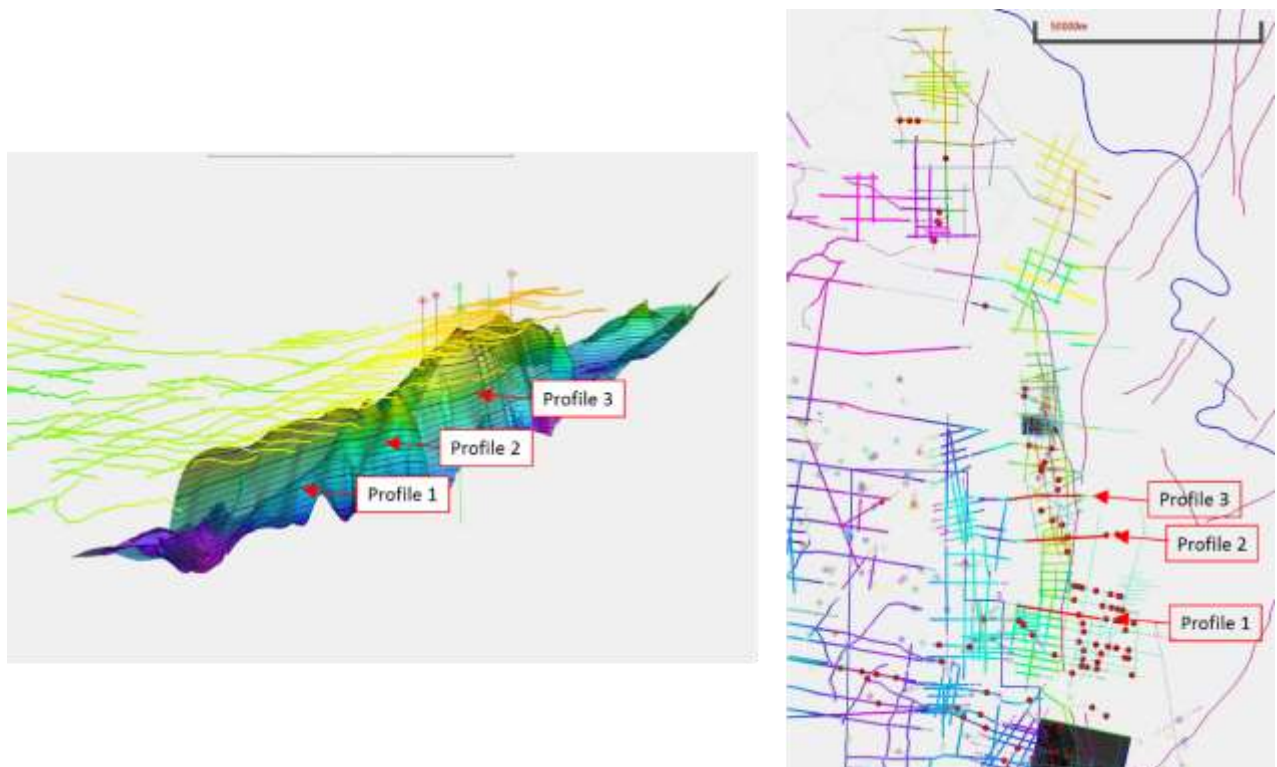


Figure 4.19 Composite view of Burunga anticline and example profiles. Left panel is "3D" structure on top Permian coal, with a horizon grid for the base Surat unconformity above. Right panel shows profile location and seismic data grid.

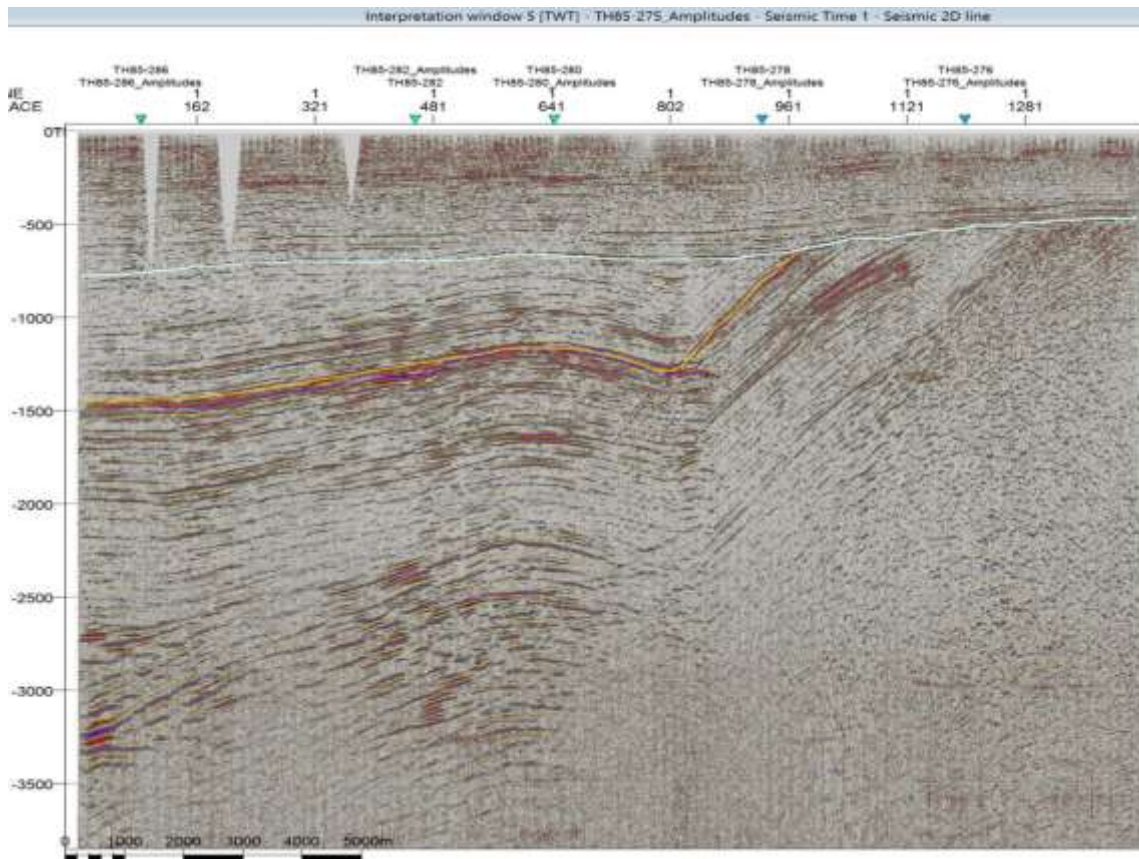


Figure 4.20 Burunga Anticline Profile 1.

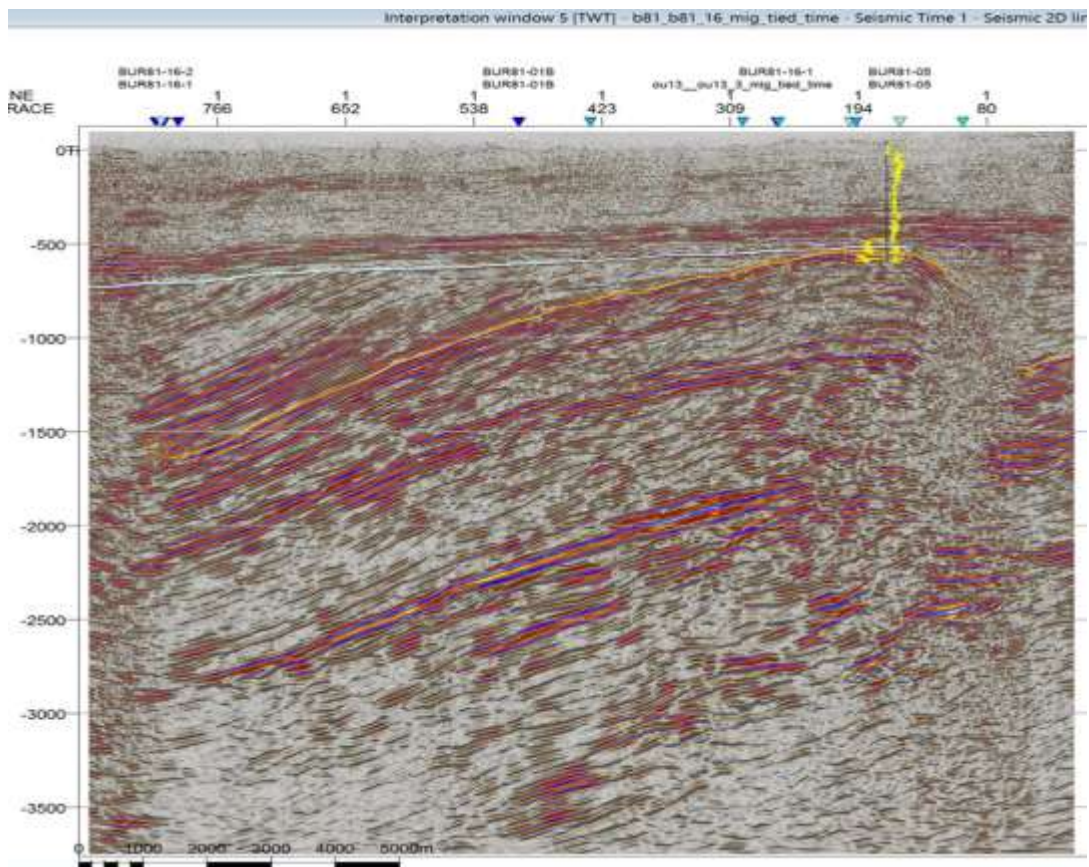


Figure 4.21 Burunga Anticline Profile 2.

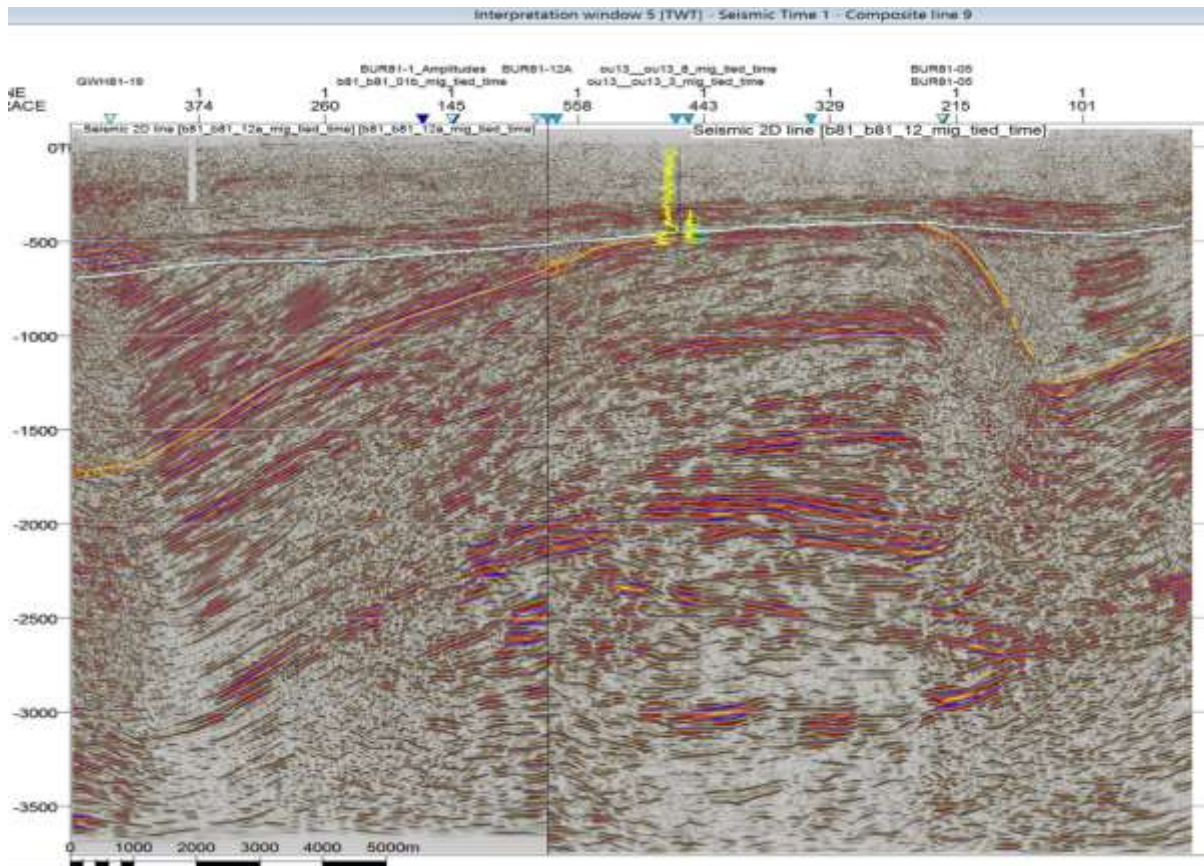


Figure 4.22 Burunga Anticline Profile 3.

4.3.5 Hutton-Wallumbilla Fault System

The Hutton-Wallumbilla Fault System (HWFS) forms the western margin of an extensive uplift on the Roma shelf extending ~100km or more. Major deformation in the late Triassic results in complex fault morphology and is consistent with strong transpression. Uplift is dominantly vertical on the west with a large area of basement rotation, gently sloping to the east. The southern portion of this structure is reactivated in the Cenozoic, beginning with inversion to the southeast and continuing along structure as additional vertical uplift in the Surat succession. The Bowen structure continues northerly until attenuating close to the Simmie Fault. The Simmie Fault is a reactivation of an earlier normal fault. J20 structure shows a modest anticlinal structure.

Figure 4.23 is a profile just south of the southernmost point of observed fault displacement for the (HWFS). In this area, a broad fold is propagated upwards through the Surat succession as part of the Cenozoic deformation. In other data discussed later in this report, these “inversion” features are found to be expressed as intense shallow extensional faulting which may affect fluid flow in Cretaceous aquifers.

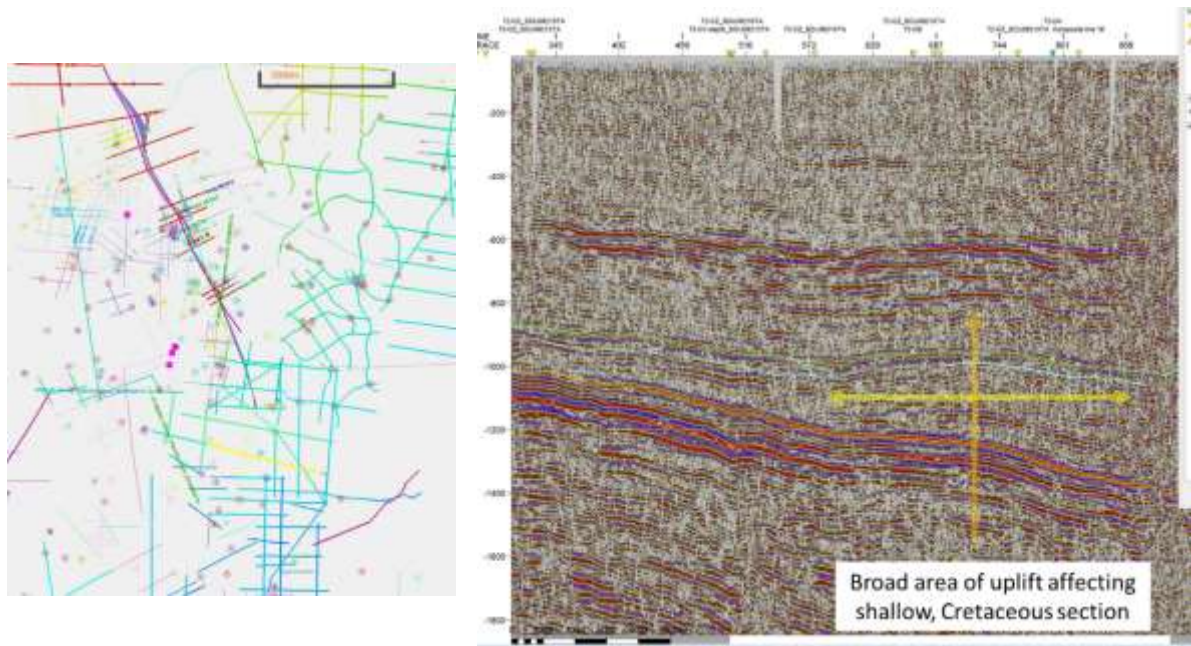


Figure 4.23 Hutton-Wallumbilla, late inversion, south end. Yellow line on the left index map is section location.

Moving to the north, a few kilometers fault displacement begins to be apparent along the HWFS and minor folding in the Surat (J20-Westgrove, green).

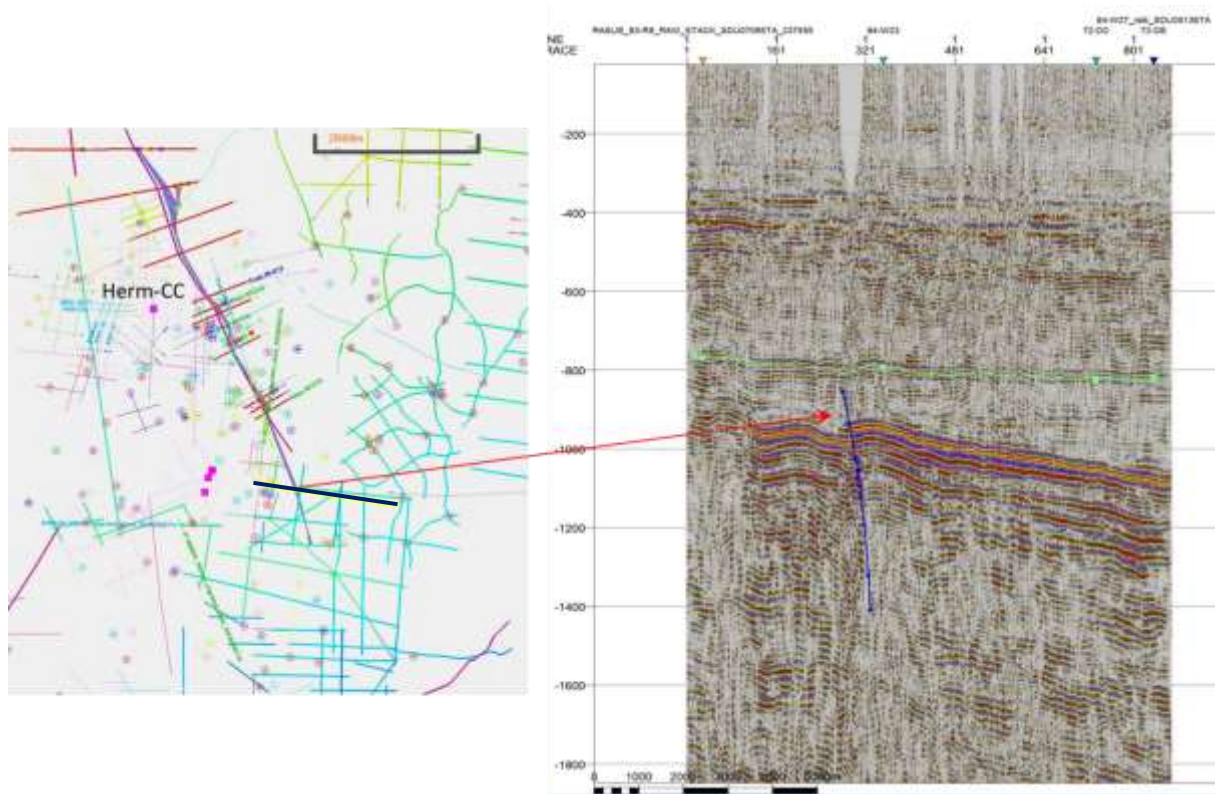


Figure 4.24 Hutton-Wallumbilla, late inversion, south end, initial faulting. Yellow line on the left index map is section location.

Figure 4.25 is a profile through the Coxon Creek area. Deformation for the Bowen structure increases at this location, with later Cenozoic movement of the order of a small fraction of relative amplitude. In addition, complex keystone faulting is observed on the uplifted block.

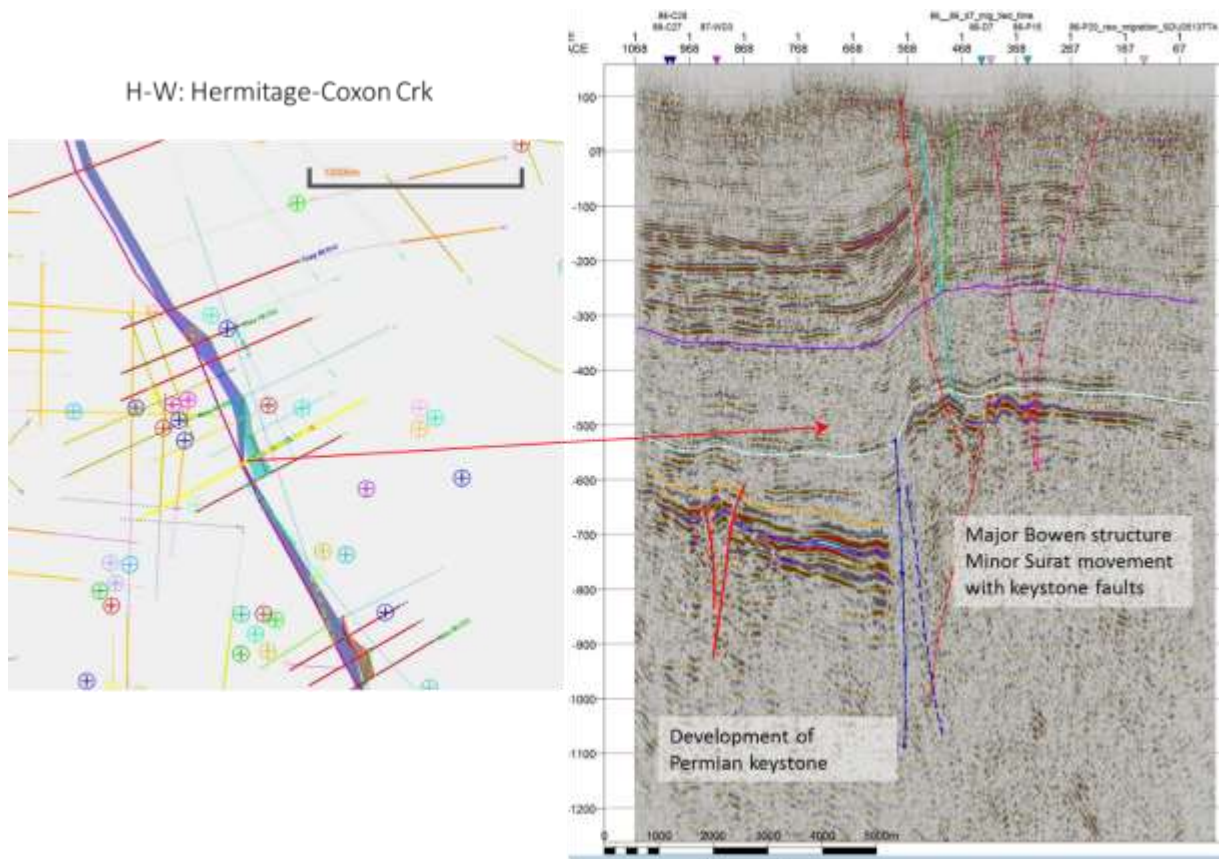


Figure 4.25 Hutton-Wallumbilla in Coxon Creek area.

North of Coxon Creek in Figure 4.26, the HWFS exhibits a similar displacement, though the Permian is eroded. A companion fault “H-W West” is developed merging with the main fault system farther north. The amplitude of deformation in the Surat is similar to the previous example at Coxon Creek.

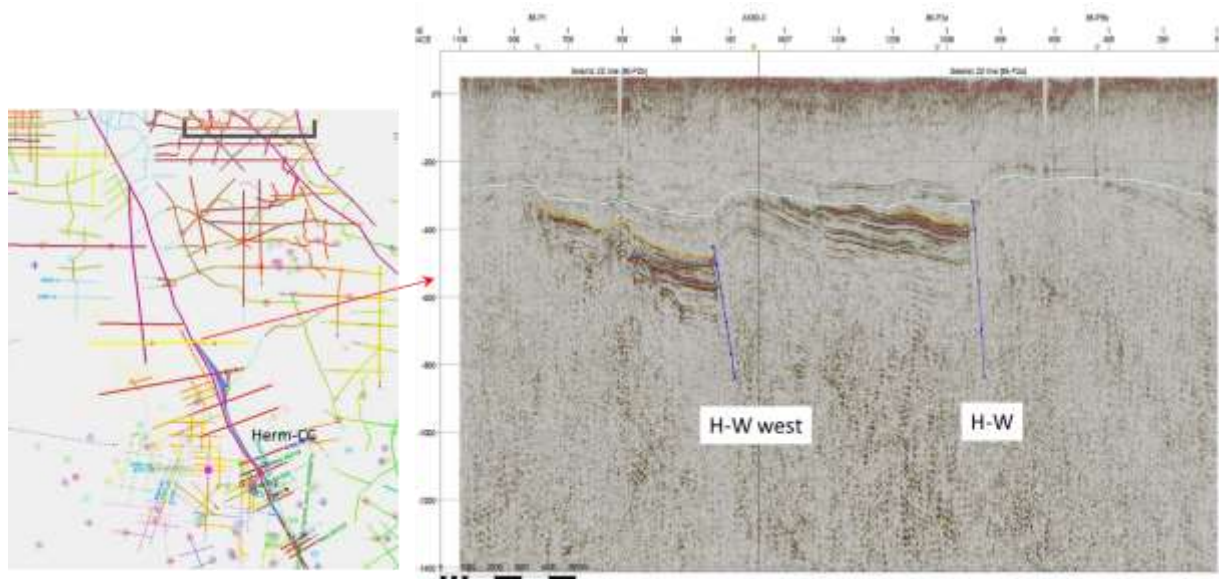


Figure 4.26 Hutton-Wallumbilla,. Yellow line on the left index map is section location. Progressive development and additional deformation to the west.

The HWFS obtains maximum deformation in the Bowen (Figure 4.28), and the uplifted block is found to have complex fault morphology. Deformation in the Surat is difficult to map in this profile because seismic coverage along this portion of the HWFS is limited, so detailed mapping is not possible.

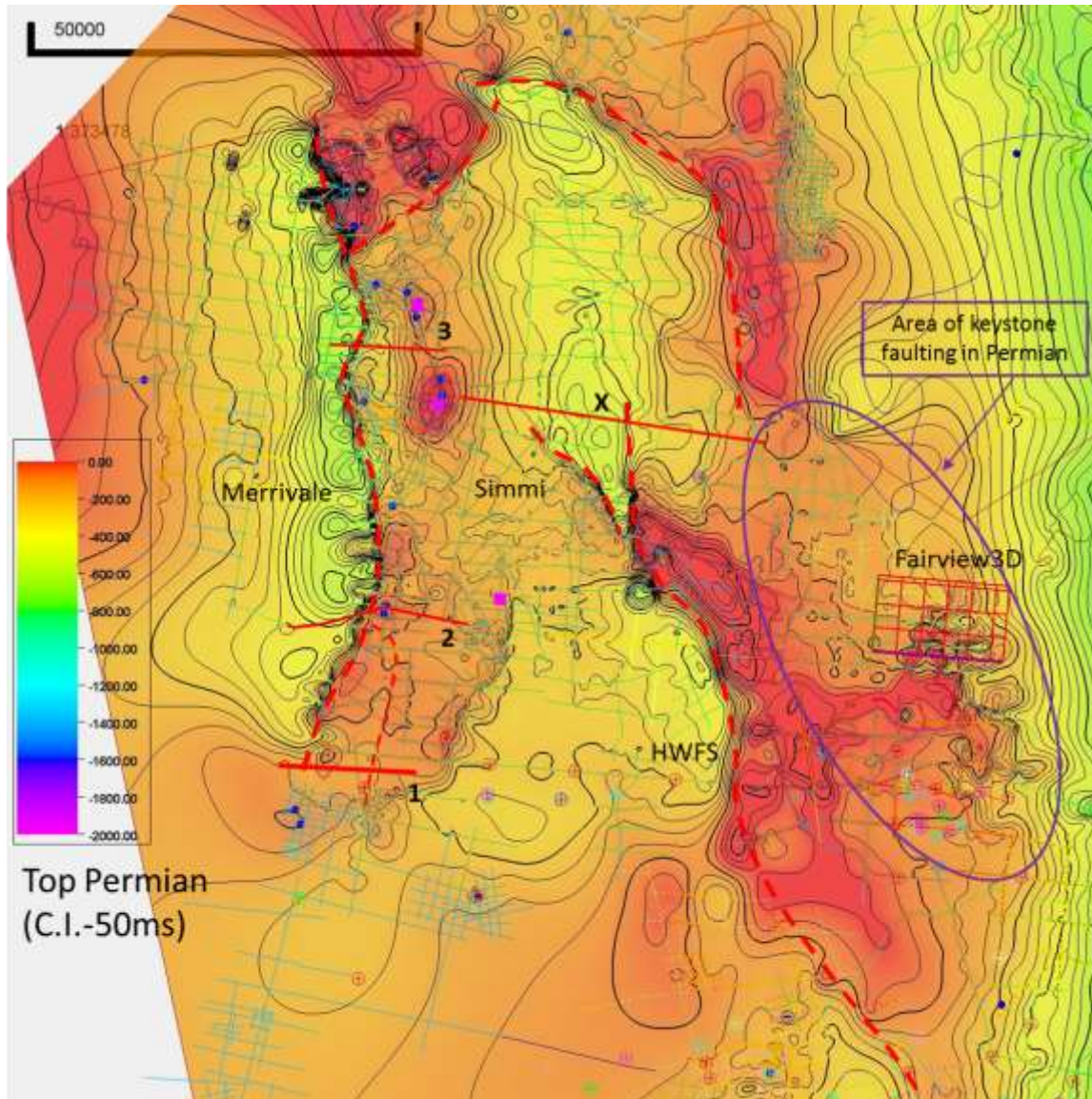


Figure 4.27 The northern Hutton-Wallumbilla and interaction with the Merivale, Simmie and other major fault systems. On the east side of HWFS, an area of Cenozoic keystone faulting is overprinted on Bowen deformation. This is an area of high productivity CSG production from the Permian coals.

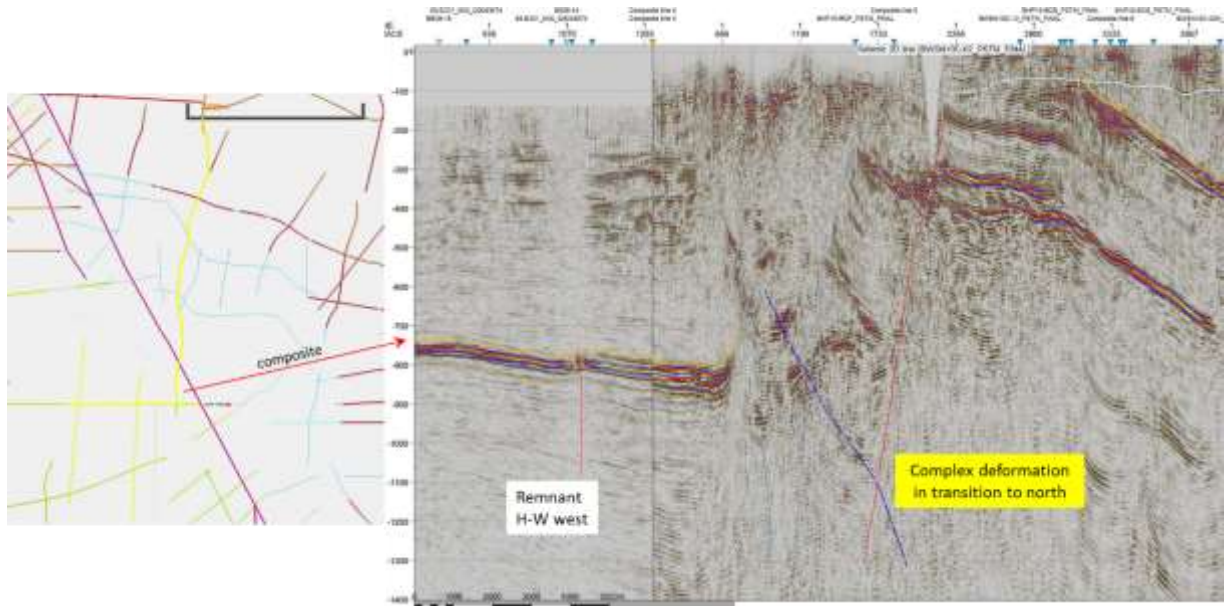


Figure 4.28 Hutton-Wallumbilla, Yellow line on the left index map is section location. Major deformation shown by the complex faulting and to the left the remnant fault.

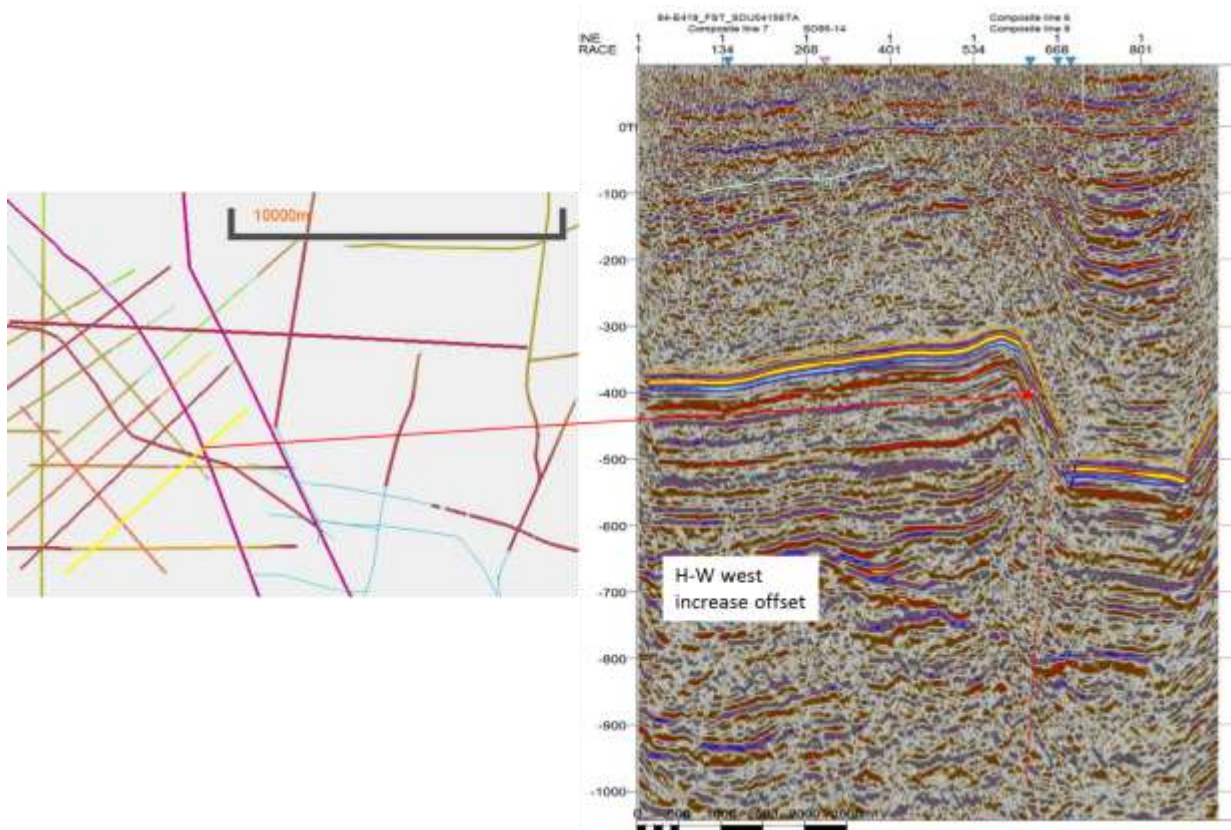


Figure 4.29 Hutton-Wallumbilla, Yellow line on the left index map is section location. Development of the graben with increasing offset on the western fault.

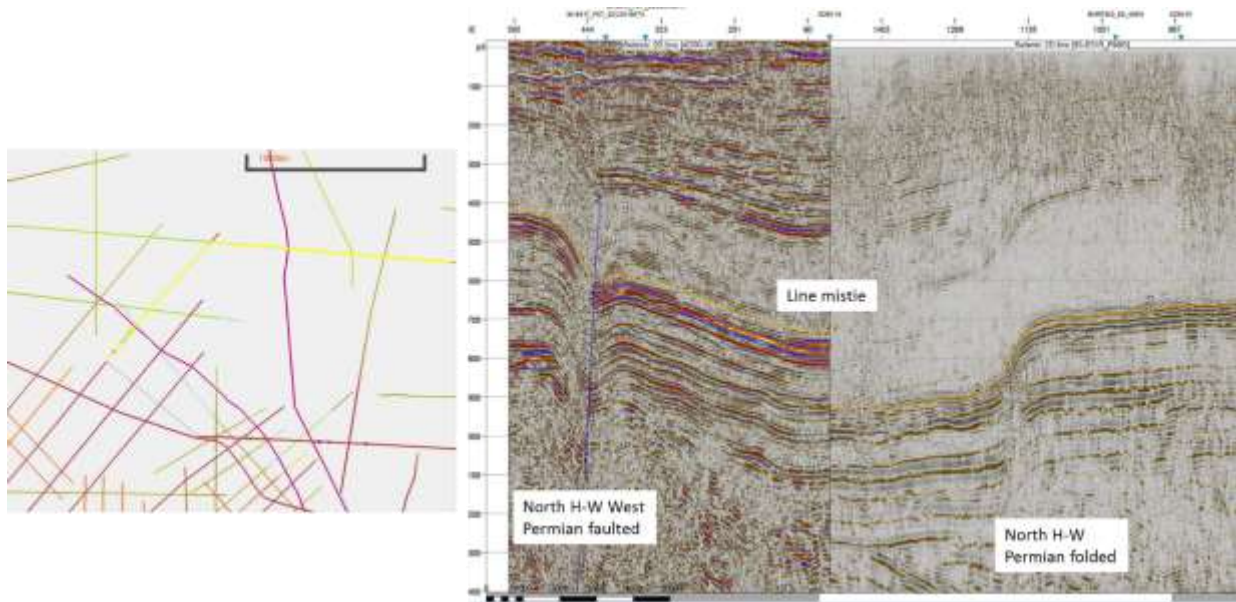


Figure 4.30 Hutton-Wallumbilla, Yellow line on the left index map is section location. Northern end of this structure with minimal deformation in the Surat.

4.3.6 Merrivale Block

The Merrivale block is another large Bowen deformation feature which is structurally reactivated in the Cenozoic. The block is bounded by high angle reverse faults on the west (Merrivale fault) and the east, forming a gently uplifted block in the Surat overlying a similar, much larger structure in the Bowen.

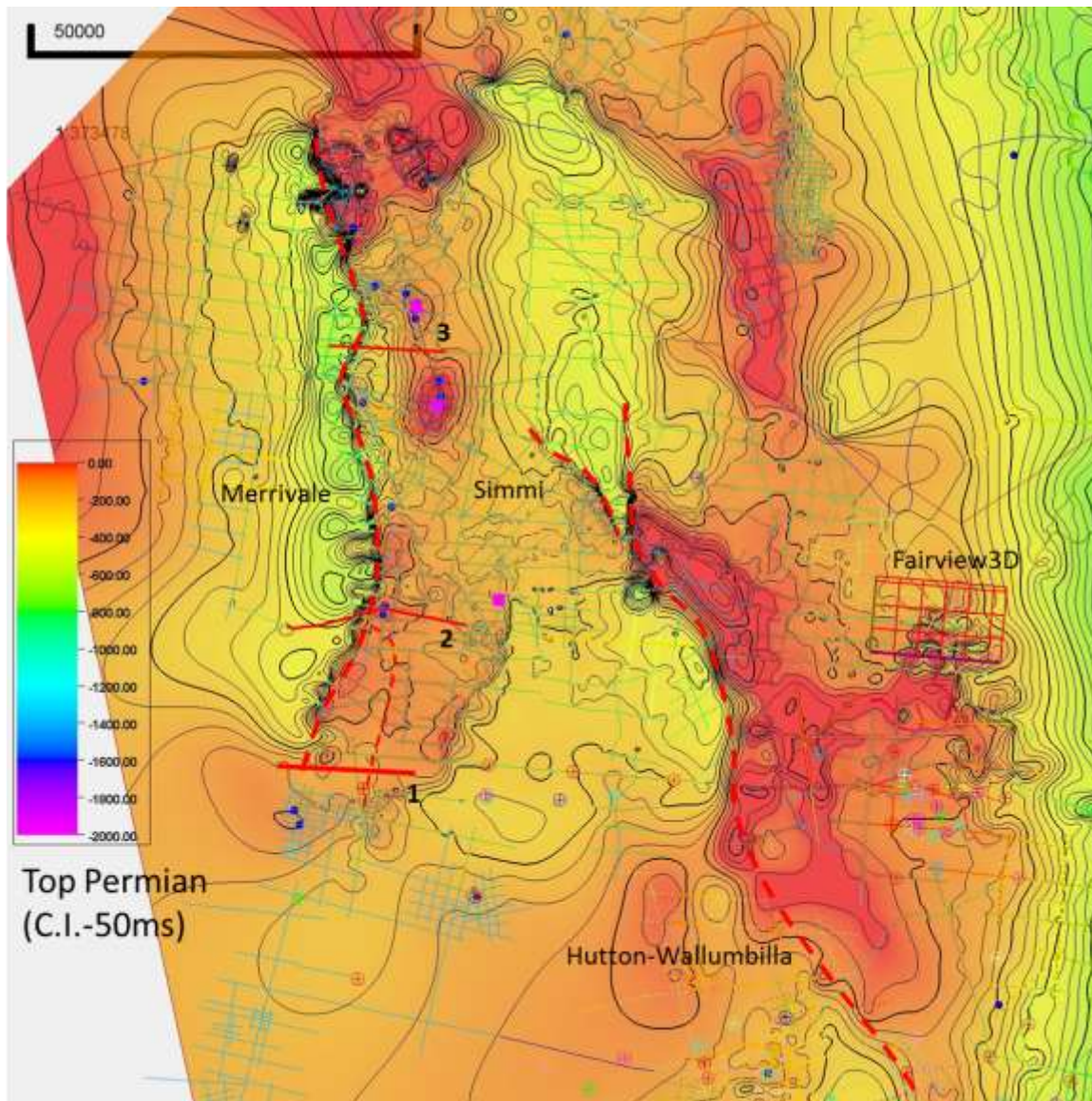


Figure 4.31 Merrivale to Hutton-Wallumbilla area with locations for Profiles 1-3.

The following 3 profiles (Figure 4.31) show the development of the Merivale fault along the system which extends for ~75km. In general, the deformation is relatively simple compared to others showing vertical uplift along its length. Profile 1 (Figure 4.32) is located at the southern extent of the Merivale fault, with minor displacement in the Bowen. A related fault, Merivale East, is also observed. These are shown as dashed lines in the map (Figure 4.31).

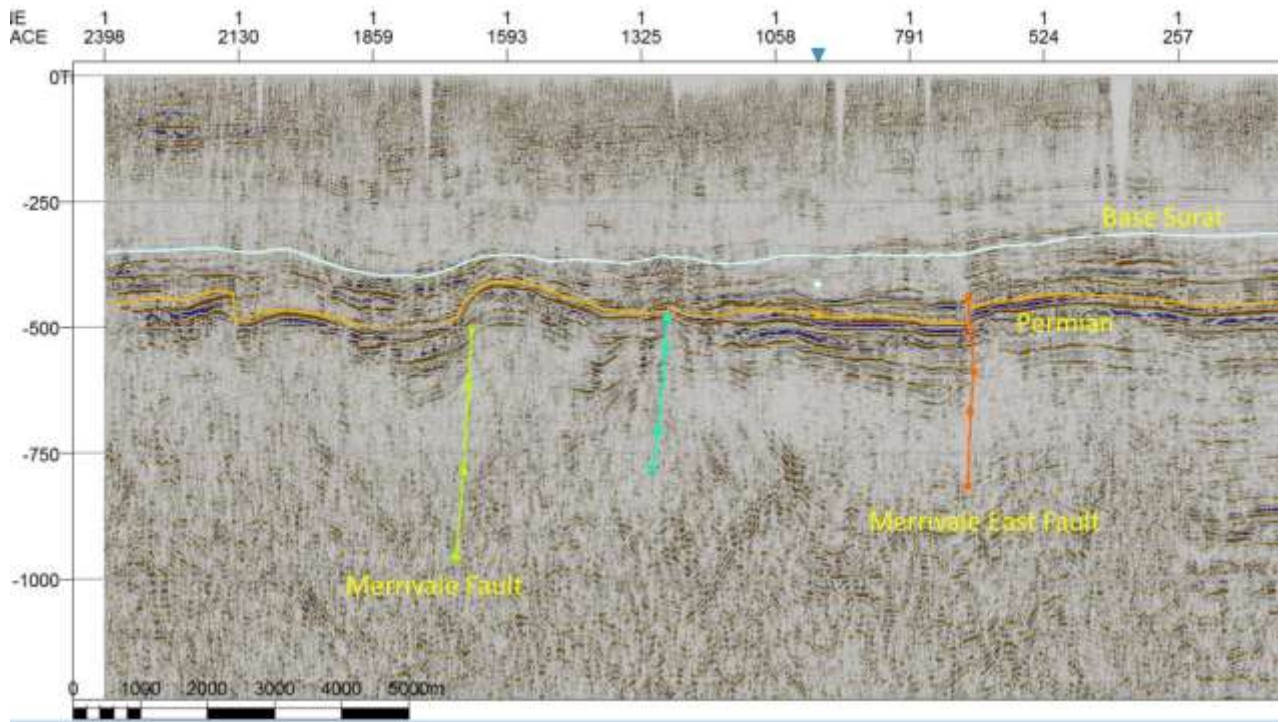


Figure 4.32 Merrivale Fault: Profile 1.

Moving north to Profile 2 (Figure 4.33), the Bowen displacement increases, but Surat folding is roughly the same amplitude and broader.

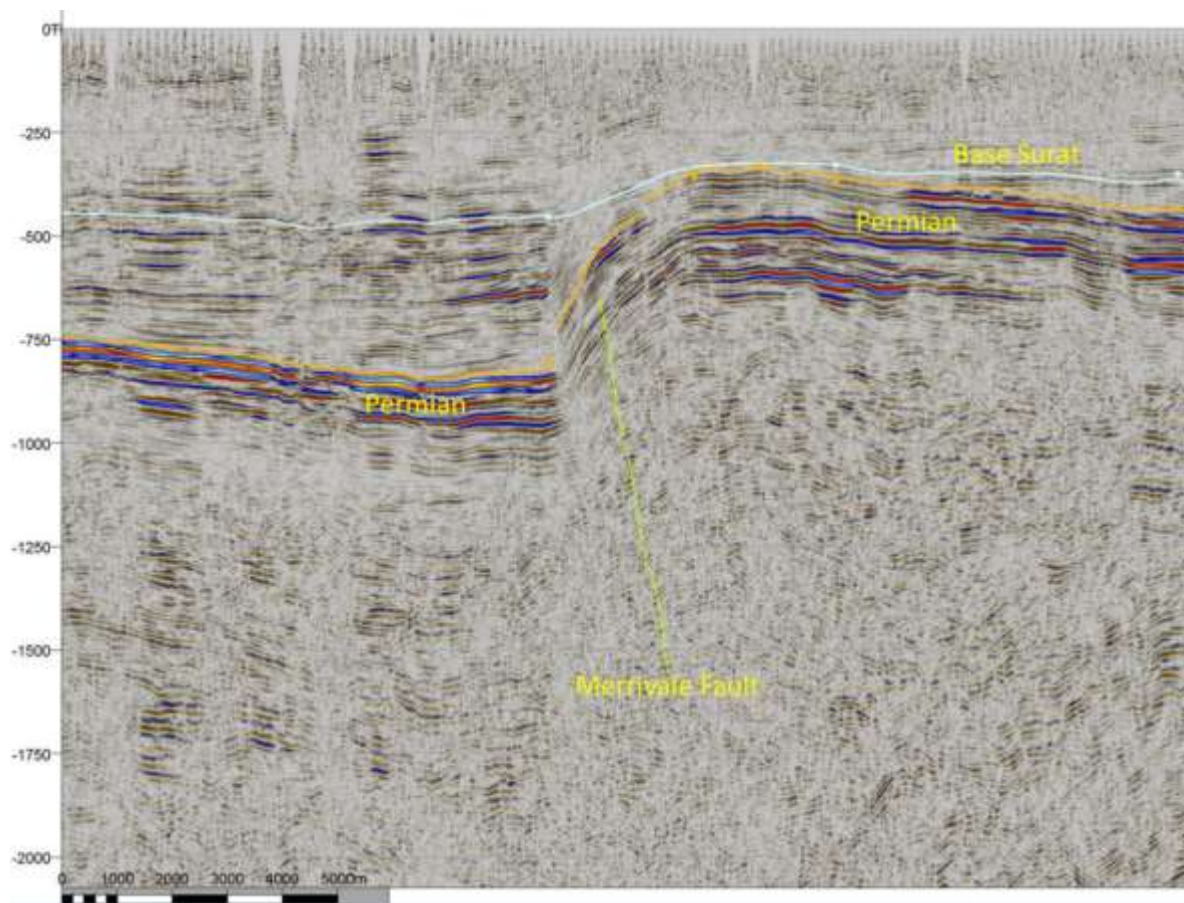


Figure 4.33 Merrivale Fault: Profile 2.

Note again that there is some ambiguity in the precise placement of fault locations relative to the break in the reflectors. In part, this can be mitigated where 2D and 3D are in close proximity and by considering several lines, weighting to the best imaged (migrated). However, details would be improved by selective reprocessing.

At the northern portion of the fault the Bowen displacement develops strong folding, probably related to increasing compression. Westward thinning of the Permian section indicates inversion during the older deformation. Continued gentle folding is found in the Surat.

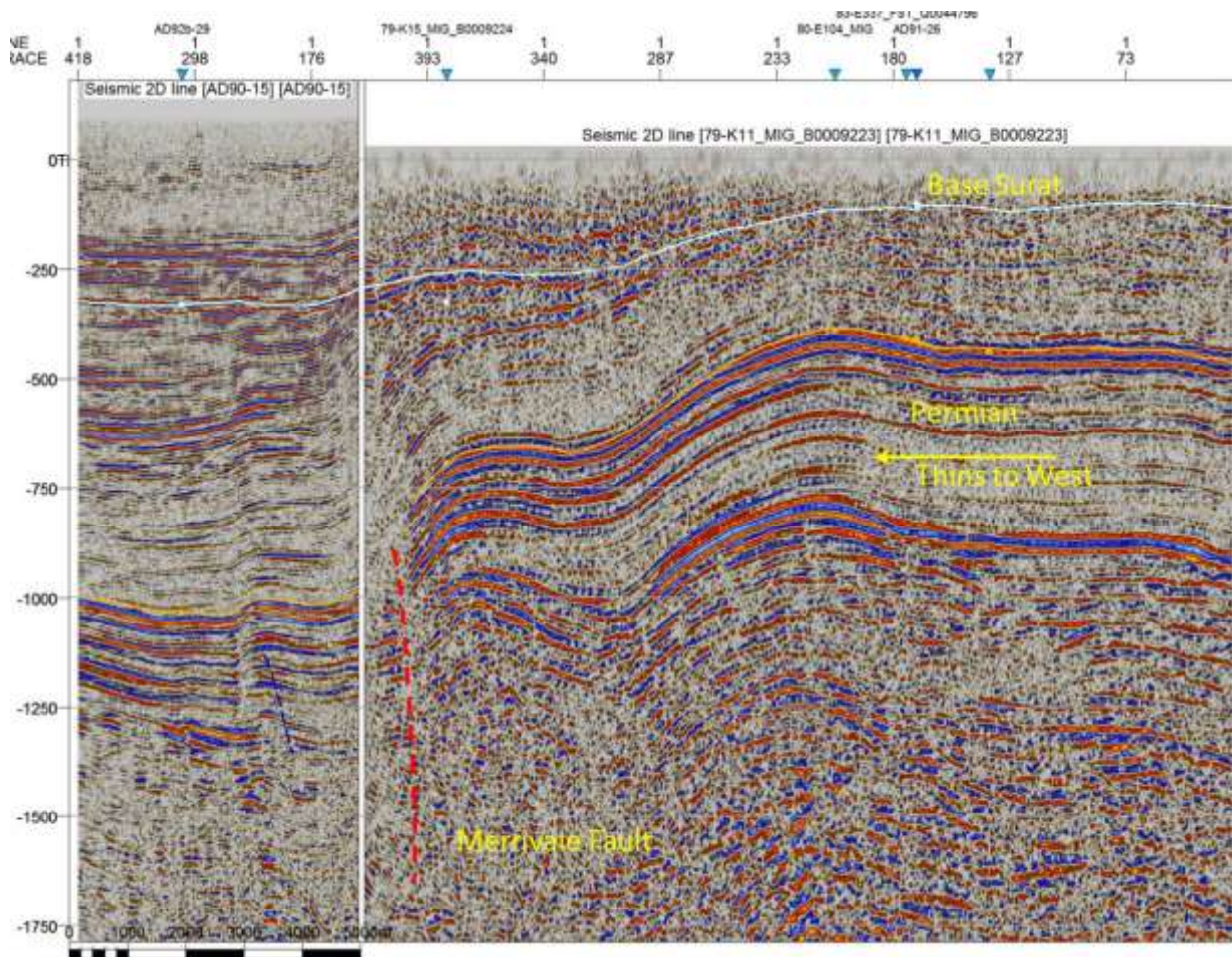


Figure 4.34 Merrivale Fault: Profile 3.

Figure 4.35 compares Permian and base Surat structure. Both maps have the same contour interval (20ms) and similar seismic control. Most of the Surat deformation or structural reactivation occurs along both margins of the block to the south. Bowen deformation in both systems is more extensive. The northern portion of the Hutton-Wallumbilla is at the right. An obvious “Y” shaped graben structure is seen in the top Permian map, but is barely apparent on the base Surat structure indicating little continued deformation in the Cenozoic.

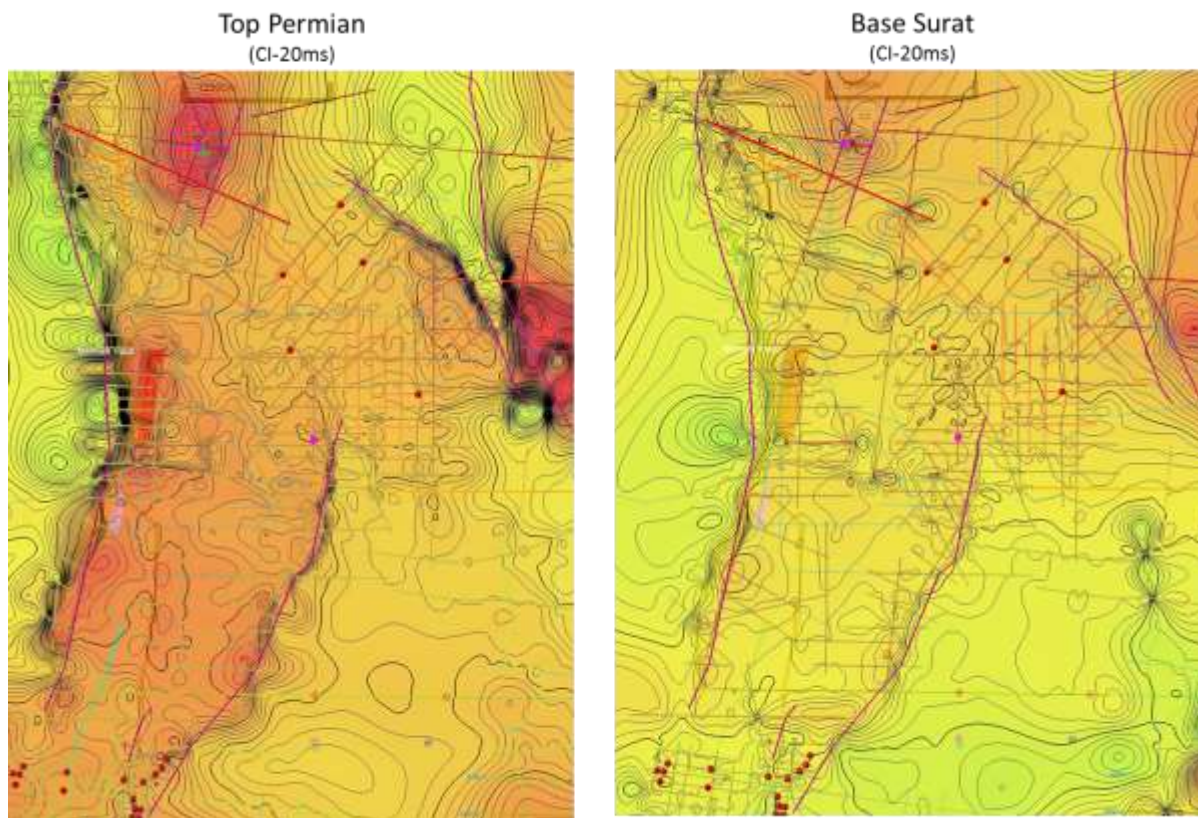


Figure 4.35 The Merivale Block, relative amplitude at Top Permian (left) and Base Surat (right) levels.

4.3.7 The Keystone Structures

The *keystone structures* are observed to be a distinctive feature of the Cenozoic deformation within the Surat Basin and are an important influence and generally enhance permeability within the WCM where encountered. Operators report greatly improved CSG flow in these areas. They are characterized as an upwardly divergent pair of normal faults with opposite movement, with the central block anticlinally folded. Often there is added internal complexity, though the upward divergence is still apparent. These normal faults converge as they are traced downward usually originating at a common point at the Base Surat unconformity. In many cases, the unconformity surface is tightly folded as the bounding faults merge. This is illustrated in a profile (Figure 4.36) from the eastern margin (Jen10 area). Also observed on this profile is the lateral change in seismic character within the WCM. This is observed in other data and provides support for a syn-depositional effect from small scale deformation. These relationships will be further investigated in the CCSG stratigraphic correlation project.

The keystones developed along the eastern margin are often associated with tightly folded structures at the base Surat, with little net offset across the zone. Analogous to “wrinkles in a rug” when the underlying section undergoes small shear movement along previous lines of weakness. The resulting structures are discontinuous but can have zones of deformation that extend for 5-10km or more, following a trend of weakness in the underlying section.

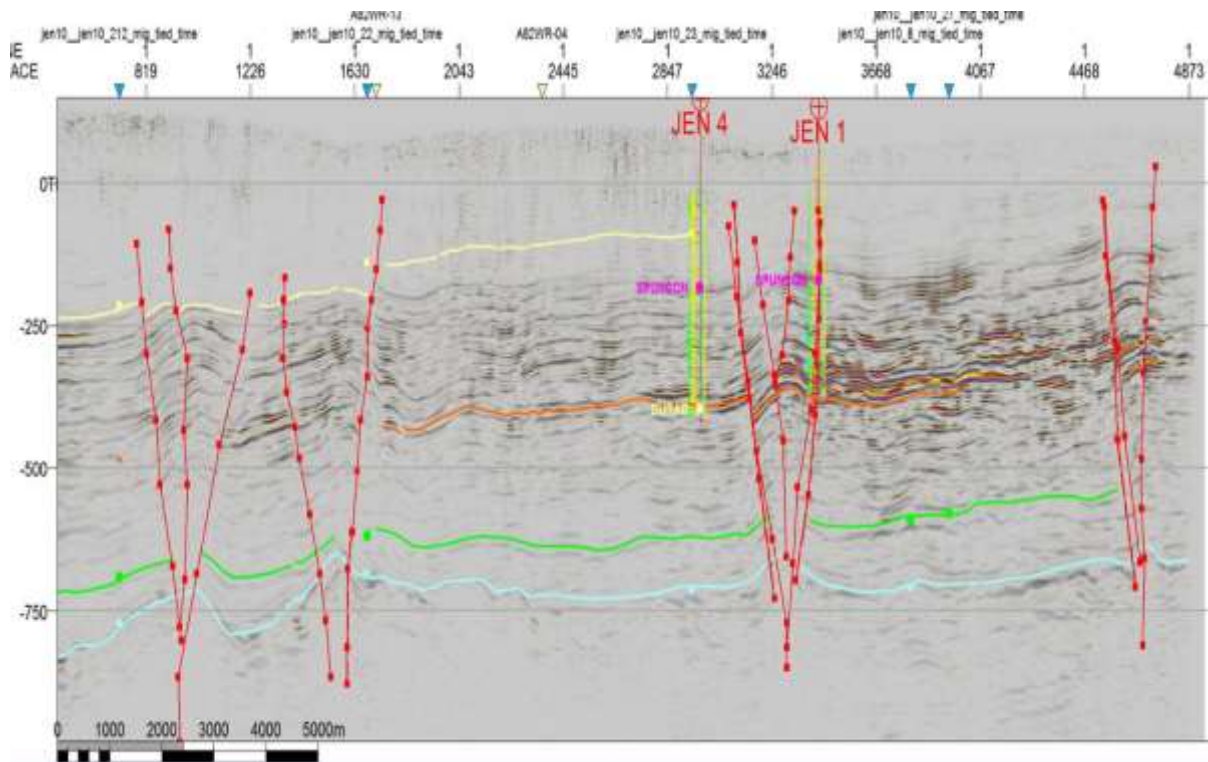


Figure 4.36 Keystone structure examples, faults shown in red. Common characteristics are multiple faults diverging upwards with generally net negative displacement between bounding faults, often with internal anticlinal folding.

Most of observed keystones have net negative displacement, with the central block down relative to the areas outside the bounding faults, indicating an extensional zone of deformation created by shear displacement. Figure 4.37 is an idealized schematic showing the generalized kinematics of deformation for flower or “keystone” structures. The fault morphology observed in the Surat has analogous features, though is rarely well enough developed and the data lacks the resolution to provide the clarity required. The following discussion will present observations from relevant 3D volumes (Undulla, Lauren and Dalwogan-Condabri), each of which has a somewhat different deformation style, but they all share key features.

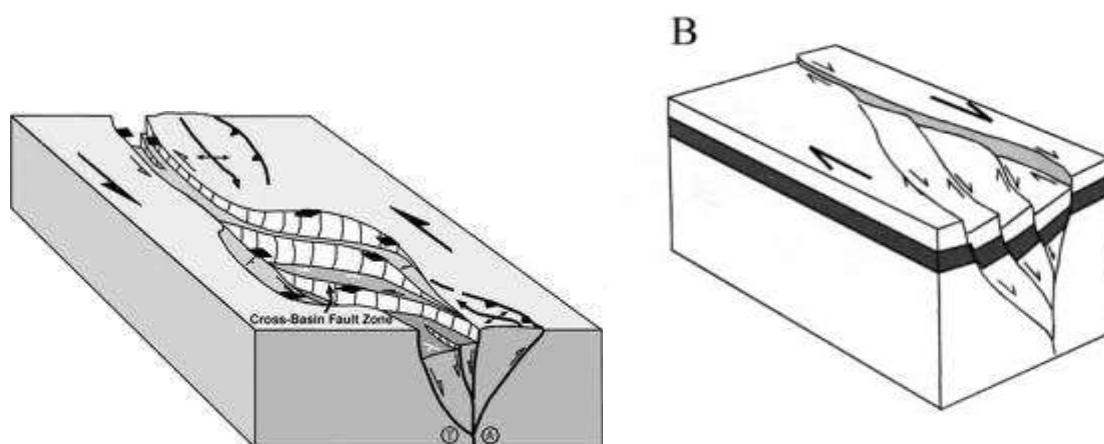


Figure 4.37 Illustration of the development of a keystone fault structure (Ben-Avraham & Zoback, 1992) The schematic diagrams provide a conceptual basis for keystone formation. Shear can develop either positive or negative flower structures depending on the geometry of the transfer zone which may be controlled by underlying zones of weakness.

While the basement roots of such transtensive deformation may be laterally continuous over many kilometres, the lateral continuity of individual 'keystone' faults in the shallow section (e.g. Walloons) is expected to be much more limited. Where these features are observed in 3D seismic volumes, the individual bounding faults may have a strike extent of 500-1500m. If the "zone" of keystone failure is more extended, the primary bounding faults are found to shift across transfer zones, with the displacement moving from one side of the feature to the other along a general zone of deformation which can extend for 5-15km. The majority of faulting affecting the WCM is interpreted to be related to these features. On 2D profiles the keystone is not always fully developed at the location of the observation. The following examples illustrate the range of morphology for this deformation.

An example of this (Figure 4.38) is taken from the Dalwogan-Condabri summary where there is a NNW-SSE trending normal fault zone overlying Permian subcrop which has a parallel strike. In the coherency slice through the WCM shown in the figure, the trend of normal faulting is highlighted in yellow and the dark red discontinuities (low coherency) are observed to be at a conjugate angle. These would be examples of Riedel shear related to keystone development.

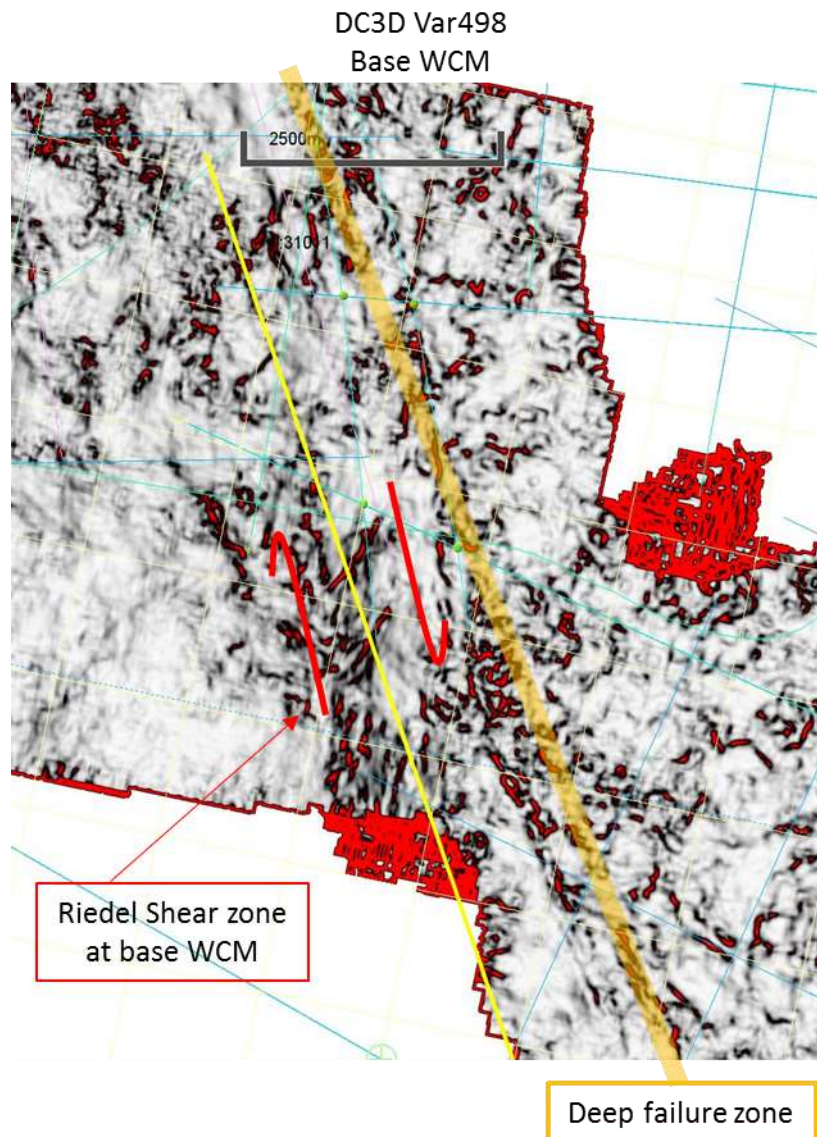


Figure 4.38 Development of Riedel shear and conjugate faulting. The figure shows a time slice (498ms, approximating the local base Walloon) through the coherency volume created with a 15 sample correlation window. Discontinuities show as red in the display colour bar.

The keystone structures have been annotated on Figure 4.39 where observed and interpreted on 2D seismic data. They are prevalent on the east side of the Surat. They also appear to have a common association with the subcrop of the Permian section along the edge of the major eastern uplift. This study's hypothesis is that they are a result of shear stress transferred from zones of weakness in the basement upward into the Surat succession (Figure 4.37). In some cases, these structures create local distortion of the regional stress field. This concept is further elaborated on in [Section 5](#) by Mukherjee (that investigates regional variability in stress and fracture relative to different structural domains).

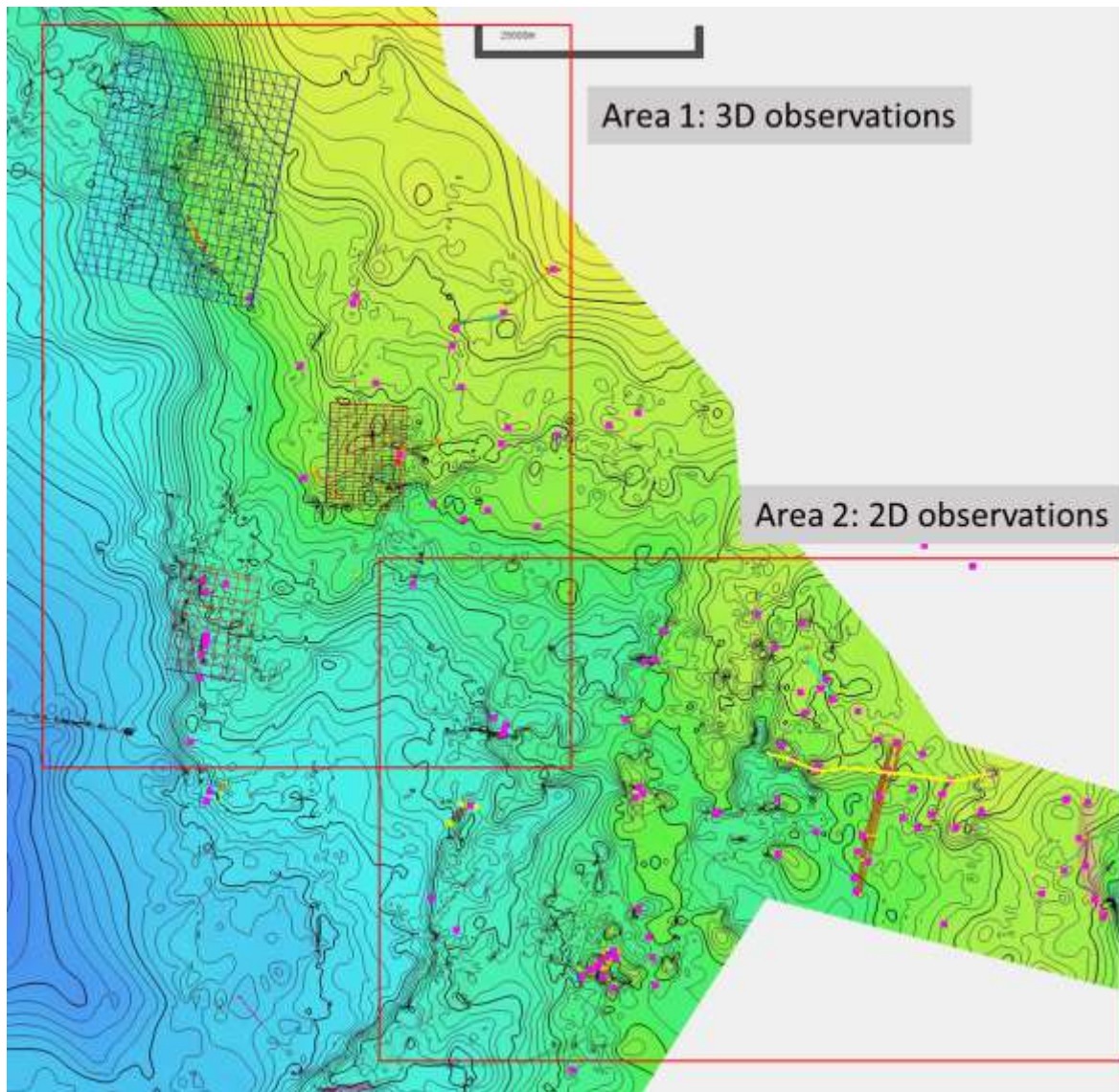


Figure 4.39 Base Surat on the eastern margin (c.i. 20 ms). Identified keystone features in pink. (C.I.-20ms).

Keystones from 3D seismic volumes

The 3D volumes on the eastern margin of the Surat Basin (Figure 4.40) show the morphology of the fault systems which contribute to the deformation. Three areas are available for this: Undulla, Lauren and Dalwogan-Condabri. Coherency attributes were created in Petrel (“Variance”) for each volume with correlation window length selected to provide the best (visual) fidelity for fault imaging. The colour bar is presented such that darker areas are discontinuities (low coherency) along reflection events. This is an important tool for both structural and stratigraphic interpretation as it provides the opportunity for an unbiased spatial observation of the discontinuity trend. More subtle variations in coherency can be related to stratigraphic features (e.g. channel edge), but these features are not discussed in this report.

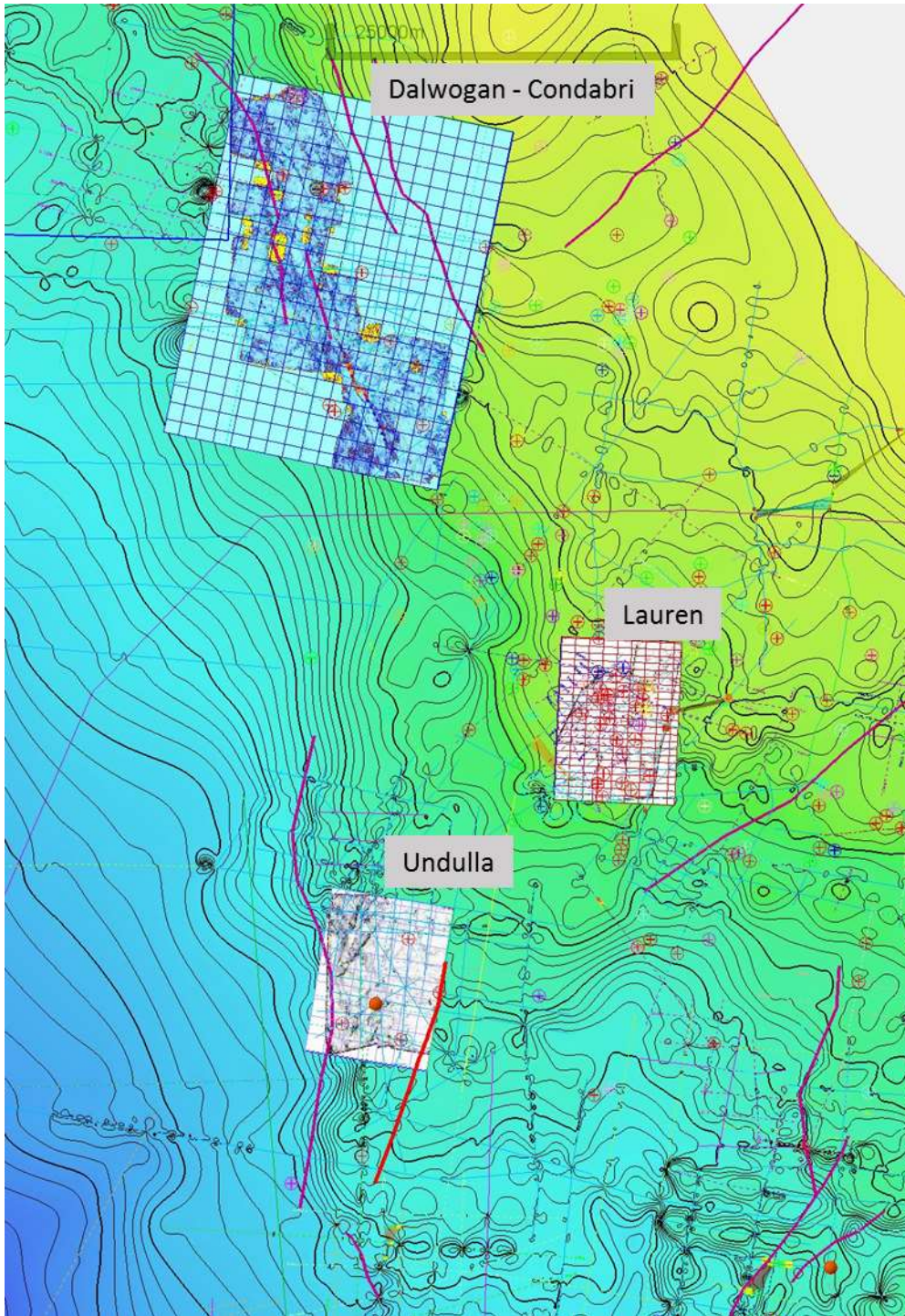


Figure 4.40 3D surveys with coherency slices through the Walloons in each survey (C.I.-20ms).

Undulla 3D

The Undulla survey covers a portion of the Undulla Nose, which is a broad fold in the Surat succession (Figure 4.41). The local structure is oriented NE-SW and extends for about 40km, dipping SW. Subcropping below the unconformity is relatively flat lower Permian uplifted during Triassic deformation (Figure 4.42).

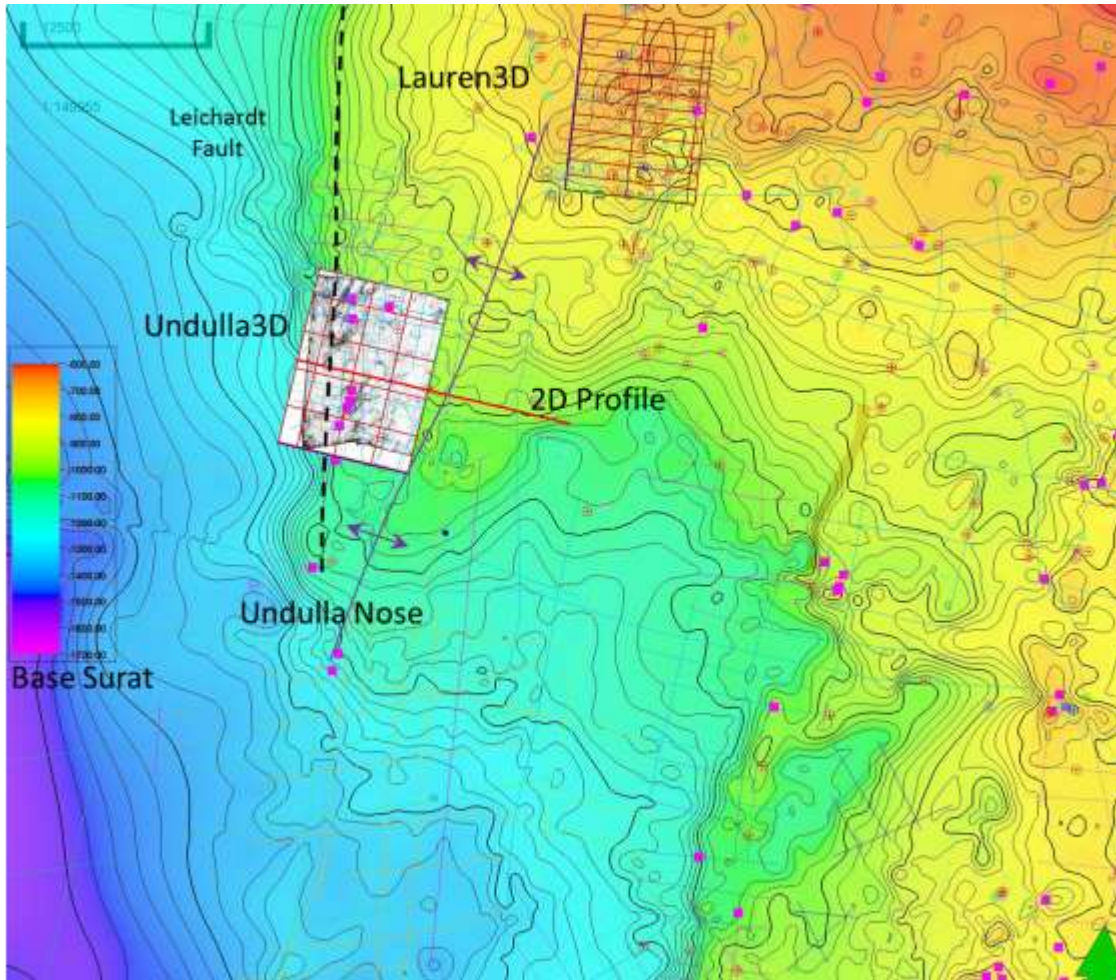


Figure 4.41 Undulla Nose Area - base Surat unconformity (C.I.-20ms).

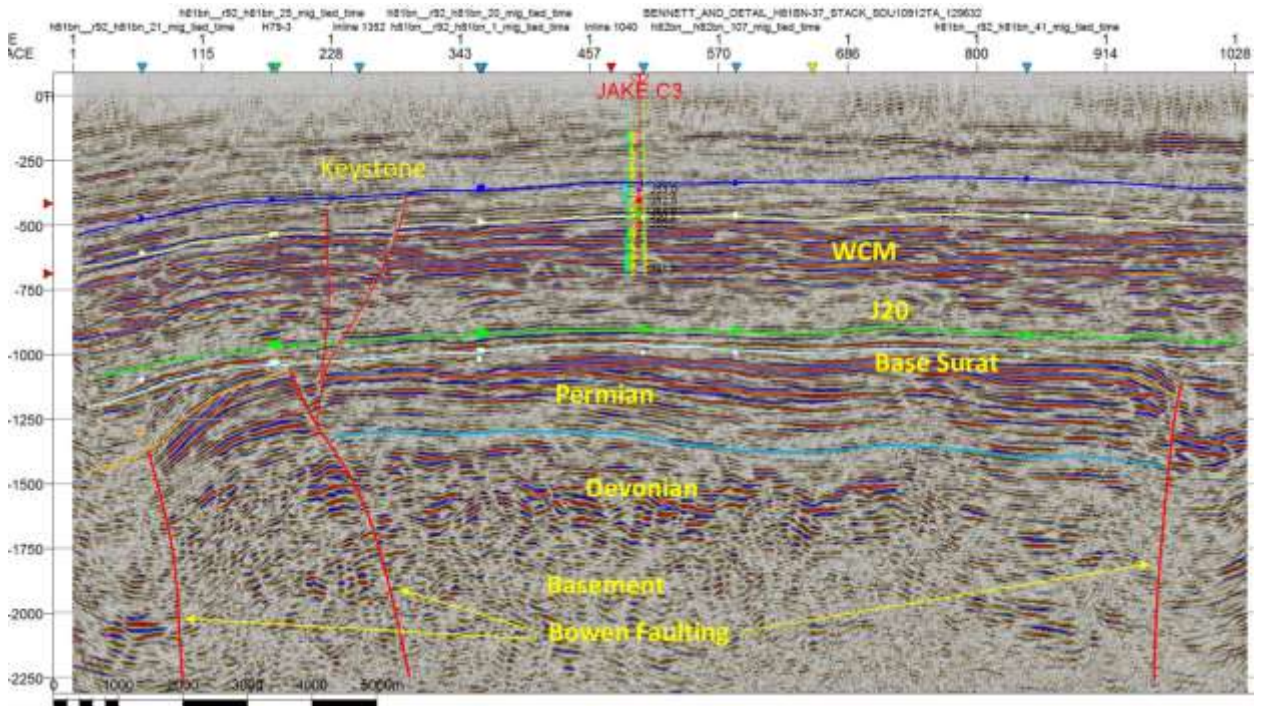


Figure 4.42 Undulla Nose 2D profile showing uplift at margin of Surat Basin. Near flat lying Permian subcrop below the base Surat unconformity. The WCM is nearly undeformed with the exception of keystone faulting on the west side of the uplift.

The following 3 examples illustrate the spatial complexity of the keystone deformation. There are two distinct keystone features within the survey area highlighted in yellow. In the first example (Figure 4.43), the coherency slice (left) is taken just below the unconformity within the upper Permian. In the profile (right), a small fault can be observed where the bounding faults of the keystone converge. The trend of this fault is highlighted on the coherency slice. A similar fault is highlighted to the NW.

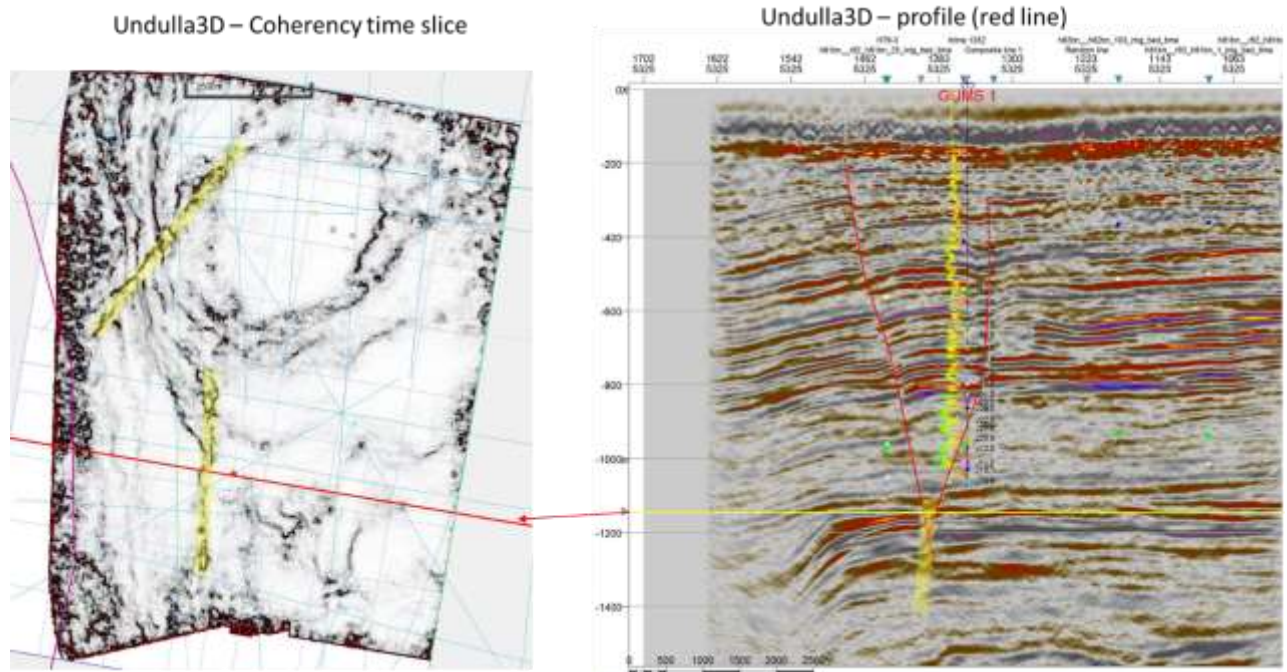


Figure 4.43 Undulla 3D coherency slice (left) at Base Surat showing the root of the keystone highlighted in yellow and (right) the profile marked red on the map.

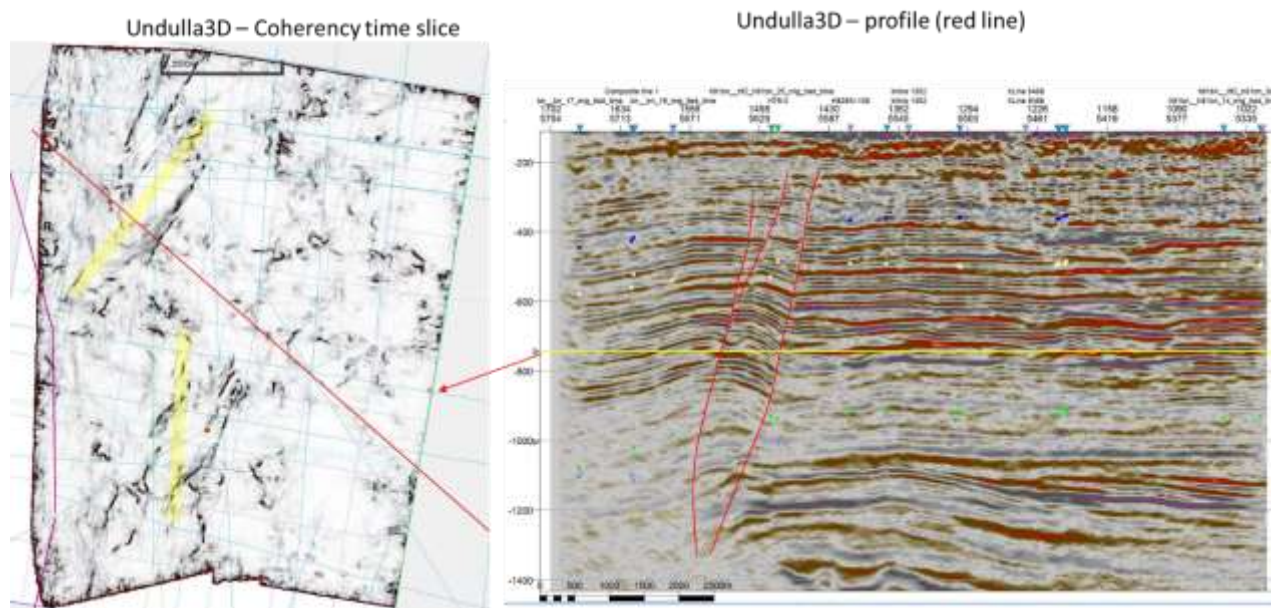


Figure 4.44 Undulla 3D coherency slice (left) at base of Walloon (yellow on profile). The faults are dark lines in the coherency display.

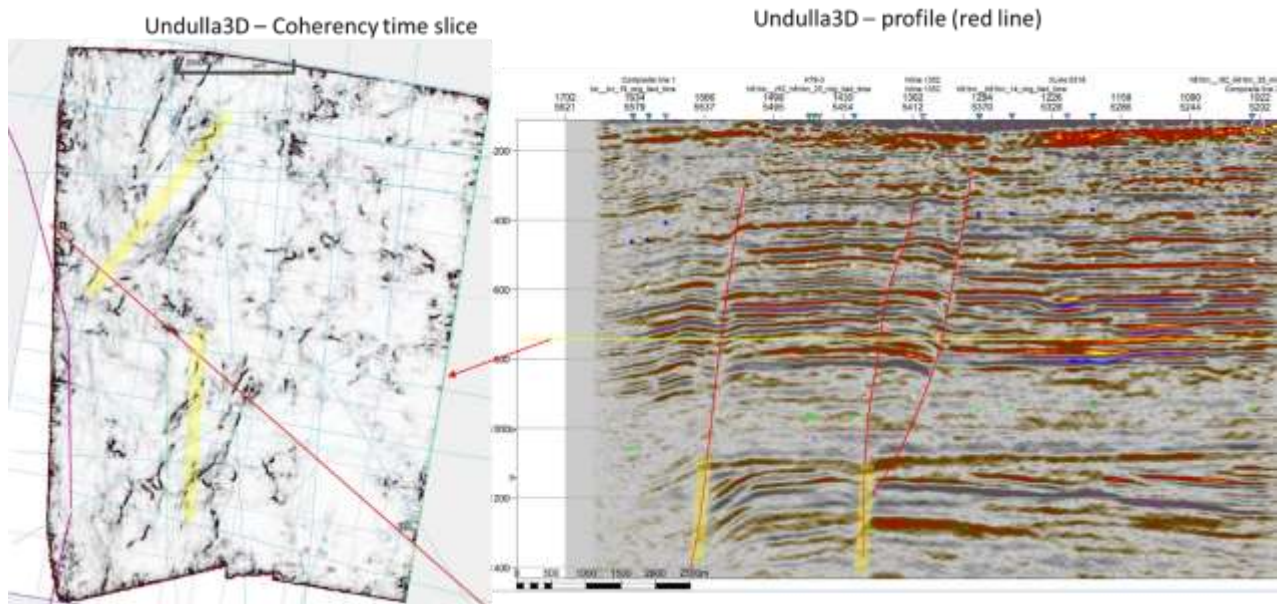


Figure 4.45: Undulla 3D coherence slice (left) at base of Walloon (yellow on profile) and shows transition in deformation from the northern keystone to the southern keystone.

Lauren 3D

The Lauren (GSQ- Werona) 3D provides another example of keystone deformation (Figure 4.46). In this case, the trend of deformation is NE-SW across the survey area for over 5km (scale bar – 1250m). The faults bounding the keystone structures are discontinuous. The coherence slice is shown in the centre of the figure and insets for profile segment shown with the slice indicated by yellow line. Profiles 2 and 3 have complete keystone morphology, while in 1 and 4 the bounding fault is dominant.

The lateral extent of individual faults can also be seen in the 3D projection (Figure 4.47). The horizon shown in the figure is an intra-WCM correlation based on nearly 100 wells in the area of 3D coverage. The structure contours (CI – 2ms) also show a N-S folding created by a small fault displacing the unconformity. Both the keystone and basement deformations are synchronous and may further illustrate the oblique shear hypothesized as the causative mechanism for this structural style.

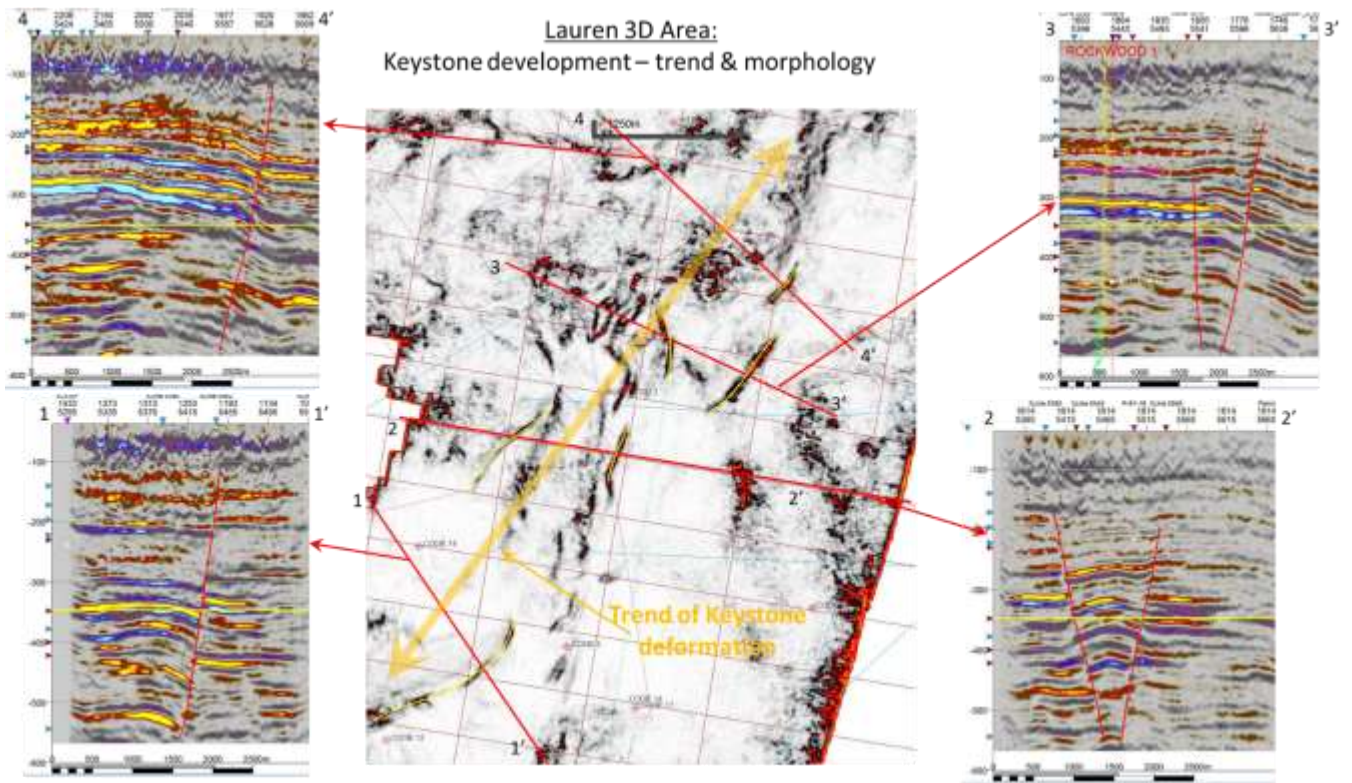


Figure 4.46 Keystone structure development in the Lauren 3D survey.

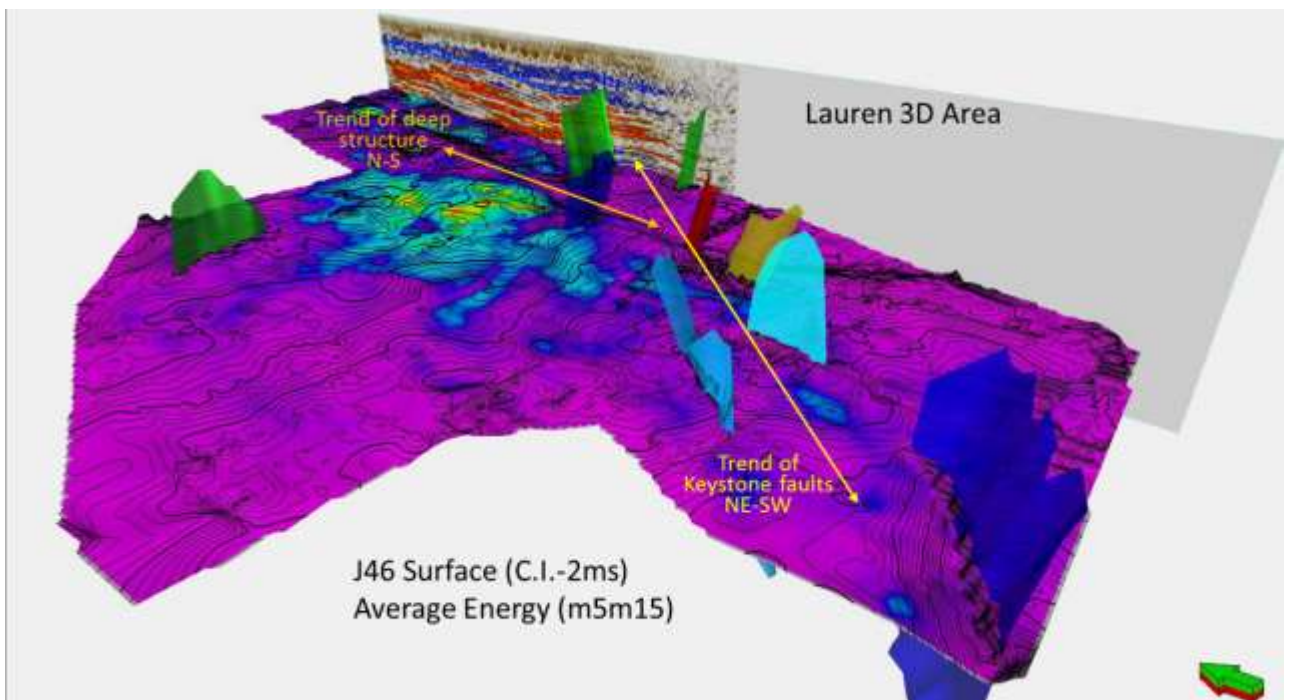


Figure 4.47 3D view of J45 horizon (upper WCM) with keystone fault trend.

Dalwogan Condabri

The Dalwogan-Condabri 3D (DC3D) is located to the north along the margin of the extensive Bowen uplift along the eastern margin of the basin (Figure 4.48). The Permian subcrops within the survey area. This is angular on the west and near parallel on the east. Bowen

faulting and the angular nature of the eastern subcrop appears to influence the mode and orientation of keystone development. It is this underlying zone of weakness, oriented at an angle to regional tectonic during Cenozoic deformation which would seem to allow the shear component required for the fault patterns.

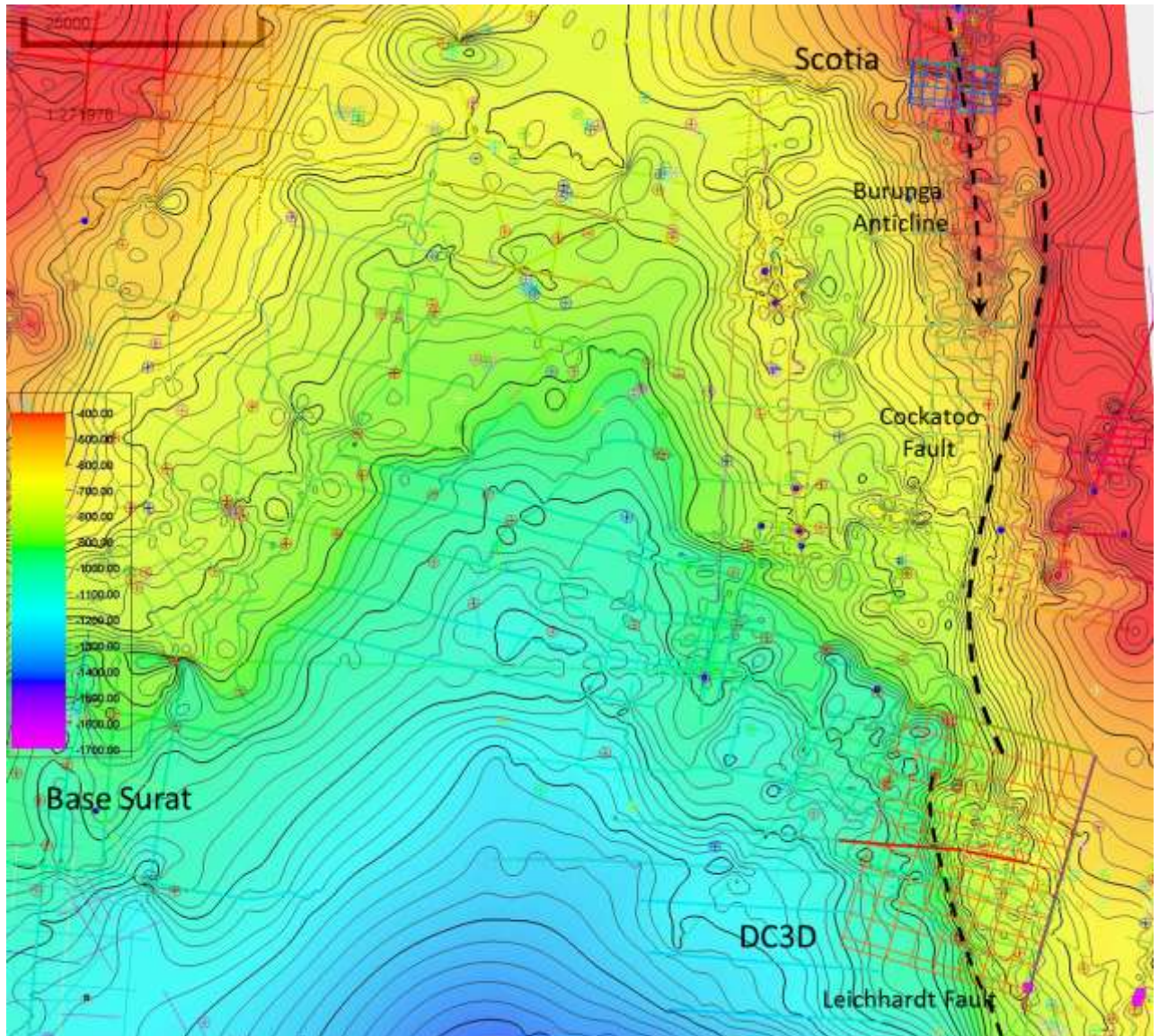


Figure 4.48 DC3D to Scotia area base Surat structure (c.i.-20ms).

In Figure 4.49, a coherency slice just below the base Surat unconformity (Figure 4.50) is presented. Arrows indicate to ~E-W zones with a conjugate pattern with individual faults generally oriented NE-SW. The NW-SE pattern is due to discontinuities from the subcropping Permian section. Note the left lateral offset of the subcrop pattern which conforms to the intersecting E-W conjugate pattern.

In Figure 4.50, the profile shown is located along the line shown on the preceding coherency display. The conjugate zones are highlighted by corresponding arrows. Subtle faulting in the underlying Permian (horizontal reflections) is observed. The hypothesis developed is that this is Cenozoic deformation overprinted on the Permian that in turn sets up the shallower

keystone features discussed next. This may also be influenced by underlying (Devonian?) zones of weakness.

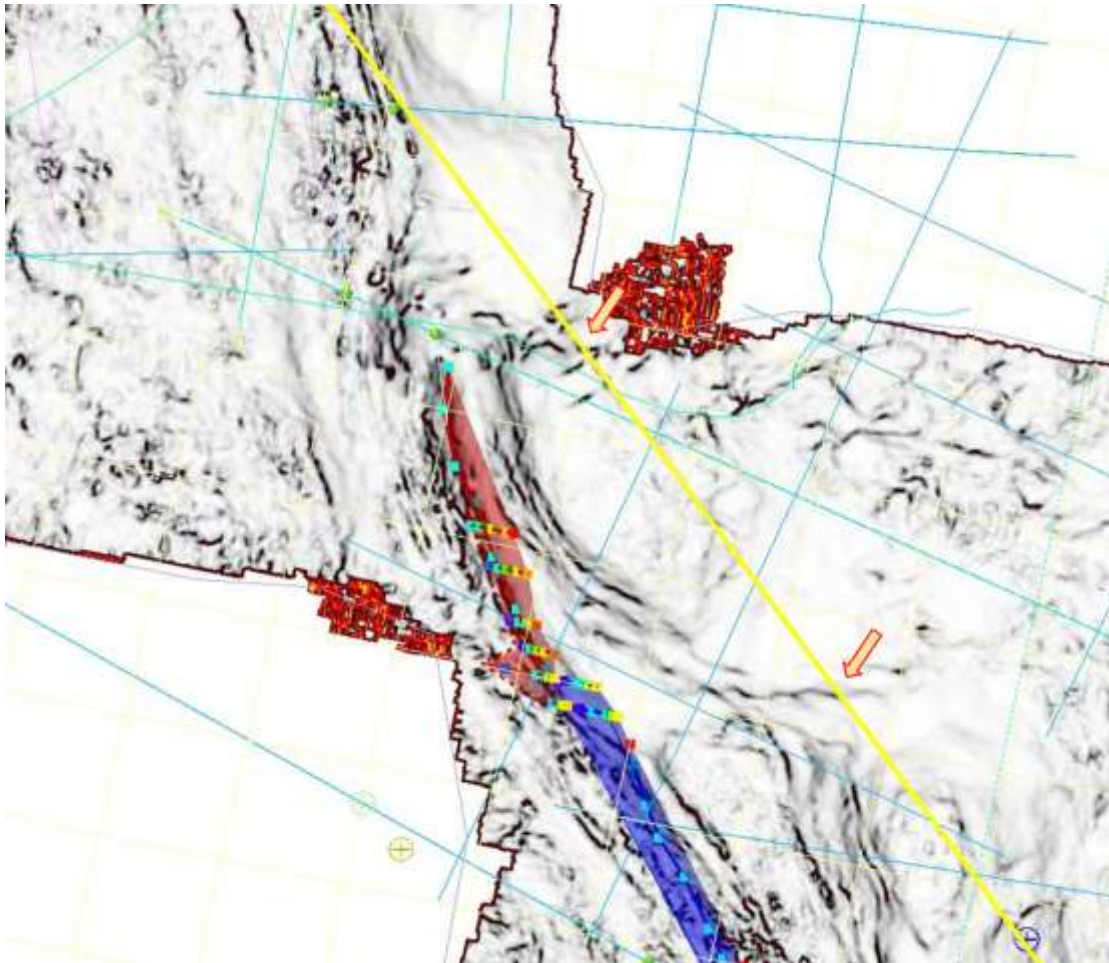


Figure 4.49 Dalwogan-Condabri (DC-3D) coherency slice below Base Surat. Shear offset within the Permian section. Conjugate faults observed as part of the shear zone.

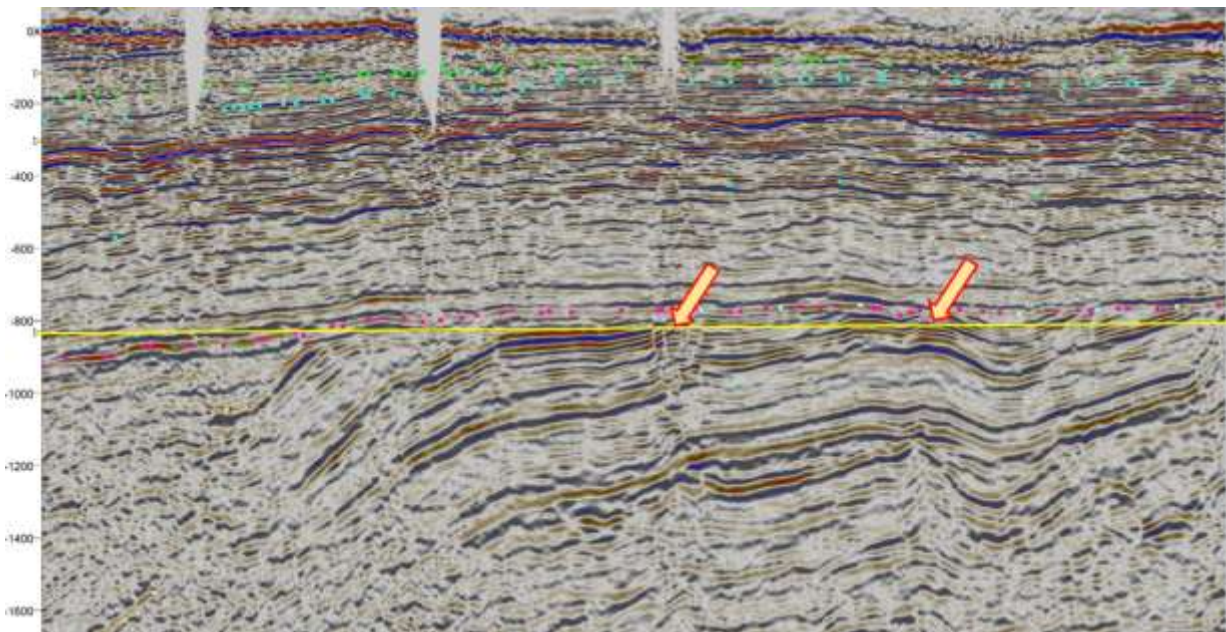


Figure 4.50 Profile DC-3D profile along the yellow line in Figure 34 and slice location indicated in yellow. The faults on both the slice and the profile are shown by the fat arrows.

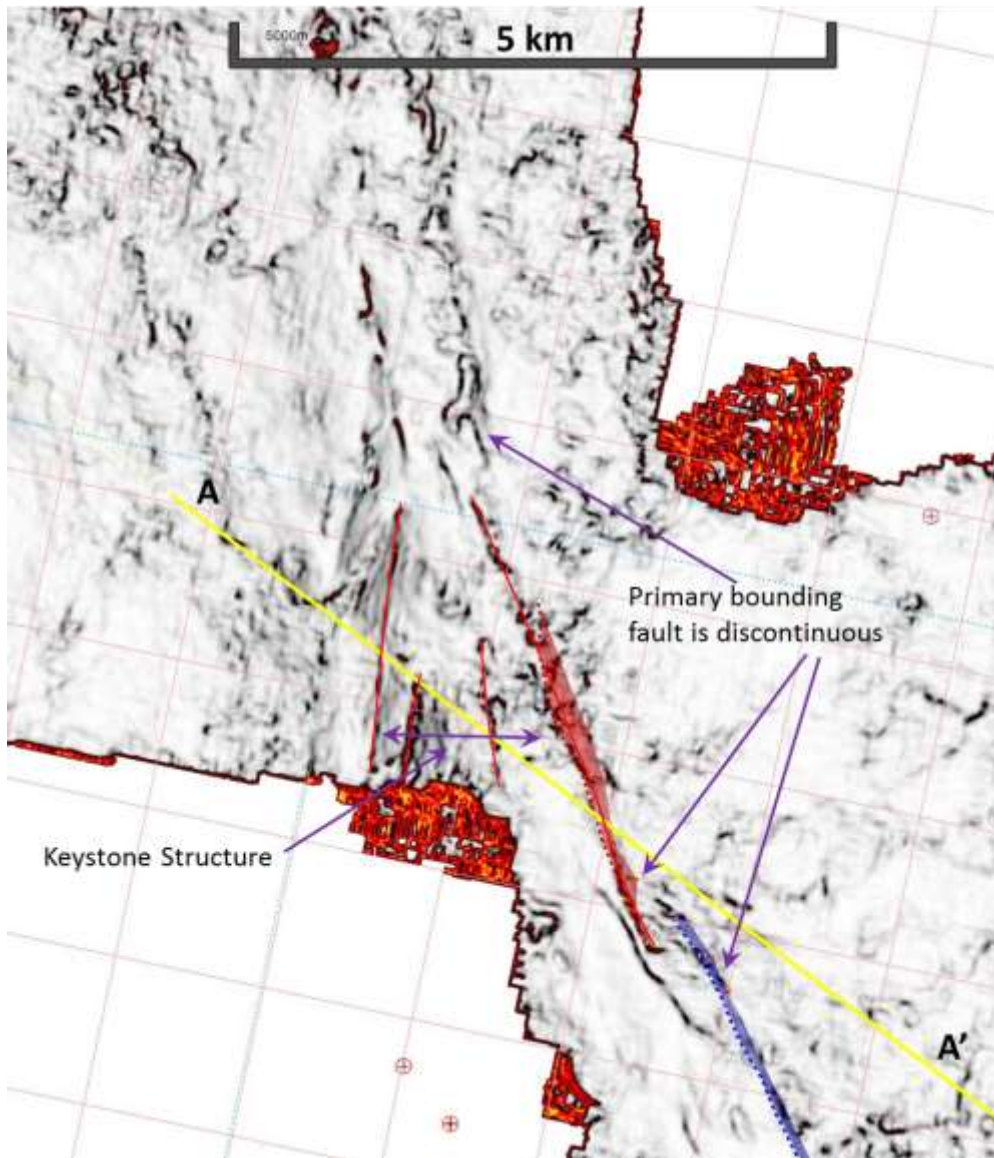


Figure 4.51 A coherency time slice in WCM showing complex keystone fault deformation.

In Figure 4.51, a time slice through the coherency volume shows the fault geometry of a keystone structure developed along the eastern margin of the Surat Basin, which overlies the uplift along the Leichardt-Burunga uplift. The primary bounding fault is oriented SSE-NNW with normal displacement down to the basin (west). This bounding fault is actually a series of fault segments which have individual lengths of 1-2km along a zone that continues for 10-15 km. On the west side of this fault, a series of subsidiary normal faults are developed with a conjugate orientation relative to the “main bounding fault”. Keystone structures are developed with complex internal fault morphology and a net negative displacement for the block.

A representative profile (yellow) is shown on the coherency map and below in Figure 4.52. On the profile, the location of the time slice is shown in red. The structure of the keystone is seen to have bounding faults which converge with depth and internal complexity.

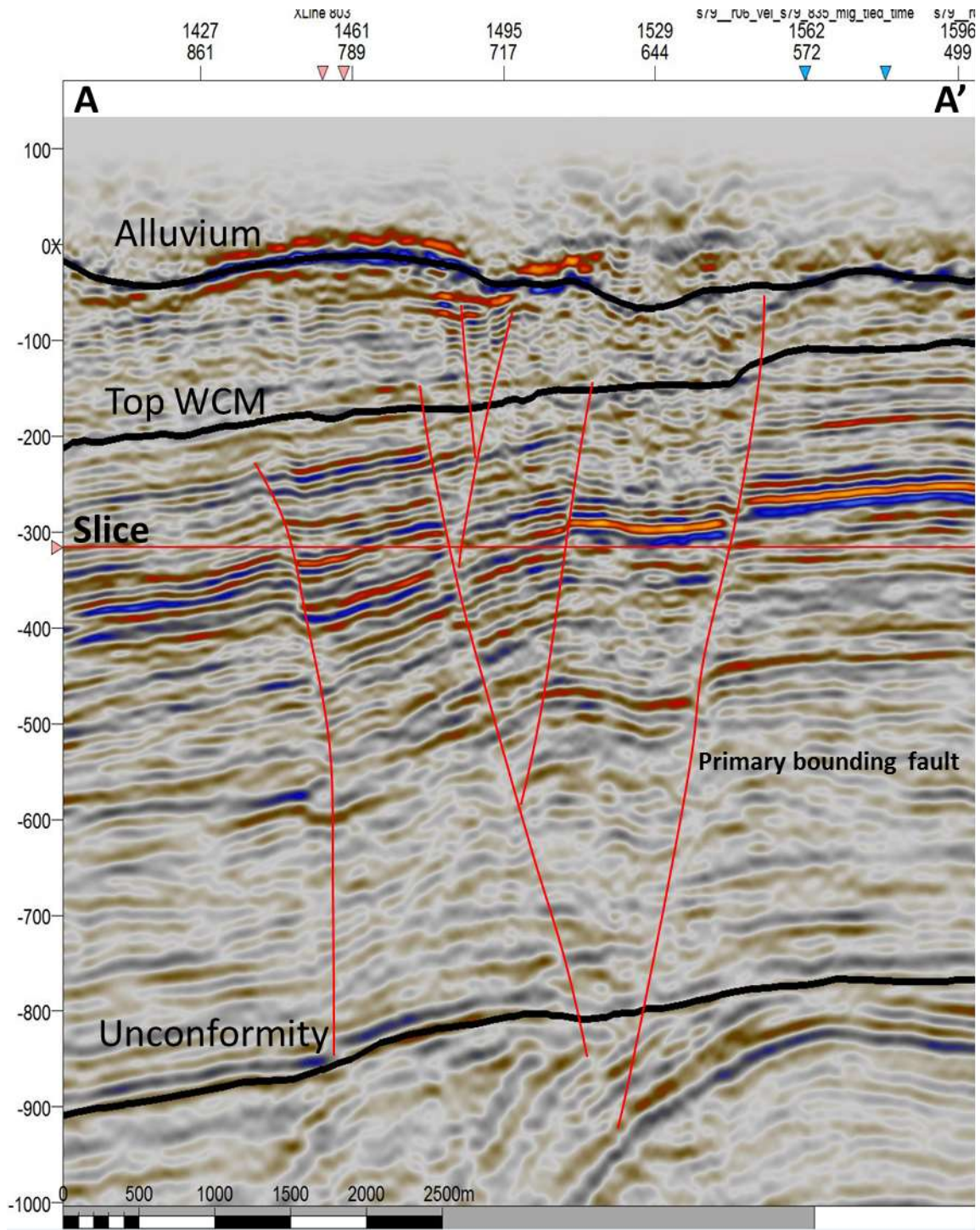


Figure 4.52 Profile from the Dalwogan-Condabri 3D volume. Dipping reflectors below the base Surat unconformity are the subcropping Permian coals. Note the offset continues to the very shallow section, with displacement above the WCM. The base Alluvium reflector appears to preferentially erode deeper above the keystone.

Eastern Surat Margin 2D Examples

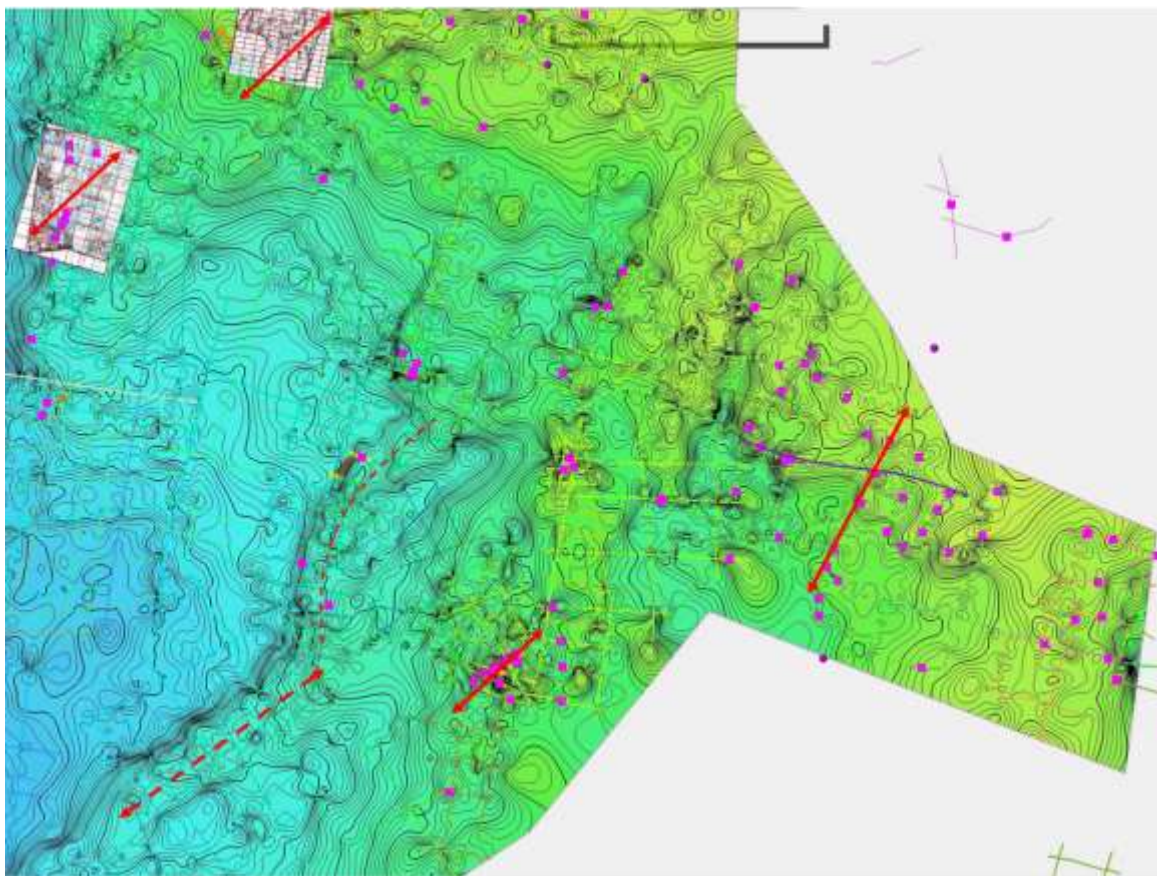


Figure 4.53 Keystone faulting on the eastern Surat margin observed to be controlled by underlying NE-SW structural weakness.

Figure 4.53 shows structure on base Surat on which is superimposed locations where keystone faulting was identified on 2D profiles (magenta). In some cases, these observations were fully developed zones of deformation with both bounding faults and a net negative compressional anticline between. Though as presented above using 3D data, in many cases only components of the keystone are observed. For example, often one of the bounding faults is present in the WCM, but the compressional anticline is observed. While the observations are somewhat sparse, there do appear to be trends that conform to the roughly NE-SW orientation of structural boundaries, presumably resulting from deformation influenced by underlying zones of weakness that are preferentially activated under the Cenozoic tectonic forces imposed.

Keystone Faulting in the Permian

Surat deformation is also overprinted on the Permian deformation in the northern portion of the Roma Shelf. This has not been generally recognized at present. In this area where the Surat section is largely eroded, the Surat deformation has overprinted on the Permian, but is not recognized due to the missing younger section. This is an explanation for open fractures supporting production where other (possibly older) fractures are found to be cemented.

Presumably it is the younger Cenozoic fractures which are open while the older are cemented. In Figure 4.54, below the location of the Fairview 3D is shown on the top Permian structure map. Several major Bowen age uplifts are shown (Merrivale, Injune, Simmie, Hutton-Wallumbilla, etc.). These are partially reactivated during period of Cenozoic deformation. The eastern side of the HWFS is further rotated upward in the more recent movement, but displacement terminates at the north. Further displacement is offset to the east along another north trending system. The hypothesis is presented that the interaction of these two systems results in the large scale keystone deformation observed in the Fairview 3D and with less clarity on the surrounding 2D profiles.

Also noted on this structure is an apparent net positive movement for the internal keystone blocks. This is in contrast to the keystone structures observed within the Surat succession. The difference in style may be due to burial depth or proximity to the underlying motive deformation. As there are few good examples of this style of deformation in the underlying Bowen section outside of this particular area (Fairview), it is difficult to speculate on possible hypotheses.

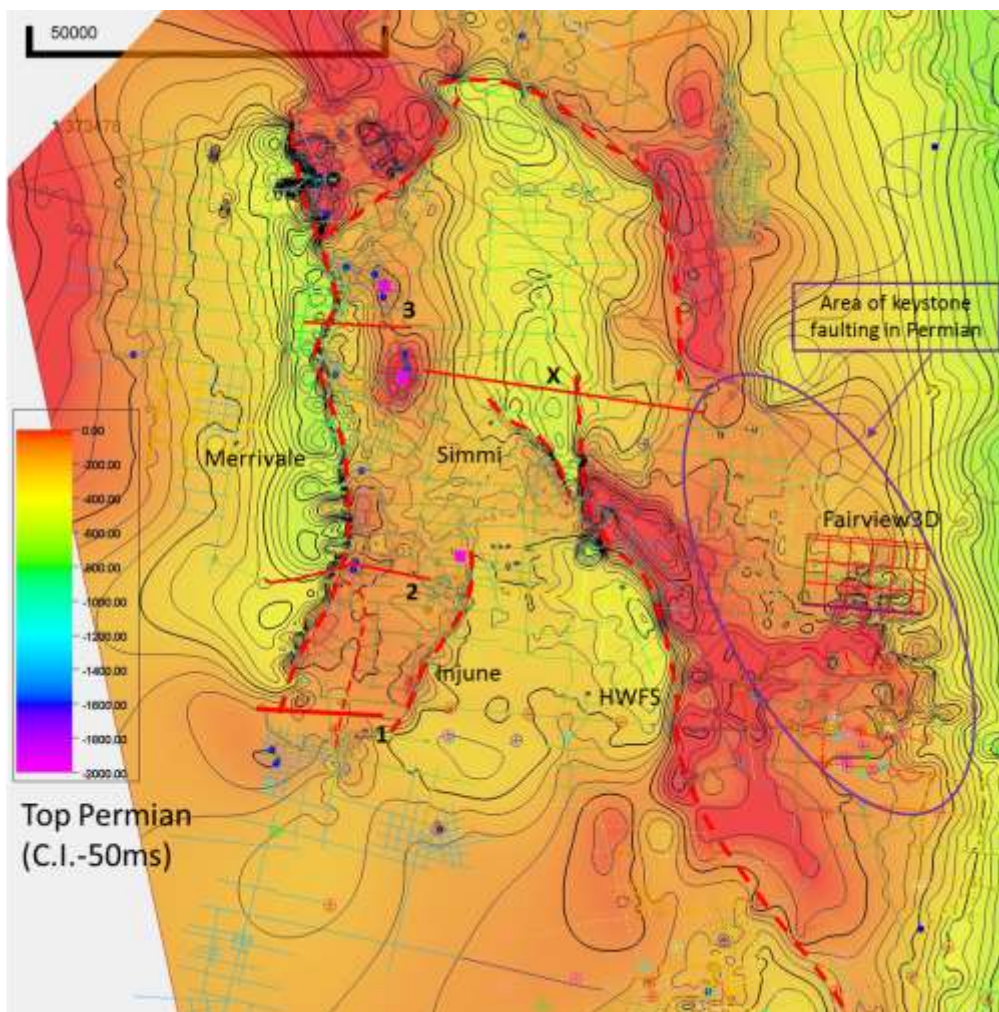


Figure 4.54 Top Permian structure and location of Fairview 3D.

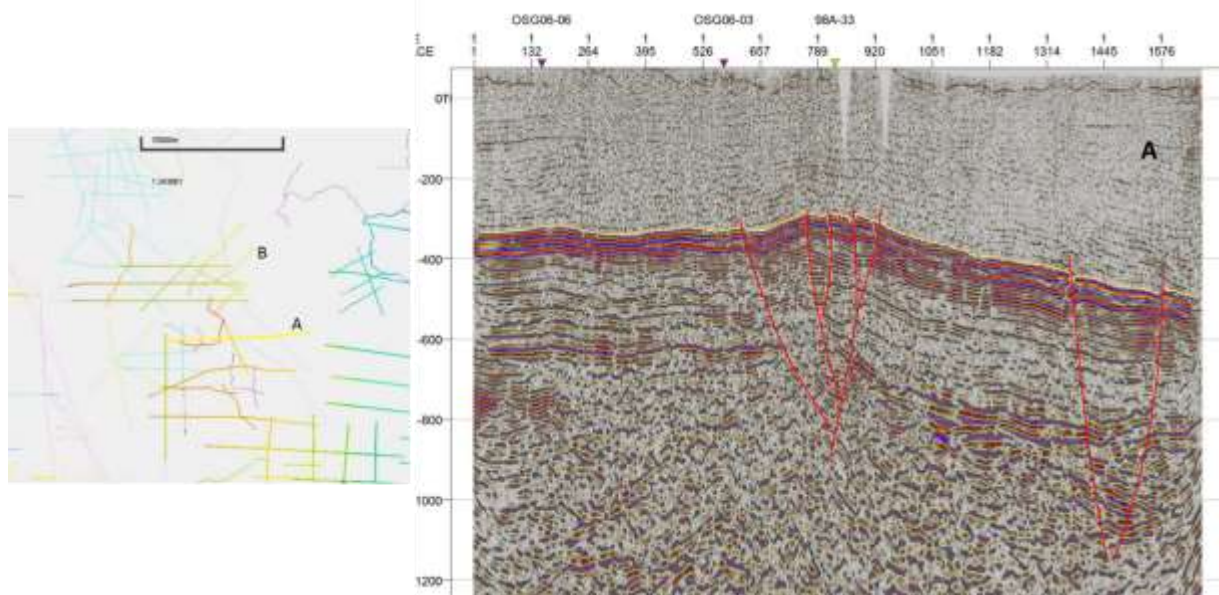


Figure 4.55 Keystone example A on 2D Permian SW Surat.

A 2D profile (Figure 4.55) located south of the 3D area is presented to demonstrate the morphology of faulting observed across the local area. A clear keystone system can be observed in the center and on the eastern side. The Permian section is the portion with the layered reflection character. A similar fault pattern can be seen in the next example (Figure 4.56). As these lines and others are 2-5km apart, it is difficult to correlate the fault planes in any detail. Though it is possible to characterize the area where this style is commonly observed as indicated in the location map.

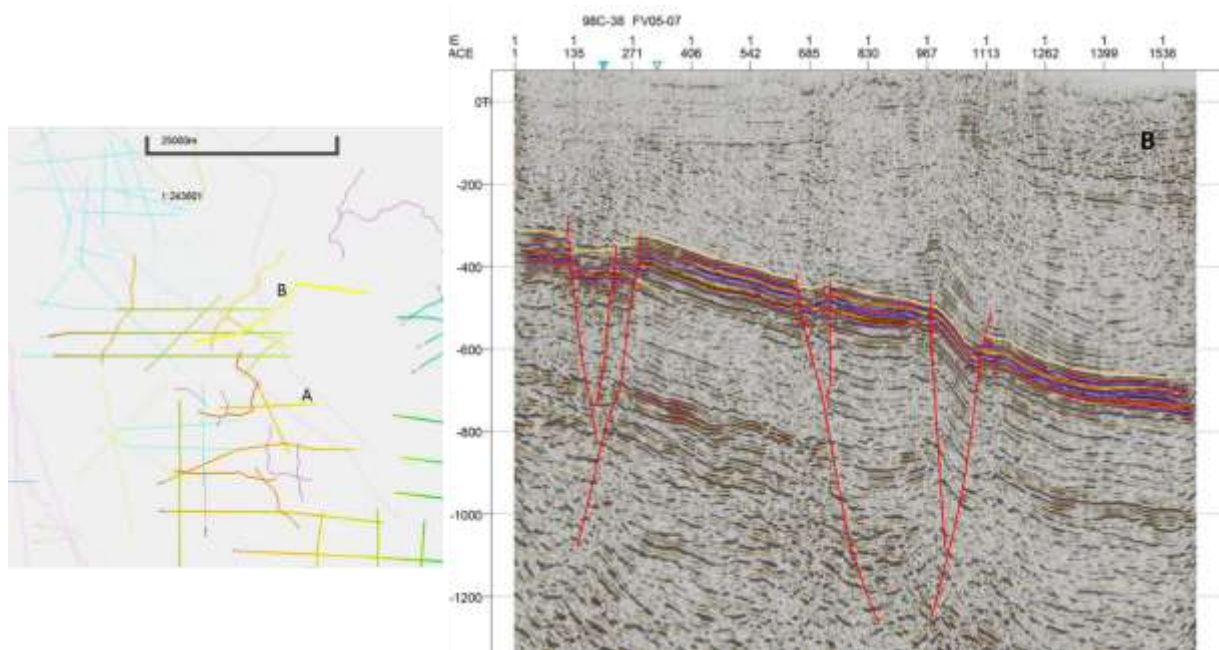


Figure 4.56 Keystone example B on 2D Permian SW Surat.

The 3D volume provides excellent detail of this deformation. As the data was not incorporated into the project until the end, only a very limited interpretation was possible.

Coherency slices are presented beginning with Figure 4.57 where an E-W profile is shown to illustrate the general structure. The Permian dips to the east with a steeper flexure that appears to overlie and older Devonian graben fault. This older fault and others may control the Bowen structural orientation. This older structure does appear to serve as a focus for Cenozoic deformation as the base Surat structure also shows flexure over this zone. The coherency slice in the figure (left) shows well developed faults oriented NE-SW with limited strike extent. As the Permian dips substantially across the profile, this particular slice only images the area on either side of the flexure with clarity. A change in morphology can be observed with the eastern side faults parallel to the flexure where close then reverting to the NE-SW orientation moving farther east.

In Figure 4.58, the profile is oriented parallel to the flexure and perpendicular to the trend of the keystone deformation. In this coherency slice, the faults are well imaged, displacement is obvious within the reflectors of the coal dominated section but more subtle at the base Permian. In part, this is due to frequency attenuation and more limited imaging, but there are small flexures at the point of convergence.

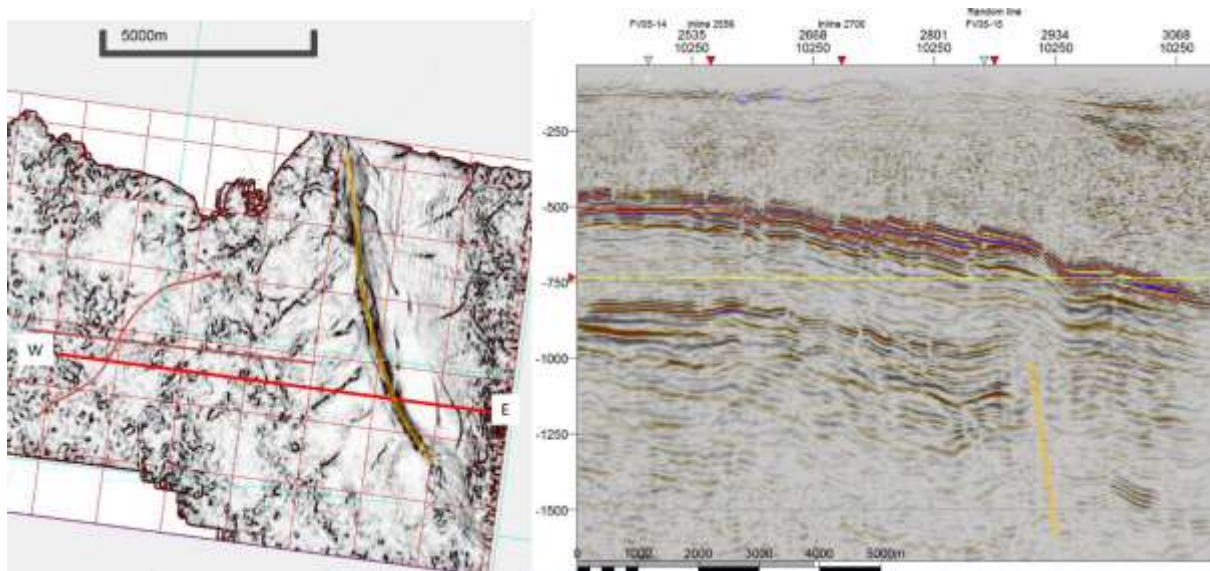


Figure 4.57 Fairview 3D coherency slice.

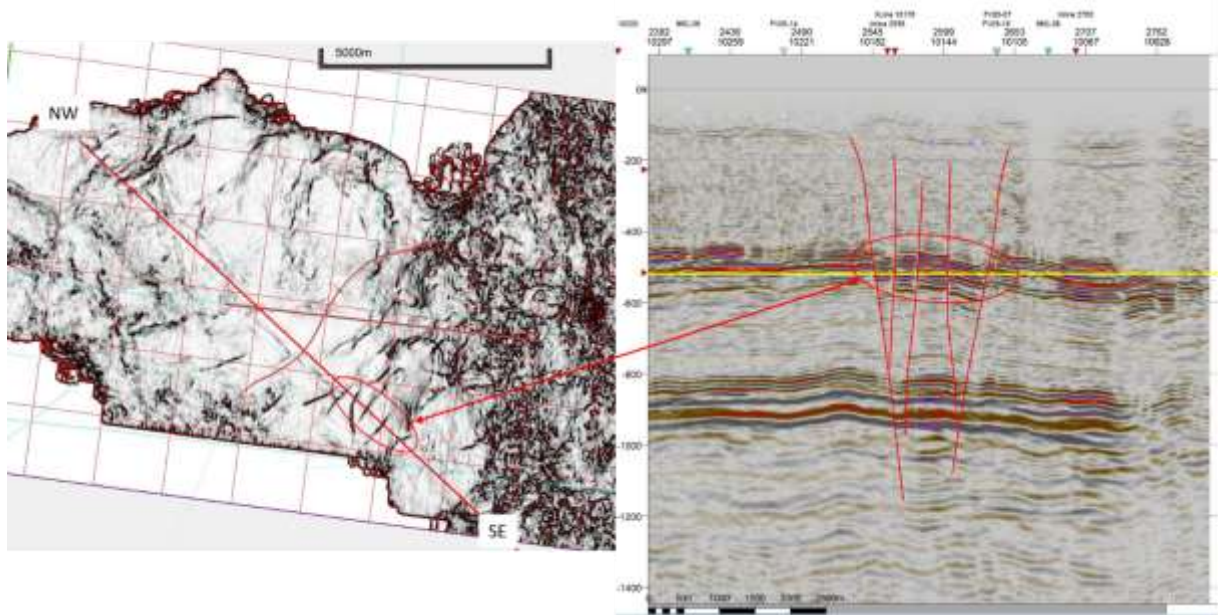


Figure 4.58 Profile through SE of larger scale structure.

In Figure 4.59, the profile is located in proximity to the flexure to the west. The keystone deformation has expanded to a zone $\sim 5.5\text{km}$ across. Faults are numbered for ease of comparison.

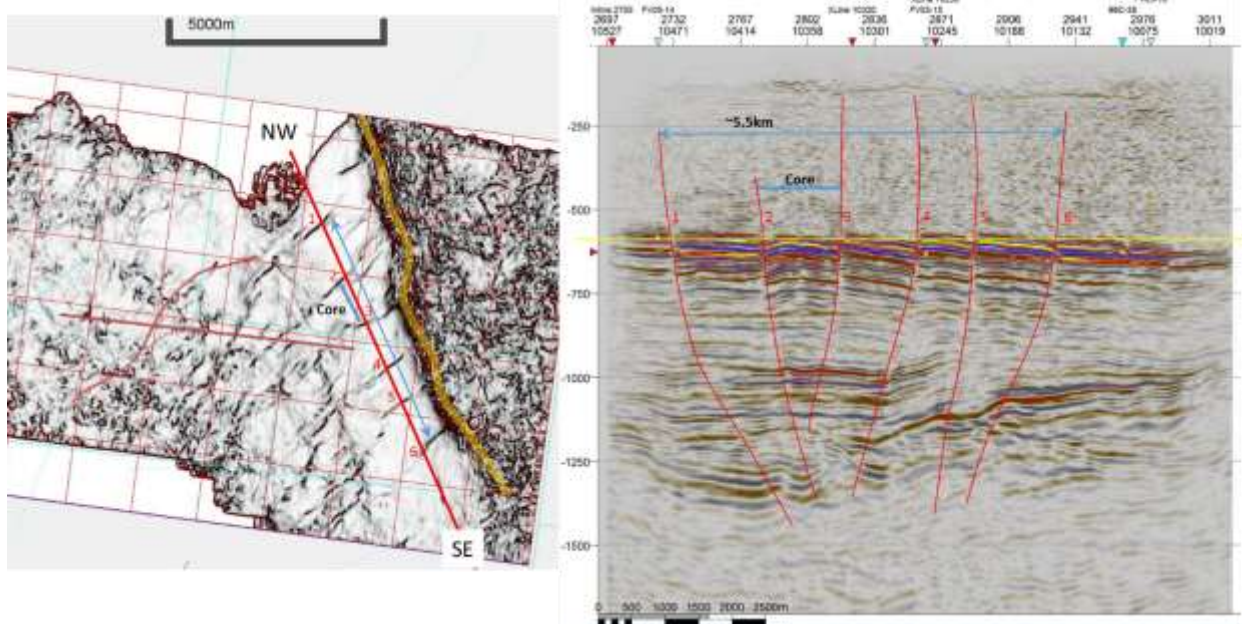


Figure 4.59 Profile through SE of larger scale structure.

4.3.8 Potential Impact of Faults on Fluid Flow

Faults and fractures will influence fluid flow in the subsurface as conduits or barriers to flow. They may compartmentalize regions limiting flow, injection or extraction of fluids. Depending on the relationship of fracture and fault orientation to the present day stress field, permeability will be enhanced or impaired.

Areas of (even slight) anticlinal deformation may enhance permeability over crestal areas towards the surface while impairing it at depth. In synclinal zones, the opposite occurs: permeability is enhanced towards depth and impaired towards shallower depths.

This project was able to examine data at a higher resolution than has been possible previously. The smaller scale structures (keystone faulting) identified are revealed to be ubiquitous in the areas of investigation. These features are expected to affect pressure distribution and therefore fluid flow related to coal seam gas developments and aquifer use significantly. Furthermore, as fluids are extracted and the stress field affected, a dynamic effect of these features on fluid flow through time is also expected.

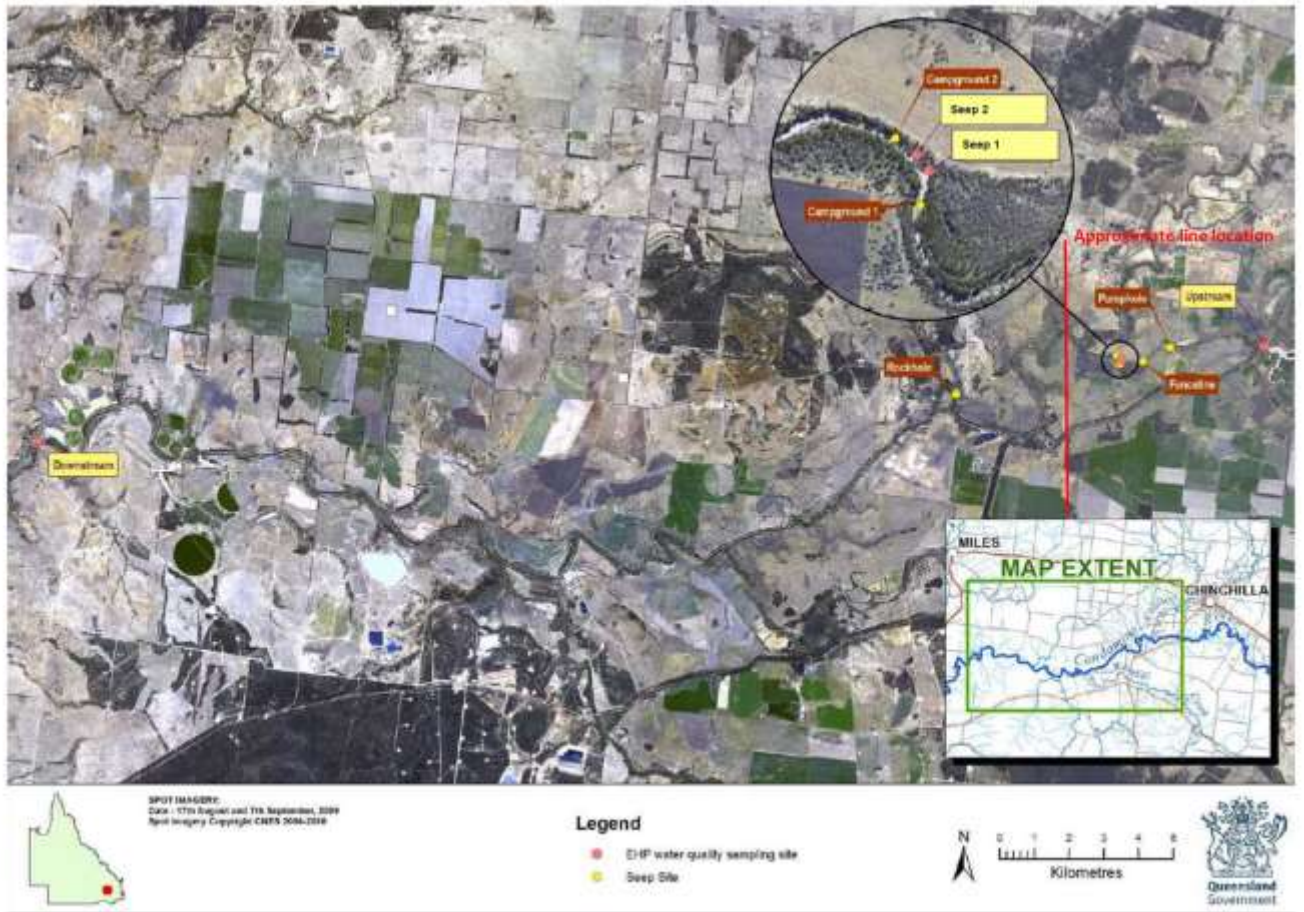
As discussed above, the initial study of stress orientation and the relative fracture orientation to maximum stress has begun to show a relationship where the more that fractures and local stress are closely aligned permeability is improved and/or preserved to greater depths. Further work on this is part of the PhD thesis by Mukherjee. In addition, the effect of changes in stress due to production will be included. The hypothesis to be investigated is whether further changes in stress orientation induced by production cause initially open fractures to close. This would result in accelerated decline curves. Alternatively, given a range of fracture orientations in a given well the changes in stress due to reservoir depletion may allow other fracture systems to open, resulting in improved reservoir performance.

4.3.8.1 Gas Seeps

Condamine River gas seeps have been reported [Summary Technical Report – Condamine River Gas Seep Investigation]. They are located in the eastern Surat in an area where the Walloon Coal Measures subcrop at the unconformity below the Condamine alluvium. Figure 4.61 shows a 2D profile which is a few km away from the location of two seeps on either side of the line and crosses the river (N-S).

The seeps are in close proximity (~1.5 km) to a well-developed keystone structure with bounding faults displacing shallow Walloon reflectors just below the erosional contact with the Condamine alluvium.

Appendix B Condamine River gas seep sites (x4) and corresponding gas seeps (x5)



Summary Technical Report – Part 1: Condamine River Gas Seep Investigation

Figure 4.60 Location of Condamine gas seeps from Summary Technical Report.

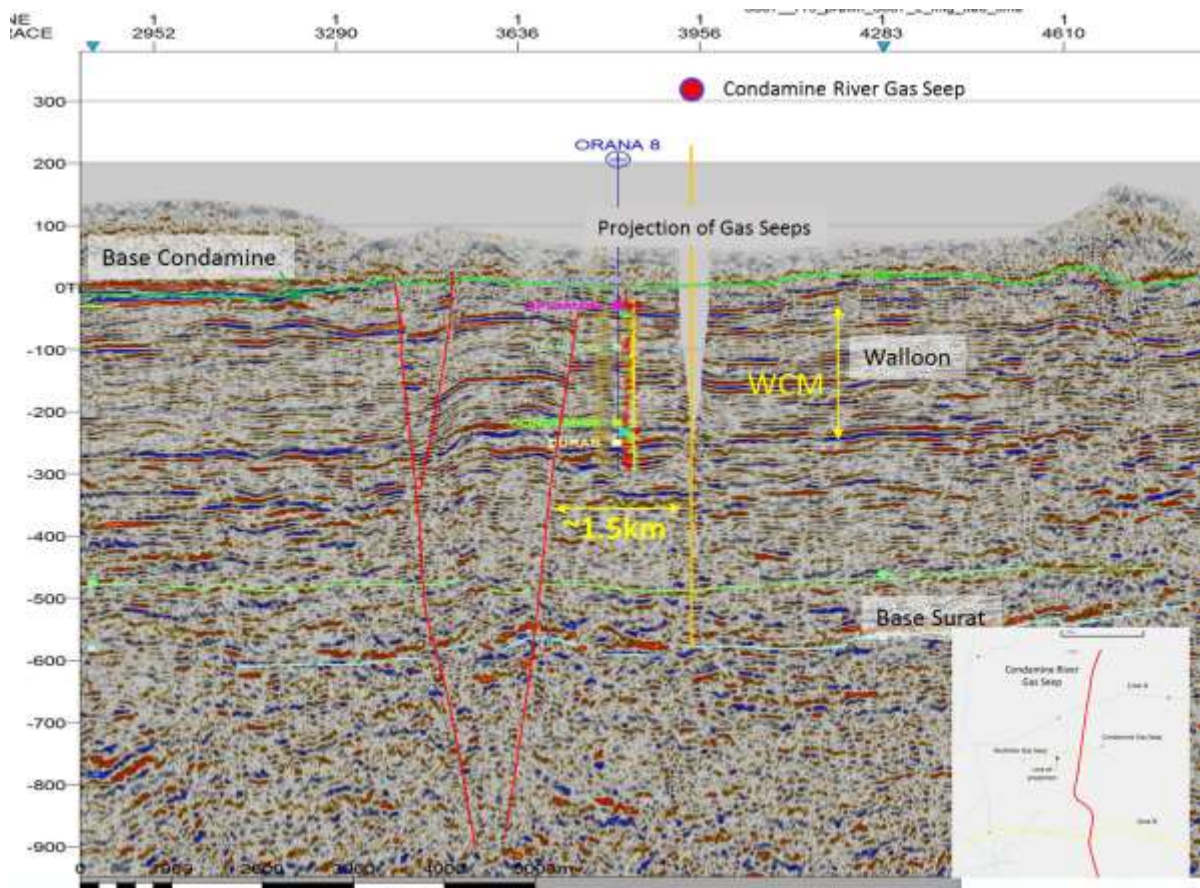


Figure 4.61 Seismic profile close to gas seeps in Condamine River (projected). Inset shows profile location (red) and 2 gas seeps with the line of projection to the seismic profile.

4.3.8.2 Condamine Alluvium

The Cenozoic deformation structures discussed above extend upwards across the base of the Condamine alluvium in some cases. Effects on flow-paths within or between aquifers are possible but not definable from this work. Further investigation is recommended to model potential impacts through a range of simple and credible scenarios. Representative observations from those areas where these effects can be observed are provided below.

Erosional topography at Base Condamine

Erosion at base Condamine is partially controlled by Surat structural development, possibly by structural offset and by abrupt changes in subcropping lithology. The Dalwogan-Condabri survey is of sufficient quality to allow mapping of the unconformity at the base Condamine. The structure map on this surface (Figure 4.63 and Figure 4.64) shows correlation to underlying structure and subcropping stratigraphy. A representative profile (Figure 4.62), shows fault displacement on the eastern bounding fault extending to the erosional contact. This provides a zone of weakness for erosional incisement. The trend of erosional topography is parallel to the trend of deformation.

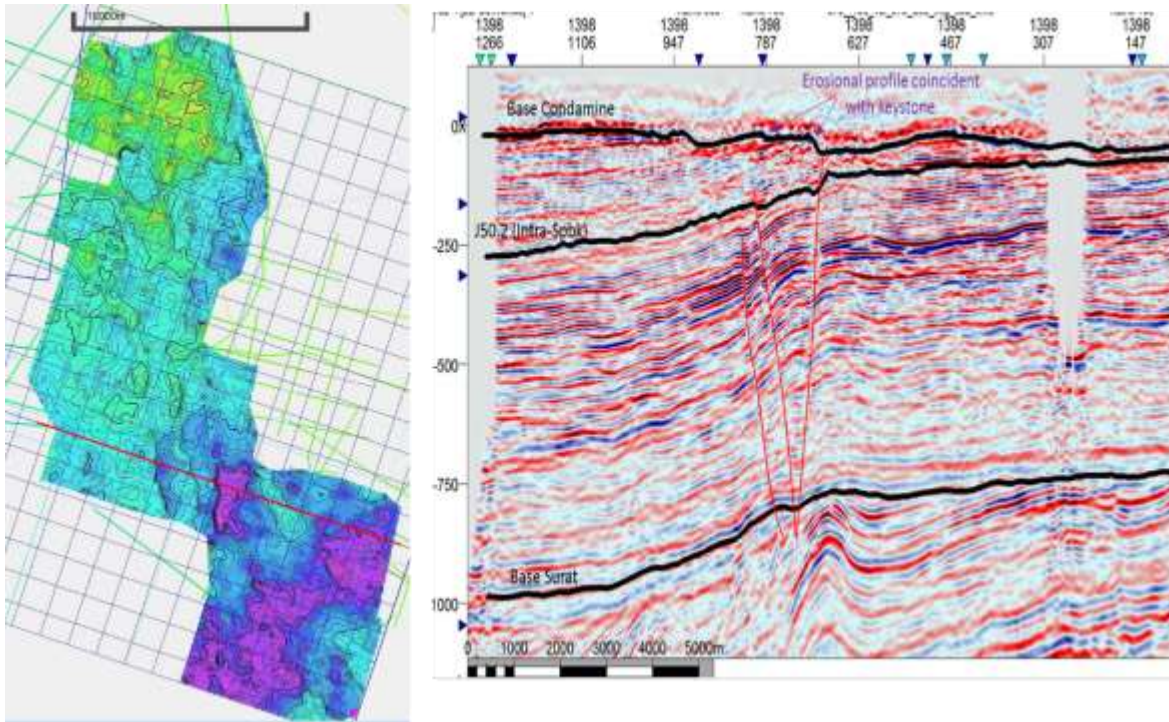


Figure 4.62 W to E profile displaying impact of the keystone structure on 'topography' of the base Condamine. Structure of unconformity to left (C.I.-5ms, yellow-shallow, purple-deep). Note conformance of keystone faults with abrupt erosional features. These features have a trend parallel to the deformation.

The relationship of erosional topography to underlying structure is also presented in Figure 4.63. Here, the map on the left is the base Condamine (alluvium) structure from the previous figure and on the right a shallow coherency slice is co-rendered with the structure with contours removed for clarity. The discontinuities from faulting are represented by the trend of darker grey-black and they directly conform to the trends of topography for the unconformity.

In Figure 4.64, a profile is shown through the northern portion of the survey. Again, the keystone deformation is observed with both bounding faults showing displacement of coherent reflectors up to the base Condamine alluvium. The coherency slice (left) is from a point above the top WCM, the regular stipple pattern seen is due to acquisition geometry and reduced fold at this shallow level and the dark red is an area with no data due to surface conditions.

In spite of this noise, a small fault is observed to trend at a conjugate angle to the zone of deformation. At the location of the orange circle is a surface spring, shown in the Google Earth image (inset Figure 4.60). This spring is located ~4km west of Miles. The coincidental location of this spring and possibly others in the area may be due to vertical flow along portions of the faults.

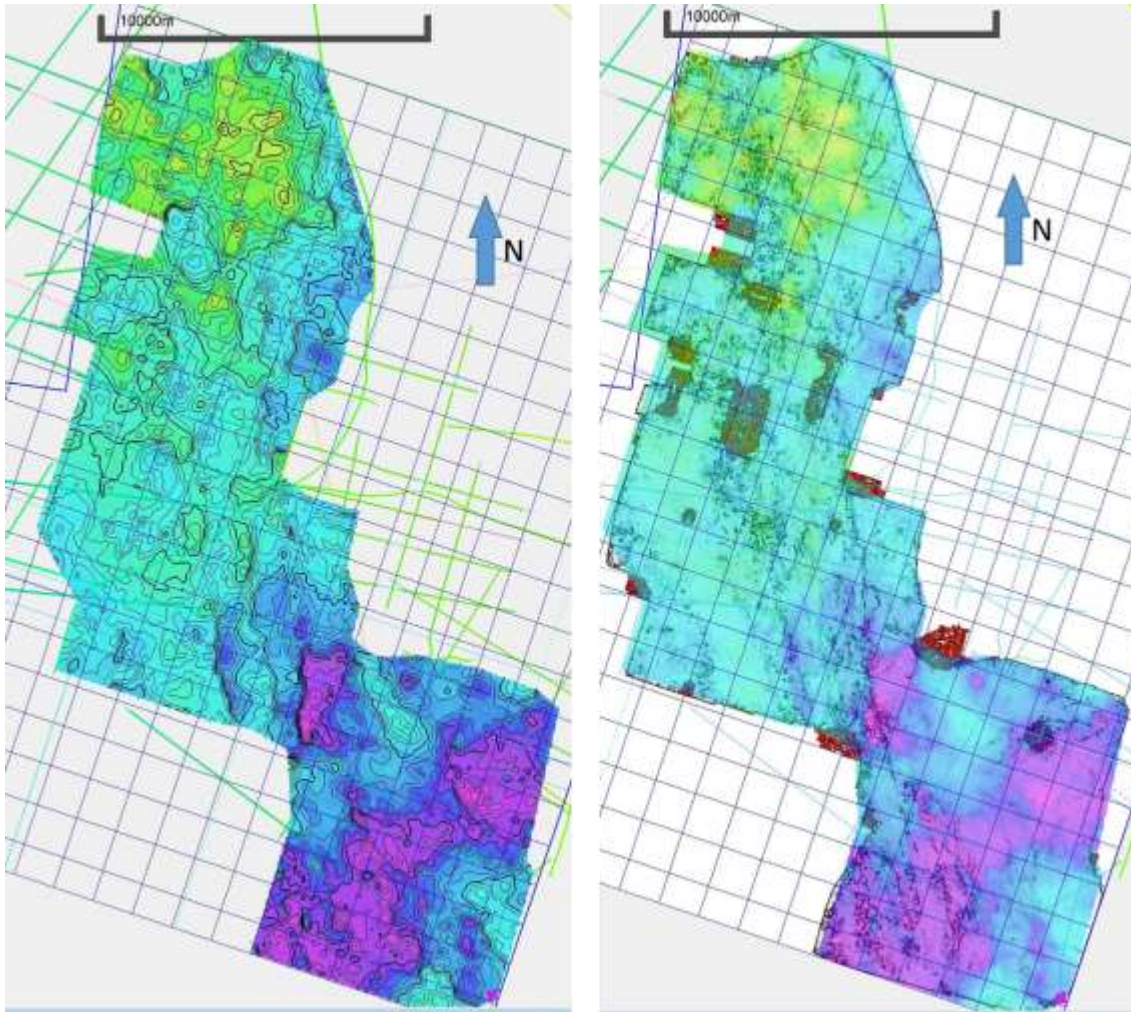


Figure 4.63 Contour of c.i. 5ms of the Base Condamine (left) and coherency superimposed (right). This demonstrates the relationship between faulting and the erosional topography.

In Figure 4.63, the erosional surface at the base Condamine alluvium is observed to downcut much deeper in the SE portion of the survey area (purple). This is where the modern Condamine River and other drainage converge and turn SW. It is apparent that the modern day drainage is also influenced by the Cenozoic deformation and subsequent zones of erosional weakness created.

While there was not a rigorous effort made to determine connectivity of shallow aquifers via faulting, at least one fortuitous example was found in the Dalwogan-Condabri area. Figure 4.64 shows a profile (right) with a narrow keystone block bounded by faults which extend to the base of the alluvium. As discussed in the previous section, it can be observed that the erosional base downcuts across this area. A surface spring is located in close proximity to the subcrop of the faults. The coherency slice shows two subtle faults oriented at a conjugate angle (NE-SW) to the trend of keystone faulting. As this slice is very shallow in the data, it is affected by the acquisition footprint (checkered pattern).

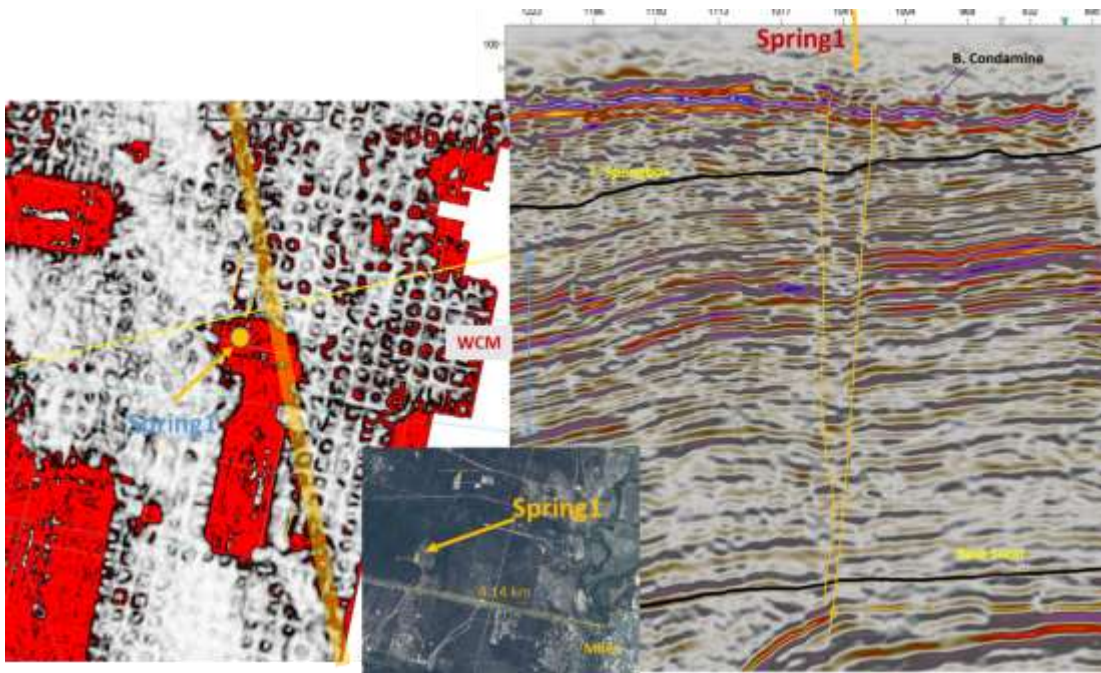


Figure 4.64 Coherency slice, Google Earth image and seismic profile show location of a spring coinciding with the location of keystone faulting.

5 Image Log Analysis

5.1 Well Data

Well data refer mostly to logs and well completion reports. Most of these data were processed and interpreted in the Surat Framework Model Project (CLX 148 342 Esterle et al. 2017). Details are described in the final report for that project.

5.1.1 Basic logging suites

Wells utilized for seismic integration were limited to those with sonic logs in the database. Of these, 580 have had integrated well ties made. The wells with integrated ties have a red symbol in the database. Some attempted well ties had incorrectly loaded sonic logs with either a problem with units (ms/m instead of ms/ft) or a dipole sonic loaded instead of compressional sonic. These problem wells generally have a bright green symbol and have not been fixed in the project as of this report.

Log suites loaded to the database and available for a given well vary. Often the gamma ray (GR), density (DEN), sonic (sonic), resistivity (RT) are present. Most wells have a limited set of logs loaded to the project. In some areas, full log suites have been loaded from the GSQ database. Where logs have been reloaded, there is no appreciable difference between existing database logs and the original *.las files.

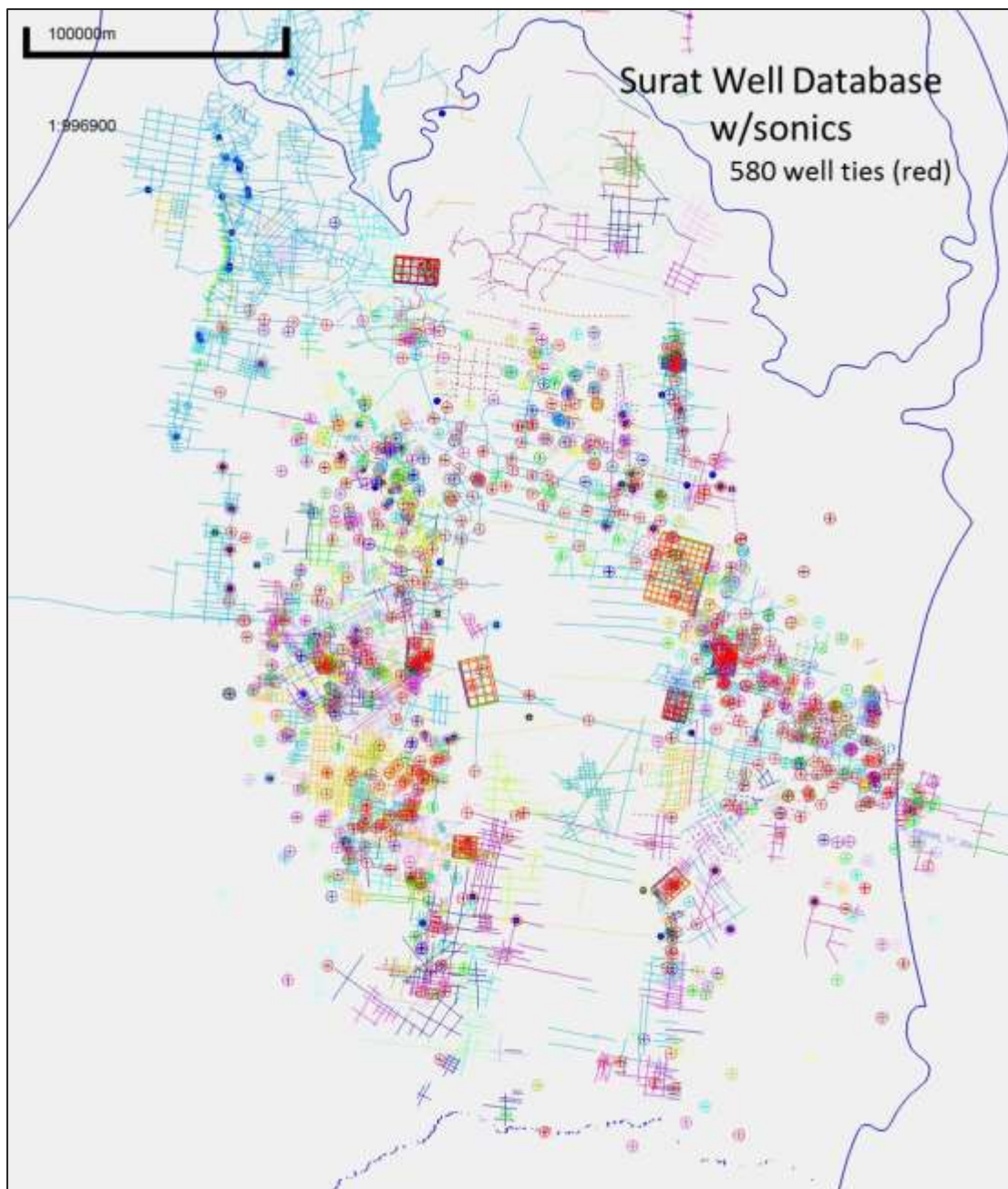


Figure 5.1 Map showing wells used in this study. Wells with sonic logs, red for well ties (~580).

5.1.2 Image logs

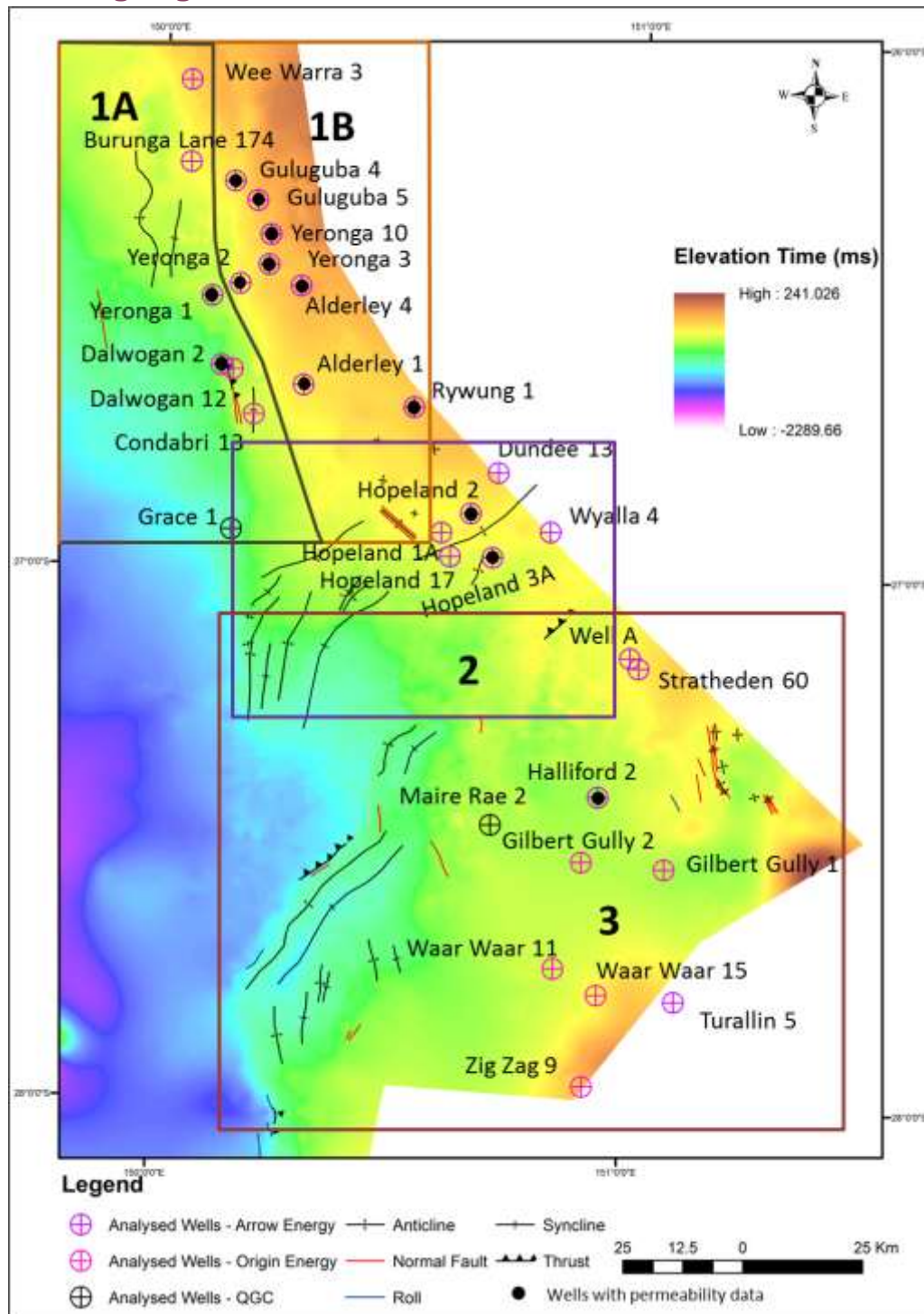


Figure 5.2 is a map with the location of image logs interpreted for stress and fracture orientation and measured permeability data analysed for this study. 32 vertical wells with resistivity and acoustic image log data were interpreted for in-situ stress (S_{Hmax}) and fracture orientation within coal and interburden. Measured permeability from Drill Stem Test (DST) data were available for 13 wells and were analysed to understand the relationship between:

- measured permeability with in-situ stress orientation; and
- measured permeability with angular relationship between in-situ stress and fracture orientation within coal.

Apart from Dalwogan 2, well (UQ in-house interpretation) permeability data for all other wells are sourced from QDEX (2016). Wells were selected based on the distribution of regional structures and small faults observed in the seismic survey data.

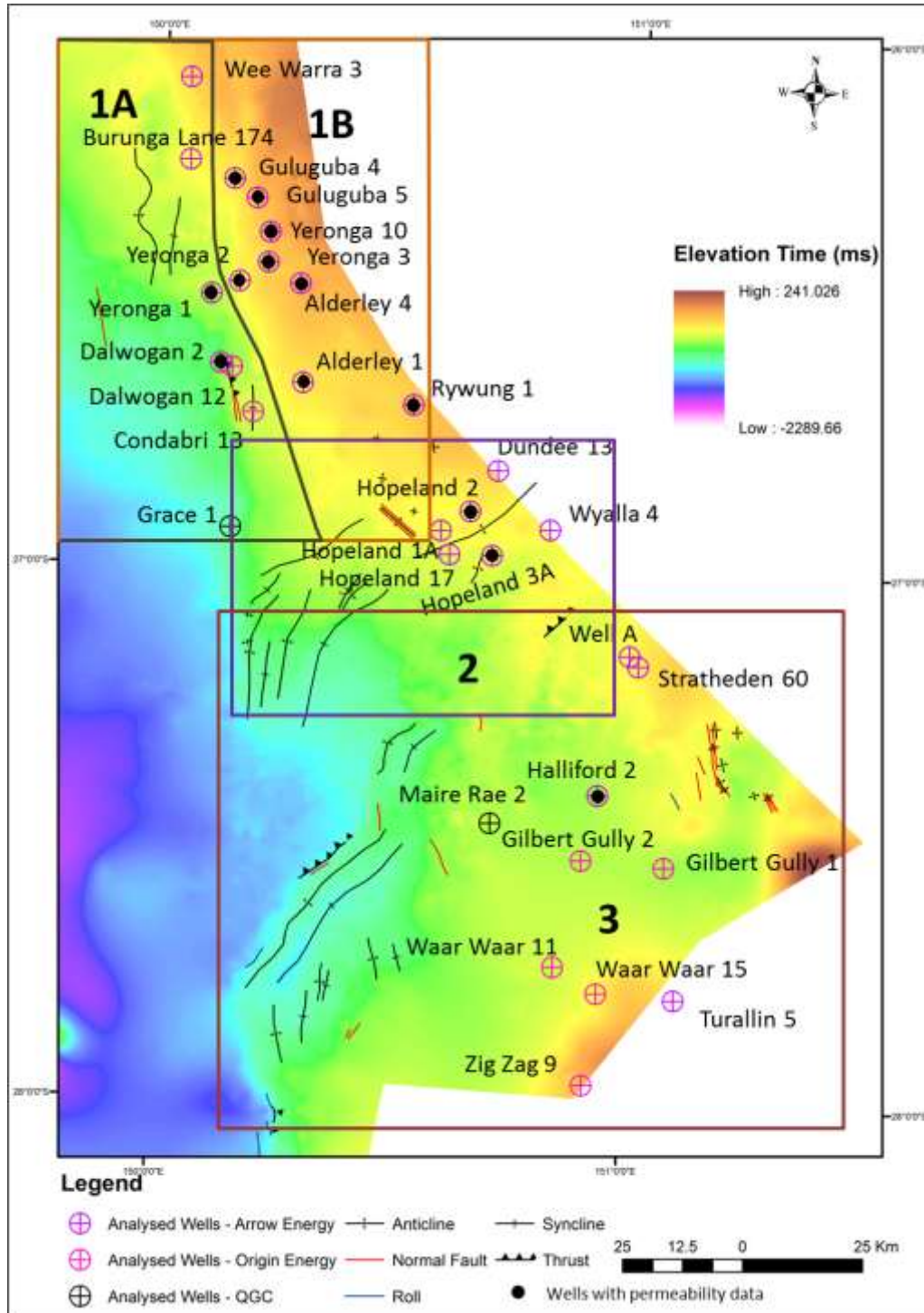


Figure 5.2 Map showing Base Surat time surface and image logs included in this study (also reported in Milestone 3a Mukherjee et al., 2016).

Stratigraphic variability in fracture distribution and stress were examined, utilizing the lithologic correlations developed by the Office of Groundwater Assessment (OGIA). Stratigraphic information from well completion reports (QDEX 2016) were also used where OGIA tops (OGIA 2016) were not available.

For this study, mostly historic and recently open file wells were used. DNRM, Santos, Shell/QGC, Arrow Energy and Origin Energy generously provided their open file datasets, and resistivity and acoustic borehole image logs were the main well log data used. Most of the borehole image data was of good quality but there were also few poor quality image log data present which were used with caution.

5.2 Image Log Analysis

A variety of wireline log data were used: standard logs for identification of coal intervals; and resistivity and acoustic image log data to interpret the in-situ stress orientations, fractures and faults within coal and interburden strata within the study area. The interpreted data from the borehole image logs were compared with the regional seismic interpretations to relate spatial variation in the in-situ stress and fracture character with the larger structural features. Where available, effective vertical stress data calculated from the density logs was examined against reservoir pressure data for any trends with depth or between structural domains. The effective vertical stress with the study area increases linearly with depth and can be assumed as the proxy to the depth of the reservoir. In-situ stress and fracture orientations interpreted from the image logs are also cross-plotted with measured permeability data to observe if any predictive relationships exist.

The image log data were loaded into Paradigm™'s Geolog (v.7.4) software and the standard workflow presented in Figure 5.3 for image log quality assessment and interpretation was followed. Examples of features observed are breakouts, drilling induced fractures, cleats, micro-faults and conductive (open to flow) and resistive (closed to flow) fractures are shown in (Figure 5.5 and Figure 5.6). The classification scheme presented in Figure 5.4 was applied for identification of in-situ stress indicators, faults and fractures. This includes the symbols used in maps and images. Fracture in general refers to rock discontinuities of all types. Joints, faults, veins, shear zones and foliation planes can be classified as fracture.

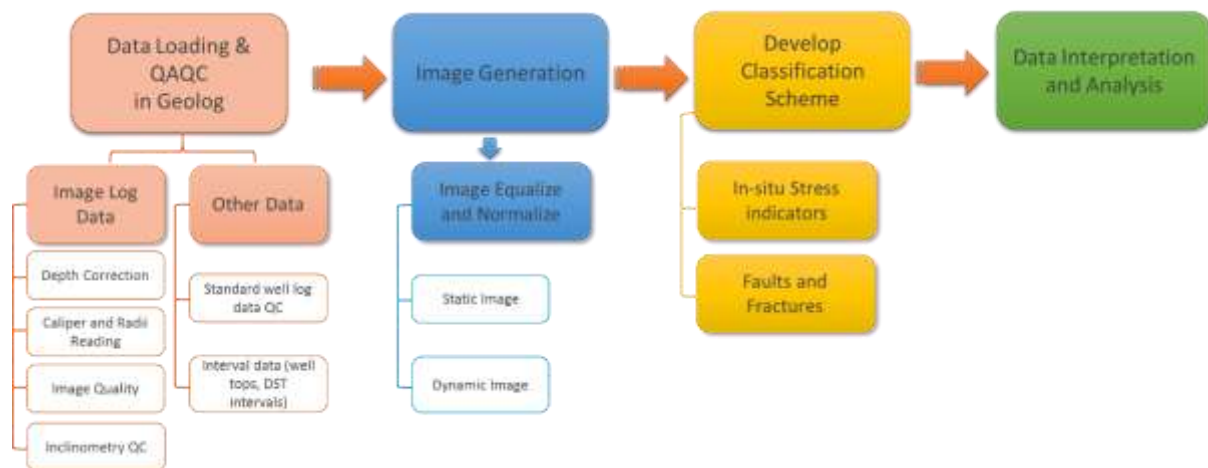


Figure 5.3 Methodology flow chart: Image logs.

Coal Fracture	Fracture that cuts coals covering entire / partial borehole circumference	Fracture		
Conductive Fracture	Lower resistivity fracture that cuts interburden rocks covering entire / partial borehole circumference	Fracture		
Resistive Fracture	Higher resistivity fracture that cuts interburden rocks covering entire / partial borehole circumference	Fracture		
Mixed Fracture	Fracture that cuts interburden rocks covering entire / partial borehole circumference showing lower resistivity in some part of the fracture length	Fracture		
Coal Fault	Fracture that cuts coals with obvious displacement covering entire / partial borehole circumference	Fault		
Fault	Fracture that cuts interburden rocks with obvious displacement covering entire / partial borehole circumference	Fault		
Breakout	Broad, parallel, poorly resolved zone of higher conductivity or low resistivity, low acoustic amplitude and long travel time that occur on opposite sides of the borehole wall	Borehole Breakout		
DITF_Inc	Steeply dipping, planar, conductive fracture that is borehole sub-parallel, perpendicular to borehole breakout orientation	Inclined Drilling Induced Tensile Fracture		
DITF	Steeply dipping, non-planar, conductive fracture that is borehole parallel, perpendicular to borehole breakout orientation	Drilling Induced Tensile Fracture		

Figure 5.4 Image log interpretation classification scheme.

5.2.1 In-situ Stress Indicators and Azimuths

In-situ stress indicators such as borehole breakout, Drilling Induced Tensile Fracture (DITF) and Inclined DITF can be visualized and interpreted from the image log data. Borehole breakouts are the stress induced enlargements (Bell and Gough 1982) that occur when the stresses around the borehole exceed the stress required to cause compressive failure of the borehole wall (Zoback et al. 1985; Bell 1990). In vertical boreholes, the breakout will show a broad, parallel, poorly resolved zone of higher conductivity or low acoustic amplitude, and long travel time occurs 180° apart from each other (Figure 5.5). The long axes of the borehole breakout indicates the minimum principal stress orientation (S_{hmin}). DITF and inclined DITF are the steeply dipping conductive fractures often created during wellbore drilling when the stress concentration around a borehole exceeds the stress required to cause tensile failure around the borehole (Aadnoy 1990). In borehole image logs two DITF / inclined DITF occur 180° apart from each other and indicate the S_{Hmax} orientation (Figure 5.5).

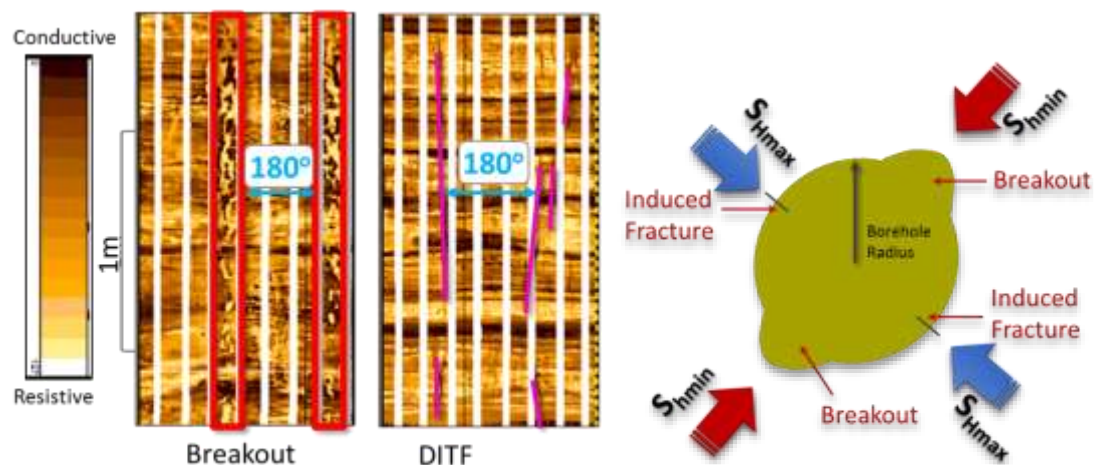


Figure 5.5 Examples of in-situ stress indicators observed in borehole image logs (Mukherjee et al. 2017, unpublished).

5.2.2 Faults and Fractures Identification

Coal is a naturally fractured reservoir rock with low matrix permeability where fractures control the primary permeability. As the WSG coals are relatively immature with poor cleat network (Johnson et al. 2010), the permeability is dominantly controlled by the joints and / or tectonic fractures developed within coal. For this study, the fractures present within interburden rocks are subdivided into conductive (open to flow), resistive (closed to flow) and mixed fracture (partially open to flow) and fractures present within coal as coal fracture (Figure 5.6). Coal cleats, vertical fractures or joints present within coal are not included for this study purpose. Only coal fractures with full or partial sinusoids are included. Due to the small depth of investigation of the image log, fracture sub categories (conductive, resistive and mixed) are valid within a borehole. Outside borehole, the opening or closing of fracture depends upon the present day in-situ stress state. Faults within coal and interburden rocks are classified as coal fault and fault, respectively (Figure 5.6).

5.3 Image Log Interpretation

5.3.1 In-situ stress and fracture variation with structure

Globally, in-situ stress orientation is broadly impacted by plate movement (World Stress Map Project data; Richardson, 1992; Zoback, 1992; Zoback et al., 1989). In the Surat Basin, mean principal horizontal stress based on geomechanical-numerical model (Burbidge 2004) and observed data (Rajabi et al. 2017a) is generally ENE-WSW, although significant spatial variation has been observed due to local stress perturbations associated with the Surat and pre-Surat Basin structures (Brooke-Barnett et al., 2015; Heidbach et al., 2017).

Based on the variation of in-situ stress and fracture orientations observed from the image log analysis of the wells in the eastern part of the Surat Basin, the study area is subdivided into four different domains (Figure 5.2 and Figure 5.8).

- Mimosa Syncline – Domain 1A
- East of the Leichhardt- Burunga Fault System (LBFS) – Domain 1B
- Undulla Nose – Domain 2
- Kogan Anticline and SE of Moonie – Goondiwindi Fault System (MGFS) – Domain 3

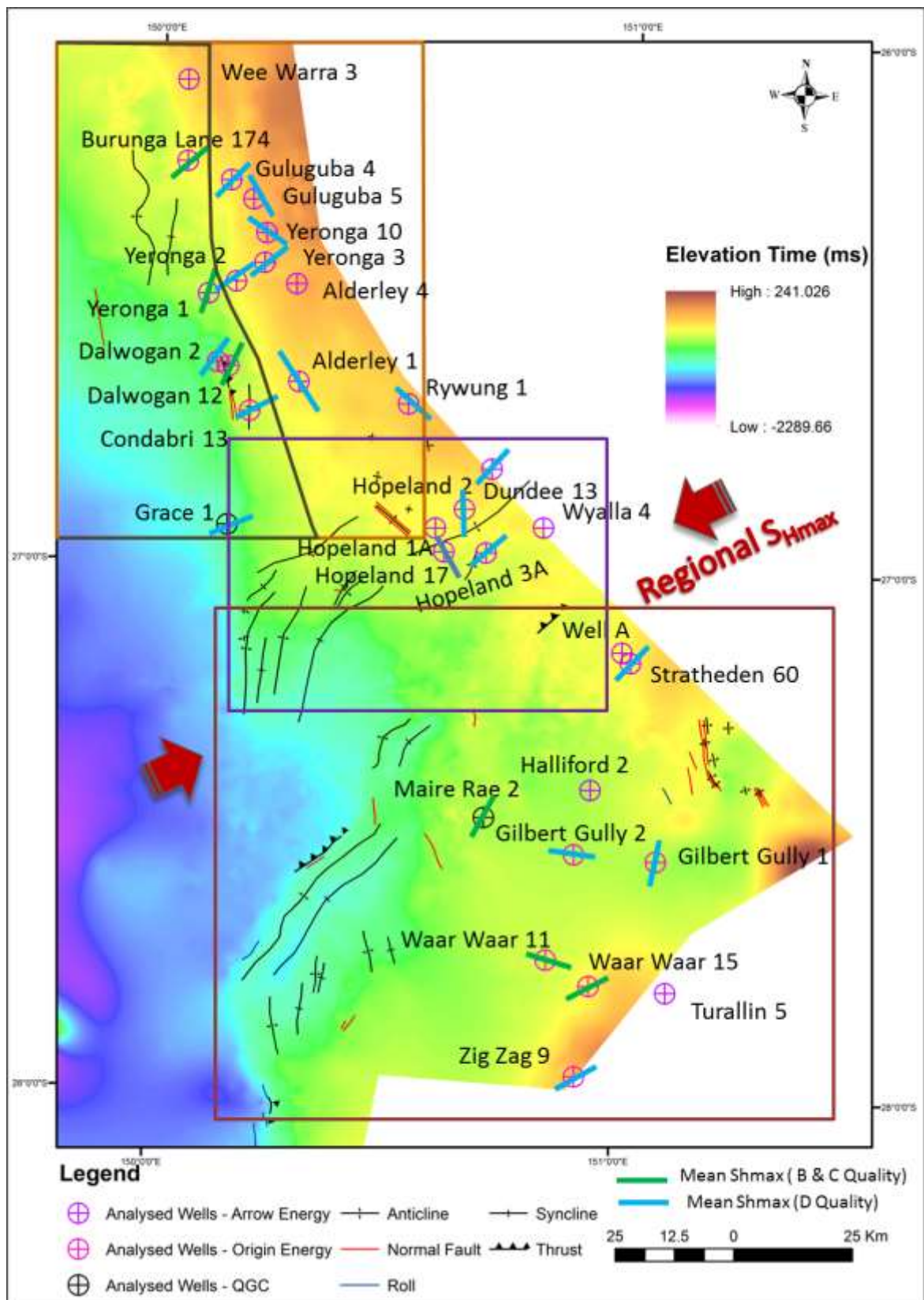


Figure 5.8 Map showing major structures observed in the Surat sedimentary succession (Babaahmadi et al. 2016, Copley et al. 2017) along with location of analysed wells and structural domains within the study area. The map overlies the Base Surat time structure map.

In-situ stress and fractures are also influenced by the major structures. Proximal to the faults, in-situ stress rotation from the regional ENE-WSW orientation is observed spatially and with depth. Rajabi et al. (2016) also observed rotation of in-situ stress near faults and fractures in the Clarence – Moreton Basin due to local stress perturbations from the faults and fractures. The in-situ stress rotations and fracture orientation variations are illustrated in the following Figure 5.8 to Figure 5.14.

Though overall S_{Hmax} orientation within the study area is similar to the regional S_{Hmax} , it varies near major basement structures (East of LBFS) and folds and/or faults within Surat sedimentary succession (Undulla Nose) (Figure 5.8 and Figure 5.9), while the Surat sedimentary succession in the Mimosa Syncline and Kogan Nose and SE of MGFS shows relatively uniform NE – SW S_{Hmax} orientation (Figure 5.9).

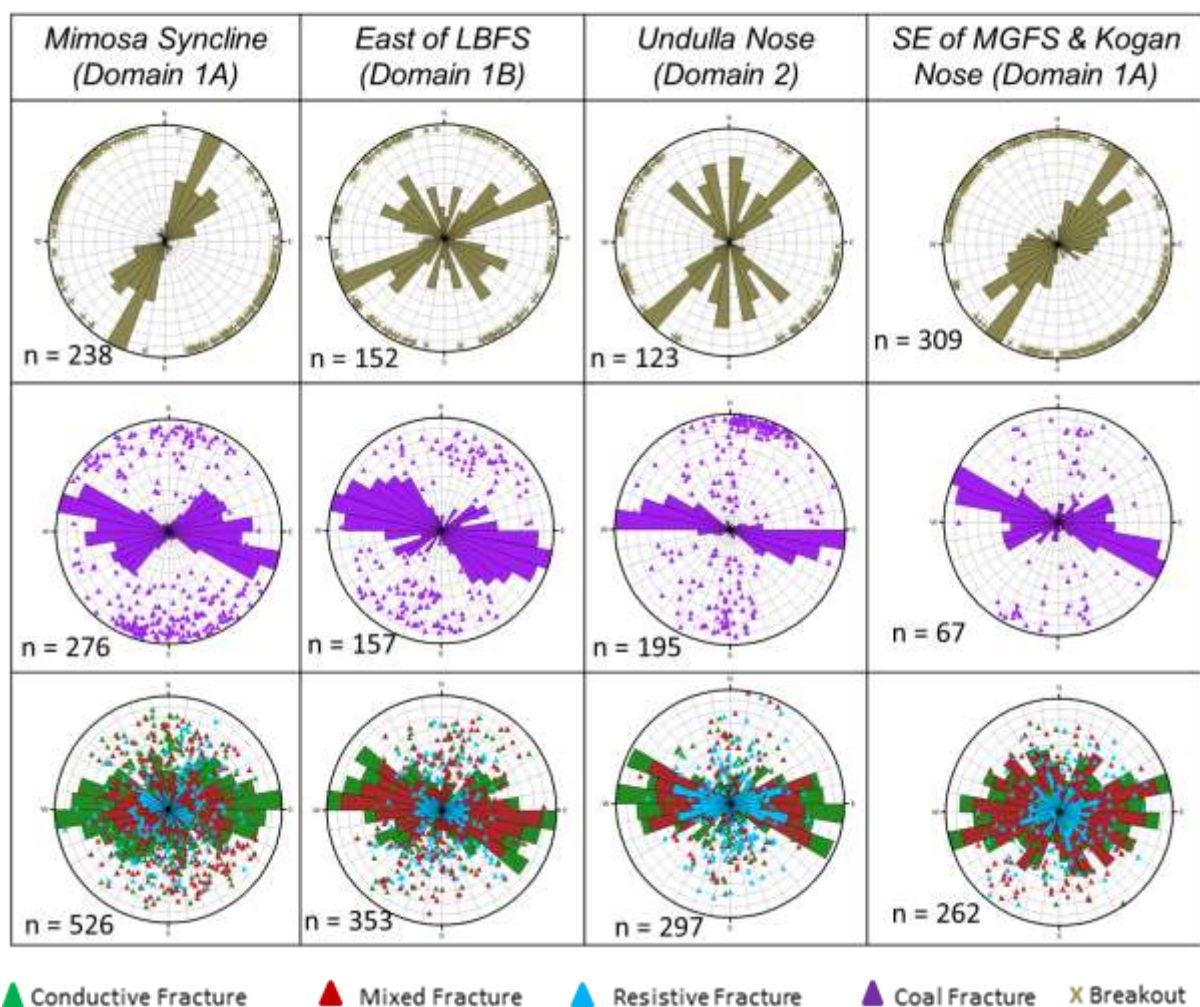


Figure 5.9 Orientation of present day maximum horizontal stress (S_{Hmax}), interburden and coal fractures in the Leichhardt – Burunga Fault system (LBFS) area, Undulla Nose and near Kogan anticline and south east Moonie – Goondiwindi Fault System (MGFS). The number of each for each area / domain is indicated below the rose diagram. Stress orientations are measured in True North. Rose diagrams are in linear radial scaling.

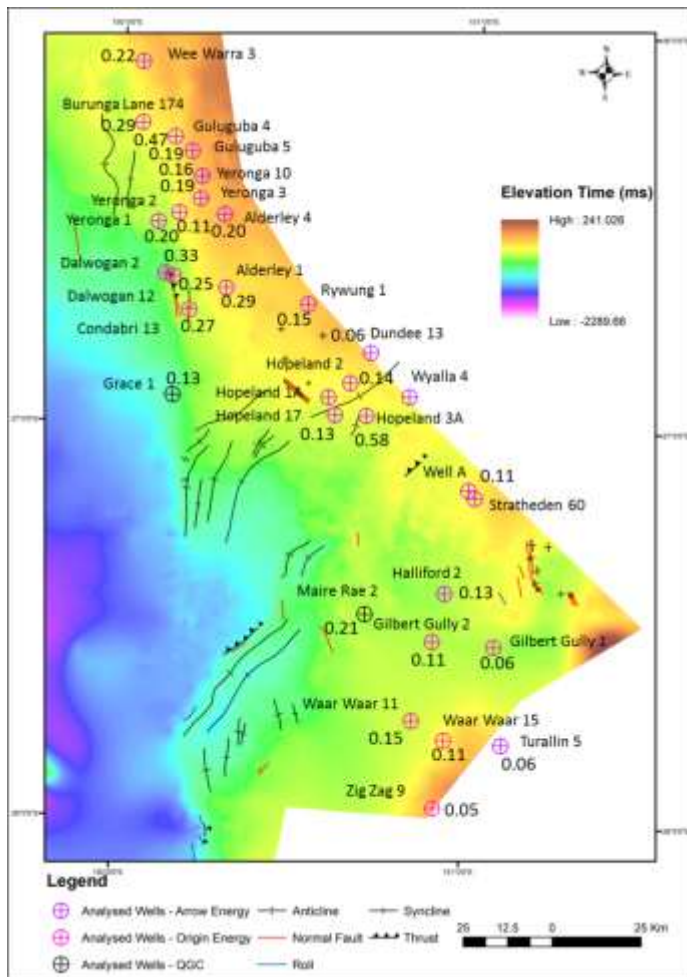


Figure 5.10 Map showing fracture density distribution (P10) within Walloon Coal Measures from the interpreted wells.

Fracture density also varies with the structures. Within the study area, fracture density is significantly increased near the folded strata in the Surat sequence. The gentle flexure and faults within the Surat sequence may be caused by the thermal subsidence and structural reactivation in the pre-Surat sequence. Fracture density also increases closer to the keystone features observed within Surat sequence.

The fracture density shown in Figure 5.10 is calculated over complete Walloon Subgroup intersected by the individual wells for every 10m interval combining fracture within coal and interburden. Fracture density (P10 i.e. number of fractures / metre) is significantly higher closer to the major structures within Surat succession. The Surat sequence overlying the deeper Burunga structure in the Mimosa Syncline area is gently folded. The wells in this area show significantly higher fracture density than the wells away from this structure. In the Dalwogan and Condabri wells, proximity to the fault within the Surat sequence may also have impacted fracture density increment. In the Undulla Nose area, the well Hopeland 3A located near the crest of the anticline exhibits higher fracture density within the Walloon sequence relative to nearby wells. Similarly near the Moonie-Goondiwindi fault system, Maire Rae2 well has relatively higher fracture density in comparison to nearby wells.

5.3.2 Seismic sections showing in situ stress and fracture variation

The following figures illustrate the variation of in-situ stress orientation and fracture density spatially and along depth in the different structural domains: east of Leichhardt-Burunga fault system (Domain 1B), Undulla Nose (Domain 2), and SE of Moonie-Goondiwindi fault system (Domain 3).

Guluguba wells located in the east of LBFS (Figure 5.11) show spatial variation of in-situ stress orientation. The Guluguba 4 well is located in the gently folded Surat sedimentary succession, which overlies the Permian Burunga structure. From the seismic section (Figure 5.11), it is evident that there is significant Permian strata underneath the Surat sedimentary succession in Guluguba 4 which dampens the in-situ stress perturbations from the deeper basement structures. Hence, the in-situ stress orientation corroborate with the far field stress and is oriented similarly to the regional ENE – WSW S_{Hmax} . Guluguba 5 located east of the Burunga structure directly overlies the deformed Permian - Triassic sediments and shallow basement rocks of the New England Orogen, and it exhibits in-situ stress rotation from the regional trend. The rotation of S_{Hmax} is attributed to the pre-existing zone of weakness within deformed Permian – Triassic and basement rocks.

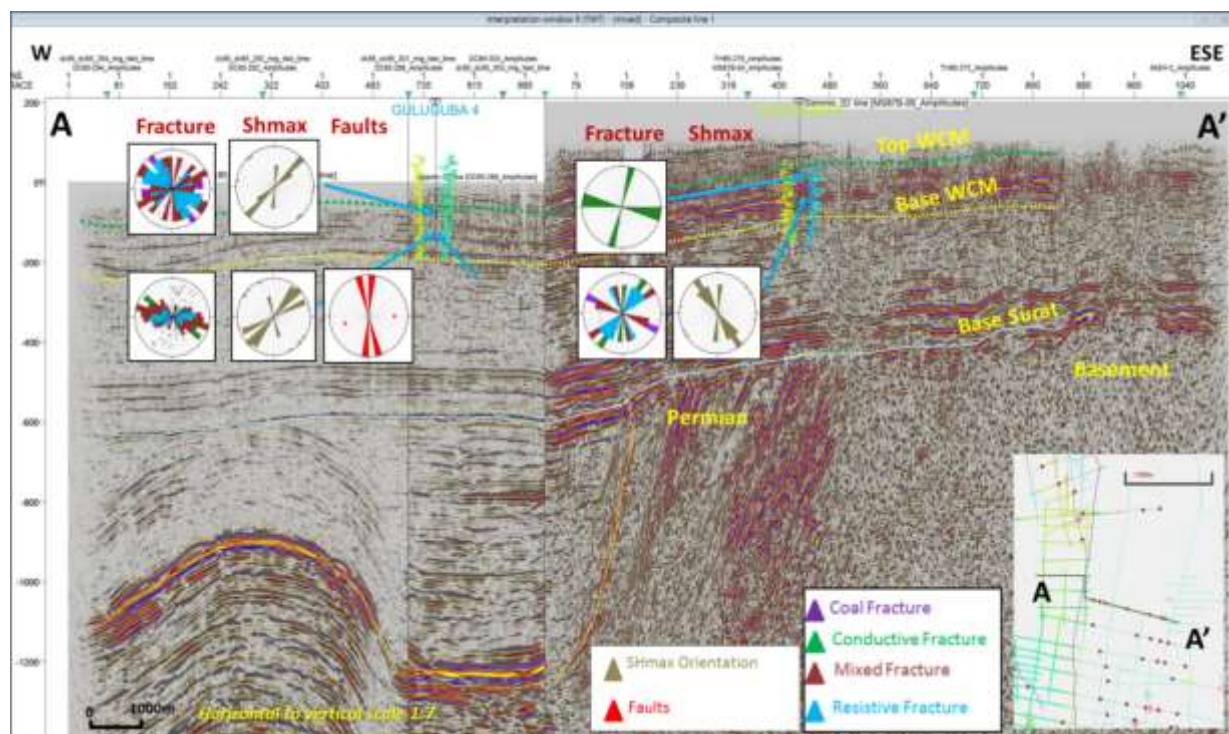


Figure 5.11 Seismic section showing in-situ stress and fracture variation in the Leichhardt – Burunga Fault System.

In the Undulla Nose area (Domain 2), Hopeland 17 well illustrates significant rotation of S_{Hmax} with depth. This well is located between two faults and the rotation of the S_{Hmax} in the upper Walloon Subgroup (WSG) is attributed to the fault intersected along the well trajectory.

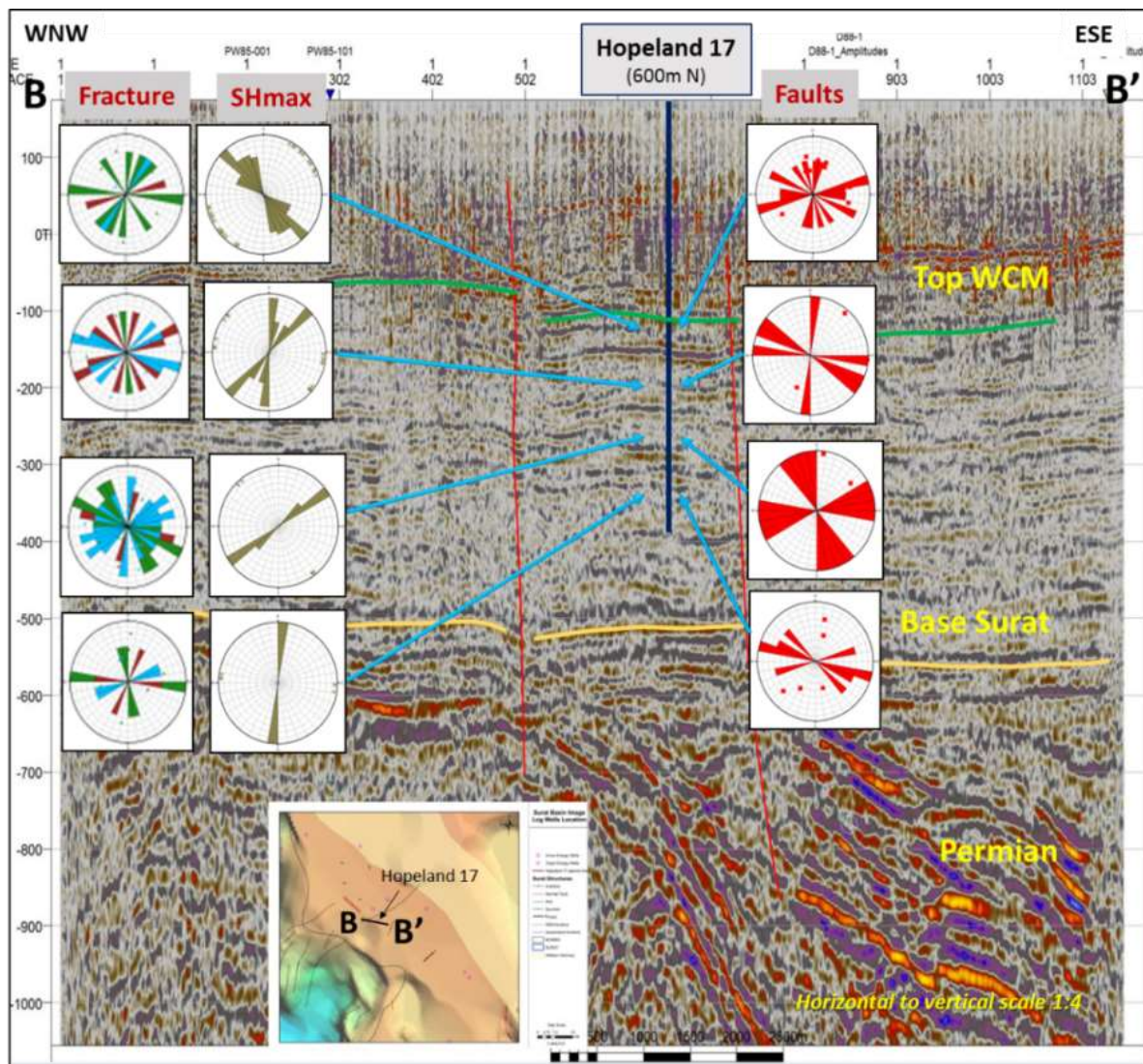


Figure 5.12 Seismic section showing change of stress orientation observed through the WSG within Hopeland 17 well in the Undulla Nose area. The stress orientation variability attributed to the structural complexity present within and near vicinity to the well.

Maire Rae 2 well (Figure 5.12) is located close to the MGFS and small variation of S_{Hmax} with depth. This well shows small variation of S_{Hmax} from the regional trend and high fracture density in the Lower Juandah. The location of the well close to a fault and within folded Surat sedimentary succession is attributed to the variation of S_{Hmax} and fracture density in this well.

In the Waar Waar area, the wells show in-situ stress variation spatially and with depth. The Waar Waar 11 well is located in gently folded strata and proximal to a fault intersecting the Surat sedimentary succession. In this well, the in-situ stress orientation is rotated up to 90° from the regional S_{Hmax} and varies with depth. This in-situ stress rotation is attributed to the location of the well in a folded and faulted Walloon sequence identified in the seismic section (Figure 5.13).

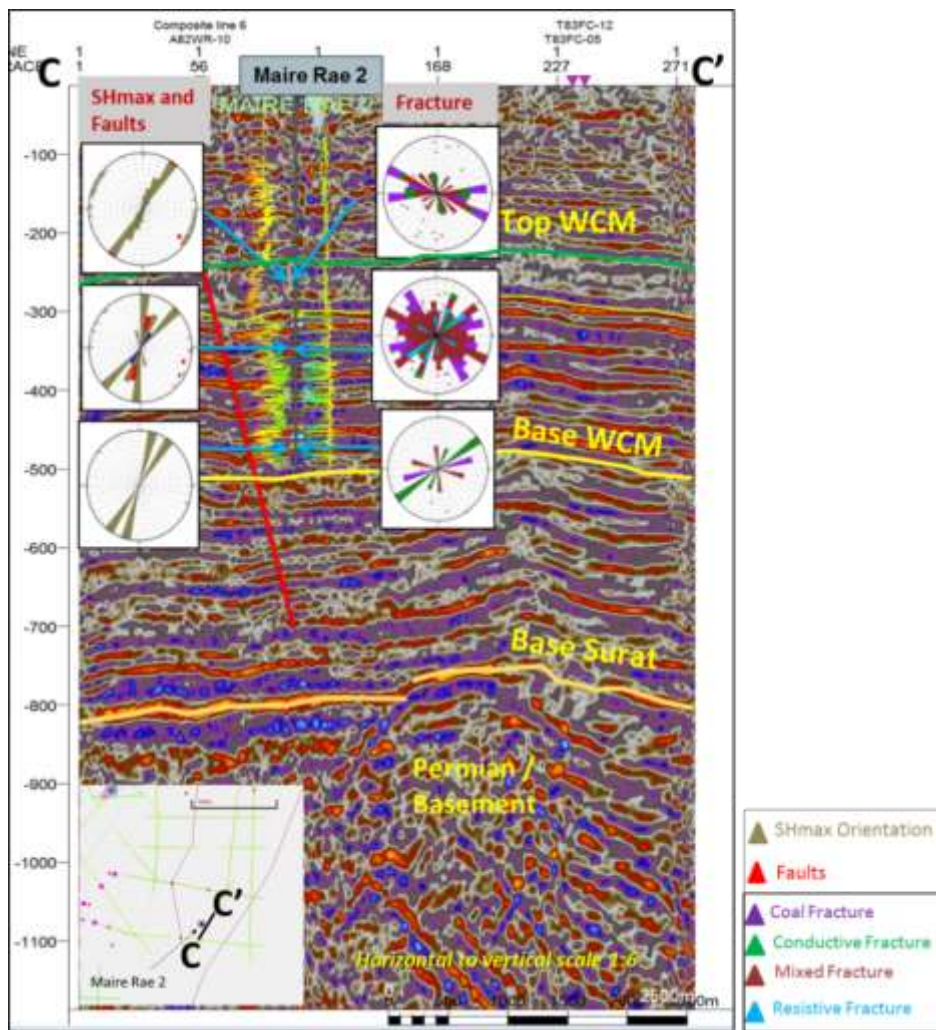


Figure 5.13 Seismic section showing the variation of in situ stress and fracture orientation in Maire Rae 2 well within the WSG in the SE part of Moonie – Goondiwindi Fault System.

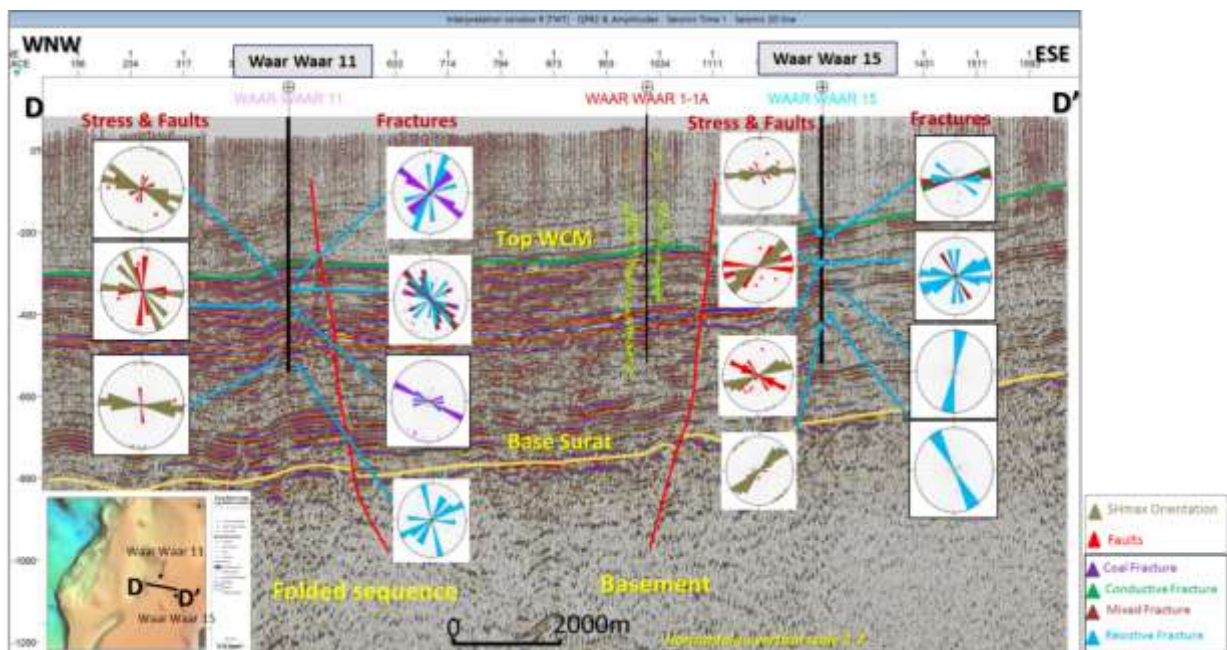


Figure 5.14 Seismic section showing in-situ stress and fracture variation in the SE of Moonie - Goondiwindi Fault System.

5.3.3 Permeability relationship with in-situ stress and fracture orientation

The rotation of in-situ stress due to the local structures significantly impact CSG reservoir permeability within the eastern Surat Basin. Figure 5.15 shows available S_{Hmax} orientation data plotted in two quadrants (NE and SE) and compared with the σ_v and permeability data. The dataset in the eastern Surat Basin indicates that the majority of the highly permeable coals occur where in-situ stress orientation deviates substantially with respect to the regional mean S_{Hmax} orientation (ENE – WSW) within the WSG reservoirs. Permeability generally declines with increasing σ_v , but wells with higher in-situ stress deviation from regional mean S_{Hmax} maintain a higher permeability to greater depth.

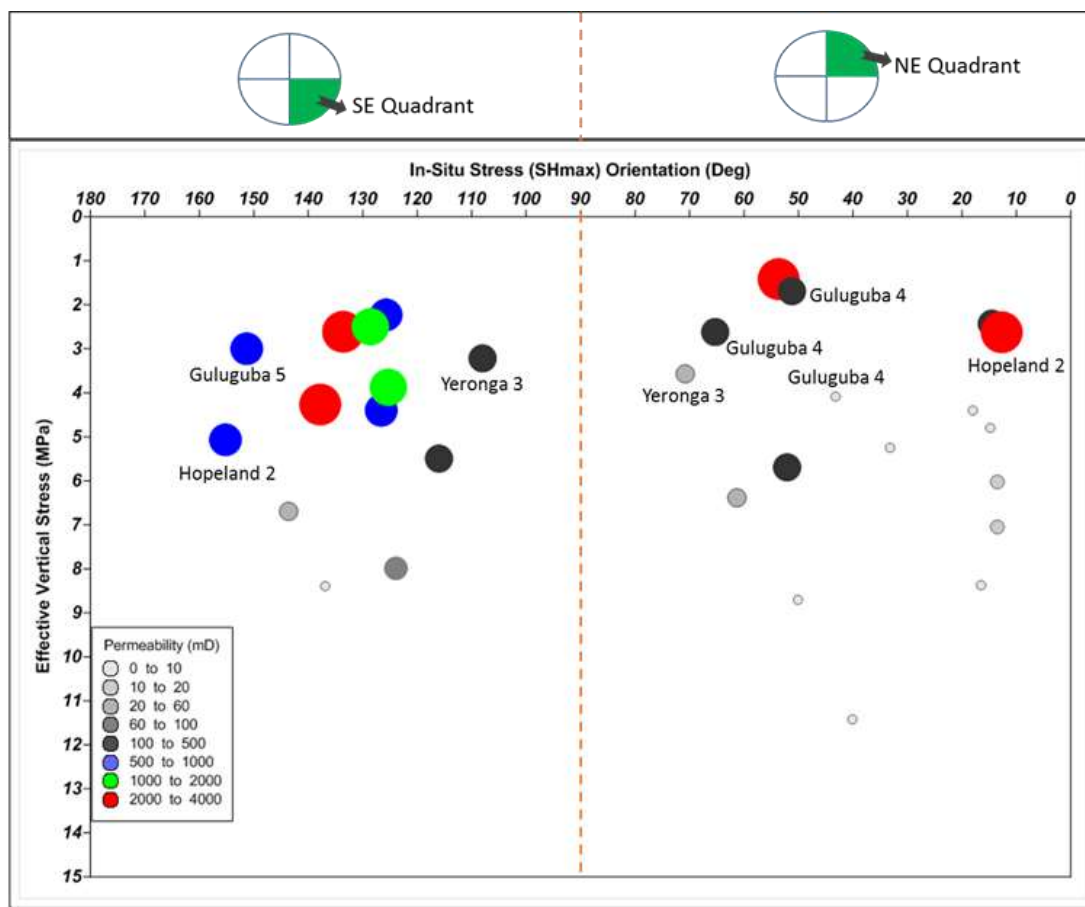


Figure 5.15 Permeability (calculated from well test) relationship with effective vertical stress (σ_v) and in-situ stress orientation.

Permeability in CSG reservoirs not only depends upon the in-situ stress orientation and magnitude, it is also controlled by the fracture orientation. Fractures that are optimally oriented and critically stressed in the current stress state (Zoback 2007, Flottman et al. 2013) will have significantly higher permeability.

Figure 5.16 shows a bubble plot where effective vertical stress (σ_v) is plotted along the X-axis, and the angle between S_{Hmax} and dominant coal fracture trend is plotted along the Y-axis with the permeability magnitude relating to bubble size. From the plot, it is evident that the fractures parallel to the S_{Hmax} are not always the most permeable. Instead fractures striking at about 30° with respect to the S_{Hmax} direction show the maximum permeability. This

indicates a shear movement along fractures in the present day in-situ stress and may relate to the oblique slip movement on faults observed in the seismic data. At an increasing angle between S_{Hmax} direction and coal fracture trend and higher effective vertical stress, permeability values decrease.

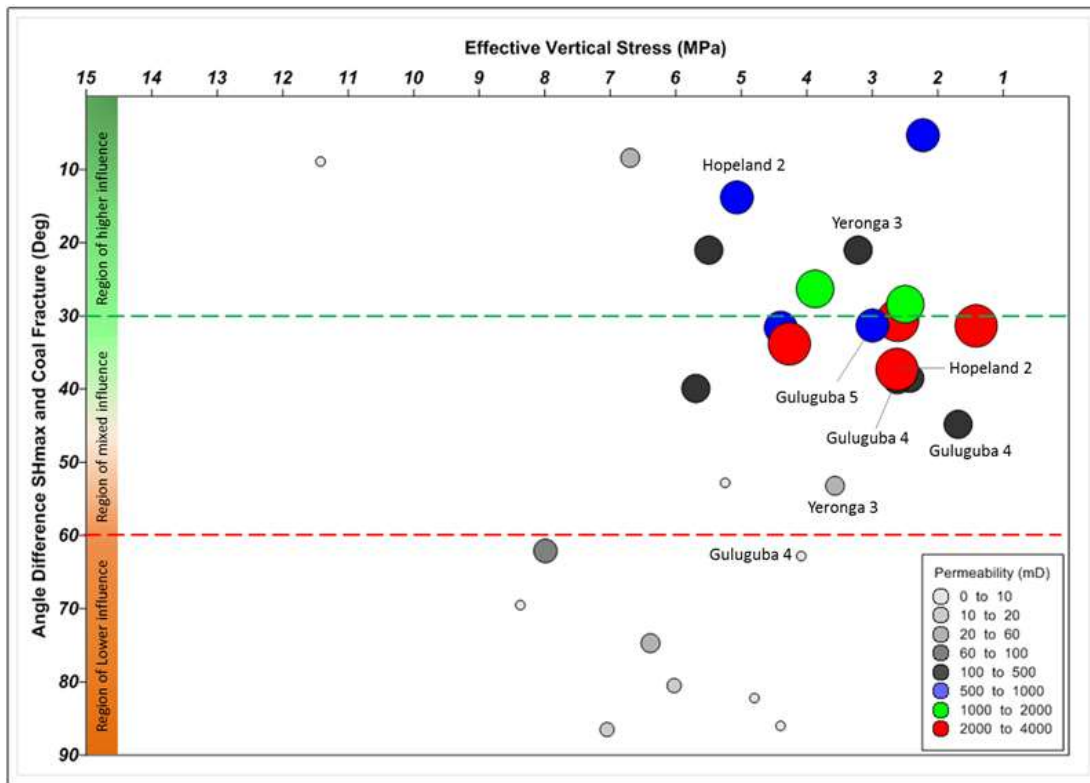


Figure 5.16 Permeability relationship with effective vertical stress (σ_v) and angle between in-situ stress and coal fractures.

An example of the local structural influence on permeability is demonstrated in Figure 5.17. Hopeland 2 is located close to an anticline observed within the WSG and it also went through a “keystone” style structure. The in-situ stress orientation rotates after the well crosses a fault along the well trajectory. Although the in-situ stress rotates, it is optimally oriented with coal fractures causing higher permeability within the test intervals. Additionally, there are significant vertical fractures observed in the core and image logs within the test intervals. These vertical and moderately dipping fractures along with their relationship with present day S_{Hmax} contribute to the higher fracture density and permeability in this well.

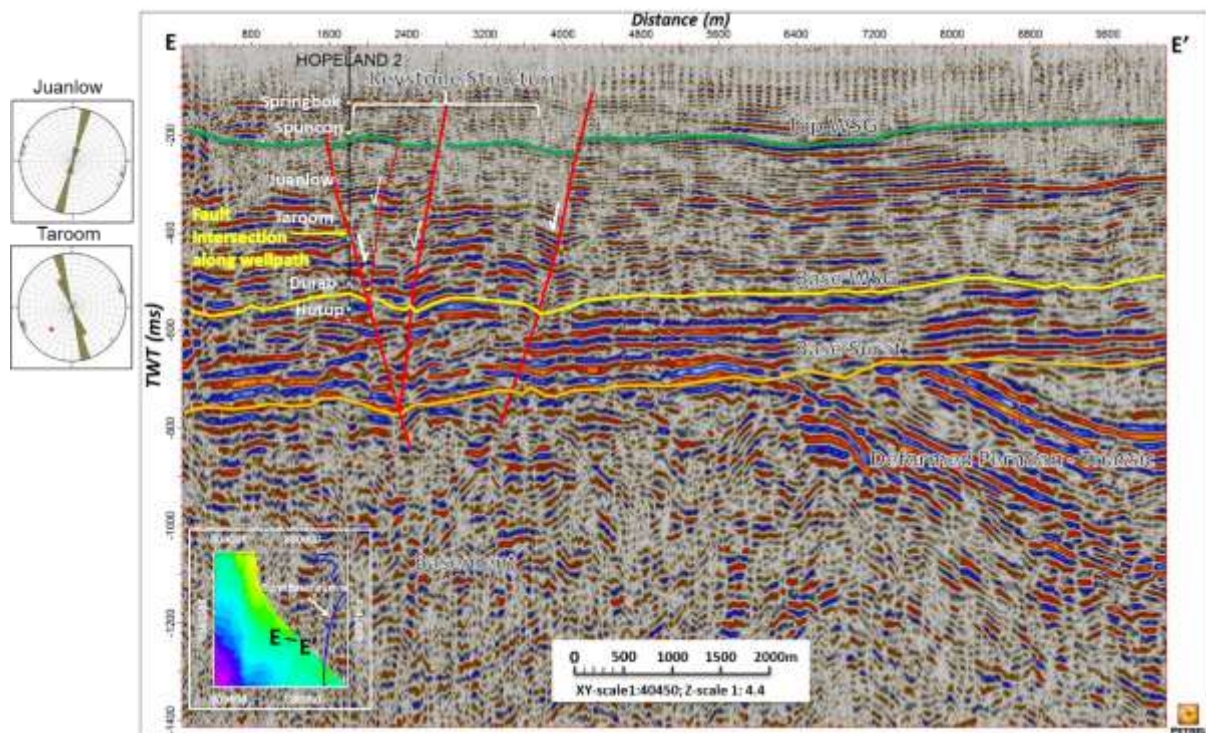


Figure 5.17 Seismic section showing keystone structures on and near the Hopeland 2 well.

5.3.4 Image log analysis summary

The mean Maximum Principal Stress (S_{Hmax}) shows an ENE-WSW orientation (Figure 5.8) but in-situ stress orientation varies spatially and along depth close to major structures and faults. The in-situ stress rotation is due to local stress perturbations from faults, fractures etc. These significantly influence the Walloon coal permeability in the Eastern Surat (Figure 5.16).

Coal fractures are dominantly oriented in WNW-ESE direction in the domain 1A, 1B and 3. However, a NE-SW to ENE-WSW coal fracture orientation is also observed (Figure 5.9). Coal fractures in the domain 2 are dominantly WNW-ESE (Figure 5.9).

Interburden fractures in the domain 1A, 1B and 2 area show two dominant orientations (WNW-ESE and ENE-WSW). There are two minor fracture orientations (NE-SW and NW-SE) present in the domain 1A and the domain 2 (Figure 5.9).

Interburden fractures are quite variable in the Kogan anticline and SE of MGFS area. Major fractures are oriented mainly in two directions (WNW-ESE and ENE-WSW). However, NE-SW and NW-SE fractures are also quite abundant in this area (Figure 5.9).

Fractures within coal are in most cases contained within the coal seam and do not penetrate adjacent interburden. Fracture Density (P10) within the WSG is significantly higher close to major basement and Surat aged structures.

Angle between dominant coal fracture and in-situ stress orientation significantly influences coal permeability within the WSG. In most cases, coal fractures oriented sub-parallel and up to 40 degree to the in-situ stress orientation indicate a good permeability zone (Figure 5.15).

Hopeland 2 is located near an anticline in a structurally complex area. The well crosses a keystone feature and in-situ stress orientation rotates after the well intersects the fault along its trajectory. This well also shows relatively higher permeability although the angle between in-situ stress and dominant coal fracture are not favourable. The Hopeland 2 well exhibit a great deal of vertical joints within coals which along with the local structure influenced permeability calculated from well test within coal (Figure 5.17).

5.3.5 Future Work

5.3.5.1 Relationship between in-situ stress and fracture orientation with the measured permeability

As discussed above, the initial study of in-situ stress orientation and angle between fracture and S_{Hmax} , shows a relationship where fracture and in-situ stress are closely aligned or sub-parallel (up to 40°) permeability improved and/or preserved at a greater depth. Also, most of the good permeability data points are concentrated where in-situ stress rotated from the regional stress orientation due to local stress perturbations. Further work on these observations will be done as part of the PhD thesis by Mukherjee.

5.3.5.2 Impact of in-situ stress and fracture on reservoir performance during depletion

In coal seam gas reservoirs, reservoir pressure depletion during production can significantly impact the in-situ stress and fractures present within coal. As the reservoir pressure decreases, in-situ horizontal stress acting on the reservoirs significantly reduces (Liu and Harpalani, 2014).

Depletion from a fault bounded reservoir changes the pore pressure which can affect the in-situ stress and rotate stress orientation with time (Zoback, 2007). As the relative orientation of fractures to stress is important, the angular distribution within the fracture system will determine the impact of stress rotation with depletion. For example, if rotation of in-situ stress causes the opening of existing fractures which are closed at initial in-situ stress condition, this may improve or maintain reservoir performance during depletion. Alternatively, in-situ stress rotation could also close the existing open fractures, impeding existing production and accelerate decline. As part of the future work, the hypothesis of in-situ stress rotation with depletion and their impact on the WSG will be investigated further.

6 Mine site photogrammetry and characterisation of joint systems in the SE Surat and western Clarence Moreton Basins

6.1 Summary

This section follows the work of Babaahmadi et al., 2016. Joint characteristics, including its spacing, height, length and orientation, are basic parameters for building discrete fracture network (DFN) models that can be used for predicting permeability, geo-mechanical properties or for dynamic fluid flow simulation. In the Mesozoic basins, joint systems and

their relationship to the local faults and folds as well as rheology of rock units are still not clear albeit large structures such as faults and folds have been studied well.

This study presents work to map joint sets in four mines in the Walloon subcrop area of the Surat - Clarence-Moreton basins. 3D photogrammetric data, 2D photos and some field measurements were used. The relationship between joint spacing and lithological unit bed thickness was analysed.

Results indicate that joints have local structural features, which have been developed in response to local faults and folds in different areas, rather than a regional trend. Joint spacing increases with the increase of lithological unit bed thickness. Within various lithological units which have similar bed thicknesses, coal seams have narrower joint spacing than jointed clastic rocks such as mudstone and sandstone. Therefore, rheology and bed thickness plays an important role in the distribution of joints. Based on this study, we suggest building DFN by using the joint height and spacing as inputs because vertical joints are poorly captured by image logs.

6.2 Introduction

Permeability of fractured rock units is dependent on the spacing, height, length and orientation of joints. Fractured rock units will have high permeabilities if joints are parallel to principle stress direction in orientation, open and intersected with each other. Discrete fracture network (DFN) models can be built based on the statistic information, e.g. spacing, height, length, and orientation of joints. DFN models provide a means to dynamic model fluid flow for hydrology, CSG production and coal mining.

Joint orientation and some idea of density can be obtained by interpreting image logs or by investigating cores from drilled holes. However, image logs and core can only provide the height of joints which are intersected with the borehole. Vertical joints are difficult to identify because they are not always intersected with the drilled borehole, especially when the joint spacing is wider than the diameter of the drilled borehole.

Interpretation of seismic survey data provides a larger scale framework, e.g. faults and folds from local structural domains.

Field work from outcrop or mine outcrop is a reliable and direct way to measure the joint height, length and spacing. Through these measurements, we can characterise joints and also develop a predictive relationship between joints characteristics with the lithology and bedding.

In this study, we investigated the joint systems in the Early Jurassic to Early Cretaceous rocks of the southern Surat Basin and the adjacent eastern Clarence Moreton Basin using available mine sites. The larger structures such as faults and folds in the Surat Basin have been previously investigated (Korsch et al., 2009; Babaahmadi et al., 2015). However, detailed work on the joint systems and their relationships to the local faults and folds and the rheology

of rock units have not been conducted. Therefore, the aims of this study are (1) to identify the orientation of joint sets, (2) to understand the relationships among the joint spacing, bed thickness, and physical properties of rocks, and (3) to understand the possible predictive relationship between the joints and folds and faults.

We used 3D photogrammetric data, 2D photos and some field measurements to map joint sets. The information from this study can be used to assist in characterising field scale variation in fractures and stress that can impact on coal seam gas production. Of particular importance is that using more joint characteristics in DFN modelling, the joints model is more reliable; the understanding of lateral variation at both local and regional scales is better.

Although the location of mines is known within the eastern margin, specific features are shown as examples and not necessarily referenced to a particular mine site.

6.3 Geological Setting

This study focuses on the joint systems in the Walloon Coal Measures in the south-eastern (SE) Surat Basin and western Clarence-Moreton Basin (Jurassic to Early Cretaceous basins in eastern Australia). The stratigraphic succession in these basins variously overly the Permian-Triassic Bowen Basin, the Paleozoic-early Mesozoic New England Orogen, and Paleozoic Lachlan Orogen as shown in Figure 6.1. Figure 6.2 shows the faults, folds, and the location of operating mine sites in the SE Surat Basin. It should be noted that these studies are only snapshots in accessible areas of the mines and not necessarily representative of any one.

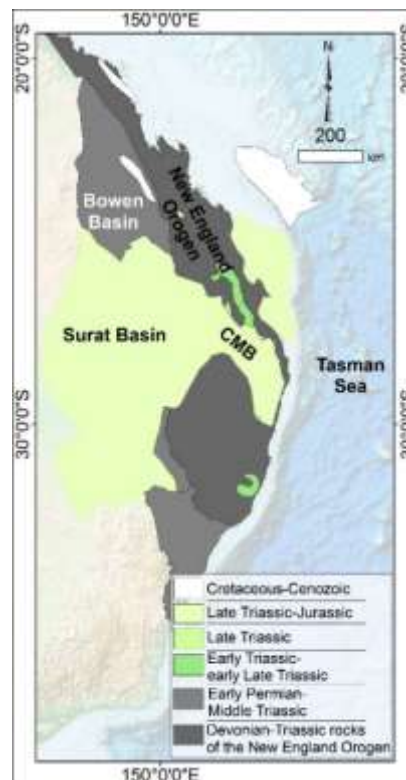


Figure 6.1 A simplified tectonic framework showing the Permian and Mesozoic sedimentary basins in the eastern Australia. CMB = Clarence-Moreton Basin.

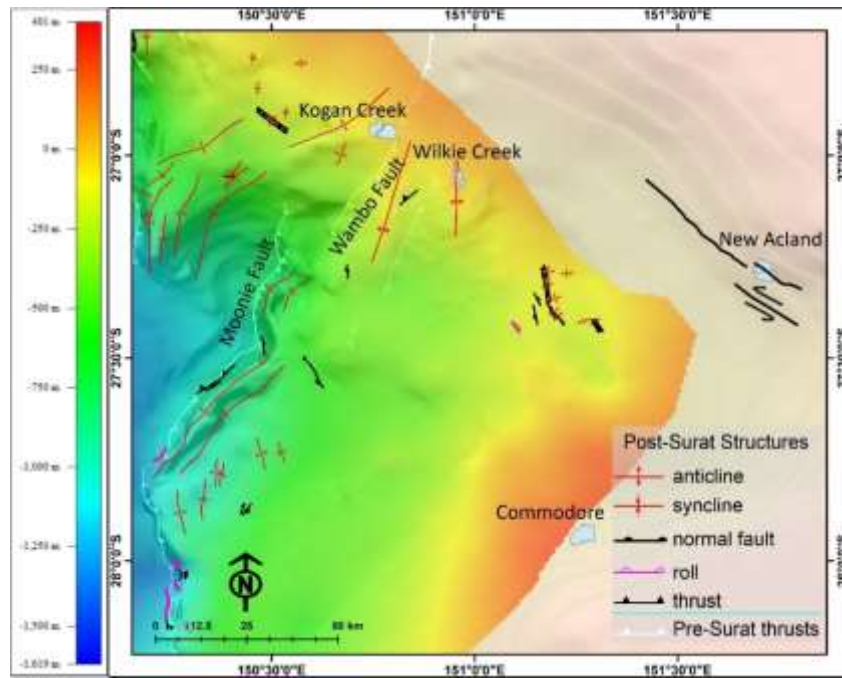


Figure 6.2 A map showing the faults and folds and the location of mine sites in the SE Surat Basin. The base map is the Phanerozoic SEEBASE map showing the burial depth to the Basement (FrogTech, 2006) which underlies the gridded image of the top of the Durabilla Formation. Faults and folds interpreted by Babaahmadi et al., 2015.

6.4 Methods

In this study, we investigated the geometry and development of the joint systems in various mine sites by using the 3D photogrammetry images, 2D photos, and some field measurements along with some datasets from previous studies. High-wall photogrammetric images for building a three-dimensional model were collected by using a process involving two camera locations which were both focused on the same object on the high-wall face. The procedure included taking a series of images from each position; locating positions by using the GPS coordinates; and setting a series of control points. The spatially referenced images have been produced in photogrammetric modelling software and can create 3D images that were used to trial for joint characterisation.

Figure 6.3 shows the 3D photogrammetric data from one of the sites including a series of long (10-15 m) to medium resolution stereo-pairs of the high-wall. The 3D modelling software, Sirovision™ and I-Site™, were used in extracting the orientation of joint sets. The extracted orientations of joint sets were used in making the rose diagrams and studying the relationship between lithological bedding thickness and joint spacing. For those locations where we have no 3D images, high-resolution photos were used to measure the lithological bedding thickness and joint spacing. Azimuth and spacing information for coal seams and clastic units (sandstone, siltstone and mudstone) were assembled in a spreadsheet file to cross plot the joint spacing and bedding thickness and to produce rose diagrams for joint azimuths.

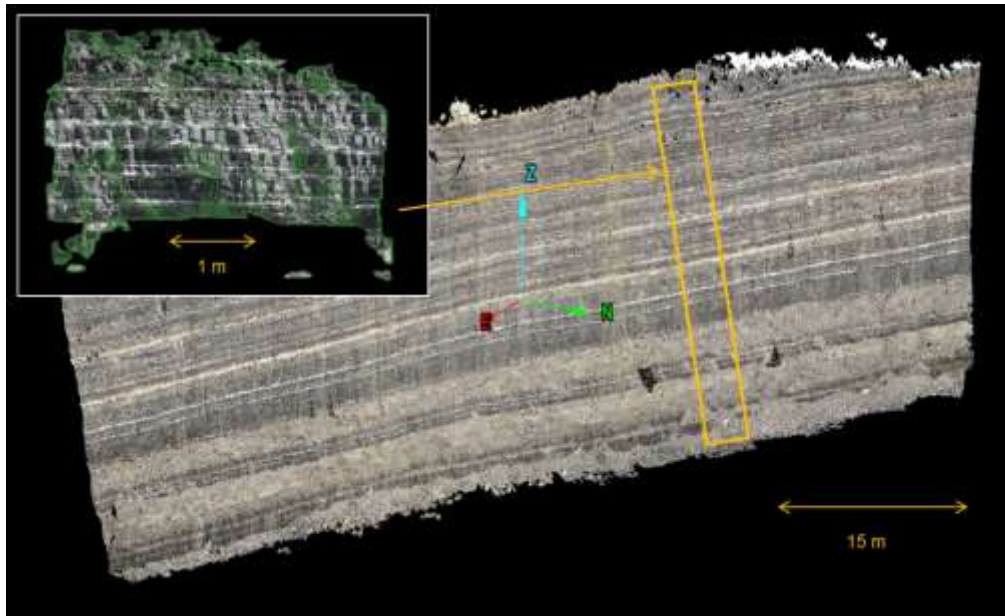


Figure 6.3 An example of a spatially registered photogrammetric model of a highwall is used for analysis of joints. Inset higher resolution photo was taken along the strip outlined in yellow. The joints were marked as green planes in the insert figure to show the joint spacing along one orientation (Rudd, 2016). Note that this highwall is not necessarily representative of all highwalls and seams.

6.5 Results

To determine whether there is any inheritance or reactivation of feature from the basement (pre-Surat and older rocks), the study locations were also plotted overlay the basement features (Figure 6.4). From the basement structural point of view, these mines are located above the hinge zone of a Permian orogenic-scale mega-fold referred to as the Texas Orocline. The Orocline is characterised by steeply dipped NW- and NE-striking foliations in the eastern and western limbs, respectively (Li et al., 2012). A recent study revealed that a series of NW- and NE- striking faults and magnetic lineaments are oriented parallel to the structural fabrics of the Texas Orocline (Babaahmadi and Rosenbaum, 2015) (Figure 6.4). Babaahmadi and Rosenbaum also observed reactivation of these Orocline paralleled faults, with strike-slip separation during the Mesozoic and Cenozoic. In theory, those to the east should show extensional structures, and those to the west, along the Moonie and Wambo faults, should show compressional features. In general, most of the faulting observable in New Acland are normal faults, albeit with some strike slip implications, whereas those observable in Kogan and Wilkie Creek were small scale thrusts.

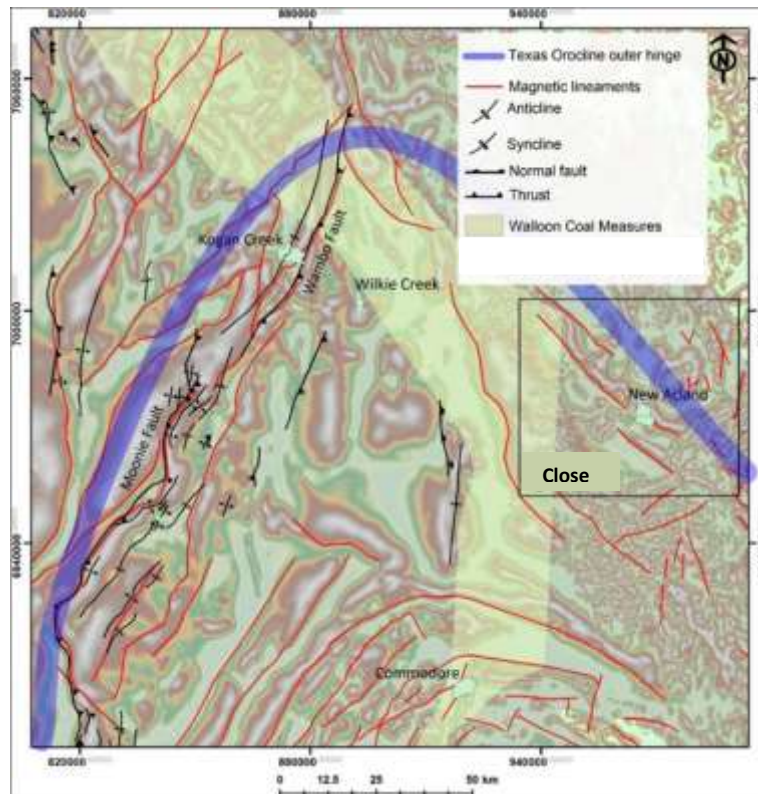


Figure 6.4 NW- and NE-striking faults and lineaments parallel to eastern and western limbs of the Texas Orocline, respectively (Babaahmadi and Rosenbaum, 2015).

6.5.1 Observations

Based on registering locations, the New Acland Coal Mine is located in the north-western part of the Clarence Moreton Basin between the two NW-striking lineaments which are parallel to the eastern limb of the Texas Orocline (Figure 6.4). The southern lineament has been interpreted as a sinistral strike-slip fault with a possible dipping slip as it is interpreted to laterally deflect the Cenozoic basalts (Babaahmadi and Rosenbaum, 2015) although other meanders in the basalt can also reflect palaeodrainage.

Several faults with different orientations have been mapped within and around the mine (Figure 6.5). The faults strike to the NW, ENE, and N, producing a quadri-modal fault system. Most faults in this mine are normal but some small scale faults (less than the coal seam height) are reverse faults. The throws of those normal fault range from 5 to 10m with a maximum of 45m and there were used to develop relationships between length and throw for the Discrete Fracture Network Model (DFN). Some small scale reverse faults were also observed around the mine (Figure 6.6).

A series of steep faults are also observed in a highwall. These faults are associated with the normal offset in the lower part, the compressional folds, and the small scale reverse faults between two fault segments in the upper part. In Figure 6.7, the main faults are the two strike-slip normal faults producing an overlap in which a small restraining step-over/ bend zone; some reverse faults and folds were developed. These are often referred to as “keystone” features.

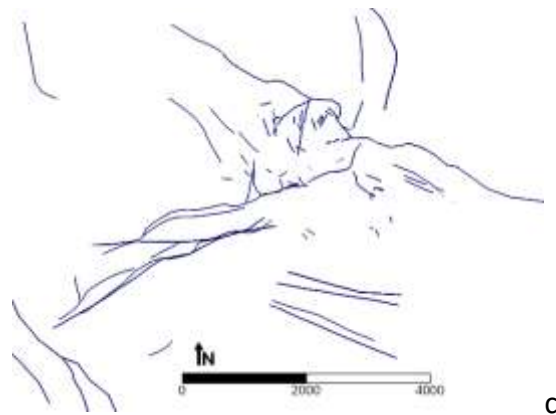
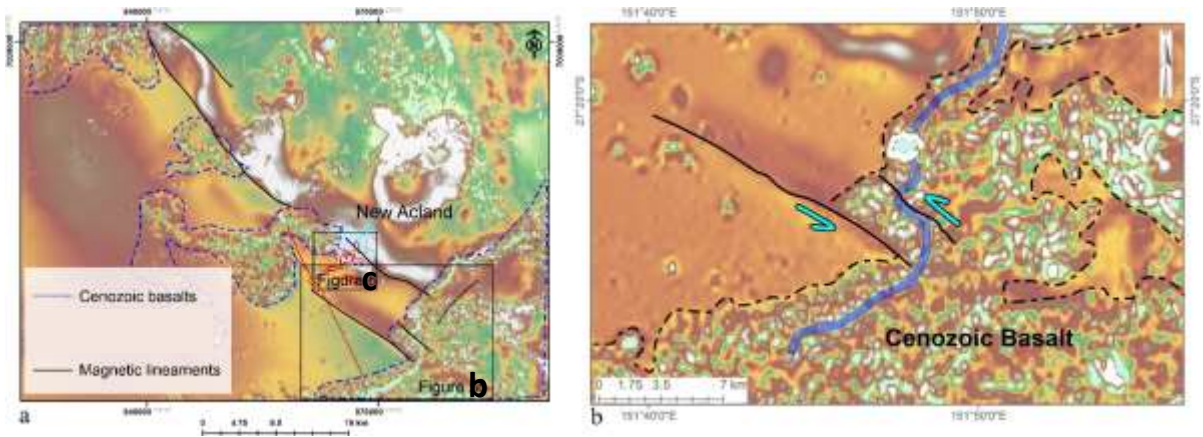


Figure 6.5 (a) A map shows the location of the New Acland Mine and the faults are interpreted as sinistral strike-slip. The background image is the first vertical derivative of aeromagnetic data showing the magnetic lineaments and the shallow Cenozoic volcanic rocks. (b) The southern lineament which is interpreted as a fault displacing Cenozoic basalts and a basaltic lava flow (Babaahmadi and Rosenbaum, 2015). (c) Faults provided by company geologists, illustrating the general orientation of and distance between the normal faults as mapped.



Figure 6.6 Example of a small scale thrust fault with a throw of about 1.5m forming kink band. The strike orientation of the high angle reverse fault is ESE.

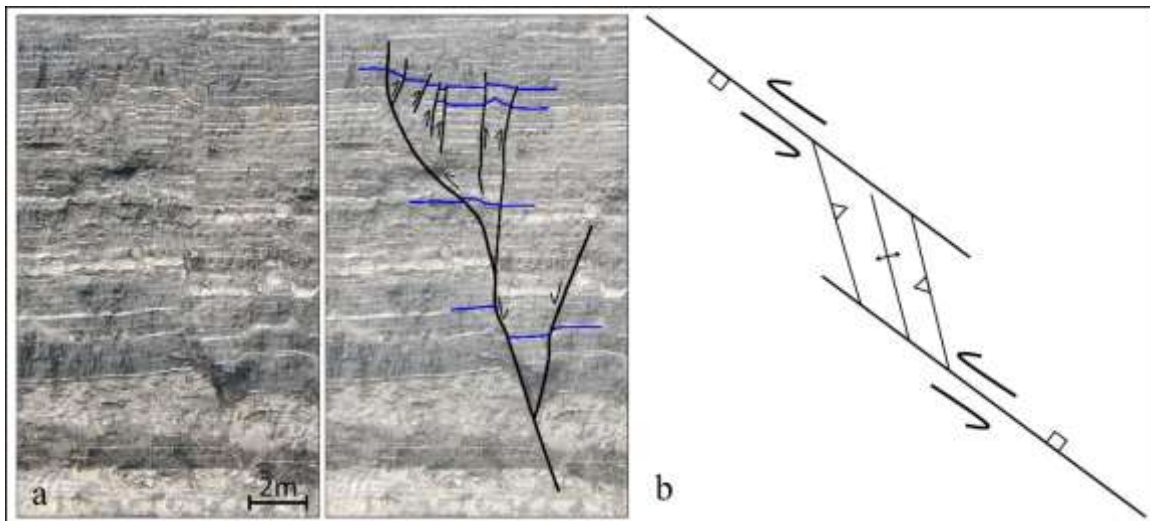


Figure 6.7. Examples of faulting in the coal measures. (a) Strike-slip normal faults. The overlap between two faults produced a restraining step-over zone, producing small reverse faults and folds in the upper part. The photo view is toward ESE. (b) A schematic map - view cartoon of a restraining step-over zone between two strike-slip normal faults, thought to be a mechanism for fault formation.

Analyses were performed from stereo-image pairs from a relatively wide section (Figure 6.8 and Figure 6.9). The stratigraphy ranges from the D8 Seam to the C3 Seam (Figure 6.8) that are plies equivalent to the Taroom Coal Measures. More than 1600 joint spacing measurements were obtained from a total lateral length of 40m along the wall. Note that the

bed thickness of the coal and partings is variable and a “thinning upward sequence” is observed from bottom to the top of the seams. This sequence allowed one to test the hypothesis that the coal joint spacing was directly related to the bed thickness.

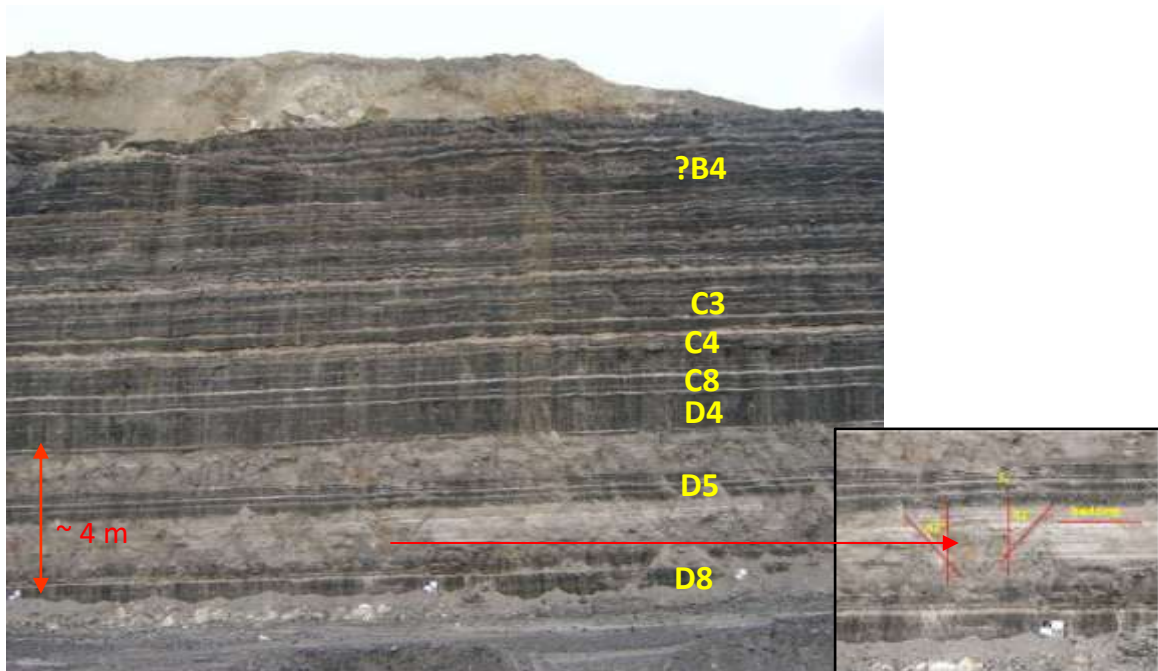


Figure 6.8 The highwall for photogrammetric survey (March 2016). The photo was taken approximately 30m away from the highwall face. The basal seam that is exposed in the foreground is the D8 Seam; black and white sheets of an A3 card (42 x 30 cm) were put at the base of the highwall. The inset figure shows the inclined joints in sandstone.

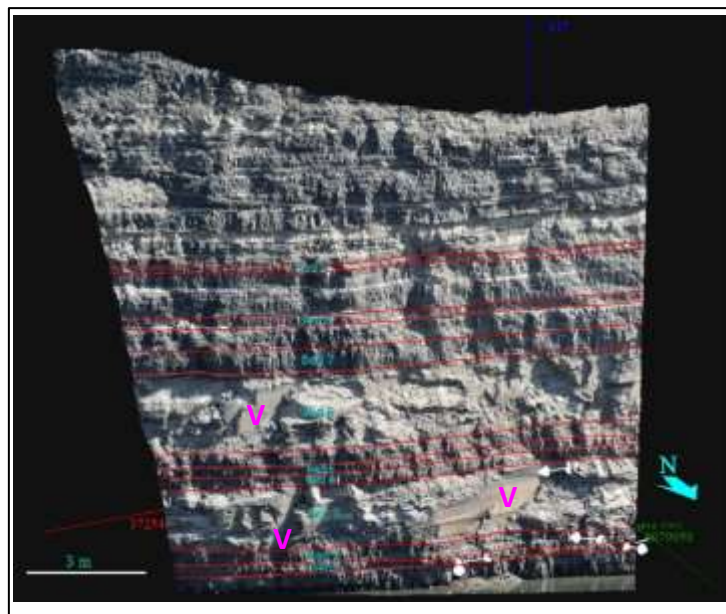


Figure 6.9 Example of a stereo-image pair was used to measure the thickness of joint and lithological bedding, and joint azimuths. Bedding boundaries are indicated by red lines. Large vertical joints were also observed in sandstone (marked by the V) as were inclined joints. These joints penetrate multiple horizons and were excluded from the test of joint spacing against bed thickness.

The strike values for the two major penetrative vertical joint sets, one along ~NNW-SSE (AZ 165) and the other along ~E-W (AZ 085), have been determined in the New Acland Mine; they are about 10 degrees from orthogonal (Figure 6.10). Similar strike azimuths were obtained from vertical joints in the sandstone units between the Seams D4-D5 and D5-D6 (location is shown in Figure 6.8). These measurements are valid for the sampled pit.

Inclined joints from the sandstone units exhibit a NNE azimuth (average AZ018) (Figure 6.10). Inclined joints are not widely distributed as vertical joints.

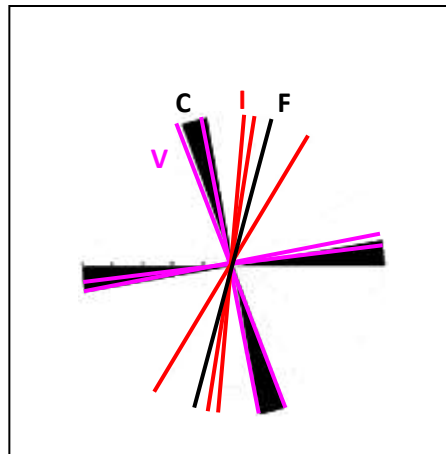


Figure 6.10 Vertical joint azimuths from the coal-clastic units (photogrammetry; azimuthal range; black, "C"), vertical joints (compass line of sight; single line; pink, "V"), inclined joints (compass line of sight; single line; red, "I"), floor shale (compass on pavement, single line, black, "F").

6.5.2 Joint spacing vs bed thickness

The analyses show that joint spacing widens with the increase of bed thickness in different lithological units (Figure 6.11 and Figure 6.12). Although considered an elementary finding, the relationship and its application to predicting joint density in coal and jointed rock masses for input to permeability or geotechnical models is underutilised. The NNW-striking joints in both coal and clastic units are more widely spaced than those with an E-W trend. The spacing of NNW-striking coal joints is on average about 20 cm larger than the E-W coal joints.

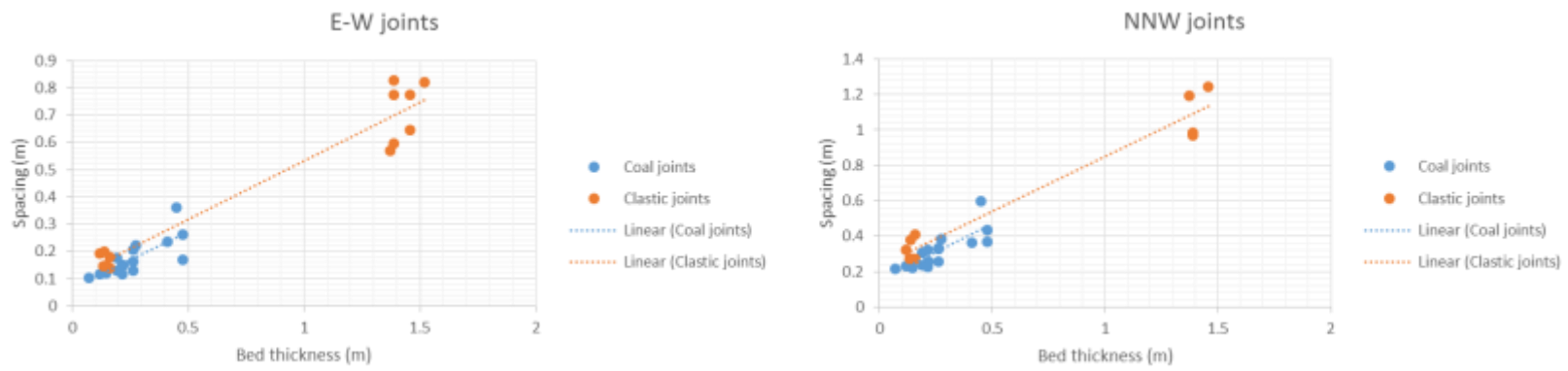


Figure 6.11 The relationship between the bed thickness and joint spacing measured from 4 photogrammetric stereo pairs.

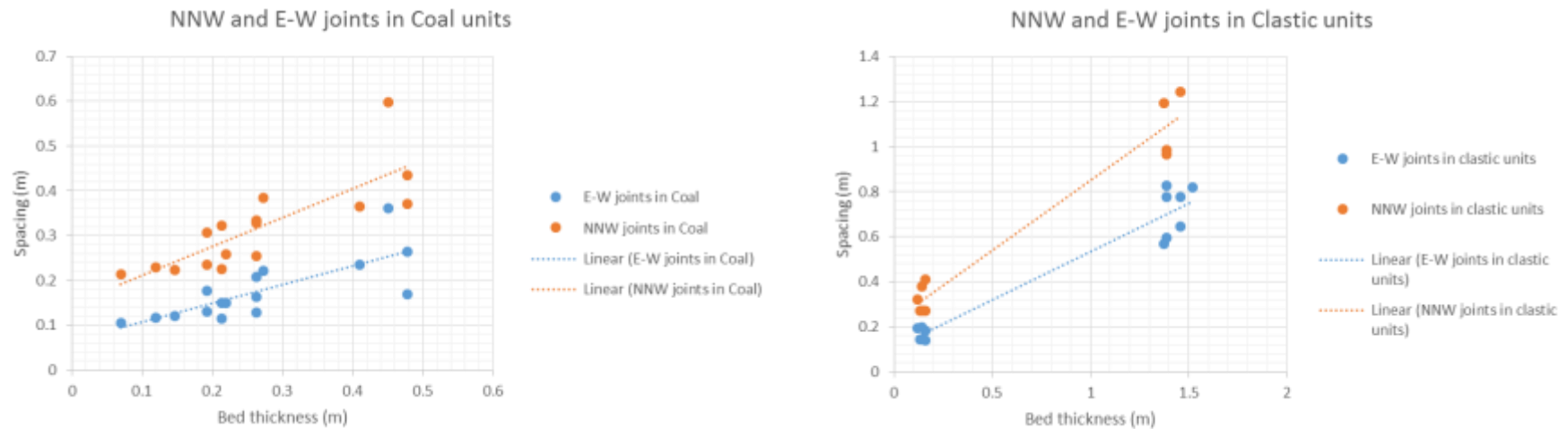


Figure 6.12 Comparison of coal joints and clastic joints measured from 4 photogrammetric stereo pairs.

The Wilkie Creek Mine is located on the crest of a gentle north-striking anticline (Figure 6.13 and Figure 6.14). This anticline is located to the east of the major Wambo Fault that strikes NE and has components of reverse and strike-slip. The lithology at the Wilkie Creek Mine includes sandstone, coal and tuff. Some reverse faults have also been observed in the eastern area of the mine, on both the western and eastern limbs of the anticline. A series of joints were measured in this mine, striking approximately N-S, NE-SW, and NW-SE (Figure 6.14). Since there are no high quality photogrammetric images for this mine, some high-resolution 2D photos were used for analysing the relationship between the joint spacing and lithological bedding thickness in coal seams. Joint spacing increases with the increase of bed thickness (Figure 6.15).

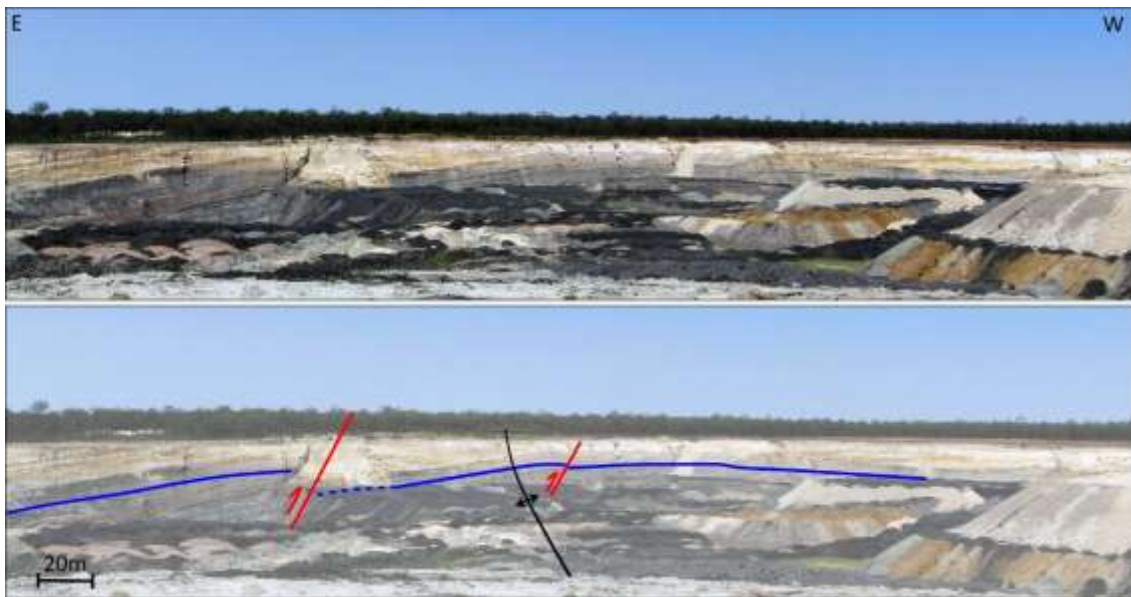


Figure 6.13 A north-striking gentle anticline in the Wilkie Creek Mine deformed the Walloon Coal Measures and Springbok Sandstone. This anticline is disrupted by two small thrusts.

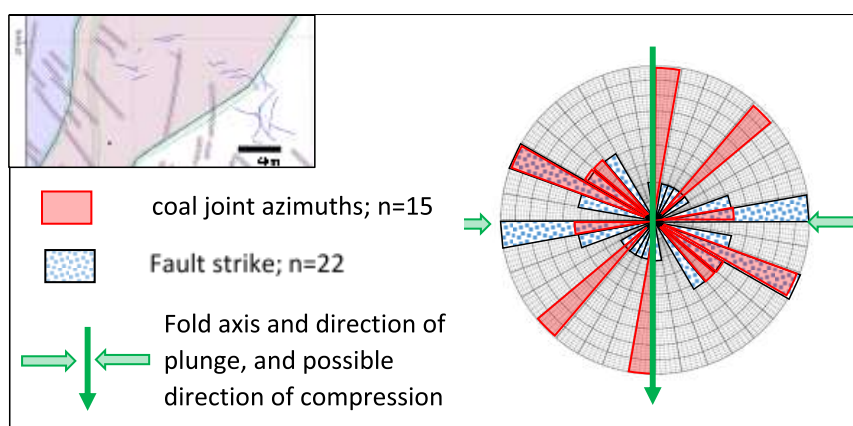


Figure 6.14 Comparison of coal joint, surface fault and fold azimuths at the Wilkie Creek Mine. Inset shows surface faults (blue lines) and faults in basement- (hatched). The mine did not disclose the style and throw of these faults.

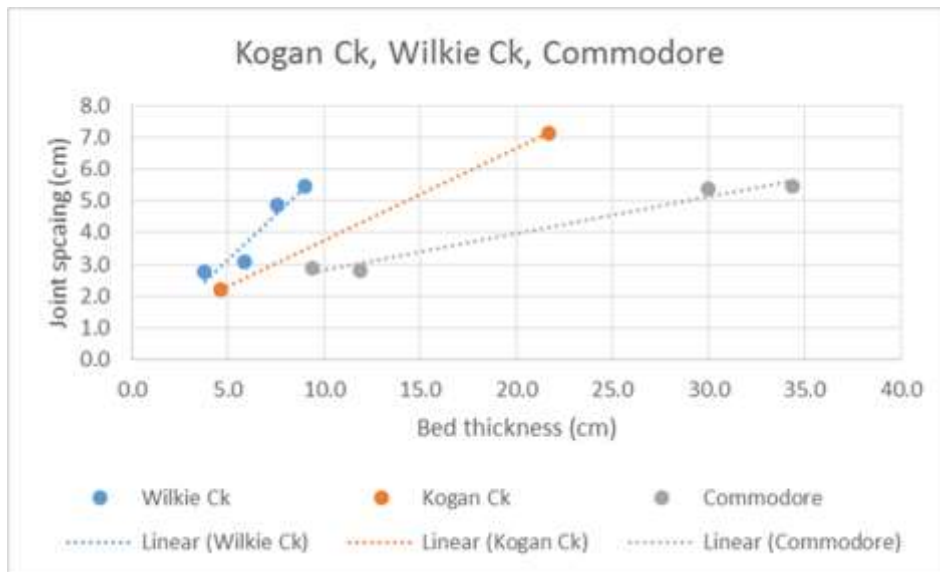


Figure 6.15 A scatter plot showing the joint spacing against bed thickness for two joint sets through the analysis of high resolution 2D small scale photos from the Kogan Creek, Wilkie Creek, and Commodore Mines.

The Kogan Creek Mine is also located near the NE-striking Wambo Fault (Figure 6.2). The lithology includes coal seam, sandstone, mudstone, and tuff. A series of reverse faults have been observed in the Kogan Creek Mine (Figure 6.17 and Figure 6.18), which are interpreted to be subsidiary faults associated with the Wambo Fault. Two dominant joint sets, striking NW-SE and NE-SW, are observed in coal in the Kogan Creek Mine (Figure 6.16). Analyses of bed thickness and joint spacing from some high-resolution 2D photos indicate that joint spacing increases with respect to the increase of bed thickness (Figure 6.15).

Figure 6.18 shows one of the thrust faults associated with a hanging-wall anticline and the development of conjugate joints in the crest of the anticline in the Kogan creek Mine.

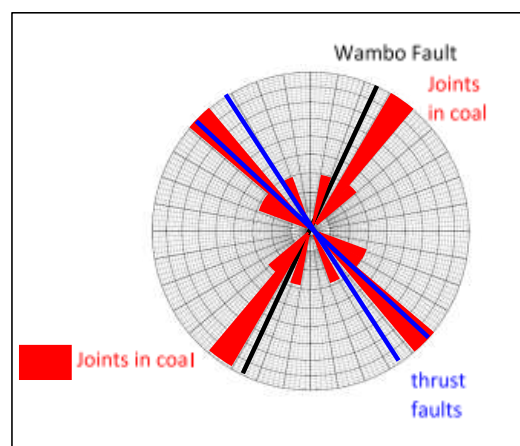


Figure 6.16 Azimuths of joints in coal and thrust faults from the Kogan Creek Mine. The azimuth of the Wambo Fault is also shown for comparison.



Figure 6.17 A map shows the observed thrust faults in the Kogan Creek Mine. Faults 1 and 2 have approximately strike azimuths of 147 and 135, respectively.

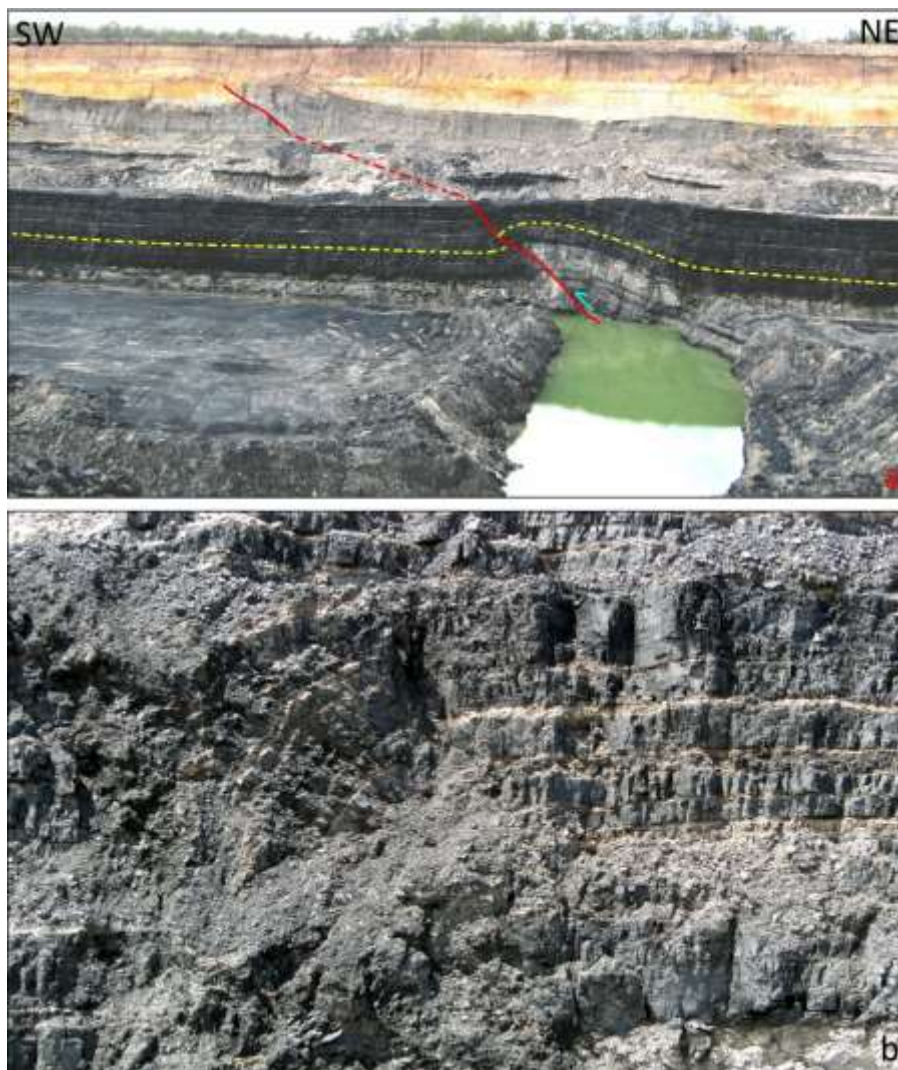


Figure 6.18 (a) One of the thrust faults associated with a hanging-wall anticline in the Kogan creek mine. (b) The development of conjugate joints in the crest of the anticline.

The Commodore Mine is located about 80km SSW of the New Acland Mine (see Figure 6.2 for the location). Two sets of joints are observed in coal seams with orientations of N-S and WNW-ESE. A NW-SE trending joint in shale units has a 23° right rotation from one of the major coal joint azimuths (Figure 6.19). As shown in Figure 6.15, the joint spacing increases with respect to the increase of bed thickness based on the measurements from some high-resolution 2D photos.

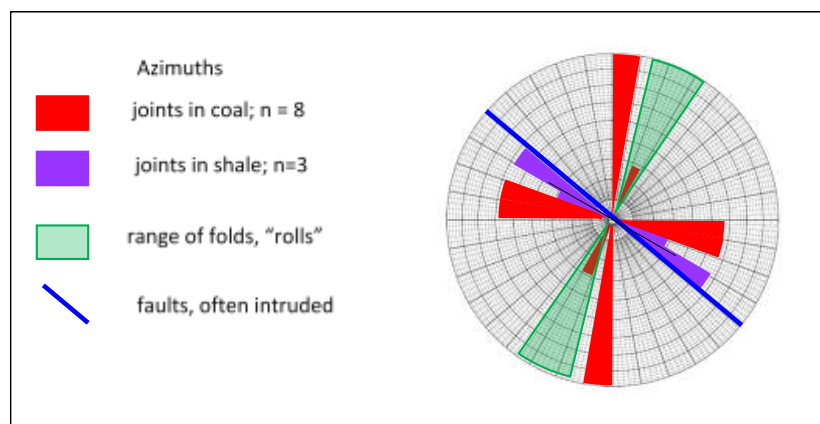


Figure 6.19 Azimuths of joints in coal and shale, faults (and dykes that have intruded faults), and folds/rolls, Commodore Mine.

6.6 Discussion and Conclusions

6.6.1 Origin of Joints

Various joint sets with different orientations are observed in the Surat and northern Clarence-Moreton basins. The origin of these joint sets is not well constrained. Our field observations indicate that they are propagated near to normal, reverse, or strike-slip fault zones or are associated with folds, which deformed the stratigraphic units of the Surat and Clarence-Moreton basins. Therefore, we suggest that the development of joint sets in the Mesozoic basins could be in response to the activity of local faults and folds.

6.6.2 Joints Associated with Faults

Joints are extensional features that should develop parallel to maximum horizontal stress (S_{Hmax}) and the strike of normal faults. In the studied high-wall in the different mines, E- and NNW-striking joints are almost parallel (~10° angle) to ENE- and N-striking faults (faults 1 and 2), respectively (Figure 6.20). One suggestion for the subtle angle of joints relative to the faults is that joints could develop in response to perturbed local stresses within the overlap zone of faults. In fact, the movement of the faults in the overlap zones results in the perturbation of local stress fields and gives rise to the development of various joints at higher angle to the strike of normal faults (Kattenhorn et al., 2000).

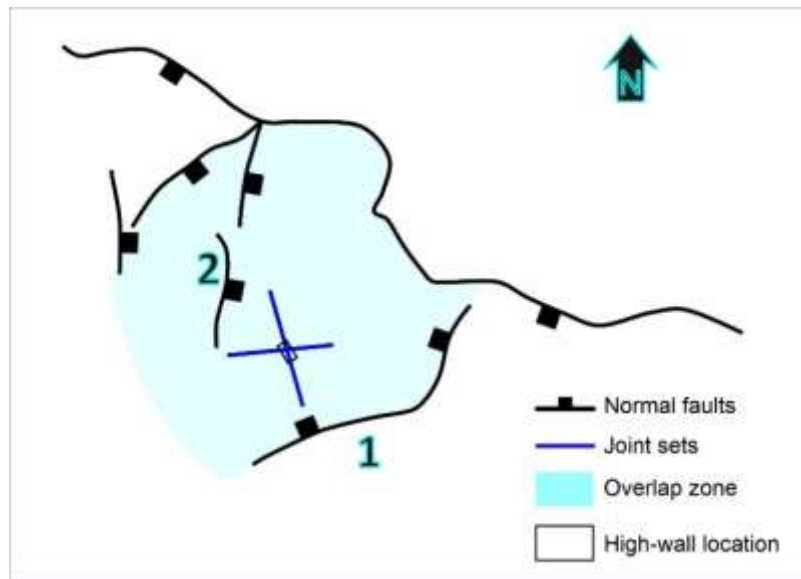


Figure 6.20 A schematic model (map view) showing the development of joints in the overlap zone of the two ENE-, N- and NW-striking normal faults.

6.6.3 Joints Associated with Folds

Local gentle folds which deformed the Jurassic units of the Surat Basin are suggested to play an important role in the development of joint systems in different mine sites. Folds associated joints are usually in three sets at different parts of the fold as shown in Figure 6.21: (1) joints parallel to the fold axis; (2) joints perpendicular to fold axis; and (3) conjugate joints oblique to fold axis.

In the Wilkie Creek and Commodore Mines, three above-mentioned sets of joints developed along with gentle anticlines. In the studied high-wall from the Kogan Creek Mine, NW- and NE-joints propagated within a zone of hanging-wall anticlines associated with NNW-striking reverse faults. We interpret NW- and NE-striking joints to be parallel and oblique to fold axes, respectively.

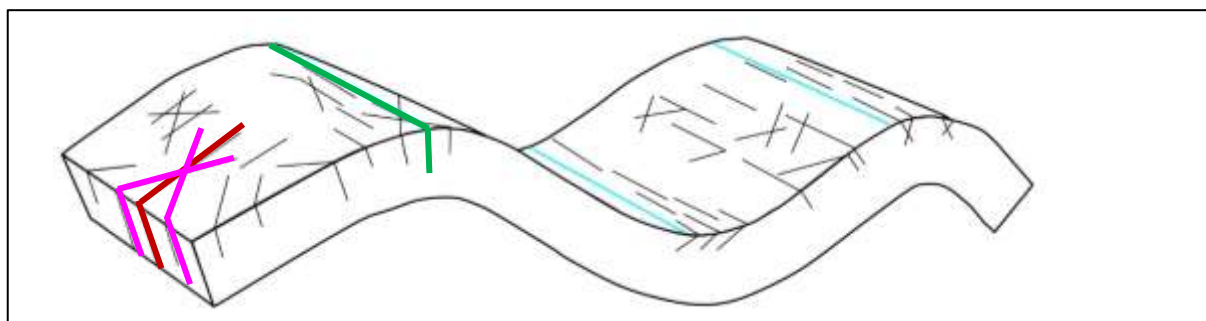


Figure 6.21 3D representation of various joints that form in folded strata (based on Twiss and Moores, 2007). Brown = cross joints (equivalent to face cleat), green = longitudinal joints, pink – diagonal joints.

6.6.4 Timing of Jointing

The timing of joints are not well constrained, but the fact that these structures are associated with post-depositional faults and folds can provide some indirect constraints. Recent studies provided constraints on Late Cretaceous-Cenozoic deformation in southeast Queensland (Babaahmadi and Rosenbaum, 2014a, b, 2015). The occurrence of normal faults are

interpreted to be related to either the Late Cretaceous-early Eocene extensional phases or to be subsidiary faults associated with the reactivation of major basement strike-slip faults during the middle to late Cenozoic (Babaahmadi and Rosenbaum, 2014b). In contrast, the contractional structures could occur in response to far-field stresses from collisional events at the eastern margins of the Australian Plate since the middle Cenozoic (Babaahmadi and Rosenbaum, 2014a). Thus, the formation of joint sets are suggested to be related to the Cretaceous-Cenozoic deformation phases along with the local compressional and extensional structures.

6.6.5 Bed Thickness vs. Joint Spacing

Our analyses of joint sets in all mine sites show that joint spacing increases with the increase of bed thickness. Detailed analyses of 3D photogrammetry data show that the NNW-striking joints in both coal and clastic units are more widely spaced than those with an E-W strike. Within various lithological units with similar thicknesses, joint spacing in coal seams is less than that in the jointed clastic rocks such as mudstone and sandstone. Therefore, rheology plays an important role in the developments of joints. This relationship will be explored as an input in DFN modelling.

6.7 Acknowledgements

The authors sincerely thank New Hope Group, Peabody, Yancoal, and CS Energy for giving us permissions to access the mine sites and to produce this report. We also acknowledge the Australian Coal Association Research Program and the UQ Centre for Coal Seam Gas for financial support. We thank Robert Rudd for access to his thesis data and images.

7 Discrete fracture network model - an approach

7.1 Introduction

The work presented here is edited from Zhou et al., 2016. Fracture prediction at the borehole and spatial distribution across any reservoir are crucial inputs for evaluation and development of a fractured reservoir (Nelson, 2001). It is difficult to characterise fractures properly because of their heterogeneity and complexity (Boro et al., 2014; Wennberg et al., 2016) especially in coal measures (Pashin et al., 2008). Geologists and engineers use different types of data to describe the fractures at different scales; e.g. seismic attributes, dip (Rijks and Jauffred, 1991), similarity, curvature (Basir et al., 2013), variance (Nasseri et al., 2015), chaos and ant tracking (Silva et al., 2005; Basir et al., 2013; Ngeri et al., 2015; Baytok et al., 2013). However, seismic survey cannot identify small-scale fractures at the borehole because of the resolution restriction of seismic data volume (Liu et al., 2015). Therefore, small-scale fractures are described by observations in cores, image logs (Lefranc et al., 2012; Weatherford, 2013; Schlumberger, 2013) and geophysical logging interpretation (Al-Anazi and Babadagli, 2010; Tokhmchi et al., 2010; Zazoun, 2013), or in outcrops by manual methods (Darcel et al., 2006) or aided by photogrammetric data (Poropat, 2001; CSIRO, 2011; Bonilla-Sierra et al., 2015).

Image log interpretation (Schlumberger, 2013; Weatherford, 2013) is used to detect and evaluate the fracture intensity and orientation. These can then provide input to mathematical

models to predict in areas of sparse data (Jafari et al., 2012). When coupled with dynamic production data, fracture density can assist in modelling the link with permeability (Al-Anazi and Babadagli, 2010). Coal as a fractured reservoir presents challenges as the fracture or cleat network varies by layer or lithotypes in terms of its spacing, height and aperture in addition to orientation (Laubach, et al., 1998; Dawson and Esterle, 2011, among others). CT and Micro CT scanning provide a means to characterise the coal fracture networks in 3 dimensions from (Mazumder et al., 2006).

The dilemma of scale is commonly approached by using a Discrete Fracture Network (DFN) model. DFN models are computer simulations of fractures at different scales created by statistical properties of natural or induced fractures (Pashin et al., 2008). Each fracture is represented in the model by a plane with specific parameters such as dip angle, dip azimuth and aperture, etc. Scalar properties such as spacing, height, length, and stratigraphic penetration are predicted, often on analogue data from outcrop where available. The fracture model built by DFN approximates the real fracture distribution in formation (Pedersen et al., 2003; Pointe, 2004) and is used to model coal geomechanics and reservoir performance (Deisman et al., 2008; Gao et al., 2014b).

In this report, we developed workflows to build a DFN for joints and a cleat distribution model. Three data sets were used: image log interpreted fractures from Dalwogan 2 and cleats from well D; cleats from the well completion report of boreholes A (Gilbert Gully 2), B (Halliford 2), and C (Hopeland 2) which were shown in Section 5; and minescale faults and fracture information (fault polygon, joint spacing and orientation) from a mine (Babaahmadi et al., 2016) in the Surat-Clarence Moreton basin. We built three DFN models using the following data.

- Field scale joint model: In an area of 67 km² with 69 faults, seam structure and thickness from 414 borehole correlations and one borehole wireline log set were provided by a company and used to create a structure framework. Grid cells based on bedding extracted from the wireline log were populated by fracture sets obtained from a direct relationship between bed thickness and joint spacing for coal and clastic rocks observed in highwall. This relationship is used in DFN modelling near a borehole.
- Borehole joint model: Fracture sets were interpreted from the image log from Dalwogan 2 well and used to build a DFN model near the well.
- Borehole cleats model: A cleats distribution model based on image log interpreted cleats and coal core observed cleat spacing data was built by using multiple-point statistics method.

Three highlights from this study are:

- The workflow and application of multiple-point statistics to simulate cleat distributions using a training image obtained from core observed cleat spacing is a new method;
- We built DFN model based on a relationship between coal bed thickness and joint spacing from minescale data;

- The DFN model from Dalwogan 2 was used in DST analysis by an in-house numerical simulator. Numerical simulation results show that the simulated pressure based on DFN model near well Dalwogan 2 matches better with the measured pressure by DST.

7.2 Methods and Results for the field scale DFN

The field scale model built from the minescale data has an area about 67 km² (Figure 7.1). The target seam across this area is displaced by a series of mostly normal faults that range from less than a 1m up to 45m throw. Small scale reverse faults also exist with throws on the order of metres and of short (unmappable) strike length. Evidence for strike slip movement on the bounding fault and smaller faults in the area has been observed. The faults database provided by the mine allowed some 69 mapped faults with different throws and strike length to be used for analysis. A wireline log was used to subdivide the stratigraphy into 34 coal beds that could also be identified in the highwall (Figure 7.1c). Highwall photogrammetry was used to measure the joint spacing and heights (Rudd, 2016 and Babaahmadi et al., 2016). These data were used to develop a DFN.

The density distribution of fractures with respect to a parameter can be defined as:

$$n_{3d}(l) = a \cdot l^{-b} \quad (\text{Eq. 6.1})$$

Where a is the scale parameter and b is the dimension (shape factor).

Figure 7.2 shows the density distribution of fracture diameters, illustrated on a log-log diagram. Figure 7.2a from Darcel et al. (2006) and Figure 7.2 b is the length distribution of the 69 faults from the mine data set.

Fracture length and height are important for fluid flow. Figure 7.3 shows the two 2D fracture models that were generated with different shape (b) and scale parameters (a); one with C=2 shows very isolated fractures but the other one with C=6 shows a very good connectivity between fractures which leads to high permeability values.

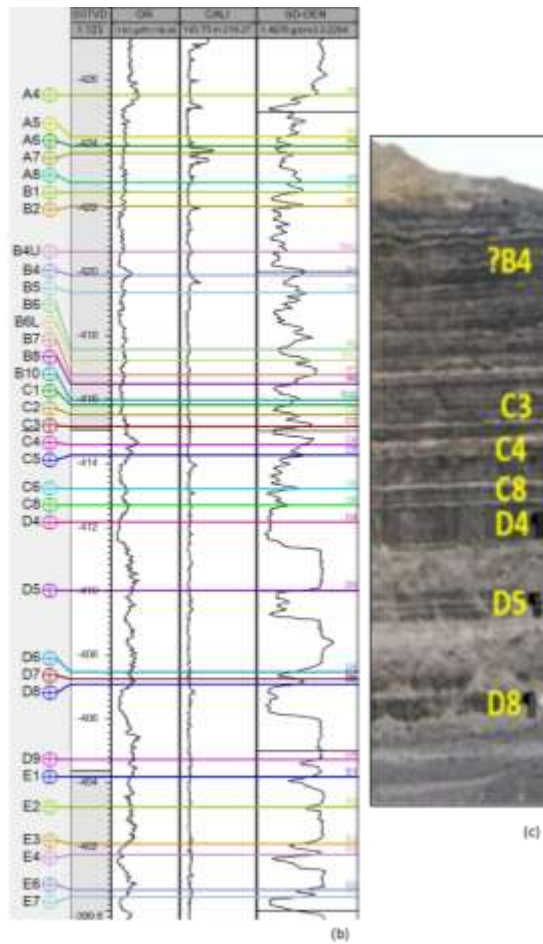


Figure 7.1 Wireline log example and well markers at a borehole near a photo showing the coal beds from a highwall. GR is Gamma ray; CALI is caliper; and SD-DEN is shallow depth density. B, C, D, and E are coal seam name and numbers are ply or coal bed number.

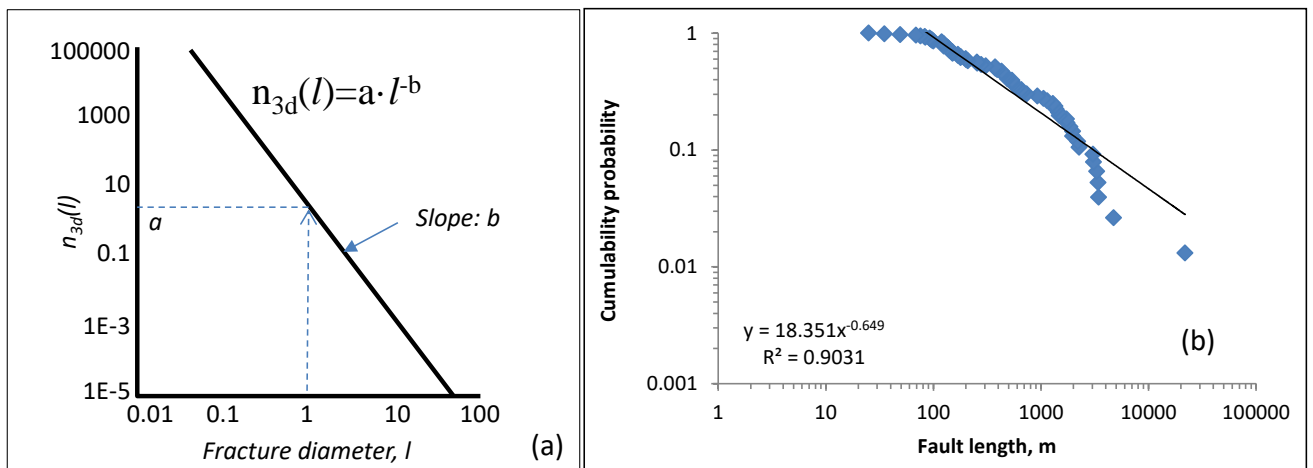


Figure 7.2. Density distribution of fracture diameters, illustration on a log-log diagram. (a) from Darcel et al. (2006); (b) length distribution of 69 faults from the mine.

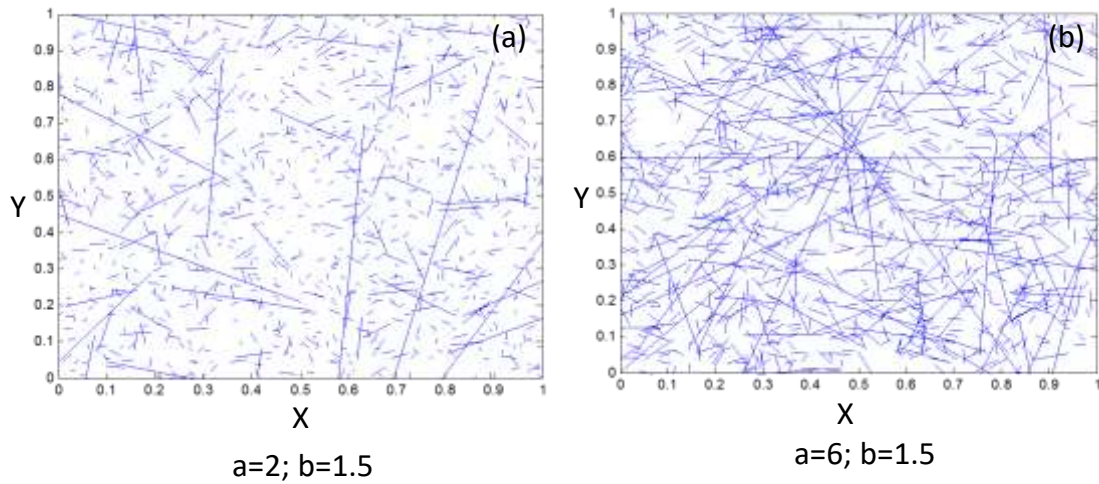


Figure 7.3 Comparison of fracture distribution with different scale and dimension parameters.

To build a discrete fracture model, the following information is needed:

Fracture density: includes P30 (fracture count per volume), P31 (fracture length per volume) and P32 (fracture area per volume). Density distribution can be as (a) grid based property or (b) surface or (c) constant value. To build joints in coal seams, we convert spacing to density using the following equation as input to the modelling package.

$$P32 \approx \frac{1}{S} \quad (\text{Eq. 6.2})$$

Where P32 is the fracture area per volume; S is the joint spacing. Figure 7.4 shows that the joint spacing increases with the increase of bed thickness in different lithological units; the NNW-striking joints in both coal and clastic units are more widely spaced than those with an E-W trend; the spacing of NNW-striking coal joints is on average about 20cm larger than the E-W coal joints.

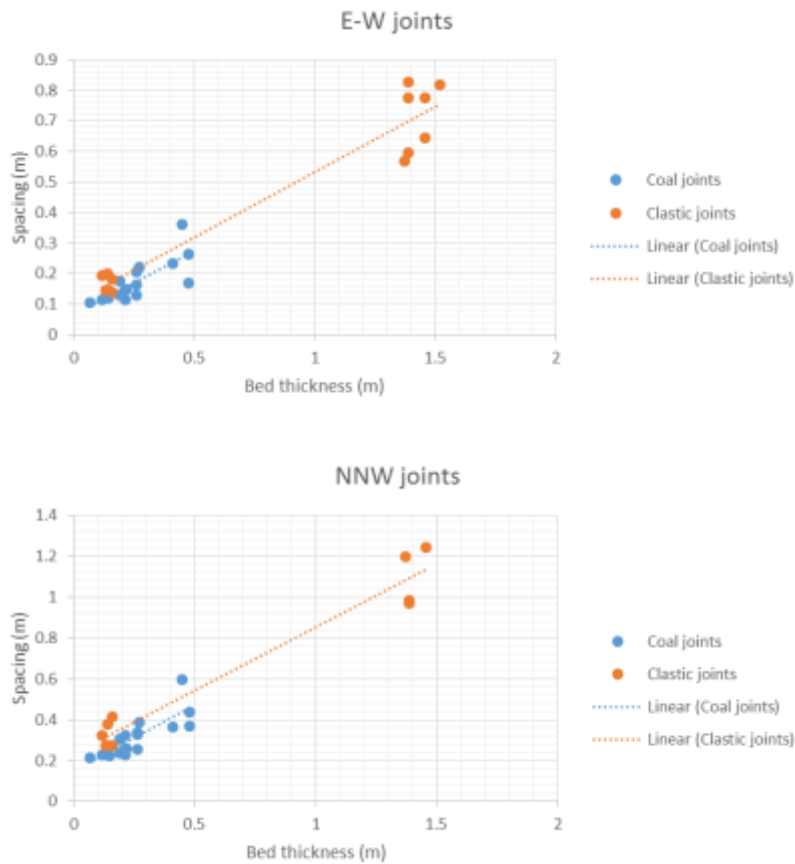
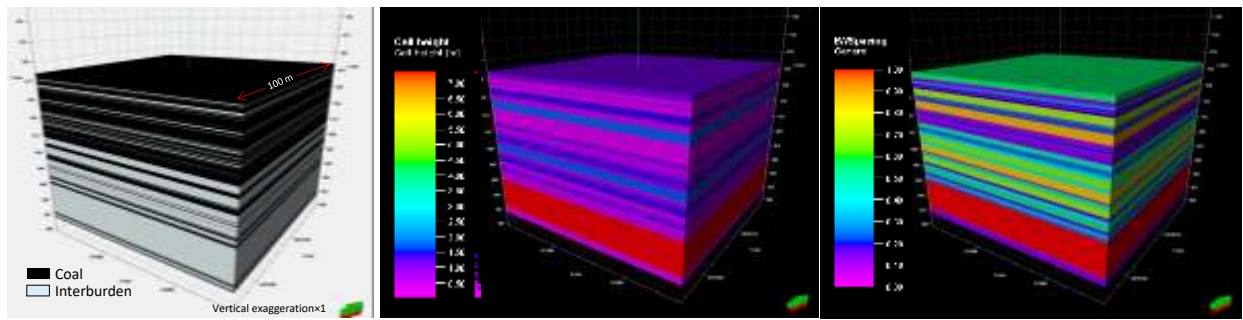


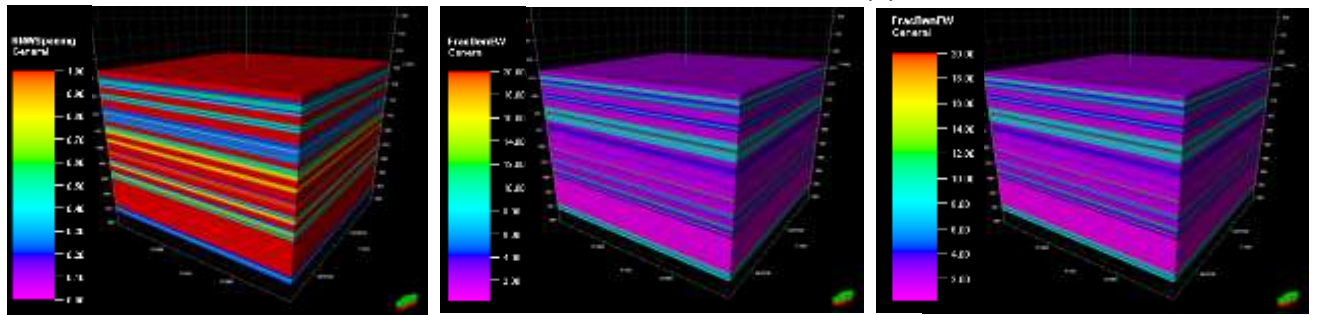
Figure 7.4 Joint spacing increases with the increase of bed thickness in different lithological units (Babaahmadi et al., 2016, report).

Figure 7.5 shows the geological model and generated properties in DFN modelling. We gridded a 100m by 100m area into 1 by 1m cells in the horizon; then we generated horizons (Figure 7.5a) at each coalbed's top and base based on the wireline log interpretation as shown in Figure 7.5b; then we generated a property as the coalbed thickness.

We generated properties as joint spacing at E-W and NNW-SSE directions (Figure 7.5c; d) based on the relationship shown in Figure 7.4. We accounted for the different spacings relative to joint orientation: the EW joints' spacings equal bed thickness and NNW ones are half of coal bed thickness. At last, we converted joint spacing properties to fracture density as shown in Figure 7.5e; f.



(a) Coalbed and interburden layers (b) Coalbed thickness (c) Joint spacing at E-W direction



(d) Joint spacing at NNW direction (e) Fracture density at E-W direction (f) Fracture density at NNW direction

Figure 7.5 Processing figures at each phase of generating the DFN near the borehole.

Fracture geometry: includes fracture shape, e.g. number of sides and length/width ratio, and fracture length. Fracture length is assumed as two times the bed thickness.

Fracture orientation: can be controlled by trends, e.g. 3D grids or surface map or by methods (Petrel, 2015), e.g. Fisher model, Bingham model or Kent model. Fisher model was used in this study, and Figure 7.6 shows two sets of joints in the mine; one along W-E direction and the other along NNW-SSE direction.

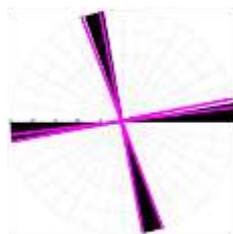


Figure 7.6 Rose diagram of the average orientations of two dominant joint sets in coal (black) and sandstone (pink) of the study area (Babaahmadi et al., 2016, report).

Fracture aperture: will be figured out by matching DST data.

Figure 7.7 shows the joints distribution for coalbeds from A4 to D8. Results follow the data in that thinner coalbeds have narrower joint spacing and higher joint density than thicker coalbeds and interburden partings.

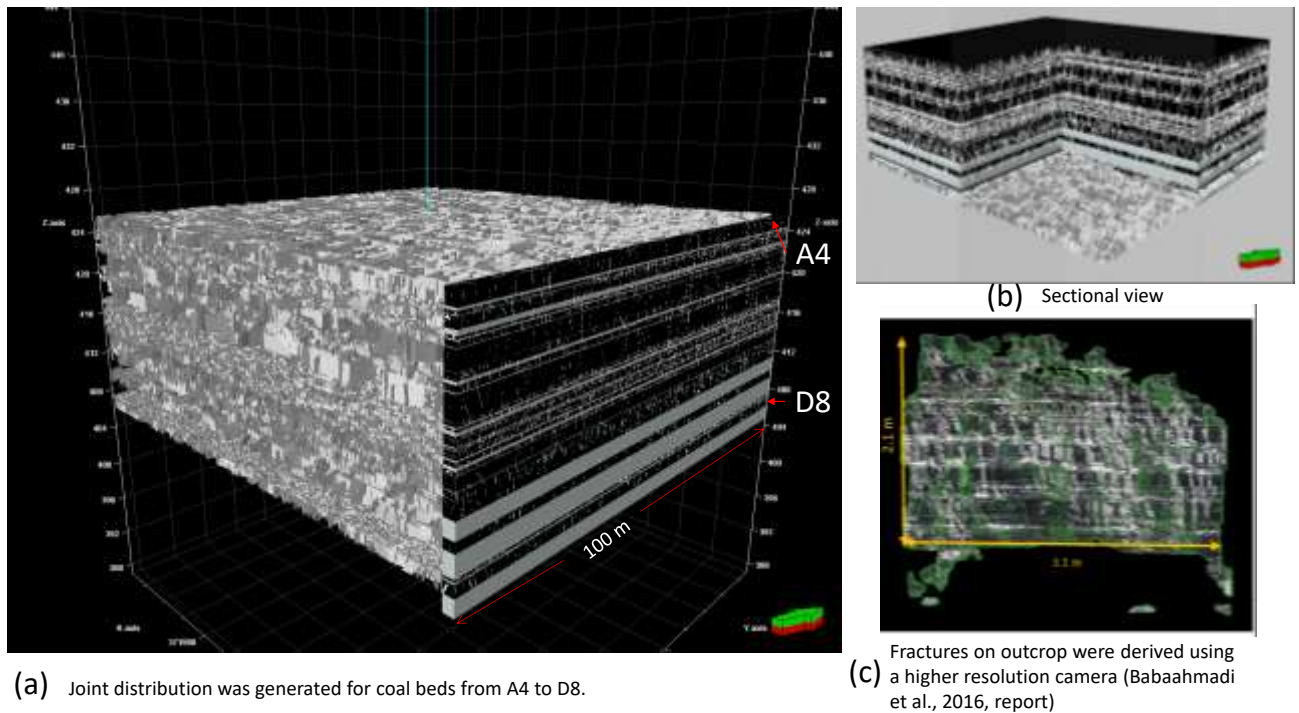


Figure 7.7 Joints distribution was generated for coal beds from A4 to D8. Results illustrate that thinner coal beds have narrower joint spacing and higher joint density than thicker coal beds and interburden partings.

7.3 Build DFN near well Dalwogan 2

Image logs were interpreted for fracture sets in 21 wells in the Surat Basin (Mukherjee et al., 2016). Table 2 lists all the image log interpreted fractures from 21 wells in the Surat Basin. In total, 919 fractures were interpreted. The number of conductive fractures is about half that of mixed fractures.

Figure 7.8 shows the interpreted DFN near wellbores. For visualisation, the fracture length is assumed as 500m and height as 50m.

Dalwogan 2 was tested for permeability in three coal seams by drill stem testing (DST); DST1 from 549.69 to 558 mGL; DST2 from 652.95-664.03 mGL; and DST3 from 814.99-825.01 mGL. Hence, this well was selected to build a DFN model which then is used for numerical simulation to history matching the DST data.

Figure 7.9 shows the geophysical logs (GR, Density), lithology, depositional facies, image log interpreted fractures (azimuth and dip angle), calculated fracture intensity (P32) and upscaled fracture density. As shown in this figure, fractures in coal seams normally have higher dip angle than those in non-coal interburden. Also, the dip azimuth of fractures in the coal seam is different from those in non-coal interburden. The image log also indicates that most fractures are limited in coal seams, where smaller scale cleats are prominent but not captured.

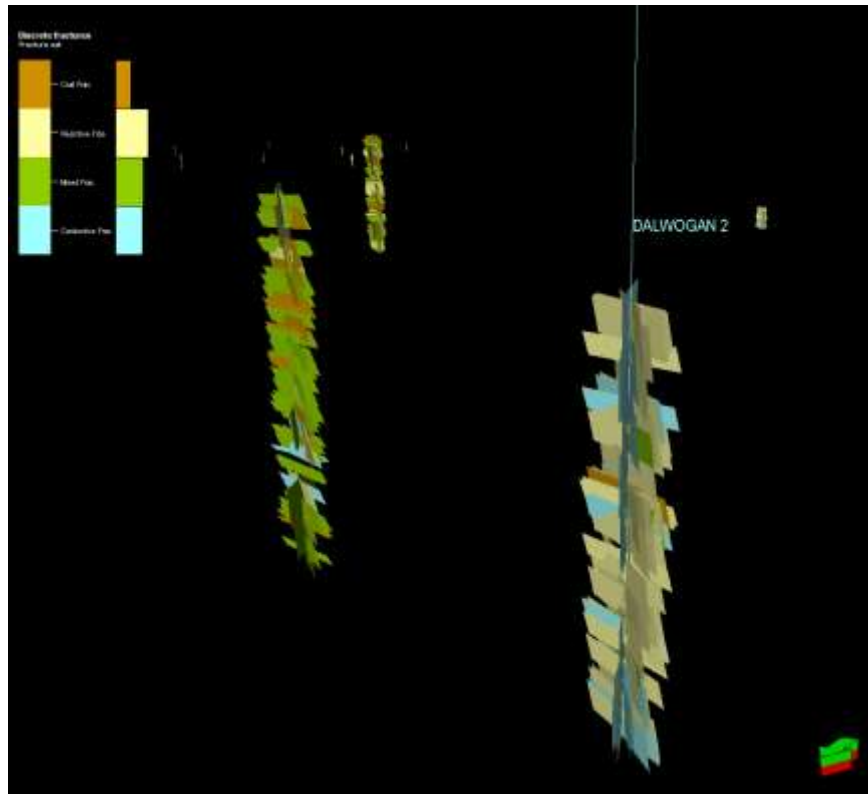


Figure 7.8 DFN at wellbores from the interpreted fractures by image logs.

For the regional DFN model, we need to predict the fracture density distribution by relating image log interpreted fracture density with spatial distribution parameters, e.g. seismic attributes or structural curvatures etc. A 1km by 1km area was gridded with 1m by 1m horizontal cells near the wellbore Dalwogan 2. Then formation markers (well tops) were used to build the horizons. Based on the horizons, image log interpreted fracture density was homogeneously distributed across the horizon (see Figure 7.7) because there was no data within this distance to suggest otherwise.

Fracture orientation is another important parameter for DFN modelling. In this study, the Fisher model (Fisher, 1953), is used to describe the fracture dip angle, dip azimuth and distribution. Note that A Fisher Distribution is commonly used for modelling the distribution of 3 dimensional orientation vectors, such as the distribution of joint orientations (pole vectors) on a sphere. The equation (Fisher Distribution, 2016) is:

$$f(\theta) = \frac{K \cdot \sin\theta \cdot e^{K \cdot \cos\theta}}{e^K - e^{-K}}$$

(Eq. 6.3)

Where f is the cumulative distribution function; θ the angular deviation from the mean vector, in degrees; K is the "Fisher constant" or dispersion factor. A larger K value represents a tighter cluster and vice versa. Table 2 lists the parameters for DFN modelling near well Dalwogan 2.

Figure 7.11 shows the built DFN models for the three coal seams with DST data. There are 8, 6 and 14 fractures intersecting the wellbore for the DST1, DST2 and DST3, respectively.

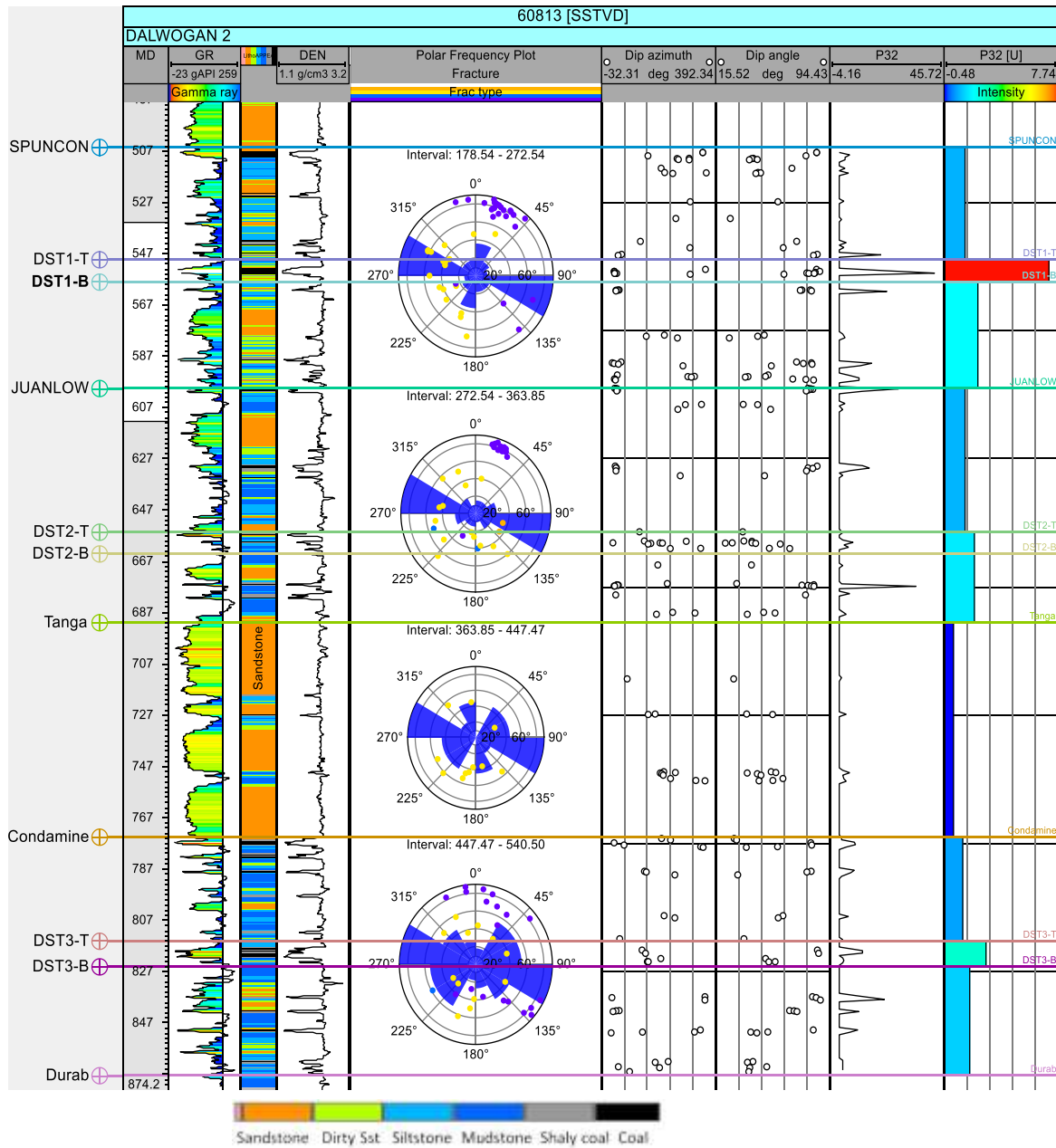


Figure 7.9 Wireline logs, lithology, depositional facies, image log interpreted fractures and their properties and formation markers (data were from Mukherjee et al., 2016, report). In rose diagrams, purple points are coal seam fractures. DST=drill stem test.

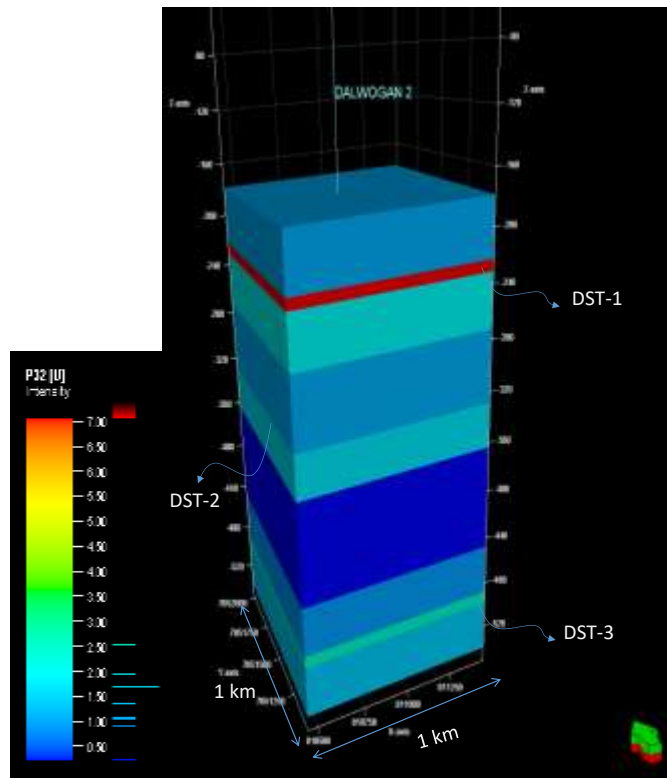


Figure 7.10 Fracture density (P32; fracture area per volume) distribution near well Dalwogan 2.

Table 2 Parameters from image log interpreted data for DFN modelling.

Coal seams	Average dip angle, °	Average dip azimuth, °	Concentration (K)
DST-1	81	6	60
DST-2	42	192	60
DST-3	47	179	60

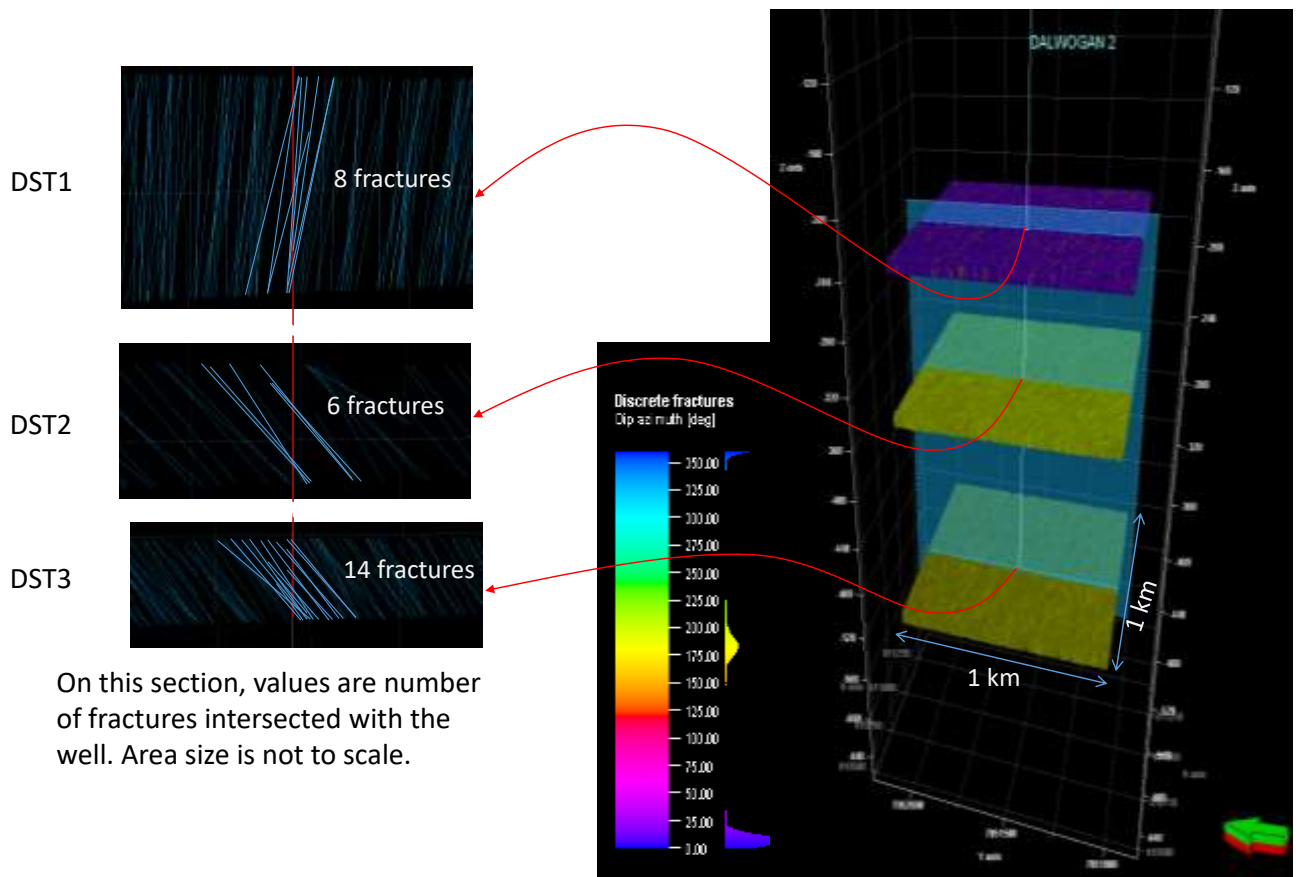


Figure 7.11 DFN modelling results near well Dalwogan 2.

Fekete is used in DST analysis (Figure 7.12a). The analysed permeability values for seams DST-1, -2 and -3 are 15.59 mD, 0.68 mD and 0.85 mD, respectively. We also tried to estimate the fracture length and aperture via fluid flow simulation using a DFN model (Figure 7.12b). Figure 7.12c shows the comparison of the simulated bottom-hole pressure based on the DFN model with measured pressure from DST for the formation of DST1 and the simulated bottom-hole pressure with a homogeneous model. Results show that the simulated pressure using the DFN model matches better with the measured pressure than using a homogeneous model (Figure 7.12d).

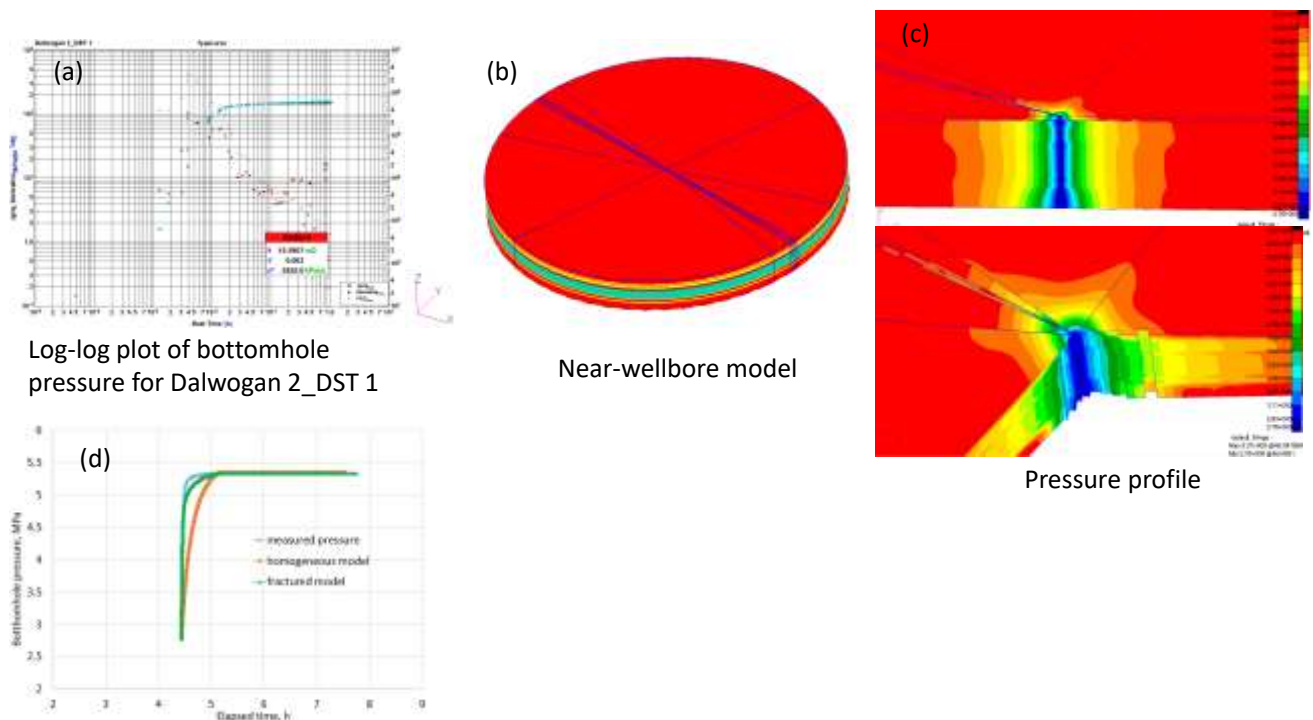


Figure 7.12 (a) DST analysis in Fekete; (b) DFN model; (c) simulated pressure profile at the end of well test; and (d) pressure comparisons of measured, simulated by using a homogeneous and DFN models.

7.4 A new workflow to build cleats distribution at small scale

Coal has a complex porous system ranging from visible including micro-, meso- and macro-porous, and fractures (including butt and face cleats, joints and fractures; Laubach et al. 1998). Butt cleats and orthogonal face cleats which contribute to the coal permeability are the main conduits for gas and water flow in coal. However, the permeability is strongly dependent on the cleats spacing, geometry, orientation, aperture size, connectivity, degree of mineralisation and topology (Close and Mavor, 1991; Laubach et al., 1998; Zhou and Yao, 2014; Jing et al., 2016).

Discrete fracture models (DFM or discrete fracture network, DFN) were built and used to analyse the coal permeability and fluid flow (Gong et al., 2014). Zhou and Yao (2014) studied the effect of cleats aperture and spacing on coal permeability by built 2D cleats models. Gao et al. (2014a) analysed the strength and deformability of coal based on $(2\text{m})^3$ DFN models with bedding planes, face cleats and butt cleats. Jing et al. (2016) built DFNs for coal cleats based on micro-computed tomography imaging (μCT) by using a Monte Carlo method. Figure 7.13 shows the comparison of different scale fractures in coal seam.

Building a DFN model for cleats near borehole can help to analyse near-wellbore coal properties, coal seam gas production, and well testing performances. However, there is a shortage of information in scientific literature regarding the processes for building DFN for coal cleats by conditioning borehole data. This study presents a workflow to build a grid based DFN near wellbore using multi-point facies simulation (MPS, a pixel-based sequential simulation algorithm; Strebelle, 2002; Strebelle and Journel, 2001; Rezaee et al., 2015) method and image log data which has a high resolution to 5mm but much smaller fractures can be imaged if there is a sufficient electrical contrast with the background (Weatherford, 2013).

MPS is capable of producing models with more geological complexity than sequential indicator simulation and is easier to conditioning honour hard data than objective modelling. Strebelle (2002) simulated a fluvial reservoir using different training images and nested sequences. Zhang et al. (2006) used a continuous MPS in modelling the porosity distribution for a carbonate reservoir. MPS was also used to generate facies and fracture distribution based on the pattern statistics inferred from some training images (Erzeybek et al., 2012). The training image is used to explain the neighbourhood relationship of facies by creating patterns which is a prior distribution function (pdf; Petrel, 2014). During the pattern creation, multi-grids (Gómez-Hernández, 1991) is used to describe both small and large scale structures as short and long variogram ranges using the two-point geostatistics (Okabe and Blunt, 2005).

This study presents a workflow to build a grid based DFN near the wellbore using multi-point facies simulation (MPS) method. Core from three wells, A, B and C shown in Figure 7.14 were measured for face and butt cleats spacing (55 points from well A, 138 from well B and 69 from well C) which were sourced from the well completion reports. Image log from well D was interpreted for cleats azimuth which was used in MPS as hard data. Firstly, we coded a program to generate cleats distribution based on the core observed cleat spacing. Then, the generated cleats were imported into Petrel to be used as the training image. Then, we built a 2D grid with cells number of 1000×1000 and grid size of 1mm in x- and y- direction which is used in MPS modelling. Finally, one realisation of cleats distribution near wellbore was generated. Figure 7.15 shows the workflow for cleats modelling by MPS used in this study.

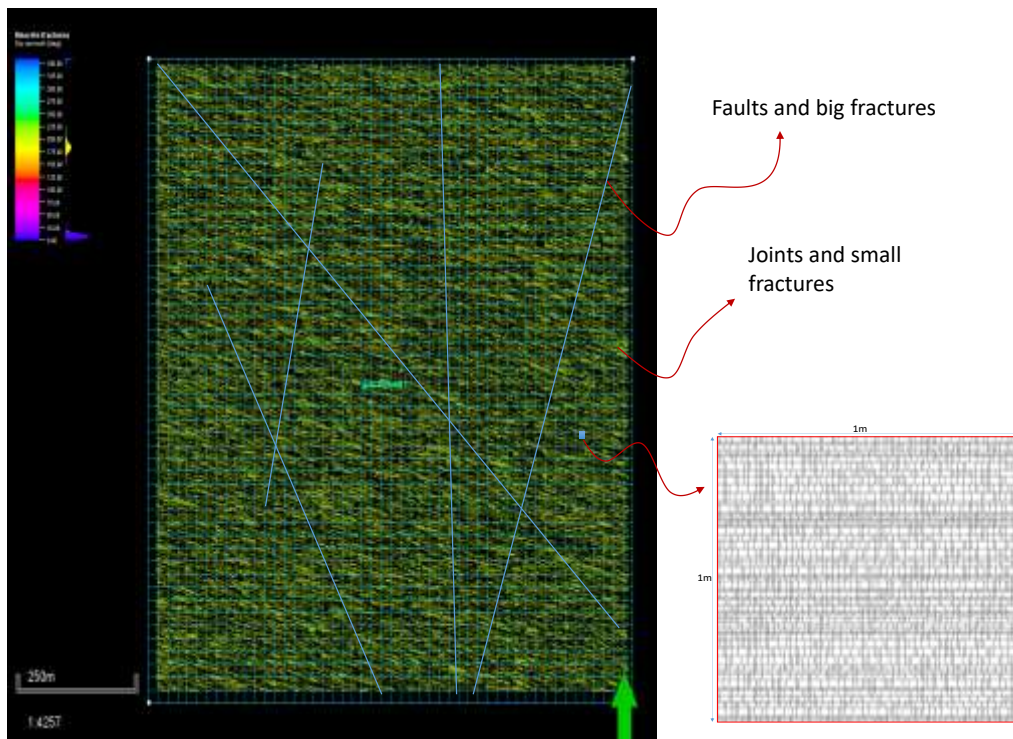


Figure 7.13 Diagram showing the fractures at different scale.

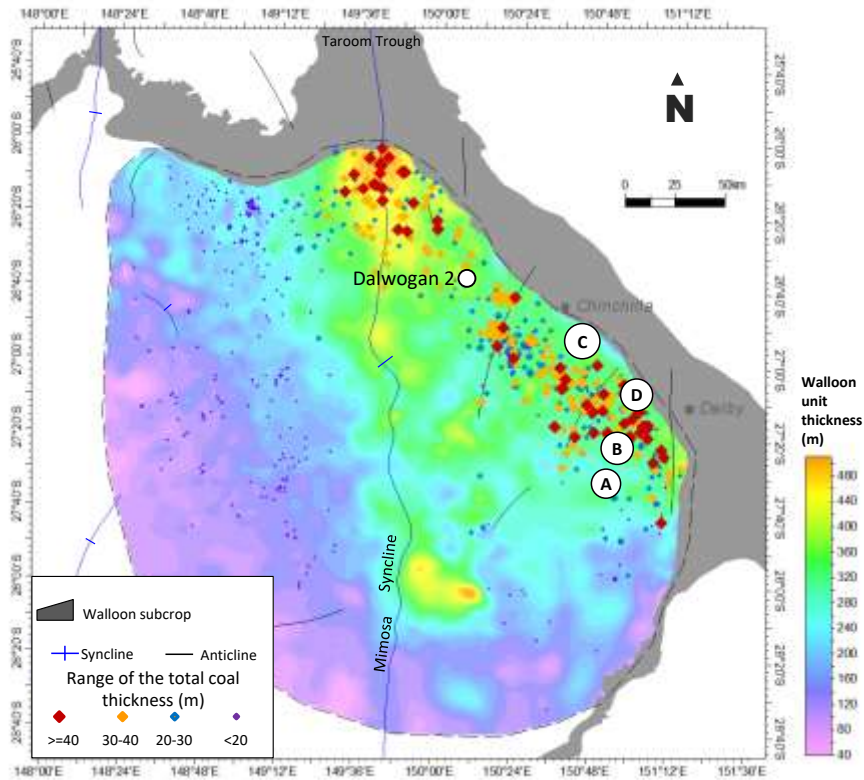


Figure 7.14 Location of wells for this study in the Surat Basin.

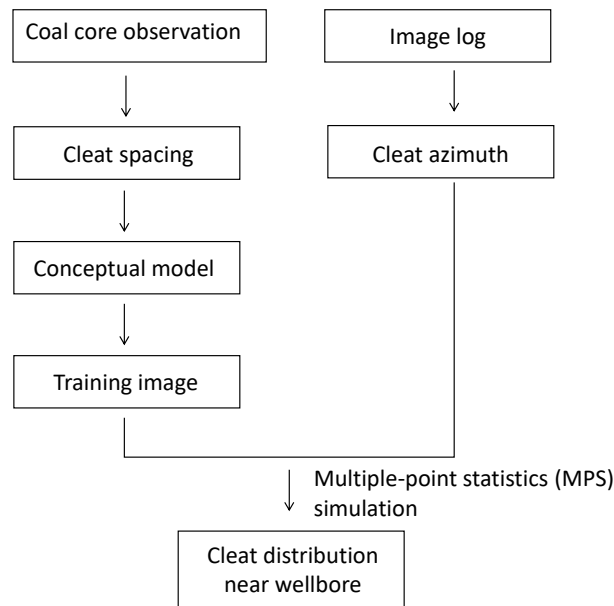


Figure 7.15 Workflow for cleats modelling by MPS used in this study.

Based on the observed average cleat spacing (Figure 7.16), we coded a program in MATLAB to generate cleats distributions as a conceptual model which will be used as a training image in modelling cleats distribution by MPS (Figure 7.17).

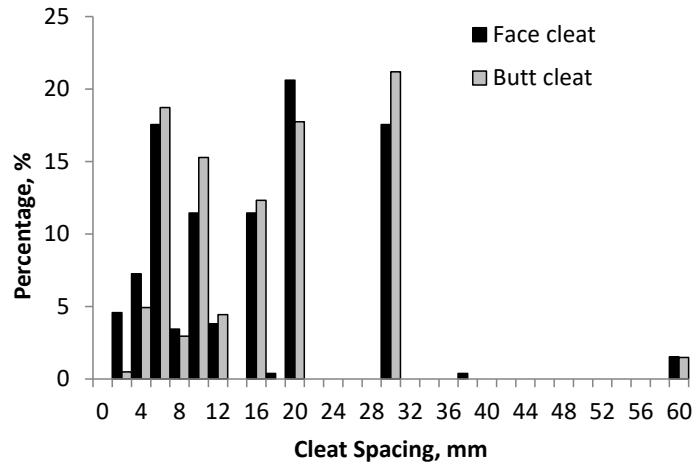


Figure 7.16 Histogram of coal cleat spacing from borehole A, B, and C which were shown in Figure 7.12. Data were sourced from the well completion reports for these three wells. Statistics of cleat spacing showing three peaks, e.g. 10mm (average from 3mm to 12 mm), 20mm and 30mm.

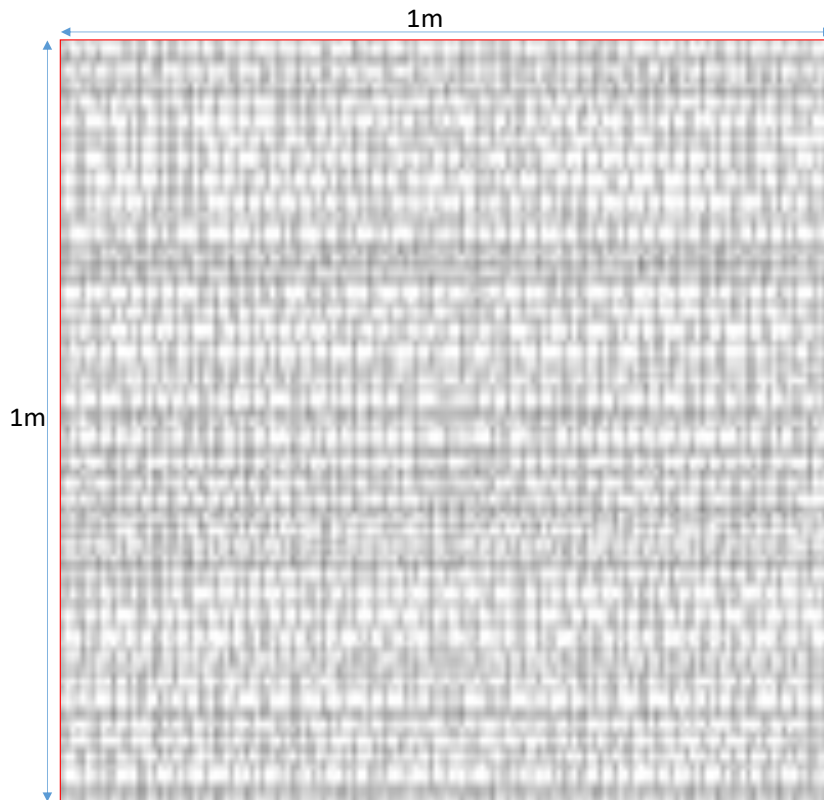


Figure 7.17 One realisation of cleats distribution. Plan view from top.

We coded a program in MATLAB to generate cleats distribution based on the cleat spacing shown in the left figure. Then, the generated cleats were imported into Petrel as FAB data because Petrel cannot generate butt cleats terminated by face cleats (Petrel, 2014). We then built a 1000x1000 2D grid with grid size of 1mm in x- and y- direction to store cleats as shown in Figure 7.18 for one realisation because MPS is a pixel-based sequential simulation algorithm.

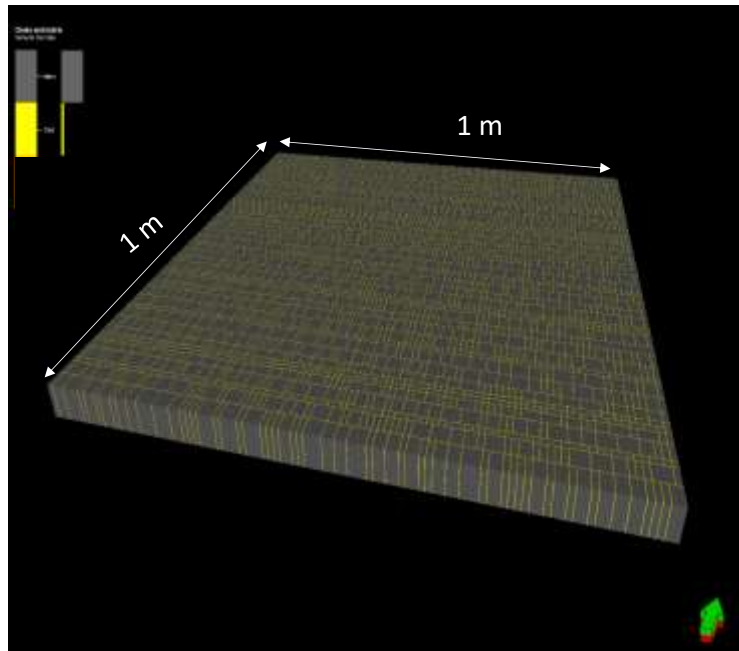


Figure 7.18 Cleats distribution in Petrel with horizontal grid size of 1 mm. Model size is 1m by 1m by 0.1 m.

Compact Microimager (CMI; Weatherford, 2013) from well D was interpreted for coal cleats (Figure 7.19) and strike azimuth for conductive fractures and faults (Figure 7.20). Results show that the strikes azimuth for conductive fractures and faults are nearly along west-east direction which was assumed as the strike for face cleats because it is difficult to identify the orientation of face cleats from an image log.

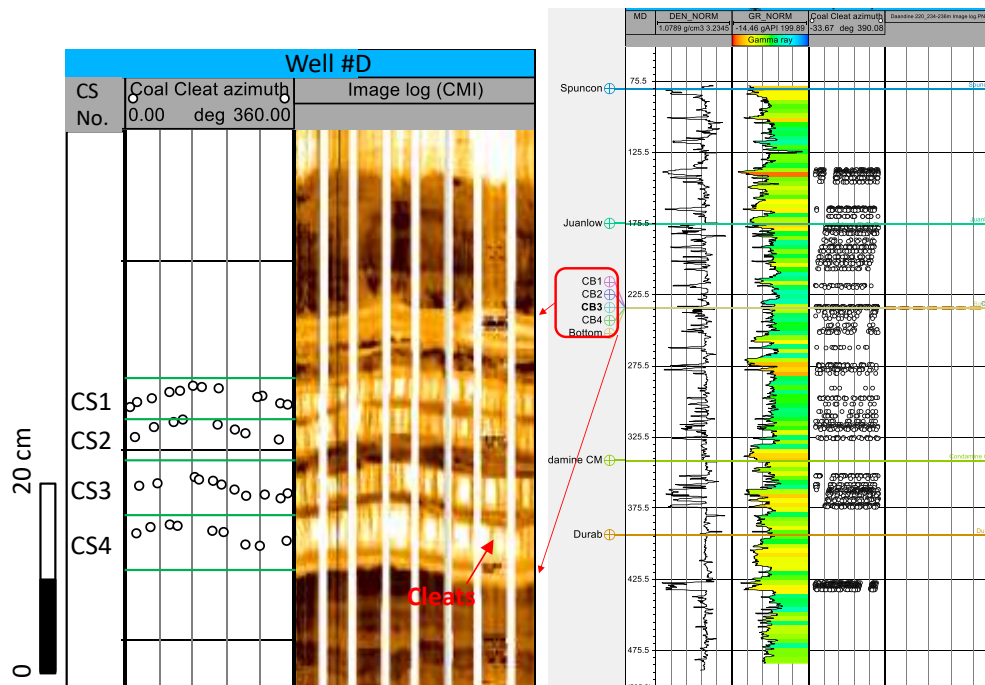


Figure 7.19 Interpreted coal cleats for four thin coal seams. Thicknesses of CS1 to CS4 are 5, 6, 5 and 6 cm, respectively (data were from Mukherjee et al., 2016, report)

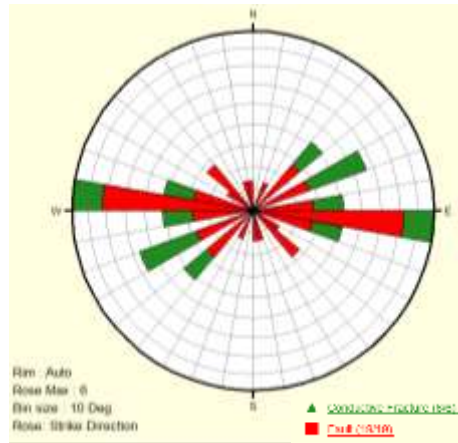


Figure 7.20 Strikes for conductive fracture and fault which was assumed as the azimuth of face cleats.

A 3D grid with grid cells of 1000×1000×4 in x-, y- and z-direction was built. The grid size is 1mm in x- and y- direction and equals coal seam thickness in vertical. Figure 7.21 shows the built zones.

The training image was used to create pattern by using an ellipsoid search mask (Petrel, 2014) with radius of 50×50×1 in x-, y- and z-direction. We also converted the log interpreted cleats to a probability model which was used in MPS modelling as a conditional data. Figure 7.22 shows the converted cleats probability.

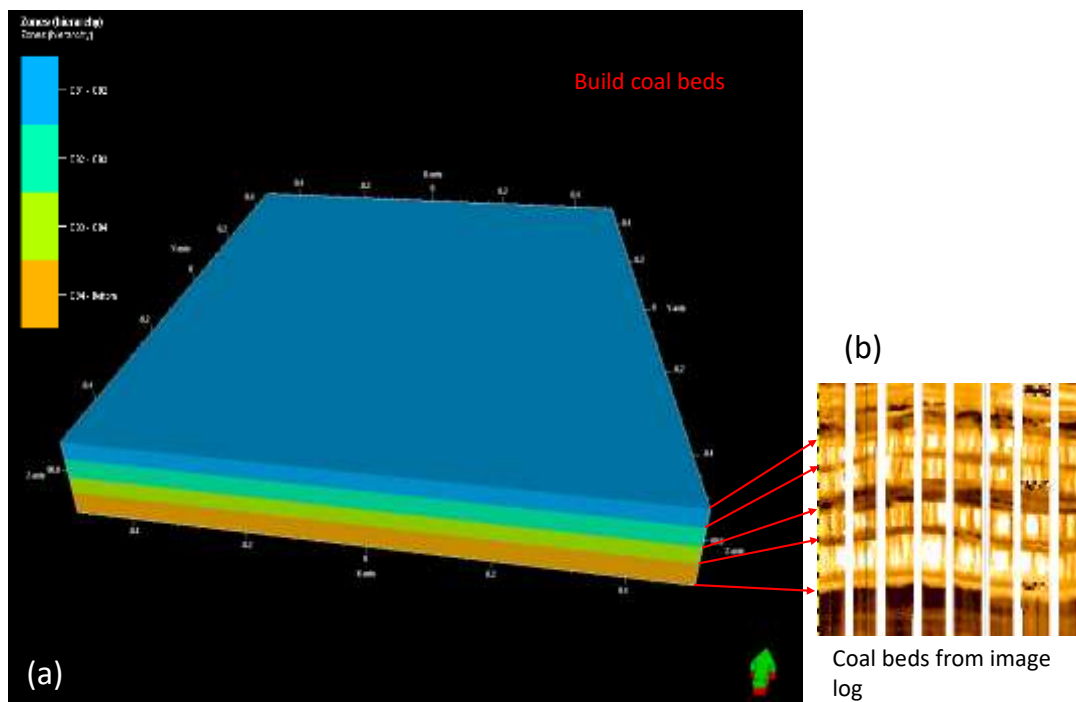


Figure 7.21 (a) Geological model shows the zones for each coal bed; (b) coal beds identified from image log.

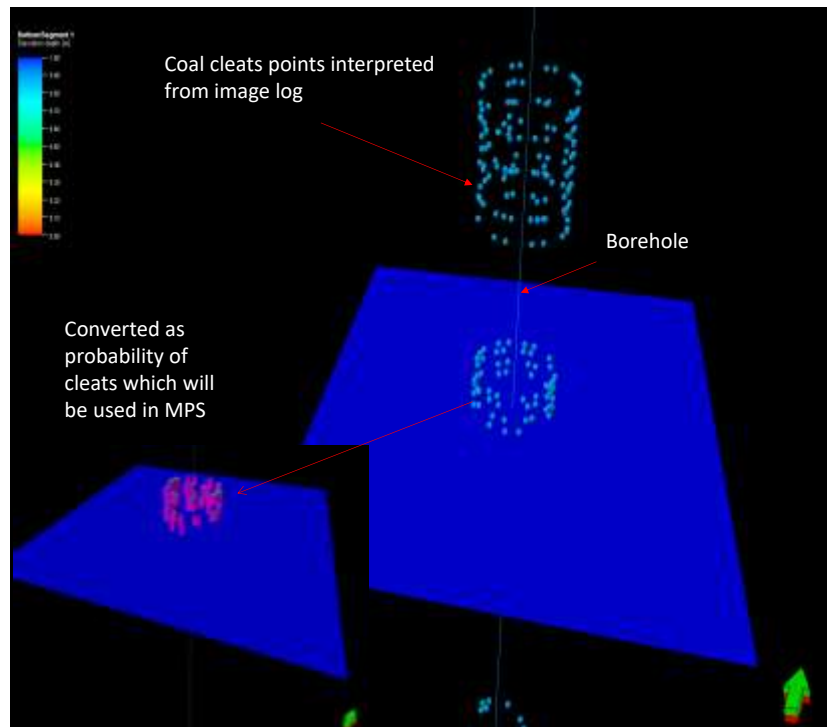


Figure 7.22 Image log interpreted coal cleats were converted to probability which is used in MPS modelling for cleats.

At last, MPS was used to generate cleats distribution with distribution pattern, conditioning data and face cleat azimuth showing in previously slides. Figure 7.23 shows the modelled cleats and matrix within 50 cm of wellbore for one realisation.

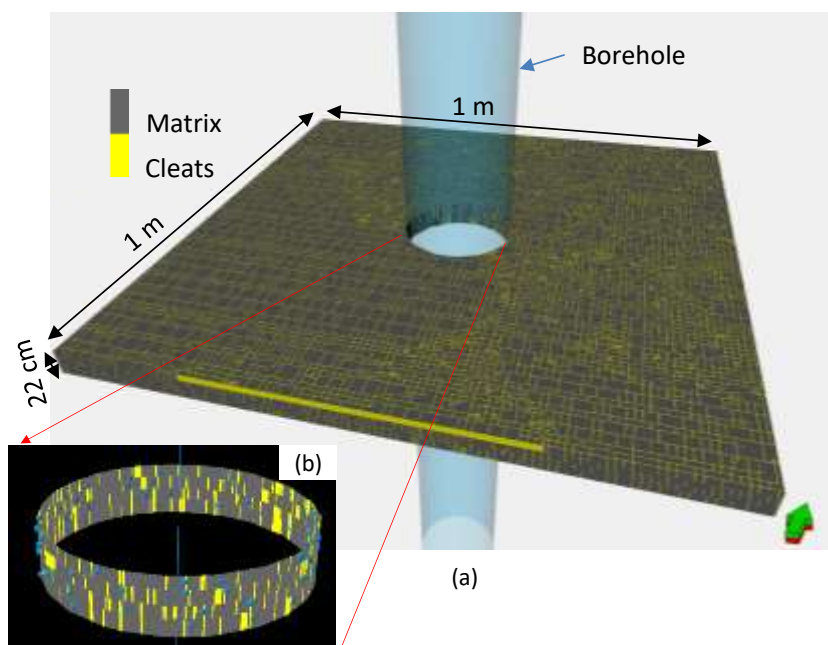


Figure 7.23 One realisation of coal cleats distribution near wellbore (a), and a ring showing cleat distribution at borehole wall.

This study presents a workflow to build cleats distribution near wellbore by integrating the image log interpreted cleats, cleats spacing data from coal core observation and MPS method. The built cleats and matrix model can help to analyse near-wellbore coal properties, coal seam gas production, and well testing performances. Well testing or production data will be used to

optimise the cleats distribution model. Figure 7.24 shows a comparison of cleats distribution with CT extracted cleats. More training images from μ CT scanned cleats will be used in future.

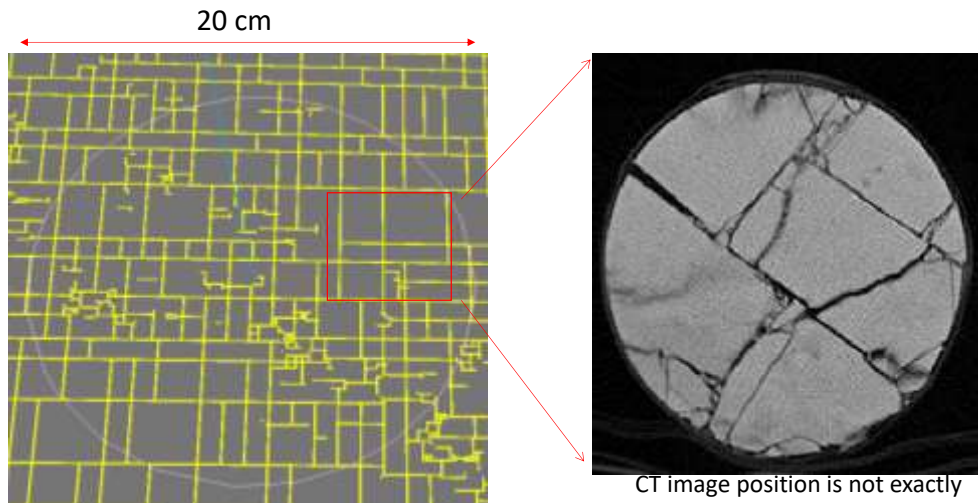


Figure 7.24 Cleats distribution compared with CT extracted cleats. Note that the position of this CT image is not exact.

7.5 Conclusions and future works

This report has experienced in building DFN using open-cut mining data, image log interpretation data, and core observed data. We built DFN for a mine dataset and Dalwogan 2, and cleat distribution near a borehole. Numerical simulation results show that the simulated pressure based on DFN model near well Dalwogan 2 matches better with the measured pressure by DST. Future work will include:

- Update models with more data, e.g. fracture geometry, density, types;
- DFN for Mine A: Validation of DFN by using well testing data;
- Cleat distribution model: Generate more training images for different coal type; modify the cleats shape by integrating the extracted cleats from CT scan;
- DFN model near well Dalwogan 2: Run more simulations to figure out the fracture length and aperture.

8 Coal Strength and Fracture Toughness Testing for Synthetic Rock Mass Models

8.1 Summary

This section of the report is adapted from Barbosa et al., 2017. Geomechanical response of coal seam gas reservoirs to stimulation, and water and gas production is estimated by numerical modelling. One approach is to use a Synthetic Rock Mass (SRM) modelling which requires knowledge of coal parameters, e.g. strength (compressive and tensile) and fracture toughness. Most coal geomechanical properties are varied with respect to coal rank, type, and grade, but whether these properties will be unchanged when upscaled to the rock mass for reservoir modelling is uncertain. In the Surat Basin, coal strength data in the public domain are few. Available data is commonly from higher rank bituminous coals in the Bowen Basin rather than from sub bituminous coals, which is a magnitude weaker in intact strength.

This report presents preliminary laboratory-derived mechanical properties for sub bituminous coal from the Surat Basin by applying tests used from mineral processing. These tests were used as an alternative to triaxial testing of core at different sizes as core was not available, and there has been some discussion whether one might utilise chip samples from open hole drilling for geomechanical characterisation. Mineral processing tests also explore the effect of sample size on coal strength and toughness, which is useful for determining how best to upscale from intact to rock mass behaviour. An outcome is to improve the understanding of geomechanical properties for coal reservoirs and potentially develop predictive indices based on the coal quality (rank, type and grade) for the given area.

Test works include surface hardness using a Shore Scleroscope Rebound Hardness (SSRH) tester and impact breakage in response to energy using the JK Drop Weight Tester (JK DWT) on different coal types at different particle sizes. A Short Impact Load Cell (SILC) is used to measure fracture toughness and estimate coal strength for different coal types. SILC was conducted on small cores and also on different particle size fractions derived from the JK DWT. The particle tests were run to investigate the possibility of using chips from open hole drilling to obtain geomechanical strength data. All samples are the same sub-bituminous rank, collected from different plies within a coal seam. Samples were obtained from the Walloon Coal Measures in an open cut mine.

8.2 Introduction

Coal strength and fracture toughness are fundamental parameters for numerical modelling of wellbore integrity, coal reservoir behaviour during gas production, and response to fracture stimulation. Along with permeability, the geomechanical behaviour of the coal varies under varying stresses. The geomechanical behaviour of coal and interburden rock strata is a function of the intact coal or rock strength and the fracture density, which discounts the strength when upscaled (i.e. downgrading properties values) to the rock mass or to a modelling grid cell. Whereas analogue data on coal strength for higher rank bituminous coals is commonly available in areas where underground mining occurs, data are sparse for lower rank sub bituminous coals that are commonly mined in open pits. Data for fracture toughness of coal in

general and for different coal ranks is even less available. This study collected data on coal hardness, fracture toughness and impact breakage behaviour for different lithotypes in the sub bituminous rank coal from the Walloon Coal Measures. It also investigated the proxy estimation of unconfined compressive strength and tensile strength from these analyses.

Analyses for coal hardness, fracture toughness and impact breakage behaviour are commonly used in mineral processing and the tests can be conducted on a range of particles (differing sizes and shapes) and might, therefore, be used on rock chips from open holes as an alternative to coring. Similar to triaxial tests, impact breakage tests could be used to test the failure behaviour of anisotropic rocks.

Size, the orientation of banding or fracture relative to stress or impact energy, as well as changes in inherent material properties all affect the response of samples to testing. It is known that strength and fracture toughness increases with decreasing coal rank and decreased banding (Stach et al., 1982; Medhurst and Brown, 1992; Esterle, 2008). Whether the strength variation between lithotypes is significant for low rank sub bituminous coals is still yet to be known. Relative to bituminous rank coal seam gas plays, the sub bituminous rank Walloon coals are expected to be stronger and tougher, although they are well bedded, contain abundant thin partings and are interbedded with variable strata. This could downgrade their strength or toughness from intact tests to the rock mass or well bore scale.

A coal seam or ply within the Walloon Coal Measures commonly consists of multiple thin beds (<0.5m to 2m), separated by carbonaceous mudstone and tuffaceous claystone, which are stacked to create coals seams of many metres thickness (Figure 8.1). Within each bed, the coals can be subdivided into even thinner (centimetre to decimetre scale) lithotypes. The cleats are poorly developed at low rank (sub bituminous), except for some incipient cleats in the bright bands, although penetrative master cleats or coal joints can be well developed and create the main planes of weakness, in addition to permeability pathways.

The different strength properties of coal and surrounding materials (carbonaceous mudstone and tuffaceous claystone) should be taken into consideration when conducting numerical simulation as well as the variation of field stress with respect to depth and permeability change. Indeed, numerical models should be calibrated using data from field measurements and the information collected from field observations; however, very little or no-field strength data is available for the Walloon Coal Measures in the Surat Basin. Common values of 6-8 MPa are used for coal strength, without considering changes in rank or type known to directly influence other mechanical coal properties such as Hardgrove Grindability Index (Stach et al., 1982; Hower et al., 1987), hardness (Klawitter et al., 2015) and unconfined compressive strength (UCS) (Medhurst and Brown, 1998; Esterle et al., 2008; Palmer et al., 2005 cited in Deisman, 2016; Figure 8.2). Mark and Barton (1997) also developed an empirical relationship between grindability and coal strength for input to coal pillar design, but scatter was quite high.



Figure 8.1 Photographs of a coal seam within the Walloon Coal Measures showing a) the interbedded nature of the plies and b) the interbedded and banded nature of the coals plies.

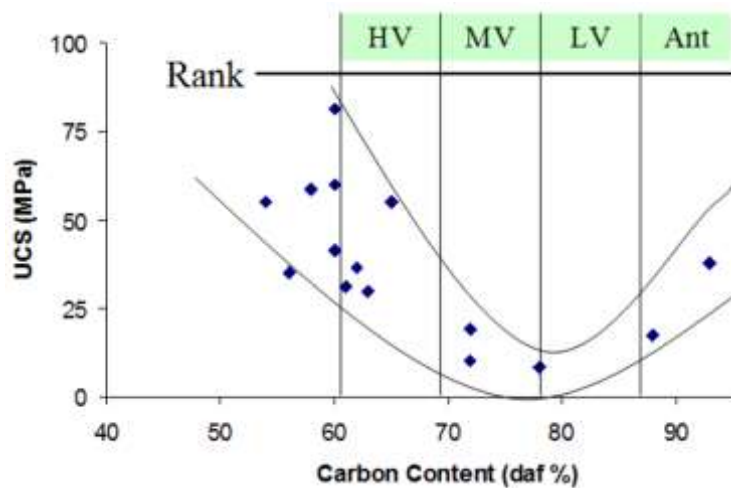


Figure 8.2 Variation in coal strength relative to rank as estimated by carbon content. From Palmer et al., 2005 cited in Deisman, 2016.

This study attempts to gather requisite data for more accurately modelling these low rank coals, and it also trials different approaches to gathering the data that might be applied to chip rather than fully cored holes. The laboratory-derived mechanical properties that are analysed include the effect of coal type as well as the size effects. Data from this study can be compared to the similar data obtained for other coals to examine the effect of coal rank on mechanical properties. The laboratory data analyses are produced while demonstrating the applicability of the following methodologies: JK Drop Weight Test (**JK DWT**), Slow Impact Load Cell (**SILC**), and

Shore Scleroscope Rebound Hardness (**SSRH**) (Figure 8.3). In addition to presenting the results of these tests, their feasibility and applicability will also be discussed.

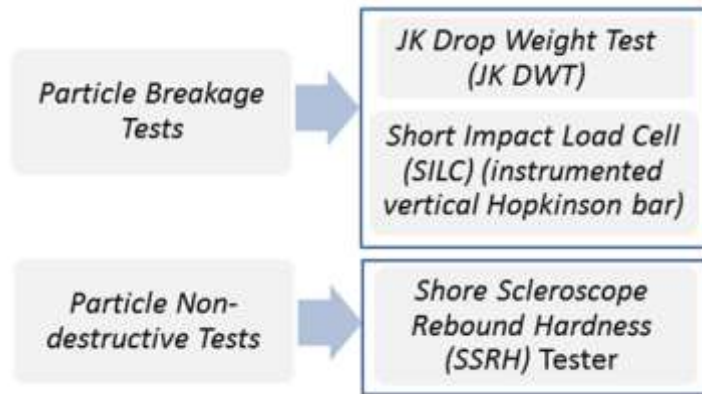


Figure 8.3 Characterisation of sub bituminous coal using destructive and non-destructive tests.

8.3 Materials and methods

The sampling approach was to test for differences in hardness, strength and fracture toughness in the coal lithotypes and stone at the same rank. If differences between lithotypes are small, they could be ignored in modelling; otherwise it must be determined whether the properties are additive and how to upscale from the intact test sample to the rock mass. The laboratory scale physical tests conducted used single particles and single small cores, and many particles must be tested to reach a reliable result. Small to large (5x5x5 to 30x30x30cm) block samples of different end member coal lithotypes representative of the Walloon coal were collected from freshly mined coal at the mine.

Samples were wrapped in plastic and sealed in plastic boxes and transported to the Julius Kruttschnitt Minerals Research Centre (JKMRC), part of The University of Queensland. The samples were collected in the north pit of the mine where three coal plies named C6 ply (dull category), C8 ply (banded with white marks which are clay lenses), and C8 ply (banded) are located from top to bottom strata over an interval of approximately 1 metre in height. The south pit presented the coal on the D8 ply low ash banded. Coarse blocks of mudstone were also collected at the west pit, though with different composition and diageneses if compared with the typical carbonaceous mudstone placed between the multiple thin beds of coal in the Walloon Coal Measures.

In addition to the samples collected from the mine (rank vitrinite reflectance $R_v=0.56\%$), the borehole Guluguba-2 ($R_v<0.50\%$, which was previously studied for petrology by Hentschel et al. 2016), supplied well preserved samples as polished epoxy blocks. The epoxy blocks are all similar dimensions, which are useful for comparison between samples using the SSRH test (see Klawitter et al., 2015). The JK DWT test data for the Goonyella Lower seam (high rank coals with $R_v\approx 1.2$) were also available for comparison (Esterle et al., 2002).

The collected samples were tested in the laboratory at JKMRC, and the conducted tests are shown in Table 3.

Table 3 Locations, rock material and conducted laboratory tests.

Location		Rock material	JK DWT	SILC		SSRH
				Cylinders	Particles	
Mine samples	North pit	Coal C6 ply: Dull	13 energy/size combination	16 (perpendicular to band)	x	•
		Coal C8 ply: Banded white marks (clay lenses)	•	12 (parallel to band)	•	•
		Coal C8 ply: Banded		13 (parallel to band) + 125 (perpendicular to band)	•	30 blocks
	South pit	Coal D8 ply: Low Ash Banded	13 energy/size combination	•	x	•
	West pit	Mudstone	12 energy/size combination	•	x	•
Guluguba-2 borehole		Coal (samples available for distinct depth and formation)		•		31 blocks
Goonyella		Coal Lower ply (data available)	x	•		

Each test required different sample preparation, which began within a week after sampling to reduce any degradation of coal properties due to storage. Proximate analyses (moisture, ash, volatile matter, fixed carbon) of the test samples are yet to be conducted as corroboration of visual classes.

The selected tests (JK DWT, SILC, and SSRH) are conducted on single coal specimens (particles, cylinders, or blocks) positioned manually on the anvil or flat surface. Although relatively simple and easy to conduct, they are time-consuming due to preparation requirements, the number of specimens/ measurements, and processing data). Considerations about the number of specimens being tested were intended to produce a statistical validity of the derived rock material characteristics. Descriptions for the conducted tests are presented below.

8.3.1 JK Drop Weight Test (JK DWT)

The JK Drop Weight Test (JK DWT) was performed at the JKMRC facilities. This test measures the impact breakage parameters/characteristics of samples using a weight of known mass dropped onto a particle sitting flat on a steel plate (Narayanan and Whiten, 1988). The particles are broken under impact at different energy levels. Typically, the procedure is conducted for five standard size fractions; for each size fraction, the required number (10-30) of particles are broken at each of three energy levels, giving 15 energy/size combinations (E_{cs}) Figure 8.4). If the number of particles per size distribution is not enough, adjustments to an energy/size combination can be made.

 JK DWT	Size distribution (mm)	Energy (kWh/t)	Number of Particles	Illustration
	63.0 x 53.0	0.4	10	
		0.25	10	
		0.1	10	
	45.0 x 37.5	1.0	15	
		0.25	15	
		0.1	15	
31.5 x 26.5	2.5	30		
	1.0	30		
	0.25	30		
22.4 x 19.0	2.5	30		
	1.0	30		
	0.25	30		
16.0 x 13.2	2.5	30		
	1.0	30		
	0.25	30		

Figure 8.4 The machine, standard sizes and energies used in the JK DWT test.

The energy utilised for breakage is dependent upon the size and shape of the specimen, the energy level and the breakage properties of the specimen. The known energy can be described by the potential energy (J/kg) of the drop weight at the initial height:

$$E = m_{dw} \times g \times h \quad \text{Equation 1}$$

Where m_{dw} is the mass of the drop weight (kg); g is gravitational acceleration (9.81 m/s^2); and h the distance (metres) from the dropping point to the top of the particle.

The practical procedure involves dropping a steel of known mass (i.e. lift the steel pneumatically from a predetermined height and then release it) to fall against each particle that has been placed on a rigid anvil underneath. Then the breakage products of all particles grouped into each size/energy combination are collected and sized. The size distribution produced is normalised with respect to the original particle size (see Narayanan et al., 1987).

For a wide range of energy inputs, particle sizes and material types, the relative size distributions remain similar in shape and can be described by a single point on the distribution. The percentage passing one-tenth of the original particle size is referred as " t_{10} " (Napier-Munn, 1996). For the size fractions in the JK DWT, the original particle size is estimated by the

geometric mean of the size range (e.g. -63+53 = 57.8mm, then the t_{10} size is: $1/10 \times 57.8 = 5.78\text{mm}$). In this way, a set of t_{10} and E_{cs} values are produced. The following equation relates to the amount of breakage, t_{10} , to the specific energy, E_{cs} (kWh/t):

$$t_{10} = A(1 - e^{-bE_{cs}}) \quad \text{Equation 2}$$

Where A is the maximum t_{10} value achieved (it is an important parameter in characterising the overall breakage curve); b is related to the overall slope of the t_{10} versus E_{cs} curve at the lower energies. A and b are interdependent. The parameters are reported as a single value of $A \times b$ indicating the hardness of the particle in terms of impact breakage.

Using the energy/size combination data values, the best fitted A and b parameters are calculated using a minimisation of error squared routine. The resulting A and b parameters are related to the resistance of the particle to the impact breakage. The product of A by b parameters, which represents the slope of the t_{10} versus E_{cs} curve at its origin (0 kWh/t), is a measure of the particle impact breakage resistance and is used for comparison, with other samples with lower values indicating harder specimen in terms of impact breakage.

This test was previously conducted on a range of coal rank and type. The results can be compared to the tests for the mine site coal to develop a predictive index for coal, similar to Hardgrove Grindability Index but at much lower energies (Esterle et al., 2000).

8.3.2 Short Impact Load Cell (SILC)

The Short Impact Load Cell (SILC) test was performed at the JKMRRC. The Short Impact Load Cell (SILC) developed by Bourgeois and Banini (2002) was modified to develop the monolayer particle breakage experimental set-up. The SILC was based on the concept of Hopkinson (1914) bar and gives information about actual energy consumed by a single rock particle during breakage. Furthermore, it allows an estimation of the rock breakage property.

The SILC test is presented in Figure 8.5. The instrument used at the JKMRRC comprises a rod with 19.99mm in diameter and 1.5m in length, and the load cell is 30 kg in weight. The device is equipped with two strain gauges located diametrically in opposite positions on the steel rod. The model strain gauges are Kulite S/UGP-1000-090 with a nominal unbonded resistance of 1000 Ω and gauge factor of + 155. The test procedure is in many respects identical to conducting a test with a JK DWT. The main difference is the bridge balancing step (or calibration) required before each test.

Single-particles and/or cylinders are used for impact breakage testing. The sample preparation occurs as follows: For cylinders, the samples are drilled from hand-picked specimens of coal to obtain mini cylindrical core samples (12.0mm in diameter and desirable length < 12.0mm). Then, the cylinders have the edges cut and polished to make them parallel. For single-particles, the samples include a number of particles sieved during the JK DWT, the selected particles generate distinct size fractions of 4.75, 6.70, and 9.50mm for those previous energy/size combinations.

For each single-particle and/or cylinder, the accurate mass and dimensions are recorded. Once the test is conducted, the signal from the SILC system together with mass, energy, and size distribution are used in the analysis.

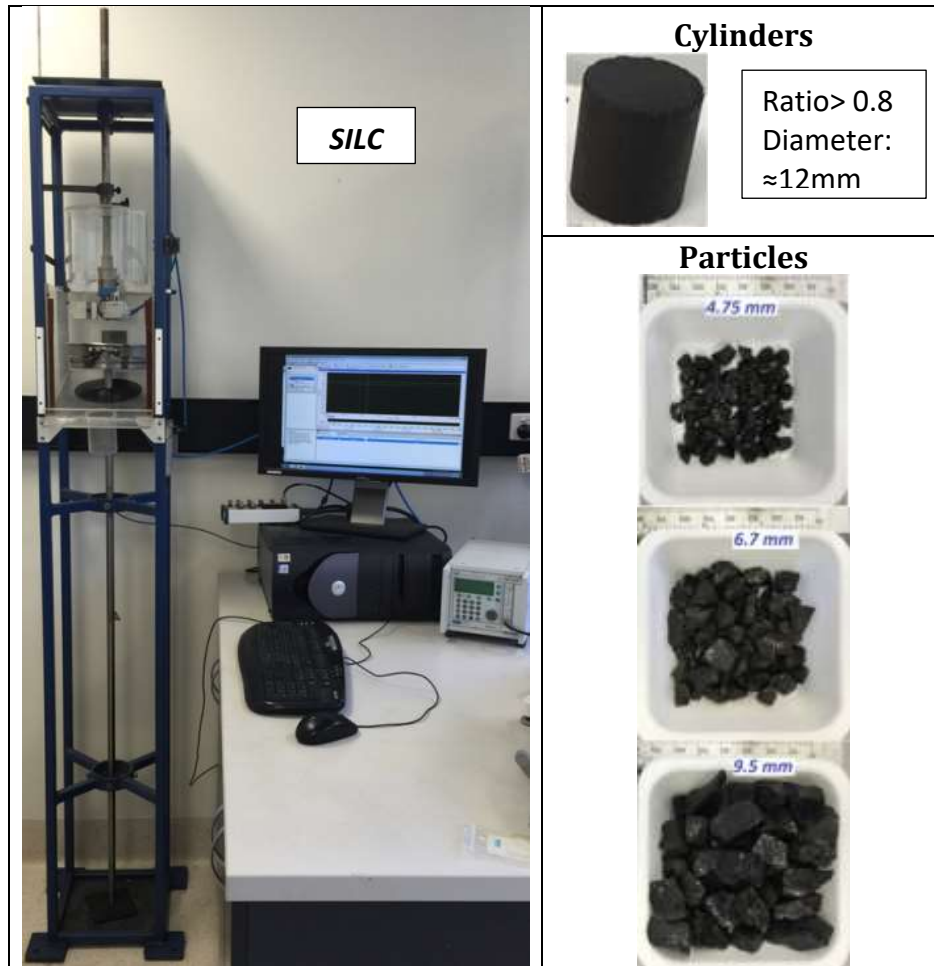


Figure 8.5 The machine and sizes used in the SILC test.

Analysis of the test data is conducted using the Excel spreadsheet provided by the JKMRC. The test results show the force (purple curve) and energy absorbed (blue curve) by each cylinder or particle as a function of time, displayed graphically. The results are evaluated by selecting the point on the force-time curve that corresponds to the occurrence of the first fracture. The SILC tests performed with cylinders generate more uniform curves where the point for the occurrence of the first fracture is quite evident (Figure 8.6). However, the curves for a single-particle can be quite different (Figure 8.7); part of the analysis consists of the verification of the signals and the selection of the correct fracturing point on the curve. The randomness of the curves resulting from the particles reflects variability in the sample size, shape and orientation, which would not be controlled in chip samples.

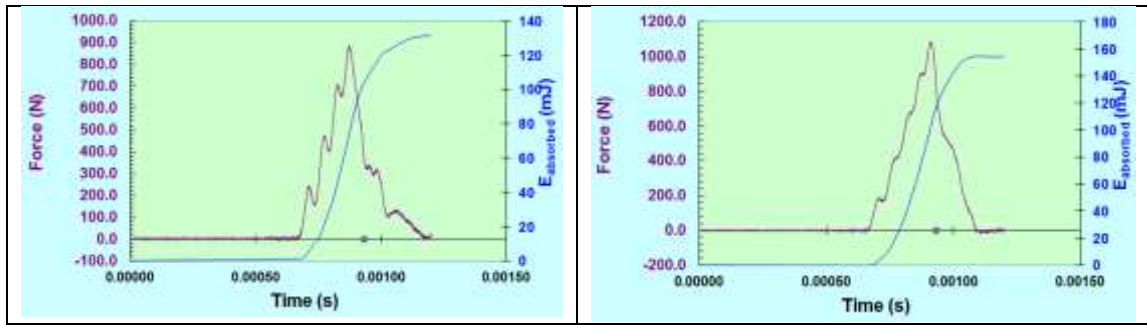


Figure 8.6 Examples of graphics for force and energy absorbed as a function of time from cylinders.

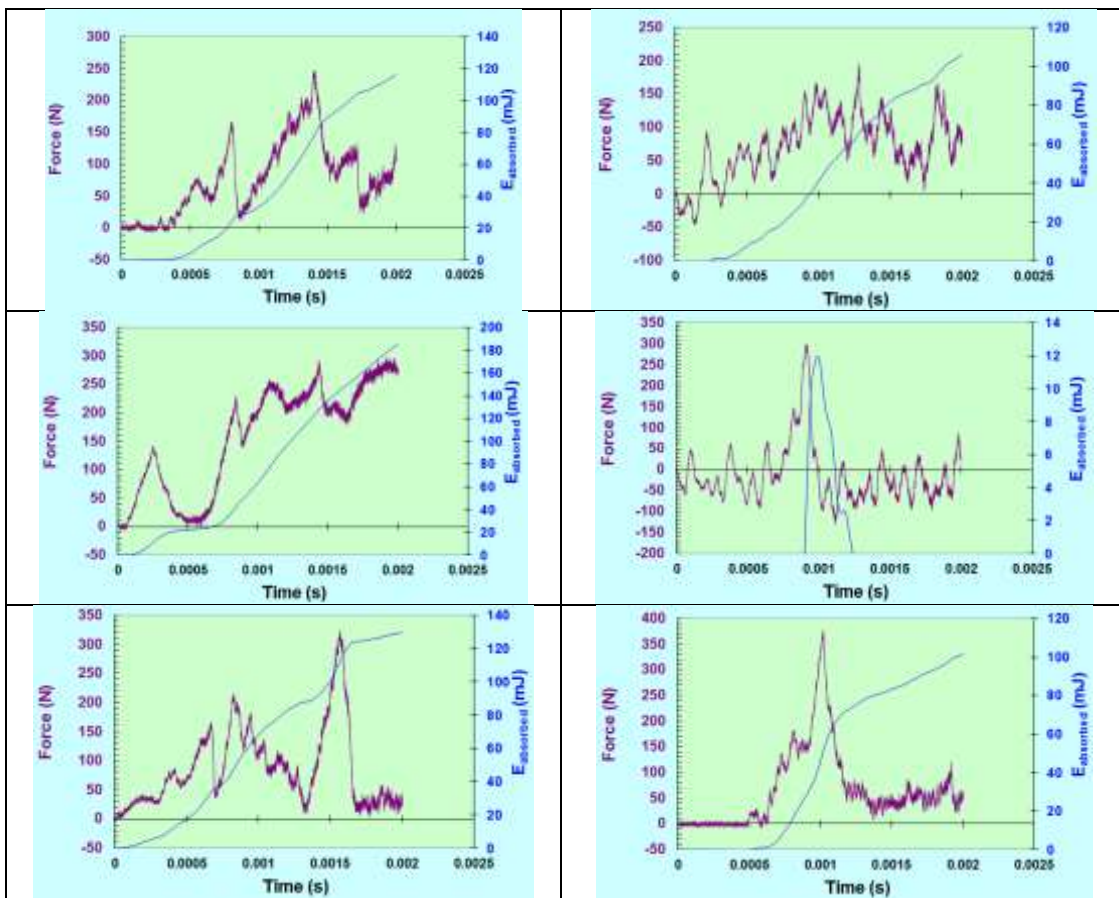


Figure 8.7 Examples of graphics for force and energy absorbed as a function of time from single particles.

The Excel spreadsheet is used to calculate a number of rock breakage properties such as fracture force, fracture energy, specific fracture energy, cylinder strength or particle strength, local deformation coefficient, energy absorbed by rod during fragmentation, particle stiffness, and the corrected specific fracture energy. Figure 8.8 illustrates the different values obtained by selecting a distinct fracture point.

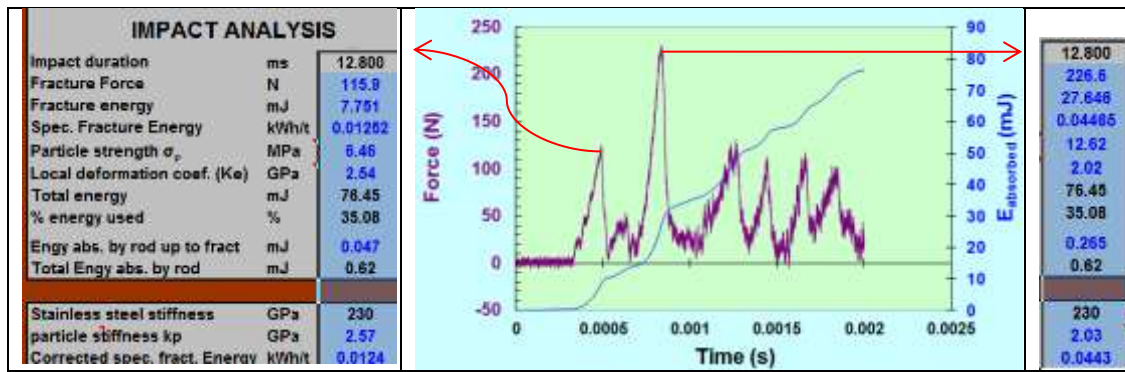


Figure 8.8 Example of selecting distinct fracture point, in this case from a difficult curve.

Below, a brief explanation is given for some properties—the reader is referred to Bourgeois and Banini (2002) for a more detailed description of the physical and operational characteristics as well as the test measurements.

The strength (σ_c) of the cylinder subject to impact is based on the Brazilian Tensile Strength (BTS) estimation (ISRM methods) (Equation 3).

$$BTS = 2 F_c / (\pi \times D \times L) \quad \text{Equation 3}$$

Where: BTS is the Brazilian tensile strength (Pa); F_c is the force at first fracture (N), π is the number PI, D is the diameter of the cylinder, and L is the length of the cylinder.

The strength (σ_p) of the particle subject to impact is estimated using the equation below (Equation 4) (Tavares and King, 1998a).

$$\sigma_p = 2.8 \times F_c / (\pi \times d_p^2) \quad \text{Equation 4}$$

Where: σ_p is the particle strength (Pa), F_c is the force at first fracture (N), π is the number PI, and d_p is the geometrical mean size of the particle (m) which uses the particle height measured.

The local deformation coefficient (K_e) is calculated for the cylinder or particle as follows (Equation 5) (Tavares and King, 1998b):

$$K_e = \sqrt{(0.576 \times F_c^5) / (d_p \times E_c^3)} \quad \text{Equation 5}$$

Where: K_e is the local deformation coefficient (Pa), F_c is the force at first fracture (N), E_c is the energy absorbed by the particle at fracture (J), and d_p is the geometrical mean size of the cylinder (m) which uses the cylinder diameter or geometrical mean size of the particle (m) which then uses the particle height measured.

Then the stiffness (k_p) of the particle or cylinder is calculated by solving the equation below, which is only valid for spherical particles (Equation 6) (Tavares and King, 1998b).

$$K_p = \frac{(K_e \times K_{b,r})}{(K_{b,r} - K_e)} \quad \text{Equation 6}$$

Where: K_p is the particle or cylinder stiffness (Pa), K_e is the local deformation coefficient (Pa) and $K_{b,r}$ is the stainless steel stiffness (Pa). Both the SILC rod and the drop weights are made of stainless steel, with Young's modulus of 210 GPa and Poisson's ratio of 0.3, hence $K_{b,r} = 230$ GPa.

All results using the Excel spreadsheet provided by the JKMRC can be copy into another Excel spreadsheet for additional analysis. Here, the final results for cylinders and single-particles are both presented using a statistical analysis of fracture. The distribution characteristics of fractures were analysed by using a method based on order statistics. This method consists of ranking the test results in ascending order and then assigning $i = 1, 2, \dots, N$ to the ranked observations. N is the total number of tests performed. The cumulative probability distribution for the measured variable (cylinder or particle fracture energy) is approximated by Equation 7:

$$P(E_{m,1}) = \frac{(i - 0.5)}{N} \quad \text{Equation 7}$$

The resulting pairs: Specific fracture energy vs cumulative probability [$E_{m,1}$, $P(E_{m,1})$] is plotted with specific fracture energy presented in a logarithmic scale. Different rock materials data can be effectively described using the log-normal distribution (Baumgardt et al., 1975; Dan and Schubert, 1990; King and Bourgeois, 1993) given by (

Equation 8):

$$P(E_m) = \frac{1}{2} \left[1 + \operatorname{erf} \left(\frac{\ln E_c - \ln E_{m,50}}{\sqrt{2\sigma_E}} \right) \right] \quad \text{Equation 8}$$

Where $E_{m,50}$ and σ_E^2 are the median and the geometric variance of the distribution, respectively.

8.3.2.1 Cylindrical samples:

The estimation of tensile strength and unconfined compressive strength for cylindrical samples takes the following into consideration:

According to Perras and Diederichs (2014), "tensile strength determined from direct and indirect methods are seldom equivalent. Direct tensile testing (DTS) is considered to yield the true tensile strength of intact rock, whereas the Brazilian tensile test (BTS) is considered to overestimate the true tensile strength of intact rock". The correlation presented below gives a reasonable relationship between DTS and BTS for sedimentary rocks (Equation 9) (Perras and Diederichs, 2014).

$$\text{DTS} = 0.7 \text{ BTS} \quad \text{Equation 9}$$

Since Brazilian Tensile Strength (BTS) is related to unconfined compressive strength (UCS), both correlations Altindag and Gurney (2010) and Nazir et al. (2013) (formerly developed for limestone) are attempted for predicting UCS of sub bituminous core samples (i.e. unconfined compressive strength of intact rock σ_c) Equation 10 and Equation 11, respectively. It is assumed that the equations are based on the strength of 50mm diameter samples tested in a

laboratory.

$$\sigma_c = 9.25 \times \text{BTS}^{0.947} \quad \text{Equation 10}$$

$$\sigma_c = 12.38 \times \text{BTS}^{1.0725} \quad \text{Equation 11}$$

The evaluation of which equation gives a better approximation for coal strength takes into consideration a study conducted by Medhurst and Brown (1998). The Hoek and Brown (1997) criterion for intact rock was applied in a series of triaxial compression tests carried out by Medhurst (1996) to investigate the effects of scale on the mechanical behaviour of coal (Medhurst and Brown, 1998). The Hoek and Brown constant, $m_i = 19.4$, determined for bituminous coal of the dull category for 61mm diameter coal samples (Medhurst and Brown, 1998) is an important outcome for this study. The reason is that by assuming m_i is a constant varying with respect to rank as well as lithotype (note that the constant s for dull coal should be $s=1$), it is anticipated that sub bituminous dull coal must present m_i similar or slightly above that for the bituminous coal ($m_i \geq 19.4$).

Using BTS to predict tensile strength (σ_t) and then using the constant m_i gives a good approximation for the unconfined compressive strength (UCS) of intact rock specimens (Perras and Diederichs, 2014). Or vice versa, using the predict tensile strength (σ_t) and the assumed UCS value (Equation 12) gives a validation based on the constant m_i .

$$\sigma_t = -DTS = -UCS/m_i \quad \text{Equation 12}$$

8.3.3 Shore Scleroscope Rebound Hardness (SSRH)

The Shore Scleroscope Rebound Hardness (SSRH) test is a non-destructive and convenient technique for rock hardness estimation (Altindag and Güney, 2006). Hardness is the property of a material that enables it to resist plastic deformation, penetration, indentation, and scratching. The SSRH test consists of dropping a diamond-tipped metallic hammer made of pure hardened high-carbon steel, which falls onto the test specimen under the force of its own weight from a fixed height. The height of the rebound travel of the hammer is measured on a graduated scale. The scale of the rebound consists of shore units, divided into 140 parts. The hardness is measured in terms of the elasticity of the material, therefore, the harder the material, the higher the rebound. The SSRH was performed at The University of Queensland, using the IMAI SIKENKI Co. equipment (Tokyo – Nov. 1970, No 700756). For this test, the samples were confined into epoxy block sized 50x30x12mm (Figure 8.9). Confinement in the blocks improves the reproducibility of the tests and also gives a different result to tests on unconfined core samples (Klawitter et al., 2015).



Figure 8.9 The equipment and sizes used in the SSRH test.

The dropping measurements represent 20 indentations (single impact events) performed on each sample (also considering distinction between bright vitrain and “dull” bands) to estimate the shore units in terms of mean, average, and mode variation of the coal matrix. Then, a conversion of the shore hardness into an approximation of the ultimate tensile strength is possible by reading the hardness conversion chart. An exploration curve is used to extend the tensile strength correlation for shore measurements >80 (where mean 80 shore measurement is equal $\sigma_t = 232$ psi or 1.60 MPa), which are not straight forward in the former conversion table (Figure 8.10).

Shore	Tensile strength (approximate)
70	186
71	189
72	196
73	200
74	203
75	210
76	214
77	217
78	221
79	224
80	232
81	236
82	240
83	244
84	249
85	253
86	258
87	262
88	267
89	271
90	276
91	280
92	285
93	290
94	294
95	299
96	304
97	309
98	314
99	319

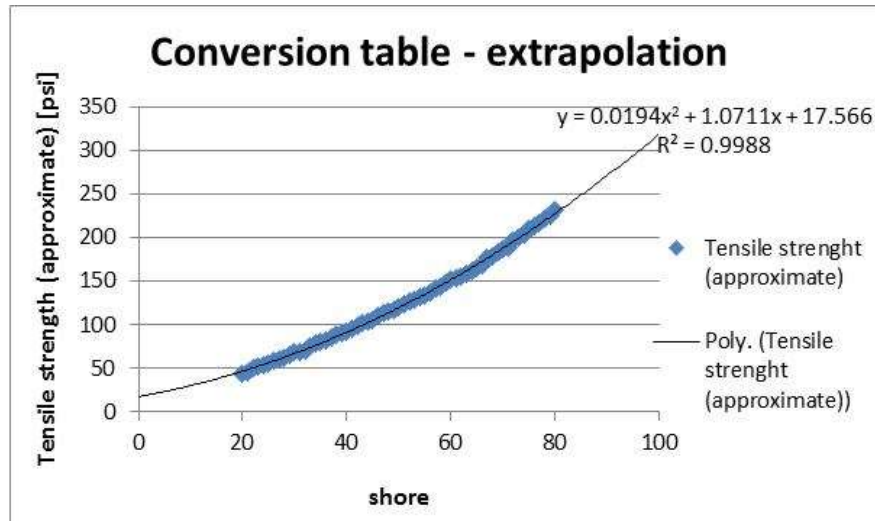


Figure 8.10 SSRH conversion table - IMAI SIKENKI Co. equipment (Tokyo – Nov. 1970, No 700756) - extrapolated for shore >80.

8.4 Results and Discussion

8.4.1 JK DWT

The JK DWT is designed to test brittle material. Coal works well, but rock material experiencing plastic deformation such as mudstone may not represent a reliable estimation of the material characteristics before breaking. After impact, the mudstone forms a compressed wafer with a lot of agglomerated silt and clay particles that can't be sieved. Nevertheless, Figure 8.11 shows the trend of t10 % values with specific energies for different size distribution at mudstone, coal D6 ply dull, and coal D8 ply low ash banded.

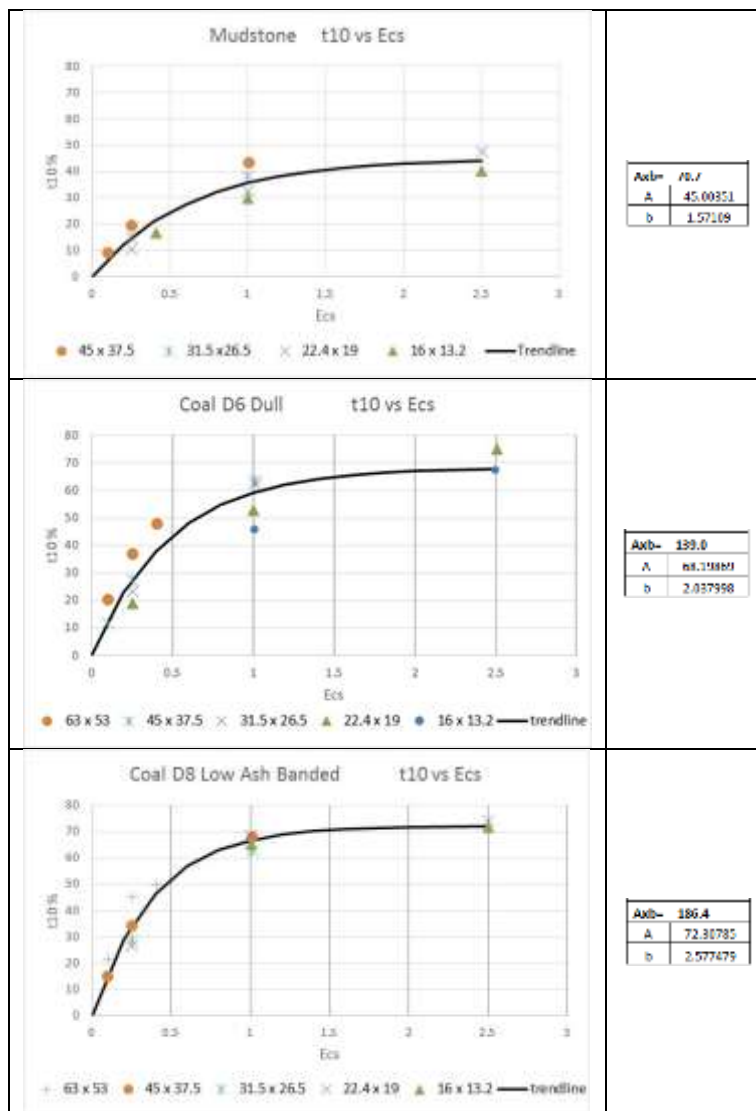


Figure 8.11 Comparison of t10 % produced at different size distribution.

Following that, the amount of breakage for each of the standard size fractions is plotted against the energy level and compared to existing data from bituminous coals. The trend lines illustrate the breakage characteristics of the Walloon coal lithotypes (low rank ≈ 0.5) compared within the Goonyella Lower seam data (high rank coal ≈ 1.2) (Figure 8.12). Overall, the amount of breakage in sub bituminous coal was at least 2.0 times less than bituminous coal for the same low energy level (0.2 kWh/t), and it gradually increased to 2.3 times at a higher energy level

(2.5 kWh/t). In other words, mine sub bituminous coal is at least 2.0 times less brittle than bituminous coal.

The t10 % values are higher for the higher energy levels for the same size distribution, which indicates the higher breakage for higher energy impacts. Also, for a same energy level, the t10% values keep on decreasing with the smaller physical sample size. That is indicating the lesser breakage in finer sizes. However, the absolute differences in breakage are not that significant for the mine coal. For instance, it is observed that the t10% for D8 ply banded and C6 ply dull at 0.25 kWh/t energy are 34.4, and 37.1, respectively, when the size distribution is 45.0x37.5mm. In other words, for the same energy of 0.25 kWh/t and size distribution of 45.0x37.5mm, the breakage difference is about 8%. Also, the JK DWT tests illustrated that larger particles are easier to break than smaller particles, except for the coal D8 ply low ash banded, where this tendency was not evident.

Overall, the hardness of the particle (parameters Axb) is 70.7, 139.0, and 186.4 for mudstone, coal D6 dull, and coal D8 low ash banded, respectively, in terms of impact breakage. These results show the increasing brittleness from the mudstone to the dull and banded coal.

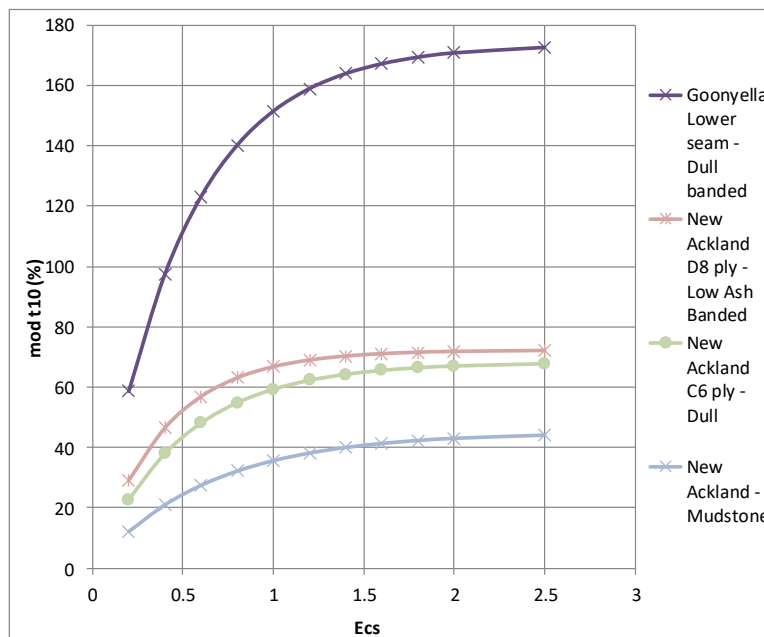


Figure 8.12 Breakage characteristics of the mine sub bituminous coal compared with Goonyella Lower seam dull banded bituminous coals.

8.4.2 SILC

The following results can be compared among each other by observing semi log plots with the cumulative probability against the specific fracture energy level. The plots are then modelled with the log normal by getting the mean of the distribution, also called E50, and the variance sigma2. The “E50” is the mean energy and the variance or sigma2 is two standard deviations either side of the mean.

8.4.2.1 Type effect and orientation on cylinders

The majority of the cylindrical samples were drilled perpendicular to the coal band at the C8 ply banded. This specimen is represented by 125 mini-cores (see example in Figure 8.13; #1, 4, 5, 6, 7, 8, 9, 10, 11-12, 13, 15, and 16). An attempt was made to keep the cylinders with ratio >0.8 (length/diameter), and the number of cylinders vary for each sample drilled (Figure 8.13).



Figure 8.13 Example of cylinders drilled for sample #1 at C8 ply banded (a) sample before and (b) after drilling.

All 125 mini-cores (cylindrical samples #1, 4, 5, 6, 7, 8, 9, 10, 11-12, 13, 15, and 16) for C8 ply banded drilled perpendicular to band have been described by the log-normal distribution, however, results are omitted for brevity (Figure 8.14). Since data for those 125 mini-cores belongs to an individual ply, the results are grouped together into one single distribution to be compared with other plies and orientations. The maceral analysis of these samples (not completed at time of writing) will determine whether the data spread is random or is related to the microstructure and composition of the samples from within the banded ply.

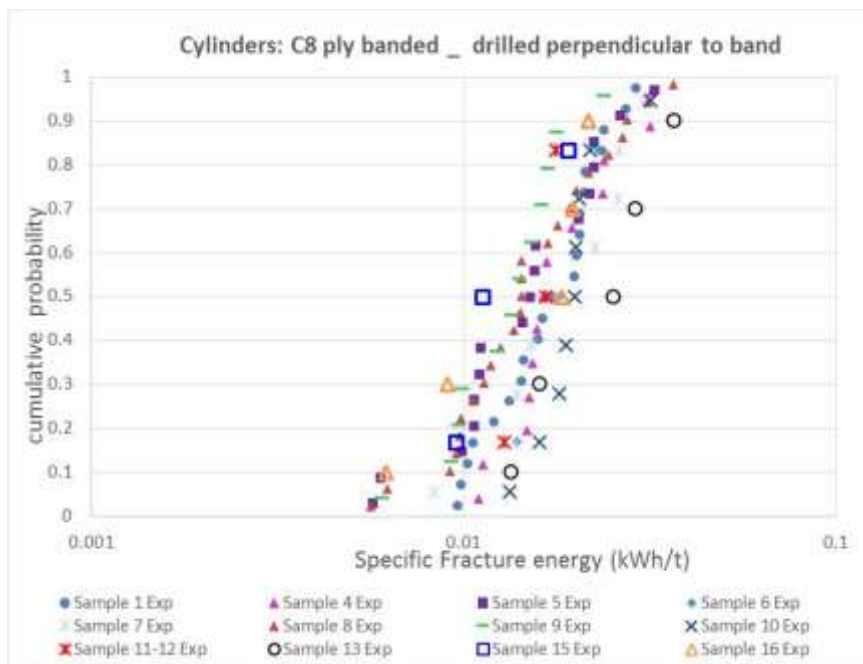


Figure 8.14 Specific fracture energy distributions for sub bituminous coal C8 ply banded of 125 mini-core cylinders ($\approx 12\text{mm}$ in diameter and ratio >0.8) of subbituminous coal.

8.4.2.2 Compare cylinders drilled perpendicular to banding: C8 ply banded versus C6 ply dull coal

The 125 mini-cores (cylinders samples #1, 4, 5, 6, 7, 8, 9, 10, 11-12, 13, 15, and 16) for C8 ply banded are compared with 16 mini-cores (cylinders sample #17) drilled at the C6 dull ply, all perpendicular to band. The trends showed some variance for the specific fracture energy between the two plies (Figure 8.15). The type effect between C8 banded and C6 dull drilled perpendicular to band is observed as dull samples are slightly stronger and thus require more energy to fracture.

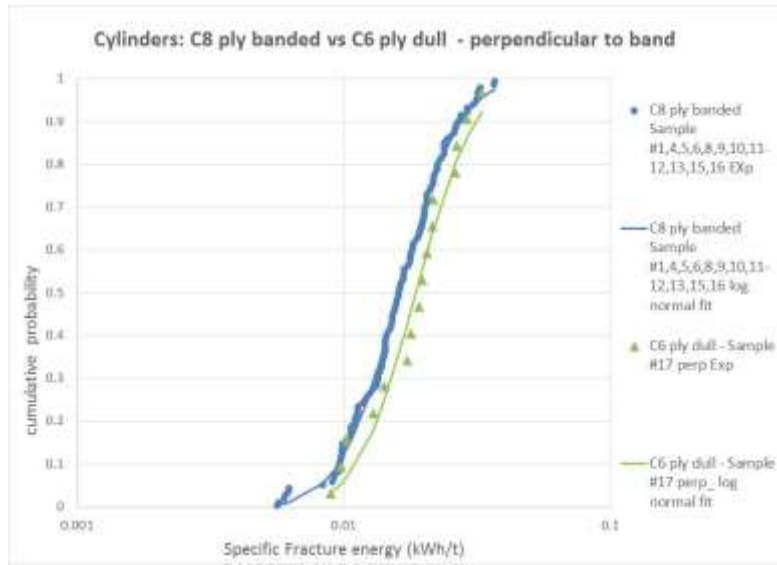


Figure 8.15 Specific fracture energy distributions of cylinders drilled perpendicular to band. Lines represent the fit to the log-normal distribution.

8.4.2.3 Compare cylinders drilled parallel to banding: C8 ply banded versus C6 ply dull coal

Fracture energy distributions for cylindrical samples of coal drilled parallel to bands are presented in Figure 8.16. The SILC data is described by the log normal distribution. Comparison between the results for C8 ply banded and those for C8 ply banded with white marks demonstrate that the richer vitrain (i.e. more brittle) C8 ply banded requires less energy to fracture. Whether these differences are significant at the rock mass scale is yet to be determined.

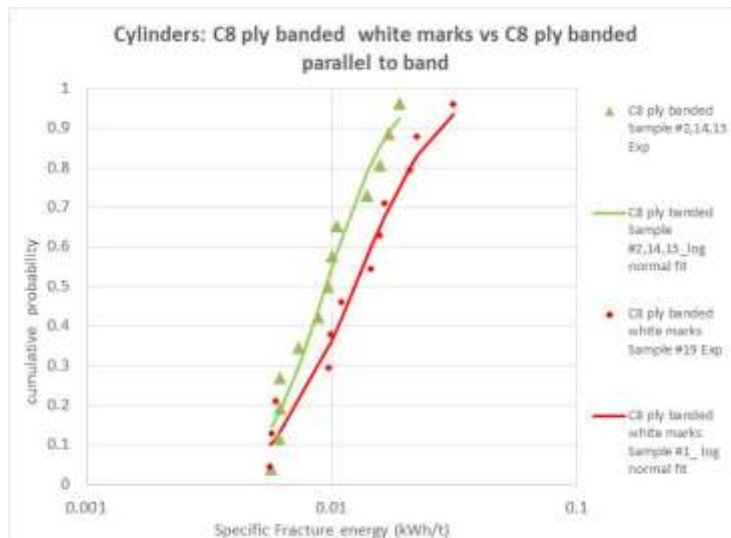


Figure 8.16. Specific fracture energy distributions of cylinders drilled parallel to bands. Lines represent the fit to the log-normal distribution.

8.4.2.4 Compare cylinders drilled parallel versus perpendicular to banding

Figure 8.17 shows the distributions of cylinder fracture energy for coal drilled perpendicular and parallel to banding plotted together. It is evident that the SILC can discriminate between the cylinder orientation and the data can be effectively described by the log-normal distribution. Overall, the SILC impact orientation for cylinders showed tougher behaviour perpendicular to band versus parallel to band, and the differences are quite significant for C8 ply banded (red and blue data).

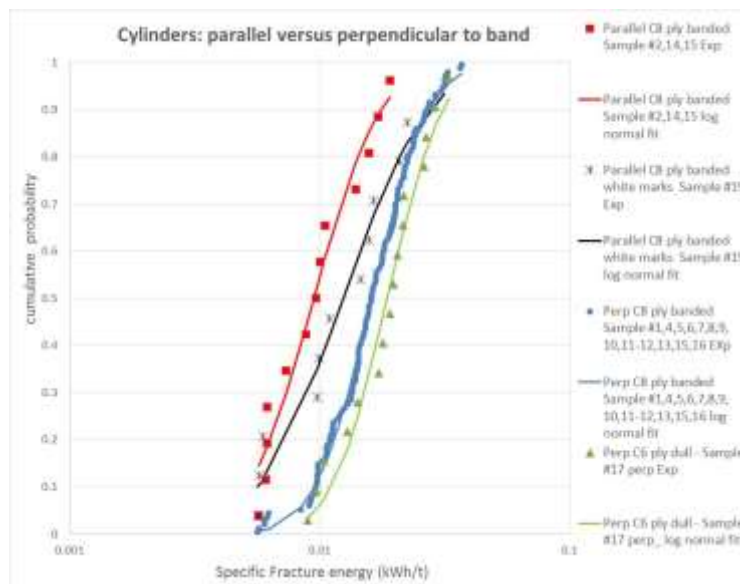


Figure 8.17 Specific fracture energy distributions of cylinders drilled perpendicular and parallel to bands. Lines represent the fit to the log-normal distribution.

8.4.2.5 Tensile strength and UCS on cylinders

Despite the natural heterogeneity of coal, and errors associated with test analyses, the variability within the data can also be related to the cylinder shape (i.e. length/diameter). The overall observation shows cylinder shape influenced the result with stumpy cylinders <0.8 being tougher than those at 0.8 or above, so only those latter results are used for comparison.

As previously discussed, the relationship between BTS (Brazilian tensile test) and direct tensile strength test (DTS) can be calculated using Equation 9. The estimated tensile strength results for C8 ply banded (125 mini-cores) and C6 ply dull (16 mini-cores) are shown in Figure 8.18. The mean DTS values being 2.9 and 3.6 MPa, while the standard deviation is 0.8 and 0.9, respectively.

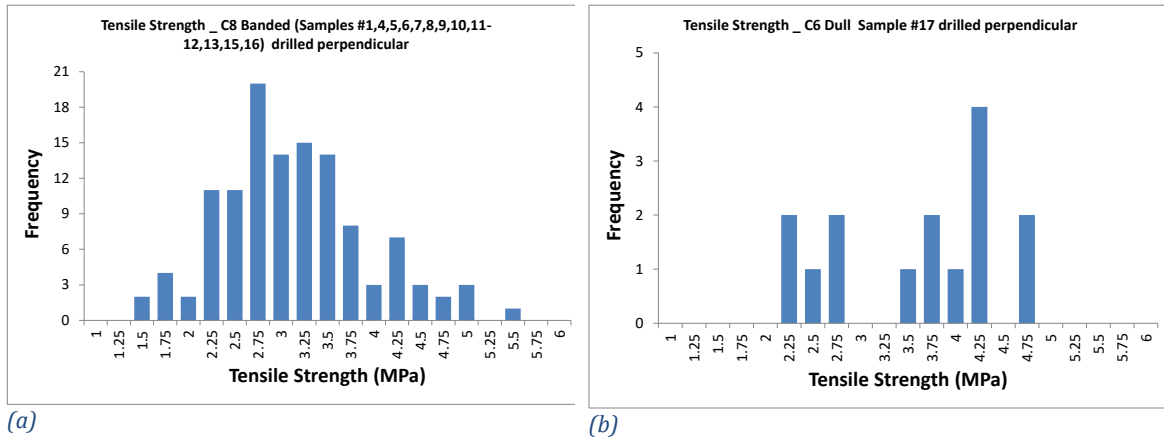


Figure 8.18 Histograms for DTS values estimated from BTS for (a) C8 ply with banded coal and (b) C6 ply with dull coal.

The authors used two calculations to compare the UCS results derived from BTS cylindrical specimens (Equation 10 and Equation 11). Then, the methodology described by Perras and Diederichs (2014) is assumed here as a verification criteria. Thus, the authors looked at triaxial testing results reported by Medhurst and Brown (1998) where $m_i = 19.4$ was considered to be representative of the bituminous coal dull category. If the same value of m_i is assumed for sub bituminous coal, the UCS calculation from Altindag and Gurney (2010) provides a close approximation. The comparison between C8 ply banded and C6 ply dull show the mean axial UCS (perpendicular to band) values being 57.0 and 72.5 MPa, with the standard deviation being 16.6 and 18.1, respectively (Figure 8.19). Histograms for UCS values estimated for (a) C8 ply banded and (b) C6 ply dull (Altindag and Gurney, 2010).

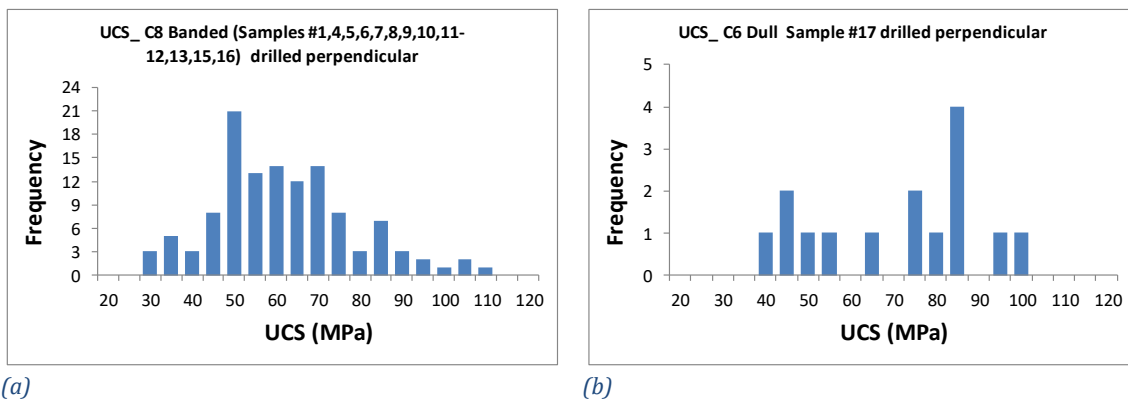


Figure 8.19 Histograms for UCS values estimated for (a) C8 ply banded and (b) C6 ply dull (Altindag and Gurney, 2010).

Below, the empirical Hoek-Brown constant m_i which varies with the respect of the rock itself (e.g. coals with different brightness profiles present distinct m_i constant values), is back-calculated (Equation 12) assuming Altindag and Gurney (2010) is valid for sub bituminous coal. The comparison between C8 ply banded and C6 ply dull show the mean and standard deviation m_i values being 19.6 ± 0.4 and 19.9 ± 0.4 , respectively (Figure 8.20).

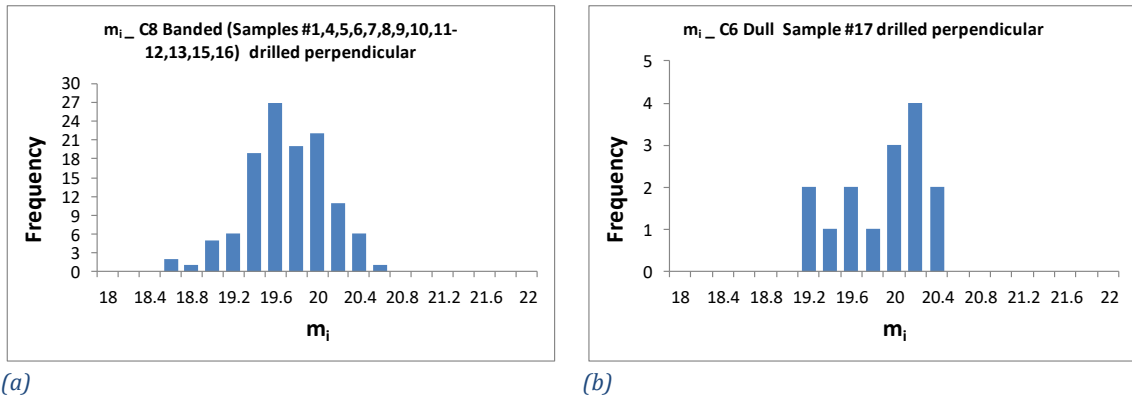


Figure 8.20 Histograms for m_i values estimated for (a) C8 ply banded and (b) C6 ply dull (Altindag and Gurney, 2010).

8.4.2.6 SILC - Particles

SILC tests on different particle size fractions obtained from the drop weight tests are yet to be analysed in more detail. The initial thoughts were that particles could show the size effect, as well as being generated for use in testing some geomechanical principles.

Preliminary analysis indicates the particle strength and particle fracture energy are affected by particle size. The effect of particle size on fracture characteristics of C6 ply dull and mudstone are demonstrated in Figure 8.21 and Figure 8.22. Note that all the particles tested, both C6 ply dull and mudstone, belong to the same initial set of particle size fractions derived from the JK DWT. That is, the C6 ply dull, presents single-particles derived from an initial set where the size distribution is equal to 31.5x26.5mm and 0.25 kWh/t energy; while the mudstone, initial set had the size distribution equal to 63x53mm and 0.1 kWh/t energy. In both cases, smaller sizes have larger specific fracture energies than larger particles. In other words, smaller size particles present greater coal strength.

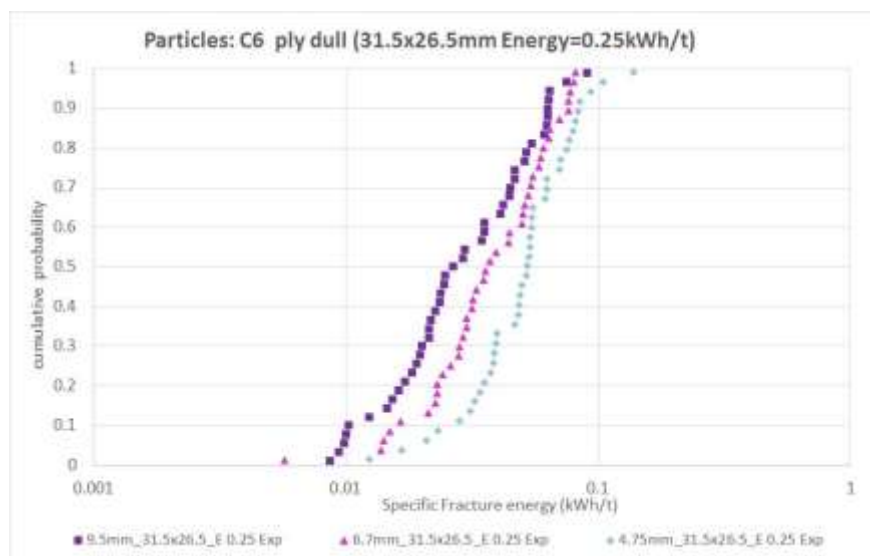


Figure 8.21 Particle fracture energy distributions for C6 ply - dull of the mine sub bituminous coal comparing different size distribution.

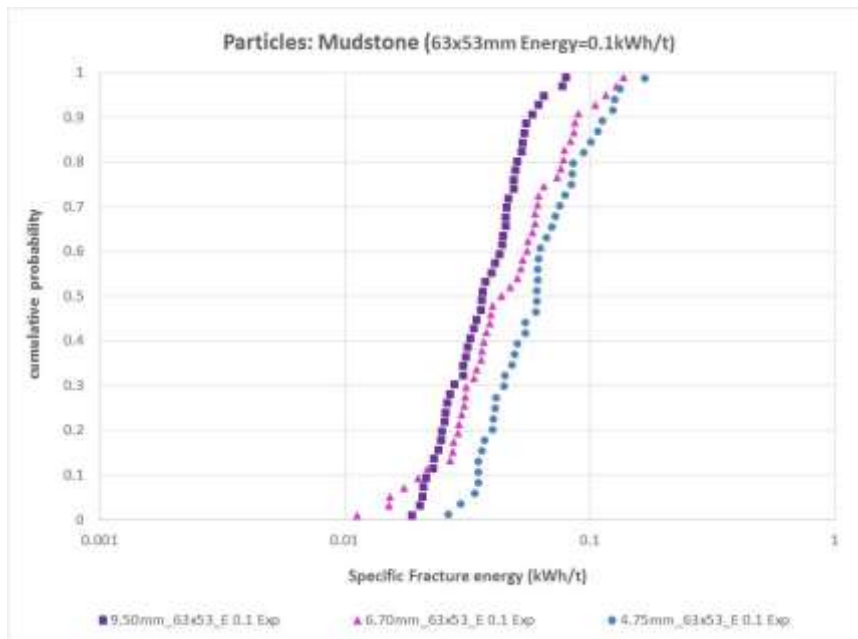


Figure 8.22 Particle fracture energy distributions for mudstone of the mine comparing different size distribution.

However, the above statement starts to fail if comparison is made between samples originating from distinct sets (i.e. different size distribution and energy results of JK DWT tests compared together). This observation can be verified in Figure 8.23 where the smaller particles (4.75 mm) for C6 ply dull derived from an initial set (size distribution 63x53mm and 0.4 kWh/t) is compared with bigger particles (6.7 and 9.5 mm) from a distinct set (size distribution 31.5x26.5mm and energy 0.25 kWh/t). This behaviour was again observed for D8 ply banded low ash sample of the mine sub bituminous coal (Figure 8.24).

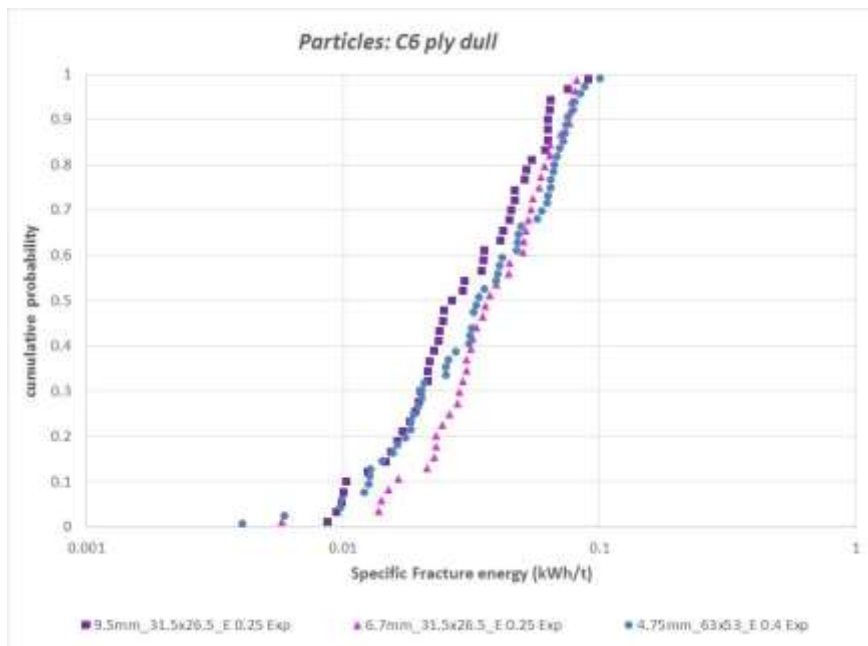


Figure 8.23 Particle fracture energy distributions for C6 ply - dull of the mine sub bituminous coal comparing different size distribution.

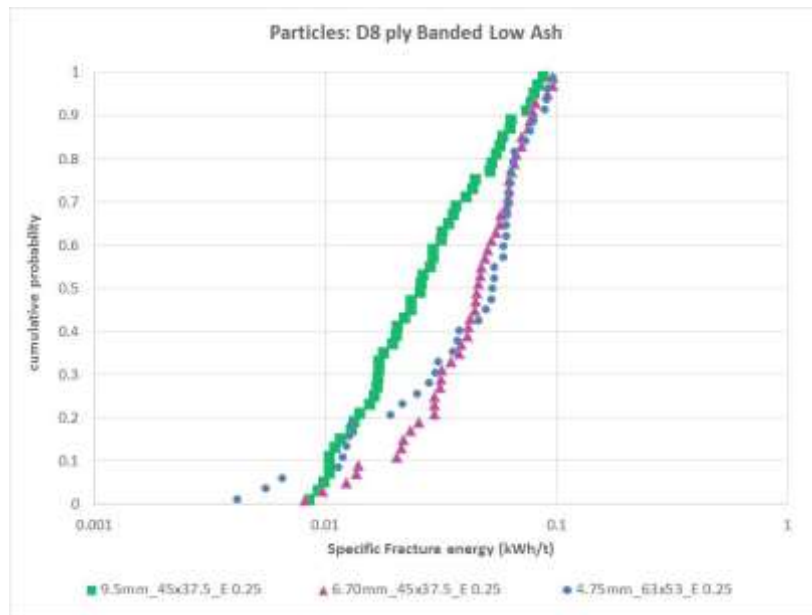


Figure 8.24 Particle fracture energy distributions for D8 ply – banded low ash of the mine sub bituminous coal comparing different size distribution.

8.4.3 Tensile strength and UCS on particles

The estimated tensile strength and uniaxial compressive strength for D8 ply low ash banded indicate that the variability in the results is significant. In order to validate the results, an assumption that $m_i = 20.6$ is made to constrain the maximum interval (Appendix 2). Further studies are required to support the assumption made, as well as identify the best option on how to explore the m_i values on particles.

Table 4 presents a summary for the SILC results obtained for particles and cylinders.

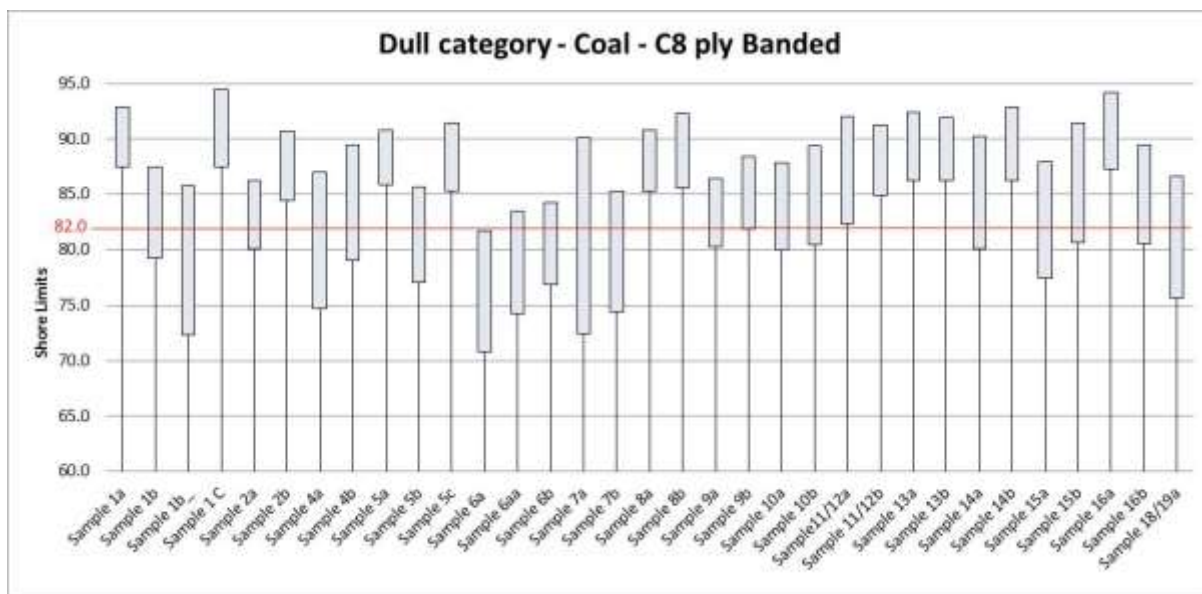
Table 4 Summary SILC results for particles and cylinders.

Rock material	Size	SILC:					
		Tensile Strength (MPa)		UCS (MPa)		m_i	
		Cylinders	Particle s	Cylinders	Particle s	Cylinders	Particles
Coal C6 ply: Dull	Φ 12mm	3.6±0.9		72.5±18.1		19.9±0.4	
Coal C8 ply: Banded	Φ 12mm	2.9±0.8		57.0±16.6		19.6±0.4	
Coal D8 ply: Low Ash Banded	9.5mm 45x37.5_E 0.25		3.0±1.2		57.5±22.6		19.6±0.6
	6.70mm 45x37.5_E 0.25		3.3±1.5		62.0±24.4		19.7±0.6
	4.75mm 63x53_E0.25		4.1±1.0		80.1±18.6		20.1±0.4

8.4.4 SSRH

The hardness test using a SSRH measures the resistance of coal materials to penetration by impact. 20 shore measurements were taken on 33 confined coal samples from C8 ply banded

sample from the mine and averaged for each to compare results between samples. The results are calibrated against the mean shore measurements for pure hardened high-carbon steel, which gives about 82(±3) shore units, approximated tensile strength is 240 (±15) psi or 1.65 (±9) MPa. All upper and lower limits (mean plus or minus standard deviation) of shore measurements done on dull category of coal - C8 ply banded are given in Figure 8.25. The plot shows that the majority of the hardness property results for dull category of coal - C8 ply banded are similar or slightly higher than the results for the pure hardened high-carbon steel. The shore hardness for all 33 samples is average 85.1±4.2. The distribution patterns of shore measurements are best understood by examining the distributions for each sample. The distribution of shore results for each C8 ply banded coal sample is shown in Appendix 3. The hardness and tensile strength are empirically related. The estimation of UCS is then considered 10 times bigger than the tensile strength. Therefore, the estimation of UCS from the SSRH test varies between 15.5 and 18.7 for the same ply (C8 ply banded – dull category); an average of 17 MPa is assumed.



*Note: red line represents the mean shore measurements for pure hardened high-carbon steel which gives about 82 (±3) shores.

Figure 8.25 SSRH test of dull category from the C8 ply banded mine sub bituminous coal.

Table 5 Average SSRH results shore and tensile strength (approximate) of dull coal C8 ply banded.

Sample	Number of tests	Shore mean	Standard deviation	Tensile Strength (MPa) (approximate)
Sample 1	4	85.9	4.3	1.7651
Sample 2	2	85.4	3.1	1.7616
Sample 4	2	82.5	5.7	1.6720
Sample 5	3	86.0	3.3	1.7697
Sample 6	3	78.6	4.6	1.5490
Sample 7	2	80.6	7.1	1.6134
Sample 8	2	88.5	3.1	1.8547
Sample 9	2	84.3	3.2	1.7133
Sample 10	2	84.4	4.2	1.7306
Sample 11/12	2	87.7	4.0	1.8237
Sample 13	2	89.2	2.9	1.8685
Sample 14	2	87.4	4.2	1.8237
Sample 15	2	84.4	5.3	1.7306
Sample 16	2	87.9	4.0	1.8375
Sample 18/19	1	81.2	5.5	1.6272

Unfortunately, only one sample (sample #5 c) from C8 ply banded tested with the SSRH presented a vitrain (bright) band thick enough to allow results for bright and dull categories from within the same sample to be compared (Figure 8.26). The shore hardness for the dull category is an average 88.4 ± 3.1 while the bright band is an average 63.8 ± 4.2 . The estimation of UCS for this particular block—taken into consideration the difference between the dull and banded coal lithotypes—is 18.4 and 11.2 MPa, respectively. The difference between the dull and bright bands for this coal sample is about 7MPa.

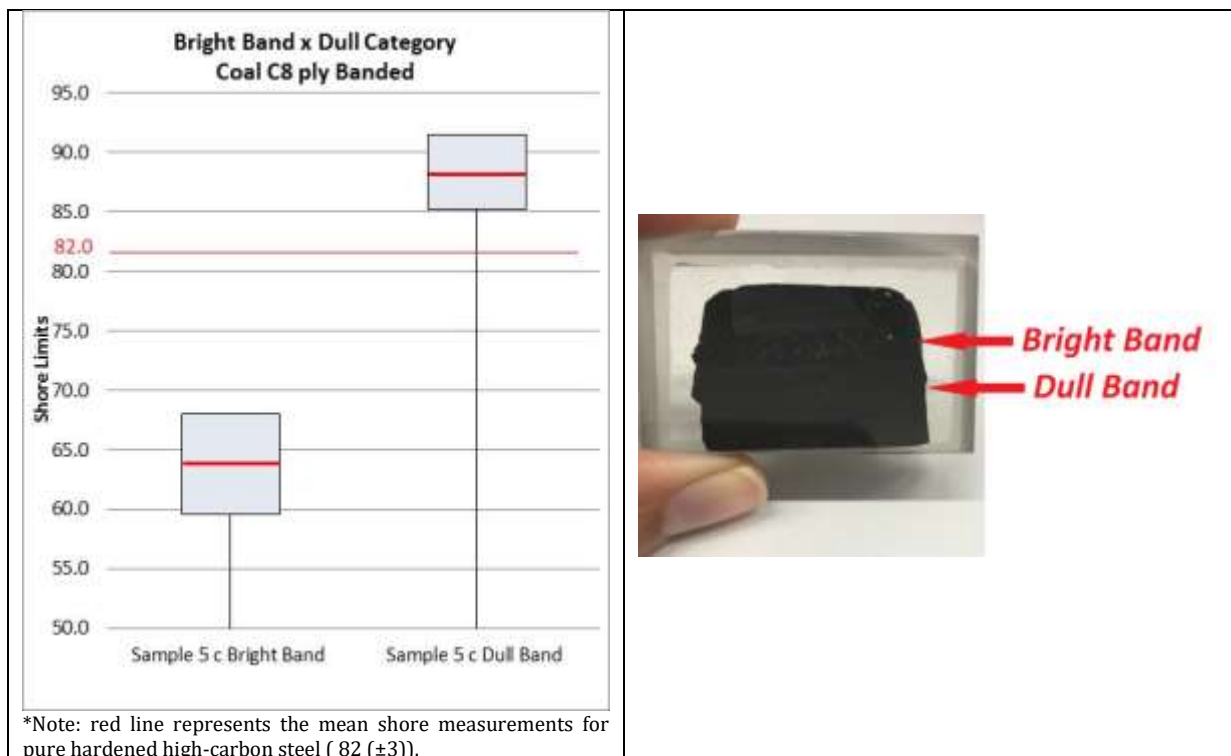
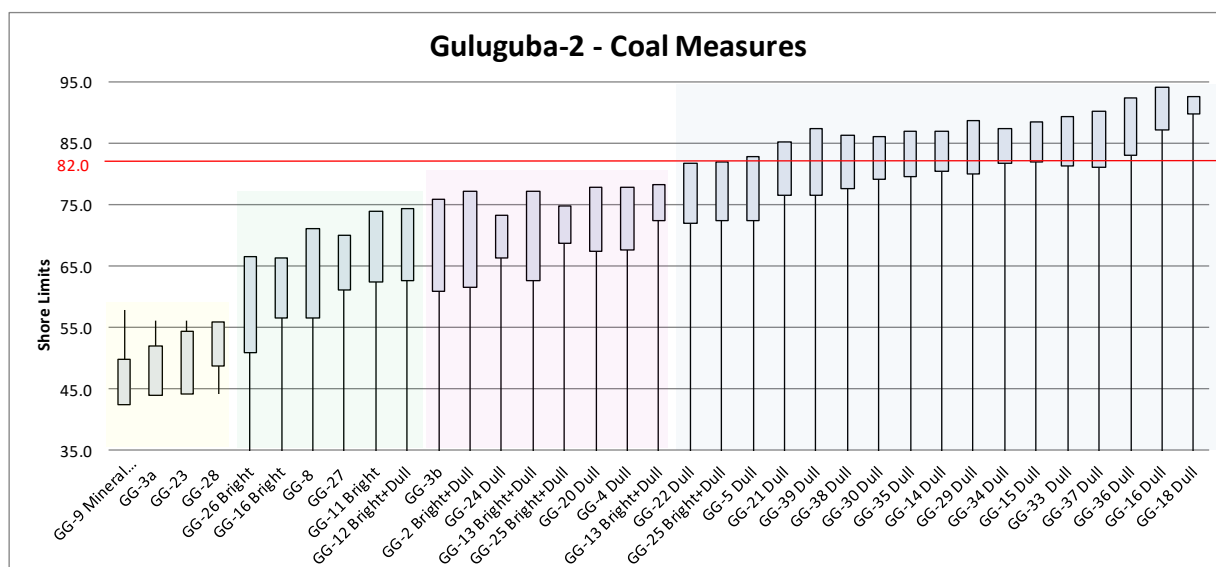


Figure 8.26 Bright band versus dull category from C8 ply banded, the mine sub bituminous coal.

Guluguba-2 borehole samples confined into epoxy blocks are illustrated for comparison within data from outcrop (the Walloon Coals presented above). The samples are of similar coal rank; therefore, some similar behaviour is expected. The dull category consistently averaged 83.5 ± 4.0 , whereas an individual bright or vitrain band averaged 64.3 ± 6.0 (Figure 8.27). Sample GG-26 presents the highest telovitrinite composition followed by GG-11 reported as 71.3 and 59.4%, respectively. The banded coal lithotypes are variable between the bright and dull and it is often difficult to resolve individual vitrain bands as the composition of the “dull bands” are a combination of laminated thin telovitrinite, suberinite, detrovitrinite and liptinite macerals. The lowest shore hardness average of 48.9 ± 4.1 is supposed to be influenced by the mineral matter composition. Sample GG-9 is composed by 57.6% of mineral matter. The GG-16 is the next on the list for maceral composition equal to 22.4% for mineral matter, in addition to 10% telovitrinite. This is followed by GG-23 with 18.2% maceral mineral matter, and 18.4% telovitrinite. Petrographic results were not available for samples GG-3 (although thick bright and dull category are both quite evident), GG-27, and GG-28. Sample GG-8 presents 6% of maceral composition and 4.8% telovitrinite.



*Note: red line represents the mean shore measurements for pure hardened high-carbon steel which gives about 82 (± 3) shores

Figure 8.27 SSRH test at bright and dull samples from Guluguba-2 sub bituminous coal.

Neither C8 ply banded nor the Gulugubba-2 present fracture propagation post-indentation. In other words, no fracture was observed from the anvil dropping onto the polished coal surface, which is really different to more brittle bituminous coals in which bright vitrain bands shatter and are much weaker (value) than dull lithotypes (value) at same rank.

Summary of the SSRH results is given in Table 6.

Table 6 Summary SSRH results.

	Outcrop data The mine		Borehole data Guluguba-2	
	Shore (mean)	Tensile Strength (MPa)	Shore (mean)	Tensile Strength (MPa)
dull category	85.1±4.2	1.74	83.5 ±4.0	1.72
bright and dull categories	-		71.2±5.3	1.3
bright category	63.8±4.2	1.12	64.3±6.0	1.12
High % mineral matter	-		48.9±4.1	0.81

8.5 Conclusions

Rock material with brittle behaviour can be characterised by fracture. In this study, strength characterisation of sub bituminous coal using principles from mineral processing is attempted. If successful, it provides an alternative means for obtaining geomechanical properties of coal where core, in particular core of different sizes, is not available. Preliminary results are as follows.

- The **JK DWT** tests illustrated the expected increase in breakage with increasing impact energy, and particles of banded coal broke more easily than dull coal. The JK DWT tests show that larger particles tend to be easier to break than smaller particles for given lithotypes and impact orientation.
- The **JK DWT** tests in comparison to results from higher rank coals support the harder, tougher and stronger nature of sub bituminous coals relative to bituminous coals, which might result in different responses of the reservoir to production and the integrity of the borehole in the coal seam (acknowledging that clay behaviour is not accounted for). This might also be reflected in the shrinkage and swelling behaviour of the coal itself during desorption and production, and this is a future research avenue.
- The brittle behavior of coal material is observed during the **JK DWT** and **SILC** tests. The very rapid break-up shows the explosive nature of coal, as the fragments tend to fly away/be ejected with considerable energy.
- The **SILC** tests using cylinders drilled on distinct sub bituminous coal plies (banded, banded with white marks (i.e., clay lenses) and dull coal) tested the variation in fracture toughness by considering the coal type effect. The SILC on cylinders also demonstrates the energy impact orientation (axial versus diametrical) on results, as cylinders showed greater toughness perpendicular to band than parallel to band.
- For **SILC** tests on cylinders, it is assumed that Altindag and Gurney (2010) calculation gives a reliable estimation of uniaxial compressive strength (UCS) for sub bituminous coal. The empirical Hoek-Brown constant m_i , which varies with respect to the rock itself (e.g. different coal lithotypes within a brightness profile present a distinct m_i constant value), ranges between 19.6 ± 0.4 and 19.9 ± 0.4 for banded and dull sub bituminous coal, while dull bituminous coal presents $m_i = 19.4$ (Medhurst and Brown, 1998).
- The tensile strength estimated from the **SILC** tests using cylinders is higher than that from the **SSRH**. Averaged values are 2.9 ± 0.8 and 1.7 ± 0.1 for a C8 ply banded coal, respectively.

- The unconfined compressive strength (UCS) is estimated using Altindag and Gurney (2010) calculation on **SILC** tests for cylinders. The UCS results for ply banded and dull coals show the mean axial UCS (i.e. perpendicular to band) values being 57.0 ± 16.6 and 72.5 ± 18.1 MPa for the intact rock. All of these estimations are stronger than the 10-14 MPa for the intact rock (or 6-8 MPa rock mass) commonly used for bituminous coal.
- Overall, the **SILC** using cylinders can be used for initial and preliminary estimation of the rock mass strength for soft rock such as sub bituminous coal. In the absence of, or limited amount of triaxial data, the SILC provides an alternative test to obtain parameters for geomechanical reservoir practical design.
- The **SILC** tests using particles (which were produced by the **JK DWT** tests), show higher variability, and also that there is cumulative damage carried by the single particles. The specific fracture energies of similarly sized daughter particles are lower when produced from higher drop weight energies, reflecting microfracturing in the sample. Hence, care is needed when analysing energy, size and type effects from all **SILC** tests on particles, which suggests testing on chips produced through open hole drilling might produce random results. These results might be used to investigate energy delivery to coal for induced fracturing.
- The **SILC** tests on particles show less consistent results than for cylinders. The particles have random shapes in addition to different sizes, and this affects the calculation of fracture energy, stiffness and strength. The different fragmentation response to impact energy between the particle sizes resulting from the **SILC** tests do however contribute to understanding size dependent behaviour that is important for upscaling from the laboratory samples to the rock mass or reservoir behaviour of coal. For our tests, the particles were obtained from drop weight tests at different energies, and a cumulative damage or conditioning was also observed in the **SILC** results: i.e. the same particle size derived from a different test energy showed microfracturing at increased energies. Therefore analyses of particles must take this into account, and compare particles on the basis of size and also the energy of fragmentation. Ideally one would standardise the drop weight test or crushing to obtain particle size fractions for testing. This has implications for the use of bulk chip samples from drill holes where there is no control on the fragmentation energy. Further investigation on how to explore the constant m_i and how to filter the upper limit (e.g. $m_i \leq 20.6$) is a future research avenue for **SILC** tests using particles.
- While the **SILC** test using mini core cylinders (12mm in diameter) generates more consistent results than the particles tests, the inherent variability of laboratory coal data is still observed.
- The **SSRH** results show that sub bituminous coals are really hard (averaging 85.1 ± 4.2 shore units across all 33 samples). No fracture propagation was observed from the anvil dropping onto the polished coal surface (indeed little indentation was observed in either bright or dull bands) which is substantially different to more brittle bituminous coals in which bright vitrain bands shatter and are much weaker than dull lithotypes at the same rank (Klawitter et al., 2015).

- The **SSRH** allows an estimation of tensile strength using the conversion table supplied with the equipment (IMAI SIKENKI Co.). If it is assumed that the provided conversion into tensile strength is an estimation of the true tensile strength of intact rock, then the **SSRH** show smaller values of tensile strength when compared to **SILC**. The **SSRH** of the finer grained non banded (dull) lithotypes consistently average 85.1 ± 4.2 shore (tensile strength is about 1.74 MPa), whereas an individual bright band averages 63.8 ± 4.2 shore (approximately 1.12 MPa of tensile strength). Comparison of data from outcrop and core (Guluguba 2) for different lithotypes showed very similar results.
- The **SSRH** test on block samples, all dull coal of similar rank, from borehole Guluguba-2 and outcrop (The mine – Walloon Coals) present quite similar **SSRH** results with averages of 83.5 ± 4.0 and 85.1 ± 4.2 , respectively.

The data are still being analysed, and the next steps involve developing a strength index and test the use of these properties in a simulation. Ideally, one should test a series of cores of increasing size.

9 Conclusions, Outlook and Recommendations

Although much more work can (and should) be done to explore the assembled data base of seismic and well data, it is possible to affirm that the combined results of this Faults and Fractures Project with the Surat Geological Framework form the basis for future studies and research.

In particular, further work is recommended on:

Time-depth conversion

An extension to this project would include the development of a layered velocity model for the basins based on this checkshot data and the time depth relations resulting from the well tie database supplemented with time-depth relations developed from synthetic matching. A Python script written by Iain Roger has been used to search through the QDEX database to find all well completion reports with velocity surveys. This work reveals over 700 checkshot surveys for the basin. This database could be used to develop a comprehensive, layered velocity model for depth conversion.

Higher resolution well to seismic ties

Comments on correlations

An important, unanticipated result of this project is the clear demonstration that current correlations (OGIA2016) are not internally consistent with all available data (core, logs, seismic). The primarily lithology-based, formation-top and subsequent inter-well correlations are often not in agreement with correlations which would be indicated by seismic reflector continuity and character.

Previous studies, including the 2015 milestone report for this project, have not benefited from the extensive seismic database assembled in 2016 for the final stage of the Fault & Fractures Project. An additional 4000 lines were added and interpreted to provide a basin wide view of the variations in Cenozoic deformation, as opposed to the original prioritisation of the eastern margin fairway. 3D seismic volumes were also utilized for detailed field scale studies during the course of the interpretation project. As discussed, new correlations have been made which are closely tied to the seismic data, based on a sequence stratigraphic framework which develops chronostratigraphic surfaces consistently correlative basin wide. Earlier work by several authors (e.g. Wells et al., 1993; Hoffman et al., 2009; Hodgkinson et al., 2011, and references therein) have proposed sequence boundaries for the pre-WCM sediments. The rigorous seismic well tie correlation possible with the nearly 600 well ties in this study to support their overall discussion of depositional succession. These time-equivalent boundaries also provide a stronger basis for understanding the succession of deformation events and, more importantly, provide a more robust framework for dynamic modelling (since 'flow zones' are best separated and mapped by correlative 'fining upwards' cycles).

A statistical comparison of OGIA 2014 vs. CSG company correlations was originally presented in the Surat Framework Project, Milestone Presentation, Oct-2015. This display of differences for lithologic correlations with CSG company correlations has since been updated from that display using a larger bin size (10m) and is shown in Figure 9.1. As previously discussed, the CSG company correlations had been internally benchmarked for agreement by circulating representative cross sections. This confirmed close agreement and consistency for primary points of correlation (Pinder, pers comm. ,TWG Meeting 2016). In the main, company picks corresponded to OGIA picks, although the deliberate shift (for flow modelling purposes) in the top Springbok pick from wirelines was obviously in disagreement with previous picks and correlations. Over 80% of the "Springbok" correlations had greater than a 10m discrepancy with a near-equal distribution across almost 100m. Numerous seismic well ties also illustrate this inconsistency. This depositional boundary, or at least a correlative reflection event, among others is imaged by the seismic data and may assist in improved correlations of these sequences.

Significant seismic horizons can be interpreted as representing depositional, chronostratigraphic boundaries in many sedimentary basins. Comparison of log (and core) formation top evaluation and inter-well correlation with the seismic data can be used to provide an independent test or benchmark which assures better internal consistency of stratigraphic correlations. Three representative profiles showing the seismic well ties with OGIA correlations and observed inconsistency at the Springbok correlation compared to seismic data beginning with Figure 9.1. Each of the 3 wells has a Springbok correlation in a different place relative to the interpreted seismic horizon (J50.2) which correlates to a consistent stratigraphic boundary on log cross section. The impact on groundwater modelling would be to create interpolated flow-zone the properties are constructed from and correlated between different genetic units between which are likely to be extensive, even if relatively thin, aquitards (sequence boundaries).

No previous study develops or presents an integrated correlation of depositional surfaces. However, historically, a small number of papers (e.g. Wells et al., 1993; Hoffman et al., 2009; Hodgkinson et al., 2011, and references therein) have discussed sequence stratigraphic concepts but did not demonstrate these with both well ties and seismic cross sections.

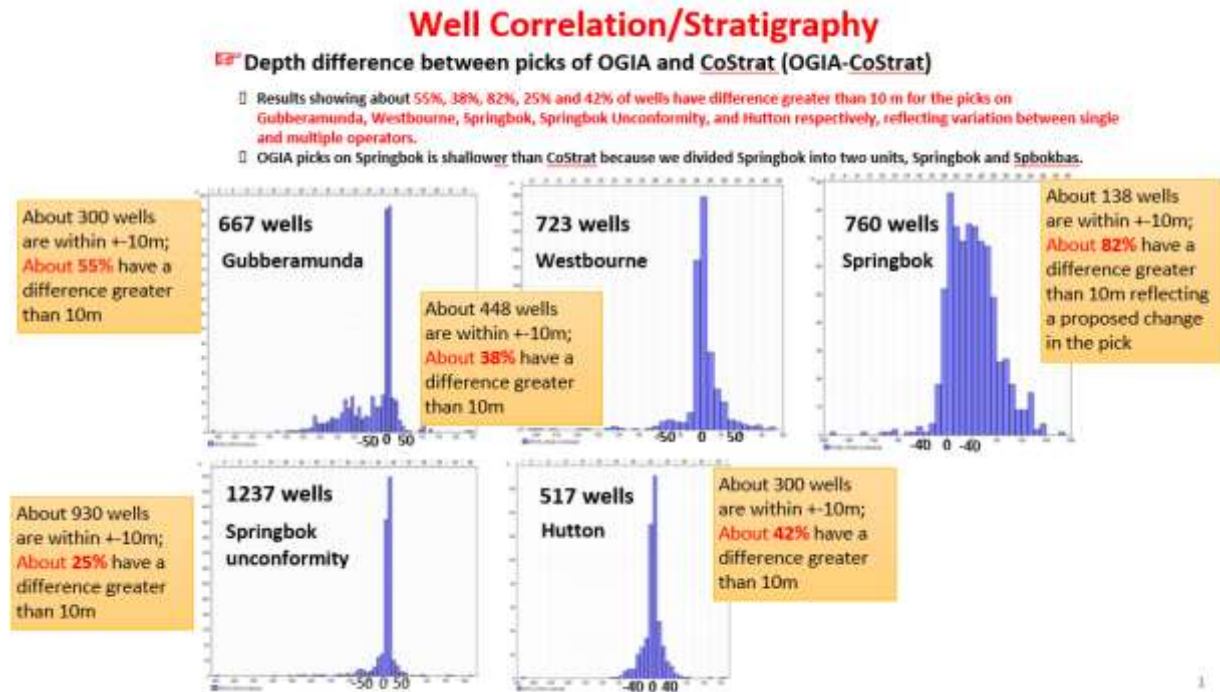


Figure 9.1 Comparison between OGIA well picks and those defined by well-seismic integration. Figure is from the Surat Framework Milestone Report, Oct-2015, bin size is increased from the original display to 10m. Annotation is added for statistical clarity. The broad range of difference (~100m) for the Top Springbok illustrates demonstrates the inconsistency. [See footnote⁴ for historical context]

Figure 9.2 and an example from the Lauren area (Figure 9.3) show OGIA lithologic correlations relative to a consistent seismic horizon above the top WCM. The wells are adjusted for a consistent fit of the “Spuncon” correlation with the seismic event that marks the nominal top WCM. The yellow horizon represents a spatially consistent seismic reflector that has been correlated throughout the area on numerous seismic lines. It provides a consistent basis for comparison.

⁴ Note this figure 13 is updated by Dr Fengde Zou – it was originally developed in 2014 and has been updated several time since. *In the context of those times*, the match was considered fair or ‘good enough’ and the focus was necessarily on adjusting the top of the Springbok to establish some consensus on that key horizon for OGIA modelling purposes against a tight deadline. *However*, subsequent UQ analysis and seismic interpretation concludes that the mismatch may have significant implications, not least from a groundwater a modelling perspective and requires further work.

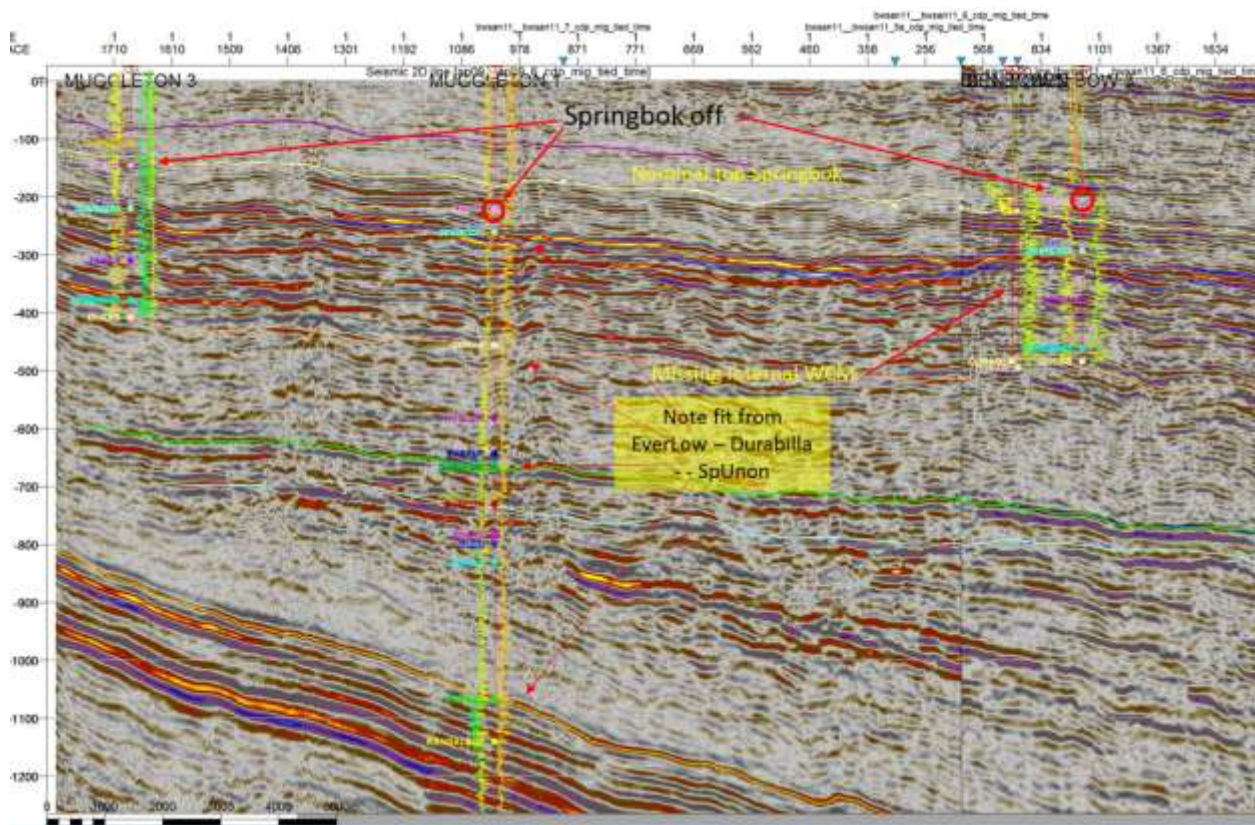


Figure 9.2 Representative profile showing inconsistent Springbok correlation in regional correlations (OGIA, 2015) with seismic profile. This is the Muggleton area near Reedy Creek.

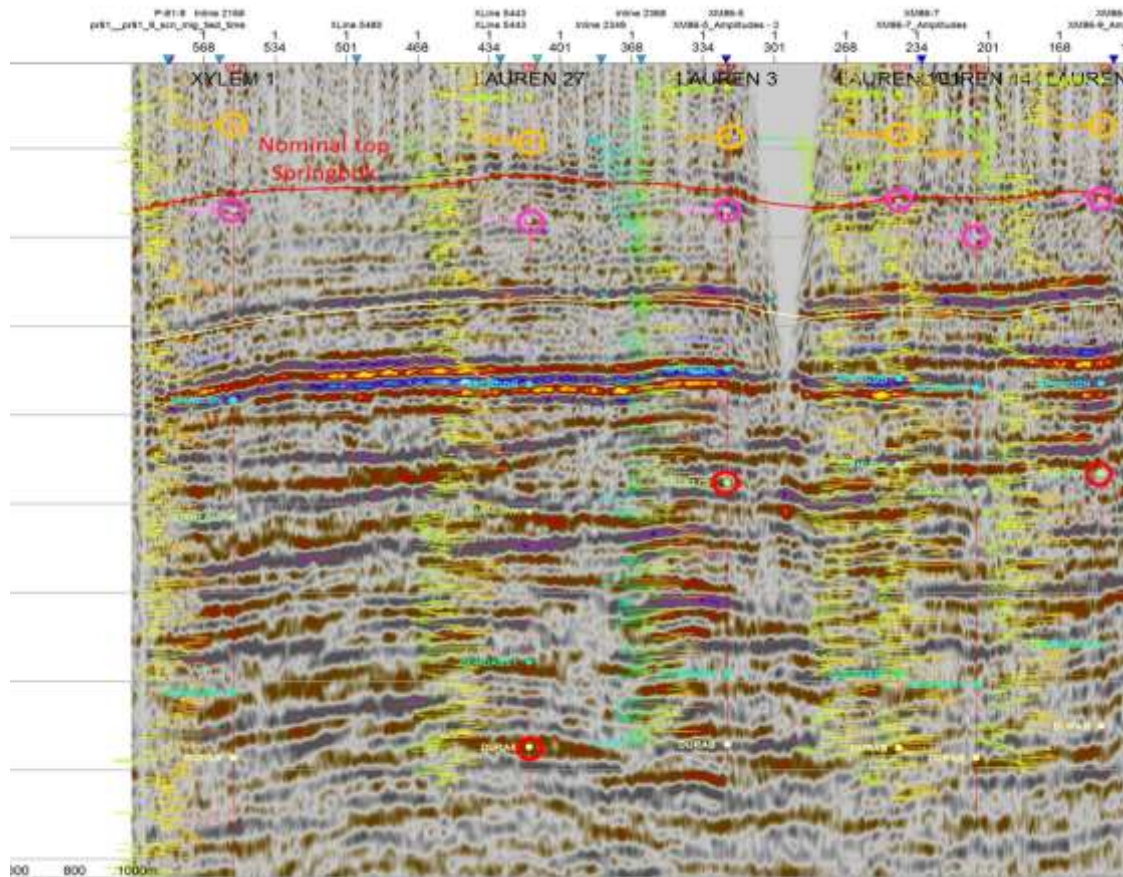


Figure 9.3 Lauren area profile with OGIA lithologic correlation inconsistency relative to interpreted seismic horizon.

In Figure 9.4, a third representative example is shown on a profile from the Burunga area. Here, one can see the relative consistency of the fit for the EverLow pick (consistent lithology) compared to the inconsistency of correlation in Evergreen and Hutton where the depositional system does not provide widespread lithologic units.

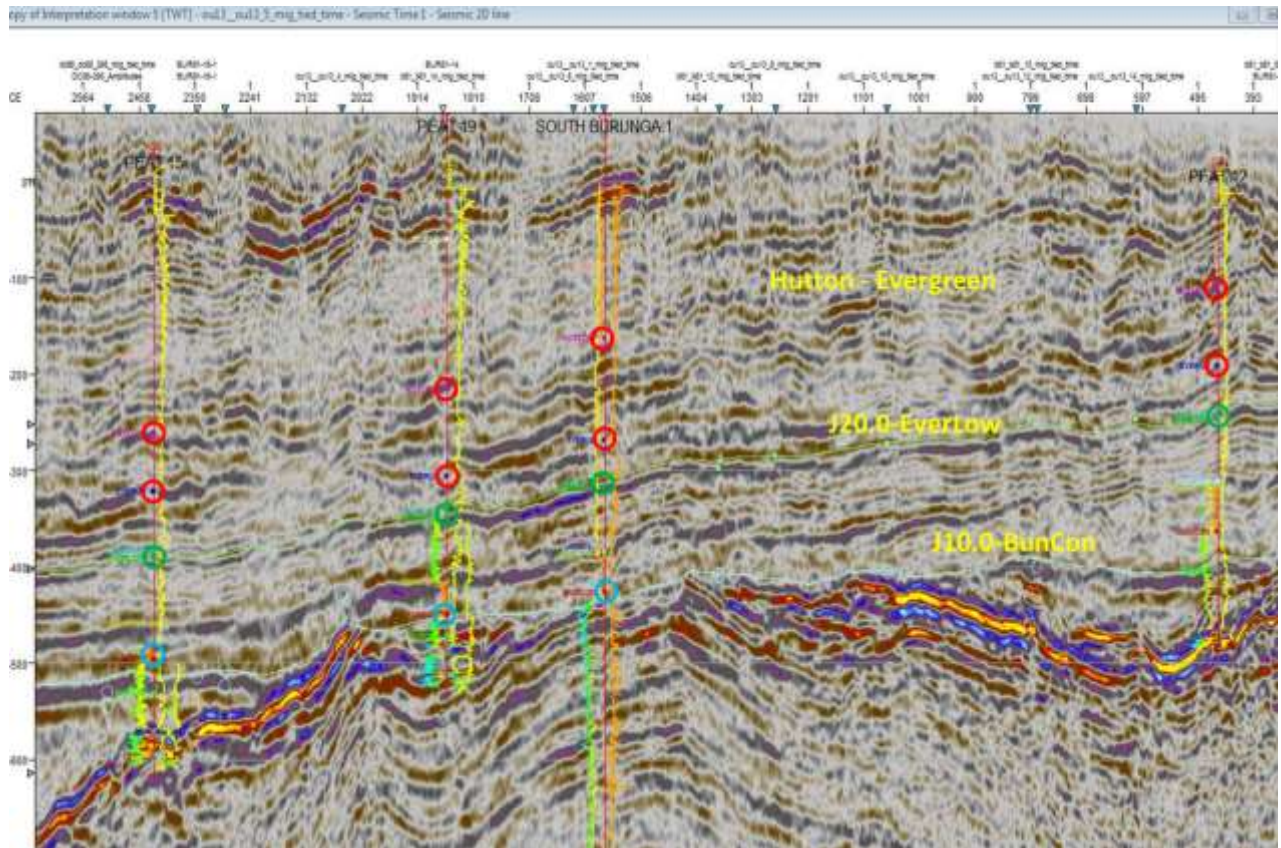


Figure 9.4 OGIA correlations from Burunga area profile.

In contrast, Figure 9.5 below shows a representative composite 2D profile through a series of Lauren wells with chronostratigraphic correlations. Wells are displayed using time-depth relationships developed from the integrated sonic log. The synthetic trace is developed from a standard reflection coefficient profile using sonic and density logs which is convolved with a zero phase wavelet found to best match the seismic data (data is vibroseis). The same wavelet is used for all wells. This synthetic trace is then time shifted to best fit the 2D data particularly at the higher amplitude events near the top WCM-Springbok. In general, the fits are very good.

Logs and correlation points are displayed using the adjusted time-depth relation. The profile is flattened, for ease of comparison, on the J50.2 (~intra-Springbok) which is a seismic horizon correlative to a consistent stratigraphic boundary. Close, consistent agreement with reflection data is observed, and sequence correlation is observed. Other points of correlation are also consistent with the reflection data within the WCM.

Correlations of formation tops between wells are considered “robust” in this study if there is internal consistency between core (where available), wireline and seismic data. Individually, each data-type yields a non-unique solution to formation top identification and inter-well correlation. **Inevitably “robustness” requires integrated and iterative interpretation of all**

these data together.

The recognition of this opportunity to improve depositional boundary correlations was an important conclusion from the Faults & Fractures Project. A separate project has been initiated in January 2017 to continue the development of a chrono-stratigraphic depositional architecture which will be fully integrated with the seismic data, with a more complete discussion of the issue.

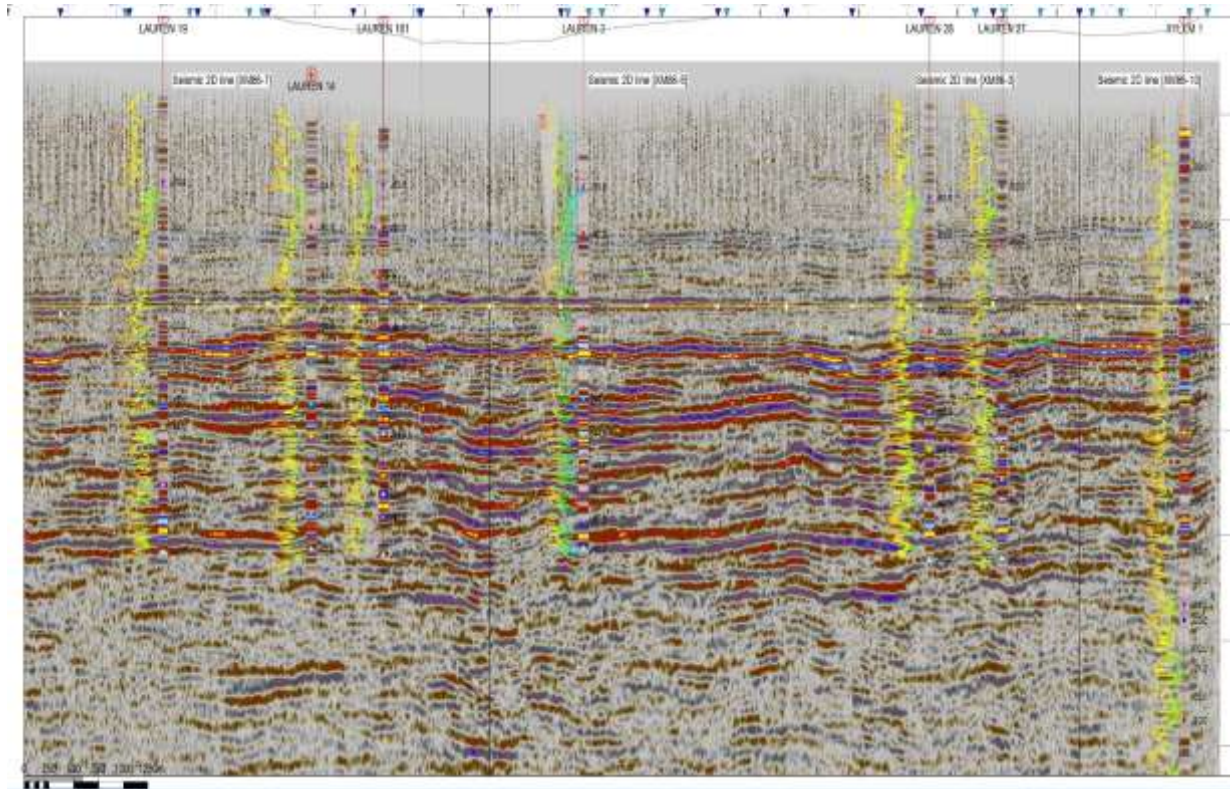


Figure 9.5 Representative profile showing integrated sequence stratigraphic correlations, Lauren area. Profile flattened on the J50.2 (above top WCM). Synthetic traces are shown to match seismic data. Note 6 correlated sequences within WCM.

10 Acknowledgement

“The parties acknowledge that copyright exists in the Licensed Data. The State of Queensland (Department of Natural Resources and Mines) gives no warranty in relation to the Licensed Data (including accuracy, reliability, completeness or suitability) and accepts no liability (including without limitation, liability in negligence) for any loss, damage or costs (including consequential damage) relating to any use of the Licensed Data.

11 References (by report section)

11.1 Regional geologic setting

Brown, R.S., Elliott, L.G. and Mollah, R.J., 1983. Recent exploration and petroleum discoveries in the Denison Trough, Queensland. *Australian Petroleum Exploration Association Journal* 23, 120-135.

Esterle, J.S. and Sliwa, R., 2002. Supermodel 2000 Bowen Basin, Report No. 676C. CSIRO Exploration and Mining.

Elliott, L.G., and Brown, R.S., 1988. The Surat and Bowen Basins – a historical review. In *Petroleum in Australia: the first century*. Australian Petroleum Exploration Association, Melbourne, 120-138.

Exon N.F., 1976. Geology of the Surat Basin, Queensland. Bureau of Mineral Resources, *Geology and Geophysics Bulletin* 166, 160-184.

Fielding, C.R., Gray, A.R.G., Harris, G.I. and Salomon, J.A., 1990. The Bowen Basin and overlying Surat Basin. In Finlayson, D.M. (ed) *The Eromanga-Brisbane Geoscience Transect: a guide to basin development across Phanerozoic Australia in southern Queensland*. Bulletin of the Bureau of Mineral Resources and Geophysics, Australia, 232, 105-116.

Finlayson, D.M., Leven, J.H. and Etheridge, M.A., 1988. Structural styles and basin evolution in Eromanga region, eastern Australia *AAPG Bulletin*, 72, 33–48.

Korsch, R.J., Totterdell, J.M., Fomin, T. and Nicoll, M.G., 2009. Contractional structures and deformational events in the Bowen, Gunnedah and Surat Basins, eastern Australia. *Australian Journal of Earth Sciences*, 56:2: 477–499. doi:10.1080/08120090802698745.

Mortimer, N., Hauff, F. and Calvert, A.T., 2009. Continuation of the New England Orogen, Australia, beneath the Queensland Plateau and Lord Howe Rise, *Australian Journal of Earth Sciences*, 55:2, 195-209. doi:10.1080/08120090701689365.

Raza, A., Hill, K.C. and Korsch, R.J., 2009. Mid-Cretaceous uplift and denudation of the Bowen and Surat Basins, eastern Australia: relationship to Tasman Sea rifting from apatite fission-track and vitrinite-reflectance data, *Australian Journal of Earth Sciences*, 56:3, 501-531.

SBEA (1994). Sedimentary Basins of Eastern Australia, Geoscience Australia, <http://www.ga.gov.au/metadata-gateway/metadata/record/14696/>.

Sliwa, R. and Esterle, J., 2008. Re-evaluation of structure and sedimentary packages in the eastern Surat Basin. In Blevin J.E., Bradshaw, B.E. and Uruski C. (eds.), Eastern Australasian Basins Symposium, 3, 527. Petroleum Exploration Society of Australia, Special Publication.

Sliwa, R., Mckillop, M., Esterle, J. and Foster, L., 2014. A consistent regional correlation for the Surat Basin, SE QLD. Department of Natural Resources and Mines, Office of Groundwater Impact Assessment.

Totterdell, J.M., Moloney, J., Korsch, R.J. and Krassay, A.A., 2009. Sequence stratigraphy of the Bowen-Gunnedah and Surat Basins in New South Wales. Australian Journal of Earth Sciences, 56, 433–459. doi:10.1080/08120090802698729.

Wainman, C.C., McCabe, P.J., Crowley, J.L. and Nicoll, R.S., 2017. U–Pb zircon age of the Walloon Coal Measures in the Surat Basin, southeast Queensland: implications for paleogeography and basin subsidence.

Waschbusch, P., Korsch, R.J. and Beaumont, C., 2009. Geodynamic modelling of aspects of the Bowen, Gunnedah, Surat and Eromanga Basins from the perspective of convergent margin processes. Australian Journal of Earth Sciences, 56, 309–34.

Woodfull, C., 2008. Bowen and Surat Basins Regional Structural Framework Study. Report and CD, Queensland Department of Natural Resources and Mines. http://nrmlibrary.com.au/record/669/bowen_and_surat_basins_regional_structural_framework_study.

11.2 Potential field Interpretation

Amante, C. and Eakins, B.W., 2009. ETOPO1 1 Arc-Minute Global Relief Model: Procedures, Data Sources and Analysis. NOAA Technical Memorandum NESDIS NGDC, National Geophysical Data Center-24, NOAA. doi:10.7289/V5C8276M.

Babaahmadi, A. and Rosenbaum, G., 2014. Late Mesozoic and Cenozoic wrench tectonics in eastern Australia: Insights from the North Pine Fault System (southeast Queensland). Journal of Geodynamics, 73, 83-99.

Babaahmadi, A. and Rosenbaum, G., 2016. Kinematics of orocline-parallel faults in the Texas and Coffs Harbour oroclines (eastern Australia) and the role of flexural slip during oroclinal bending. doi:10.1080/08120099.2015.1125388.

Babaahmadi, A., Sliwa, R. and Esterle, J., 2015. Understanding Faults in the Surat Basin, from interpretation of seismic lines, aeromagnetic and gravity data, report for Centre for Coal Seam Gas, The University of Queensland, Brisbane, Confidential.

Blakely, R.J., 1995. Potential Theory in Gravity and Magnetic Applications. Cambridge University Press, New York, 435pp.

- Brooke-Barnett, S. and Rosenbaum, G., 2015. Structure of the Texas Orocline beneath the sedimentary cover (southeast Queensland, Australia). *Australian Journal of Earth Sciences* 62, 425-445.
- Cooper, G.R.J. and Cowan, D.R., 2005. Differential reduction to the pole. *Computers & Geosciences*, 31, 989-999.
- Exon, N.F., 1976. *Geology of the Surat Basin in Queensland*, 166. Bureau of Mineral Resources, Geology and Geophysics, Canberra.
- Glen, R.A., 2013. Refining accretionary orogen models for the Tasmanides of eastern Australia. *Australian Journal of Earth Sciences* 60, 315-370.
- Glen, R.A. and Beckett, J., 1997. Structure and tectonics along the inner edge of a foreland basin: The Hunter Coalfield in the northern Sydney Basin, New South Wales. *Australian Journal of Earth Sciences* 44, 853-877.
- Glen, R.A., 2005. The Tasmanides of eastern Australia, In: Vaughan, A.P.M., Leat, P.T. and Pankhurst, R.J. (eds). *Terrane Processes at the Margins of Gondwana*. Special Publication of The Geological Society, London, 246, 23-96.
- Kassan, J., 1994. Basin analysis of the Triassic succession, Bowen Basin, Queensland. The University of Queensland, unpublished PhD thesis.
- Korsch, R.J. and Totterdell, J.M., 2009. Subsidence history and basin phases of the Bowen, Gunnedah and Surat Basins, eastern Australia. *Australian Journal of Earth Sciences*, 56, 335-353.
- Korsch, R.J., Totterdell, J.M., Cathro, D.L. and Nicoll, M.G., 2009a. Early Permian East Australian Rift System. *Australian Journal of Earth Sciences*, 56, 381-400.
- Korsch, R.J., Totterdell, J.M., Fomin, T. and Nicoll, M.G., 2009b. Contractional structures and deformational events in the Bowen, Gunnedah and Surat Basins, eastern Australia. *Australian Journal of Earth Sciences*, 56(3), 477-499.
- Miller, H., G. and Singh, V., 1994. Potential field tilt-a new concept for location of potential field sources. *Journal of Applied Geophysics*, 32, 213-217.
- Nabighian, M., Grauch, V., Hansen, R., LaFehr, T., Li, Y., Peirce, J., Phillips, J. and Ruder, M., 2005. The historical development of the magnetic method in exploration. *GEOPHYSICS*, 70(6), 33-61.
- Ryan, D.J., Hall, A., Erriah, L. and Wilson, P.B., 2012. The Walloon coal seam gas play, Surat Basin, Queensland. *APPEA Journal*, 52, 273-289.
- Swain, C.J., 2000. Reduction-to-the-pole of regional magnetic data with variable field direction, and its stabilisation at low inclinations. *Exploration Geophysics*, 31, 078-083.

Sliwa, R., 2013. Eastern Surat Basin structural framework from 2D seismic interpretation. Arrow Energy Limited, Confidential.

11.3 Integrated well-seismic interpretation

Ben-Avraham, Z. and Zoback, M.D., 1992. Transform-normal extension and symmetric basins: An alternative to pull-apart models; *Geology*, 20, 423-426.

Dixon, O., Hoffmann, K.L. and Simpson, G.A, 1993. Progress report on the sequence stratigraphic interpretation of seismic data from the Roma transect, Bowen & Surat Basins, Queensland. Queensland Department of Minerals and Energy, Queensland Geological Record, 1993, 24.

Dixon, O., Mckillop, M. and Hodgkinson, J., 2011: Seismic horizon mapping in the Surat Basin – refinement of key stratigraphic surfaces as a foundation for subsurface fluid flow modelling. Queensland Geological Record, 2011, 06.

Hoffmann, K.L., Totterdell, J.M., Dixon, O., Simpson, G.A., Brakel, A.T., Wells, A.T. and Mckellar, J.L., 2009. Sequence stratigraphy of Jurassic strata in the lower Surat Basin succession, Queensland. *Australian Journal of Earth Sciences*, 56, 461–476. doi: 10.1080/08120090802698737.

Jell, P.A. (Peter A.) and Jell, P.A. (Peter A.), (ed), 2013. *Geology of Queensland*. Brisbane, Queensland Geological Survey of Queensland.

Wartenberg, W., 2005. The concealed Tamworth Belt (New England Orogen) - stratigraphic and geophysical observations depicting a thrust-related geometry in southern Queensland, Australia. Unpublished Doctorate Thesis, Faculty of Mathematics and Natural Science, University of Bonn.

Wells, A.T. (Allan Thomas) and Australian Geological Survey Organisation, 1994. Sequence stratigraphic interpretation of seismic data north of 26°S, Bowen and Surat Basins, Queensland. Australian Geological Survey Organisation, Canberra.

Zhou, F., Esterle, J. and Tyson, S., 2015. An integrated geological framework for the Surat Basin. Centre for Coal Seam Gas Milestone Report.

Ziolkowski, V., Hodgkinson, J., McKillop, M., Grigorescu, M. and McKellar, J.L., 2014 Sequence stratigraphic analysis of the Lower Jurassic succession in the Surat Basin, Queensland – preliminary findings Queensland Minerals and Energy Review Series, Queensland Department of Natural Resources and Mines CD ROM.

11.4 Image Log Analysis

Aadnoy, B.S., 1990. Inversion technique to determine the in-situ stress field from fracturing data. *Journal of Petroleum Science and Engineering*, 4, 127-141.

Bell, J.S., 1990. The stress regime of the Scotian Shelf offshore eastern Canada to 6 kilometres depth and implications for rock mechanics and hydrocarbon migration. In Maury, V. and

Fourmaintraux, D. (eds) *Rock at Great Depth*. Balkema, Rotterdam, 1243-1265.

Bell, J.S. and Gough, D.I., 1982. *The Use of Borehole Breakouts in the Study of Crustal Stresses*. U.S. Geological Survey, Open File Report 82-1075, 539-557.

Brooke-Barnett, S., Flottmann, T., Paul, P.K., Hennings, P., Buseti, S., Reid, R. and Rosenbaum, G., 2015. Influence of basement structures on in situ stresses over the Surat Basin, southeast Queensland. *Journal of Geophysical Research Solid Earth*, 120. doi:10.1002/2015JB011964.

Burbidge, D.R., 2004. Thin plate neotectonic models of the Australian plate. *Journal of Geophysical Research: Solid Earth*, 109, B10405. doi:10.1029/2004JB003156.

Dershowitz, W.S. and Herda, H., 1992. *Interpretation of Fracture Spacing and Intensity*, Proc. 33rd. U.S. Symp. on Rock Mechanics, Balkema.

Flottmann, T., Brooke-Barnett, S. and Trubshaw, R. et al., 2013. Influence of in-situ stresses on fracture stimulations in the Surat Basin, southeast Queensland. Paper SPE 167064-MS, presented at the SPE Unconventional Resources Conference and Exhibition-Asia Pacific, 11–13 November 2013, Brisbane, Australia. doi:10.2118/167064-MS.

Heidbach, O., Rajabi, M. and Reiter, K. et al., 2016. *World Stress Map Database Release 2016*. GFZ Data Services. doi:10.5880/WSM.2016.001

Johnson, R.L., Glassborow, B. and Scott, M.P. et al., 2010. Utilizing Current Technologies to Understand Permeability, Stress Azimuths and Magnitudes and their Impact on Hydraulic Fracturing Success in a Coal Seam Gas Reservoir. *Society of Petroleum Engineers*. doi:10.2118/133066-MS.

Liu, S., and Harpalani, S., 2014. Evaluation of in situ stress changes with gas depletion of coalbed methane reservoirs. *Journal of Geophysical Research: Solid Earth*, 119(8), 6263-6276. doi:10.1002/2014JB011228.

Mauldon, M. and Dershowitz, W., 2000. A Multi-dimensional system of fracture abundance measures, Summit 2000, Geological Society of America Annual Meeting, Nevada.

Mukherjee, S., Zhou, F., Copley, J., Babaahmadi, A., and Esterle, J., 2016. Milestone 3a: Borehole image log analysis in the Eastern Surat. UQ Centre for Coal Seam Gas internal monitors report.

OGIA, 2016a. *Hydrogeological conceptualisation report for the Surat Cumulative Management Area*. Department of Natural Resources and Mines Office of Groundwater Impact Assessment, Queensland.

Oz SEEBASETM, 2005. Public domain report to Shell Development Australia by FrOG Tech Pty Ltd., Brisbane.

QDEX 2016. www.business.qld.gov.au/industry/mining/mining-online-services/qdex-data.

Rajabi, M., Tingay, M. and Heibach, O. et al., 2017a. The present-day stress field of Australia, *Earth-Science Reviews*, 168, 165-189, ISSN 0012-8252. doi:10.1016/j.earscirev.2017.04.003.

Rajabi, M., Tingay, M., King, R., and Heibach, O., 2016. Present-day stress orientation in the Clarence-Moreton Basin of New South Wales, Australia: a new high density dataset reveals local stress rotations. *Basin Research*, n/a-n/a. doi: 10.1111/bre.12175Reilly, personal comm., 2016.

Richardson, R.M., 1992. Ridge forces, absolute plate motions and the intraplate stress field, *Journal of Geophysical Research*, 97, 11,739–11,748. doi:10.1029/91JB00475.

Zoback, M.D., Moos, D. and Mastin, L., 1985. Wellbore Breakouts and in Situ Stress. *Journal of Geophysical Research*, 90, B7, 5523-5530.

Zoback, M.L., Zoback, M.D. and Adams, J. et al., 1989. Global patterns of tectonic stress, *Nature*, 341, 291–298.

Zoback, M. L., et al., 1989. Global patterns of tectonic stress, *Nature*, 341, 291–298. *Journal of Geophysical Research: Solid Earth* 10.1002/2015JB011964.

Zoback, M.L., 1992. First- and second-order patterns of stress in the lithosphere: The World Stress Map Project, *Journal of Geophysical Research*, 97, 11,703–11,728. doi:10.1029/92JB00132.

Zoback, M.D., 2007. *Reservoir Geomechanics*, Cambridge University Press, Cambridge, U.K.

11.5 Mine site photogrammetry and joints

Babaahmadi, A. and Rosenbaum, G., 2014a. Late Cenozoic intraplate faulting in eastern Australia. *Journal of Structural Geology*, 69, 59-74.

Babaahmadi, A. and Rosenbaum, G., 2014b. Late Mesozoic and Cenozoic wrench tectonics in eastern Australia: Insights from the North Pine Fault System (southeast Queensland). *Journal of Geodynamics*, 73, 83-99.

Babaahmadi, A. and Rosenbaum, G., 2015. Kinematics of oroclinal-parallel faults in the Texas and Coffs-Harbour oroclines (eastern Australia) and the role of flexural slip during oroclinal bending. *Australian Journal of Earth Sciences*, 62, 933-948.

Babaahmadi, A., Sliwa, R. and Esterle, J., 2015. Understanding Faults in the Surat Basin, from interpretation of seismic lines, aeromagnetic and gravity data, report for Centre for Coal Seam Gas, The University of Queensland, Brisbane, Confidential.

Babaahmadi, A., Titheridge, D., Rudd, R., Pistellato, D. and Esterle, J., 2016. Milestone 3b: Minescale study of joints and cleat as input to discrete fracture network model. CCSG Internal Report.

FrogTech, 2006. OZ SEEBASE™ Proterozoic Basins Study. Report to Geoscience Australia by FrogTech Pty Ltd.

Kattenhorn, S.A., Aydin A. and Pollard, D.D., 2000. Joints at high angles to normal fault strike: an explanation using 3-D numerical models of fault-perturbed stress fields. *Journal of structural Geology*, 22, 1-23.

Korsch, R.J., Totterdell, J.M., Fomin, T. and Nicoll, M.G., 2009. Contractional structures and deformational events in the Bowen, Gunnedah and Surat Basins, eastern Australia. *Australian Journal of Earth Sciences*, 56, 477-499.

Li, P., Rosenbaum, G. and Donchak, P.J.T., 2012. Structural evolution of the Texas Orocline, eastern Australia. *Gondwana Research*, 29, 279-289.

Rudd, R., 2016. Variation in Joint Spacing in Layered Sedimentary Rocks, Walloon Coal Measures. Unpublished Honours Thesis, The University of Queensland.

11.6 Discrete Fracture Network Modelling

Babaahmadi, A., Titheridge, D., Rudd, R., Pistellato, D. and Esterle, J., 2016. Milestone 3b: Minescale study of joints and cleat as input to discrete fracture network model. CCSG Internal Report.

Bonilla-Sierra V., Scholtès L., Donzé F.V. and Elmouttie, M.K., 2015. Rock slope stability analysis using photogrammetric data and DFN–DEM modelling. *Acta Geotechnica*, 10(4), 497-511.

Close, J.C. and Mavor, M.J., 1991. Influence of coal composition and rank on fracture development in Fruitland coal gas reservoirs of San Juan Basin. In Schwochow, S., Murray, D.K., Fahy, M.F. (eds), *Coalbed Methane of Western North America*. Rk. Mt. Assoc. Geol., Field Conference, 109-121.

CSIRO, 2011. Large Open Pit Mine Slope Stability Project. <http://www.lop.csiro.au/>.

Darcel C., Davy, P., Bour O., de Dreuzay J.R., 2006. Discrete fracture network for the Forsmak site. SKB Report R-06-79. <http://www.skb.com/publication/1169119/R-06-79.pdf>.

Deisman, N., Gentzis, T. and Chalaturnyk, R.J., 2008. Unconventional geomechanical testing on coal for coalbed reservoir well design: The Alberta Foothills and Plains. *International Journal of Coal Geology*, 75, 15-26.

Elmouttie, M.K. and Poropat, G.V., 2011. Uncertainty propagation in structural modelling. *Proceedings, Slope Stability, Vancouver*.

Erzeybek, S., Srinivasan, S., Janson, X., 2012. Multiple-point statistics in a non-gridded domain: Application to karst/fracture network modelling. *Quantitative Geology and Geostatistics*, 17, 221-237.

Fisher Distribution, 2016.

https://rocscience.com/help/swedge/webhelp/swedge/Fisher_Distribution.htm (accessed on 13 December 2016).

Fisher, R.A., 1953. Dispersion on a sphere. *Proceedings of the Royal Society of London, Series A*, 217, 295-305.

Gao, F., Stead, D. and Kang, H., 2014a. Numerical investigation of the scale effect and anisotropy in the strength and deformability of coal. *International Journal of Coal Geology*, 136, 25-37.

Gao, F., Stead, D., Kang, H. and Wu, Y., 2014b. Discrete element modelling of deformation and damage of a roadway driven along an unstable goaf – a case study. *International Journal of Coal Geology*, 127, 100-110.

Gómez-Hernández, J., 1991. A stochastic approach to the simulation of block fields conductivity upon data measured at a smaller scale. PhD thesis, Stanford University, Stanford.

Gong, B., Zhang, Y., Fan, Y. and Qin, G., 2014. A novel approach to model enhanced coal bed methane recovery with discrete fracture characterizations in a geochemical simulator. *Journal of Petroleum Science and Engineering*, 124, 198-208.

Jing, Y., Armstrong, R.T., Ramandi, H.L. and Mostaghimi, P., 2016. Coal cleat reconstruction using micro-computed tomography imaging. *Fuel*, 181, 286-299.

Laubach, S.E., Marrett, R.A., Olson, J.E. and Scott, A.R., 1998. Characteristics and origins of coal cleat: a review. *International Journal of Coal Geology*, 35, 175-207.

Mazumder, S., Wolf, K.H.A.A, Elewaut, K. and Ephraim, R., 2006. Application of X-ray computed tomography for analyzing cleat spacing and cleat aperture in coal samples. *International Journal of Coal Geology*, 68, 205-222.

Mukherjee, S., Zhou, F., Copley, J., Babaahmadi, A. and Esterle, J., 2016. Milestone 3A: Borehole image log analysis in the Eastern Surat. Internal CCSG Report.

Nelson, R.A., 2001. *Geologic Analysis of Naturally Fractured Reservoirs*, 2nd ed. Gulf Professional Publishing, Houston, Texas, USA.

Okabe, H. and Blunt, M.J., 2005. Pore space reconstruction using multiple-point statistics. *Journal of Petroleum Science and Engineering*, 46, 121-137.

Pashin, J.C., Jin, G., Zheng, C., Chen, S. and McIntyre, M.R., 2008. Discrete fracture network models for risk assessment of carbon sequestration in coal. Final technical Report DE-FC26-05NT42435, U.S. Department of Energy, National Energy Technology Laboratory, 124.

Petrel, 2014. Petrel Help Center. Schlumberger.

Poropat G., 2001. New methods for mapping the structure of rock masses. *EXPLO 2001 Conference Proc.*

Rezaee, H., Marcotte, D., Tahmasebi, P. and Saucier, A., 2015. Multiple-point geostatistical simulation using enriched pattern databases. *Stochastic Environmental Research and Risk Assessment*, 29, 893-913.

Schlumberger. High-definition formation microimager, 2013. Available online: www.slb.com/fmi-hd (accessed on 23 November 2016).

Strebelle, S.B., 2002. Conditional simulation of complex geological structures using multiple-point statistics. *Mathematical Geology*, 34, 1-21.

Strebelle, S.B. and Journel, A.G., 2001. Reservoir modeling using multiple-point statistics. SPE paper 71324 presented at the SPE Annual Technical Conference and Exhibition held in New Orleans, Louisiana, 1-11.

Weatherford Compact Microimager, 2013. <http://www.weatherford.com/doc/wft268562> (accessed on 23 November 2016).

Weatherford, 2013. Compact Microimager. <http://www.weatherford.com/doc/wft268562>.

Zhang, T., Bombarde, S., Strebelle, S.B. and Oatney, E., 2006. 3D Porosity Modeling of a Carbonate Reservoir Using Continuous Multiple-Point Statistics Simulation. *SPE Journal*, 11(3), 375-379.

Zhou, F. and Yao, G., 2014. Sensitivity analysis in permeability estimation using logging and injection-falloff test data for an anthracite coalbed methane reservoir in southeast Qinshui Basin, China. *International Journal of Coal Geology*, 131, 41-51.

Zhou, F., Mukherjee, S., Li, Q. and Esterle, J., 2016. Milestone 3D: Discrete Fracture Network Modelling. UQ Centre for Coal Seam Gas internal monitors report.

11.7 Coal strength and fracture toughness

Barbosa, K., Bonfils, B. and Esterle, J., 2017. Coal Strength and Fracture Toughness Testing for Synthetic Rock Mass Models. Unpublished UQ Centre for Coal Seam Gas PhD thesis internal report.

Baumgardt, S., Buss, B., May, P. and Schubert, H., 1975. On the comparison of results in single grain crushing under different kinds of load. *Proc. 11th International Journal of Mineral Processing. Congr., Cagliari*, 3-32.

Bourgeois, F. S., and Banini, G.A., 2002. A portable load cell for in-situ ore impact breakage testing. *International Journal of Mineral Processing*, 65(1), 31-54.

Dan, C.C. and Schubert, H., 1990. Breakage probability, progeny size distribution and energy utilization of comminution by impact. *Aufbereit.-Tech.*, 31, 241-247.

Deisman, N., 2016. Geomechanical characterization of coal for CBM reservoir engineering. University of Alberta PhD thesis.

Esterle, J., 2008. Mining and beneficiation in Suarez-Ruiz, I. and Crelling, J.C. (eds) applied coal petrology: The role of petrology in coal utilisation. Elsevier, 61-83.

Esterle, J., Thornton, D., O'Brien, G. and Cocker, A., 2000. Optimising coal fragmentation for improved recovery. Final Report for ACARP Project C6046.

Esterle, J., Kolatschek, Y. and O'Brien, G., 2002. Relationship between in situ coal stratigraphy and particle size and composition after breakage in bituminous coals. *International Journal of Coal Geology*, 49, 195-214.

Hawkes, C.D. Assessing the mechanical stability of horizontal boreholes in coal. *Canadian Geotechnical Journal*, 44(7), 797.

Hentschel, A., Esterle, J., Golding, S.D. and Pacey, D.V., 2016. Petrologic and stable isotopic study of the Walloon Coal Measures, Surat Basin, Queensland: peat accumulation under changing climate and base level. *International Journal of Coal Geology*, 15, Vol. 160-161, 11-27.

Hoek, E. and Brown, E.T., 1997. Practical estimates of rock mass strength. *International Journal of Rock Mechanics and Mining Sciences*, 34(8), 1165-1186.

Hopkinson, B., 1914. A method for measuring the pressure produced in the detonation of bullets. *Philos. Trans.*

Hower, J.C., Graese, A.M. and Klapheke, J.G., 1987. Influence of microlithotype composition on hardgrove grindability for selected eastern Kentucky coals. *International Journal of Coal Geology*, 7(3), 227-244.

King, R.P. and Bourgeois, F., 1993. Measurement of fracture energy during single-particle breakage. *Minerals Engineering*, 6, 353-367.

Klawitter, M., Esterle, J. and Sarah Collins, S., 2015. A study of hardness and fracture propagation in coal. *International Journal of Rock Mechanics and Mining Sciences* 76, 237–242.

Mark, C. and Barton, T.M., 1997. Pillar design and coal strength. In Mark, C. and Tuchman, R.J. (eds). *Proceedings: New technology for ground control in retreat mining*. NIOSH Information Circular 9446, 49-59.

Medhurst, T.P., 1996. Estimation of the in-situ strength and deformability of coal for engineering design. PhD thesis. Brisbane: The University of Queensland.

Medhurst, T.P. and Brown, E.T., 1998. A study of the mechanical behaviour of coal for pillar design. *International Journal of Rock Mechanics and Mining Sciences and Geomechanics Abstracts*, 35(8), 1087-1105.

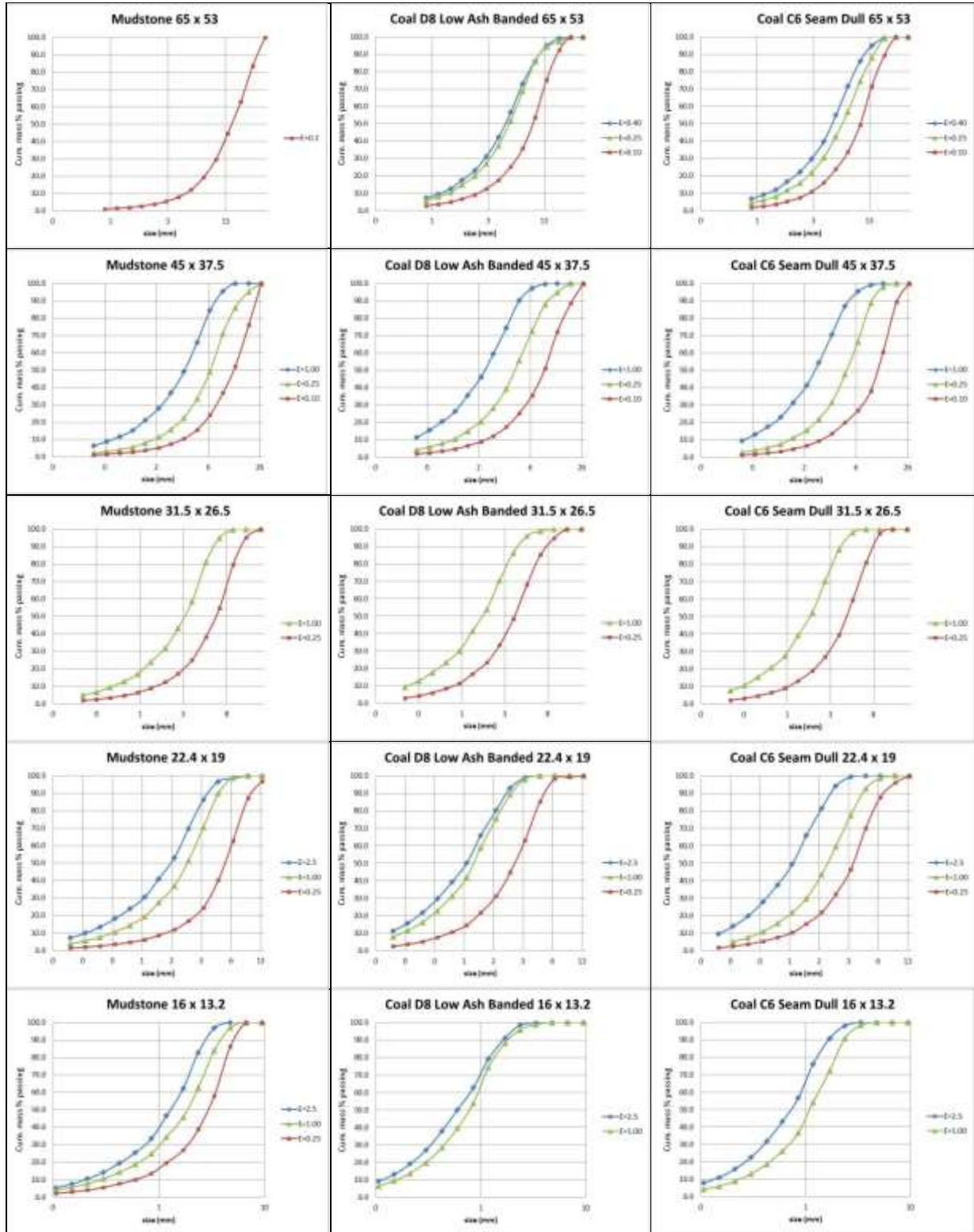
Narayanan, S.A., Lean, P.J. and Baker, D.C., 1987. Relationship between breakage parameters and process variables in ball milling - An industrial case study. *International Journal of Mineral Processing*, 20, 241-251.

- Narayanan, S.S. and Whiten, W.J., 1988. Determination of comminution characteristics from single particle breakage tests and its application to ball mill scale up. *Trans Inst Min Metall*, 97, C115-124.
- Napier-Munn, T.J., 1996. *Mineral Comminution Circuits: their Operation and Optimisation*. Julius Kruttschnitt Mineral Research Centre.
- Nazir, R., Momeni, E., Armaghani, D.J. and Amin, M.F.M., 2013. Compressive strength and indirect tensile strength of limestone rock samples. *Electronic Journal of Geotechnical Engineering (EJGE)*, 18, bund. I.
- Palmer, I., Moschovidis, Z.A. and Cameron, J., 2005. Coal failure and consequences for coalbed methane wells. SPE No. 96872, Society of Petroleum Engineers Annual Technical Conference and Exhibition. Dallas, Texas, USA, Oct. 9-12.
- Perras, M.A. and Diederichs, M.S., 2014. A review of the tensile strength of rock: concepts and testing. *Geotechnical and Geological Engineering*, 32, 525-546.
- Stach, E., Mackowsky, M.Th., Teichmuller, M., Taylor, G.H., Chandra, D. and Teichmuller, R., (eds), 1982. *Coal Petrology*. Gebruder Borntraeger, Berlin - Stuttgart, 535.
- Tavares, L.M. and King, R.P., 1998a. Microscale Investigation of Thermally Assisted Comminution, in *Proceedings of the XIX IMPC*, Chapter 36, 203-208.
- Tavares, L.M. and King, R.P., 1998b. Single-particle fracture under impact loading. *International Journal of Mineral Processing*, 54, 1-28.

12 Appendices

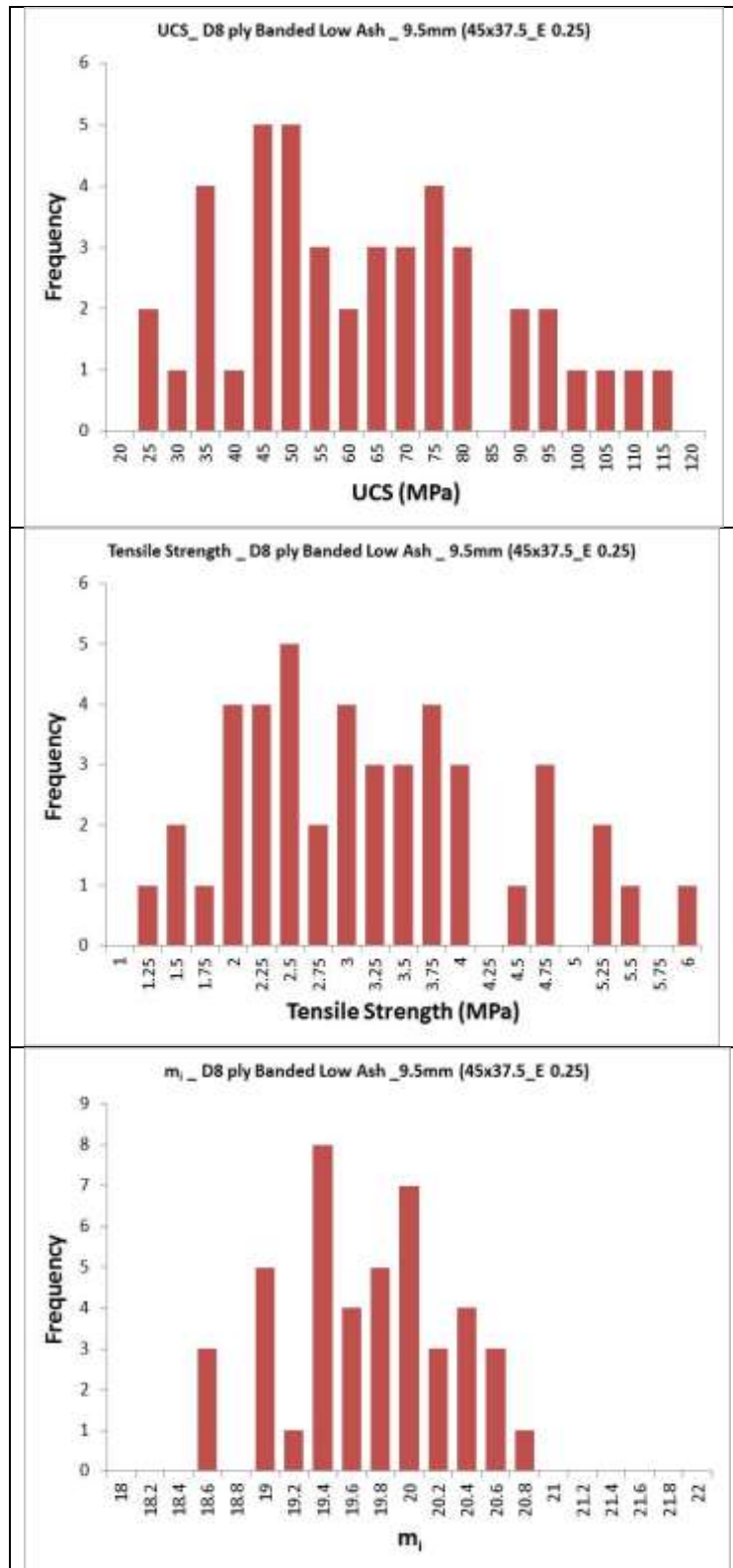
12.1 Appendix 1

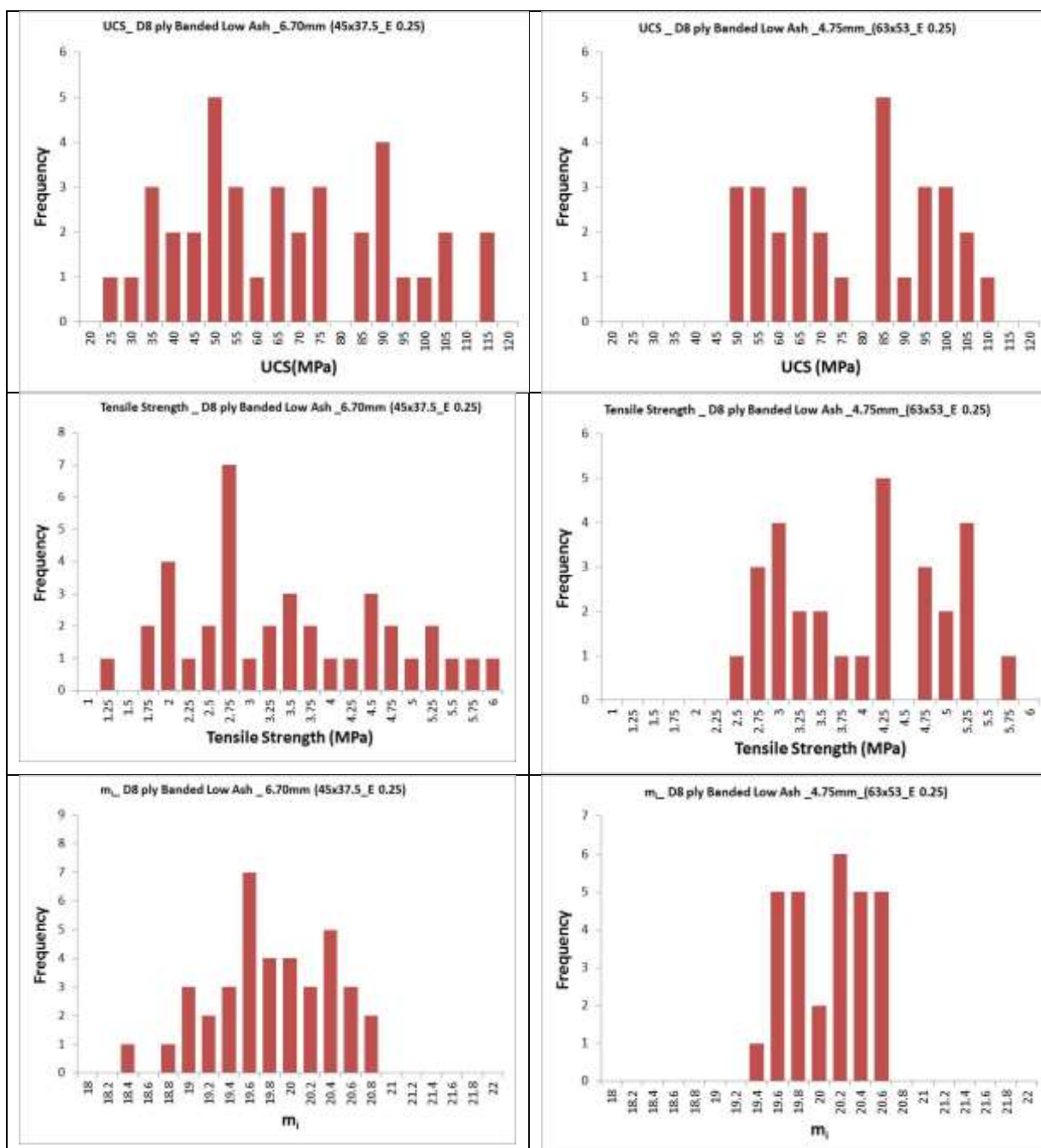
12.1.1 JK DWT: The mass distribution as a function of particle size for different samples



12.2 Appendix 2

12.2.1 SILC particles





12.3 Appendix 3

12.3.1 SSRH

